Hadron Resonance Gas and Nonperturbative QCD Vacuum at Finite Temperature

N. O. Agasian* and S. M. Fedorov**

Institute of Theoretical and Experimental Physics, ul. Bol'shaya Cheremushkinskaya 25, Moscow, 117218 Russia
*e-mail: agasian@heron.itep.ru
**e-mail: fedorov@heron.itep.ru
Received October 2, 2003

Nonperturbative QCD vacuum with two light quarks at finite temperature was studied in a hadron resonance-gas model. Temperature dependences of the quark and gluon condensates in the confined phase were obtained. It is shown that the quark condensate and one-half (chromoelectric component) of the gluon condensate are evaporated at the same temperature corresponding to the quark–hadron phase transition. With allowance for the temperature shift of hadron masses, the critical temperature was found to be $T_c \simeq 190$ MeV. © *2003 MAIK "Nauka/Interperiodica".*

PACS numbers: 12.38.Mh; 12.38.Lg; 11.10.Wx

1. It is known that the phase transition from the hadron phase characterized by the confinement and spontaneous breaking of chiral symmetry to the phase of hot quark–gluon matter occurs at a finite temperature in QCD. The thermodynamic characteristics of the system such as energy density ε, specific heat, "nonideality" $(\varepsilon - 3P)/T^4$, etc. substantially change their behavior at the critical point T_c of phase changing. Moreover, the quark–gluon vacuum is strongly rearranged upon the phase transition in QCD.

Lattice calculations in finite-temperature QCD show that deconfinement and reconstruction of the chiral symmetry occur at the same temperature, and the critical temperature for two light quarks ($N_f = 2$) lies in the interval $T_c \sim 175$–190 MeV [1, 2]. According to the lattice analysis of QCD thermodynamics and experimental data on high-energy collisions, the energy density of the system at the quark–hadron phase transition is $\varepsilon_c \sim 1$–1.5 GeV/fm³.

Recent numerical simulations on lattice for the SU(3) gauge theory without quarks and in QCD with $N_f = 2$ revealed a strong suppression of the electric component and a slight increase in the magnetic component of the gluon condensate as the temperature increases and passes through the critical temperature T_c [3]. This behavior was theoretically predicted by various methods ten years ago in [4, 5]. More recently, the temperature dependence of the gauge-invariant bilocal chromomagnetic field-strength correlator and spacelike string tension $\sigma_s(T)$ was analytically determined in [6]. It was found that the chromomagnetic condensate increases only slightly with temperature at $T < 2T_c$, $\langle H^2 \rangle_T = \langle H^2 \rangle_0 \coth(M/2T)$, where $M = 1/\xi_m \simeq 1.5$ GeV is the inverse magnetic correlation length that is independent of temperature at $T < 2T_c$. With an increase in temperature in the region $T > 2T_c$, the amplitude of the magnetic correlator increases as $\langle H^2 \rangle_T \propto g^8(T)T^4$, and the correlation length decreases as $\xi_m(T) \propto 1/(g^2(T)T)$. In the framework of the stochastic-vacuum model, this behavior of the magnetic correlator explains the magnetic confinement phenomenon. The temperature dependence obtained for the spacelike string tension fully agrees with the lattice data over the entire temperature range [7].

Thus, taking into account the above circumstances, it is necessary to show in a unified approach that, at the critical point $T_c \sim 175$–190 MeV in QCD with $N_f = 2$, the energy density is $\varepsilon_c \sim 1$–1.5 GeV/fm³, the quark condensate $\langle \bar{q}q \rangle_T$ turns (or tends) to zero, and only one-half (the chromoelectric component responsible for the formation of string and confinement) of the gluon condensate is evaporated, which is necessary for magnetic confinement to be retained.

In this work, we study the properties of quark and gluon condensates within the approach based on the description of the confined phase as a hadron resonance gas. We show that the phenomena described above can be quantitatively explained in this approach with due allowance for the temperature shift of hadron masses.

2. We consider QCD with two light quarks. In this case, knowing the pressure in the hadron phase $P_h(T)$ and using the Gell-Mann–Oakes–Renner relation, one can find the temperature dependence of quark condensate

$$\frac{\langle \bar{q}q \rangle_T}{\langle \bar{q}q \rangle_0} = 1 - \frac{1}{F_\pi^2}\frac{\partial P_h(T)}{\partial m_\pi^2}, \tag{1}$$

where $F_\pi = 93$ MeV is the axial π-meson decay constant. The expression for the gluon condensate $\langle C^2 \rangle_T \equiv \langle (gC_{\mu\nu}^a)^2 \rangle_T$ was obtained in [8] on the basis of renormalization-group consideration of the anomalous contribution to the trace of the energy–momentum tensor in QCD with $N_f = 2$ at a finite temperature. The gluon condensate is related to the thermodynamic pressure in QCD by [8]

$$\langle G^2 \rangle_T = \langle G^2 \rangle_0 + \frac{32\pi^2}{b}\left(4 - T\frac{\partial}{\partial T} - m_\pi^2 \frac{\partial}{\partial m_\pi^2}\right)P_h(T), \quad (2)$$

where $b = 11N_c/3 - 2N_f/3 = 29/3$ and $\langle G^2 \rangle_0 = 0.87$ GeV^4 [9]. When deriving Eq. (2), the low-energy QCD theorems [10] and the Gell-Mann–Oakes–Renner relation between the mass of light quark and the mass of π meson were used. Expressions for $\langle \bar{q}q \rangle_T$ and $\langle G^2 \rangle_T$ in QCD with $N_f = 3$ were obtained in [11]. Thus, knowing the pressure P_h as a function of temperature and π-meson mass, one can find the temperature dependence for the quark and gluon condensates in the hadron phase.

To describe QCD thermodynamics in the confined phase, we use the hadron resonance-gas model. In this approach, the thermodynamic properties of the system are determined by the overall pressure of relativistic Bose and Fermi gases that describe the thermal excitations of massive hadrons. The use of this approach is primarily motivated by the fact that all essential degrees of freedom of a strongly interacting matter are included in the consideration. Moreover, the use of the hadron resonance spectrum effectively takes into account the interaction between stable particles. In addition, the application of the hadron resonance-gas model to the multiparticle production in heavy-ion collisions [12] gives good agreement with experimental data. Thus, the pressure in the confined phase is written as

$$P_h = T\sum_i g_i \eta_i \int \frac{d^3 p}{(2\pi)^3} \ln(1 + \eta_i e^{-\omega_i/T}),$$

$$\omega_i = \sqrt{p^2 + m_i^2}, \quad (3)$$

$$\eta_i = \begin{cases} +1, & \text{fermions} \\ -1, & \text{bosons,} \end{cases}$$

where g_i is the spin–isospin degeneracy factor (e.g., $g_\pi = 3$, $g_N = 8$, etc.). The energy density $\varepsilon_h = T\partial P_h/\partial T - P_h$ in the hadron phase is given by the formula

$$\varepsilon_h = \sum_i g_i \int \frac{d^3 p}{(2\pi)^3} \frac{\omega_i}{\exp(\omega_i/T) + \eta_i}. \quad (4)$$

3. For the quantitative investigation of condensates in the confined phase, it is necessary to know the pressure P_h as a function of the light-quark mass (for $N_f = 2$)

or, equivalently, as a function of the π-meson mass. In the hadron resonance-gas model, this is equivalent to knowing the masses of all resonances as functions of the light-quark mass. These functions were numerically studied in the lattice calculations, and Karsch *et al.* [13] proposed a five-parameter formula inspired by the bag model. With the appropriately chosen parameters, this formula well reproduces the masses of all particles considered in [13]:

$$m_i = N_u a_1 x \sqrt{\sigma} + \frac{m_h}{1 + a_2 x + a_3 x^2 + a_4 x^3 + a_5 x^4},$$

$$x \equiv m_\pi/\sqrt{\sigma},$$

$$a_1 = 0.51, \quad a_2 = a_1 N_u \sqrt{\sigma}/m_h, \quad (5)$$

$$a_3 = 0.115, \quad a_4 = -0.0223, \quad a_5 = 0.0028.$$

Here, m_h is the hadron physical mass, N_u is the number of light quarks ($N_u = 2$ for mesons and $N_u = 3$ for hadrons), and $\sigma = (0.42$ GeV$)^2$ is the string tension.

It is necessary to take into account that the hadron masses change with temperature. For the finite-temperature conform-generalized nonlinear sigma model with light and massive hadrons [14], it was shown that the temperature shift of hadron masses can be taken into account through the replacement

$$m_h \longrightarrow m_h(\chi_T/\chi_0), \quad m_\pi \longrightarrow m_\pi\sqrt{\chi_T/\chi_0},$$

$$\chi_T/\chi_0 = (\langle G^2 \rangle_T/\langle G^2 \rangle_0)^{1/4}, \quad (6)$$

where χ is the dilaton field. The fact that the dependence for the π-meson mass is different from the dependences for other particles is a manifestation of its Goldstone origin. In the chiral limit $m_q \longrightarrow 0$, the above relation for the hadron masses is a rigorous conclusion of the low-energy QCD theorems [10].

4. Formulas (1)–(6) determine the thermodynamic properties of the system in the hadron phase and allow the quark and gluon condensates to be calculated over the entire temperature range below the critical point T_c.

We take into account all hadron states with masses below 2.5 GeV for mesons and below 3.0 GeV for baryons. The number of these states (with allowance for the degeneracy factors g_i) is equal to 2078. It is clear that, for the temperatures below the pion mass $T < m_\pi = 140$ MeV, the main contribution to the thermodynamic quantities comes from the thermal excitations of π mesons, because other states are much heavier and suppressed exponentially by the Boltzmann factor $\propto\exp(-m_h/T)$. However, a large number of heavy states have an appreciable effect on the thermodynamics of the system at $T > m_\pi$. The pion contribution is shown by the dash–dotted line in Fig. 1. It is seen that, indeed, pions make the main contribution to P_h up to the temperature $T = 120$ MeV. At higher temperatures, the main contribution to pressure comes from the remaining had-
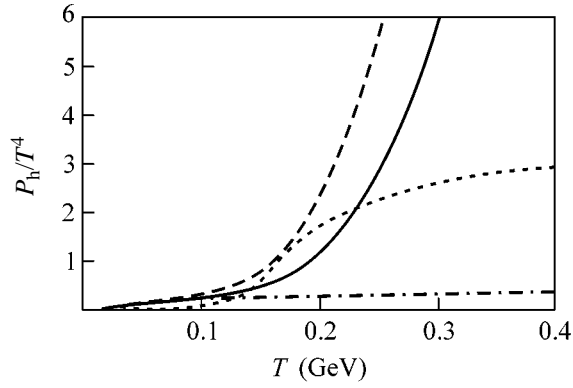
Fig. 1. Temperature dependence of P_h/T^4, where P_h is pressure. Solid line is the zero-temperature hadron spectrum, dashed line is the spectrum with the temperature shift for $\chi_T/\chi_0 = 0.84$, dash–dotted line is obtained including only pion excitations, and dotted line is lattice calculation [15].
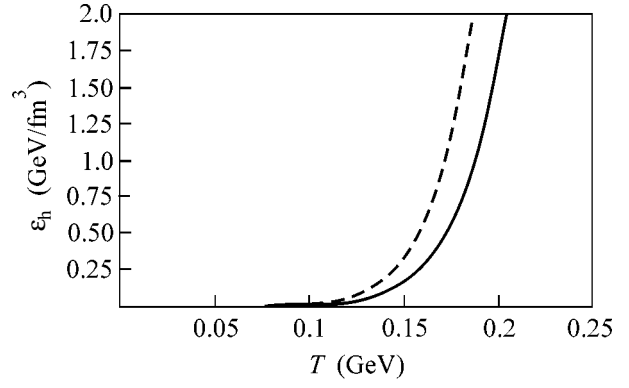

Fig. 2. Temperature dependence of the energy density ε_h. The solid line is the zero-temperature hadron spectrum and the dashed line is the spectrum with the temperature shift; $\chi_T/\chi_0 = 0.84$.
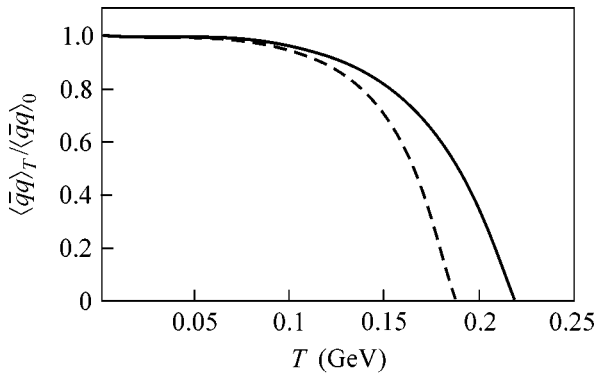

Fig. 3. Same as in Fig. 2, but for the quark condensate $\langle \bar{q}q \rangle_T / \langle \bar{q}q \rangle_0$.
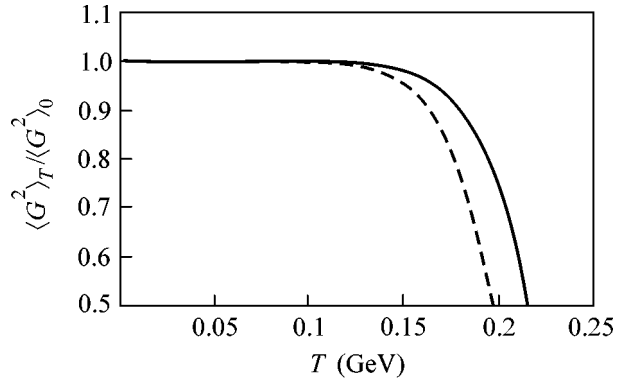

Fig. 4. Same as in Fig. 2, but for the gluon condensate $\langle G^2 \rangle_T / \langle G^2 \rangle_0$.

ron states. The lattice data [15] for pressure P_h in QCD with $N_f = 2$ are also shown in Fig. 1. It is seen that the hadron resonance-gas model with the temperature-induced mass shift correctly reproduces the increase in pressure with temperature in the range $T < T_c$.

Figure 2 shows the energy density ε_h as a function of temperature. A value of 1 GeV/fm³ corresponding to estimates of the energy density at the quark–hadron phase transition is achieved at $T \simeq 175$ MeV, i.e., in the phase-transition temperature range obtained in the lattice calculations [16].

Figures 3 and 4 show the temperature dependences of the quark and gluon condensates, respectively. It is essential that the quark condensate vanishes at the same temperature at which one-half of the gluon condensate is evaporated. With allowance for the temperature shift of hadron masses, this temperature is $T \simeq 190$ MeV.

Strictly speaking, the temperature shift of gluon condensate must be determined self-consistently (using the effective dilaton Lagrangian at $T \neq 0$) with allow-

ance for the hadron-mass shifts (see [14]). However, numerical calculations show that the gluon condensate decreases only slightly up to temperatures $\sim m_\pi$, and $\Delta \langle G^2 \rangle_T \approx 0.02 \langle G^2 \rangle_0$ at $T = m_\pi$. With an increase in temperature, $T > m_\pi$, the gluon condensate decreases dramatically and changes by $\sim 50\%$ mainly in a "rather narrow" temperature interval $\Delta T \sim 50$ MeV. Correspondingly, we present the results of numerical calculations with a hadron-mass temperature shift of 16% ($\chi_T/\chi_0 = 0.84 \simeq (0.5)^{1/4}$). We emphasize that the quark condensate and one-half of the gluon condensate are evaporated at the same temperature $T \sim 215$ MeV even if the temperature decrease in m_h is disregarded.

5. In this work, we have studied a nonperturbative QCD vacuum with two light quarks at a finite temperature in the hadron resonance-gas model. The temperature dependences of the quark and gluon condensates in the confined phase have been obtained. It was shown that the quark condensate and one-half (chromoelectric component) of the gluon condensate are evaporated at

the same temperature corresponding to the quark–hadron phase transition. This fact corroborates the pattern of magnetic confinement; i.e., the chromoelectric condensate vanishes upon the phase transition, while the chromomagnetic condensate remains virtually unchanged [3–6]. The energy density of the hadron resonance gas at the phase transition temperature is $\varepsilon_h(T_c) \sim 1.5$ GeV/fm^3. With allowance for the temperature shift of hadron masses, the critical temperature is $T_c \simeq 190$ MeV.

REFERENCES

1. F. Karsch, E. Laermann, and A. Peikert, Nucl. Phys. B **605**, 579 (2001).

2. Y. Nakamura, V. Bornyakov, M. N. Chernodub, *et al.*, hep-lat/0309144.

3. M. D'Elia, A. Di Giacomo, and E. Meggiolaro, Phys. Rev. D **67**, 114504 (2003).

4. Y. A. Simonov, JETP Lett. **55**, 627 (1992).

5. N. O. Agasian, JETP Lett. **57**, 208 (1993).

6. N. O. Agasian, Phys. Lett. B **562**, 257 (2003).

7. G. S. Bali, J. Fingberg, U. M. Heller, *et al.*, Phys. Rev. Lett. **71**, 3059 (1993); G. Boyd, J. Engels, F. Karsch, *et al.*, Nucl. Phys. B **469**, 419 (1996).

8. N. O. Agasian, Phys. Lett. B **519**, 71 (2001); JETP Lett. **74**, 353 (2001).

9. S. Narison, Phys. Lett. B **387**, 162 (1996).

10. V. A. Novikov, M. A. Shifman, A. I. Vainshtein, and V. I. Zakharov, Nucl. Phys. B **191**, 301 (1981); Sov. J. Part. Nucl. **13**, 224 (1982); A. A. Migdal and M. A. Shifman, Phys. Lett. B **114B**, 445 (1982).

11. N. O. Agasian, hep-ph/0212392.

12. P. Braun-Munzinger, D. Magestro, K. Redlich, and J. Stachel, Phys. Lett. B **518**, 41 (2001); J. Cleymans and K. Redlich, Phys. Rev. C **60**, 054908 (1999); Phys. Rev. Lett. **81**, 5284 (1998); F. Becattini, J. Cleymans, A. Keranen, *et al.*, Phys. Rev. C **64**, 024901 (2001).

13. F. Karsch, K. Redlich, and A. Tawfik, Eur. Phys. J. C **29**, 549 (2003).

14. N. O. Agasian, D. Ebert, and E.-M. Ilgenfritz, Nucl. Phys. A **637**, 135 (1998).

15. F. Karsch, E. Laermann, and A. Peikert, Phys. Lett. B **478**, 447 (2000).

16. F. Karsch, Lect. Notes Phys. **583**, 209 (2002).

Translated by R. Tyapaev

Search for the Resonance Environmental Effect on the Decay Periods of Long-Lived Nuclear Isomers

V. G. Alpatov, Yu. D. Bayukov, A. V. Davydov, Yu. N. Isaev, G. R. Kartashov, M. M. Korotkov, and V. M. Samoylov

Institute of Theoretical and Experimental Physics, ul. Bol'shaya Cheremushkinskaya 25, Moscow, 117218 Russia
Received September 8, 2003; in final form, October 21, 2003

Experiments on a search for the resonance environmental effect on the decay periods $T_{1/2}$ of long-lived nuclear isomers are described. It is shown that a change in $T_{1/2}$ obtained upon sample cooling in previous experiments with the ^{180m}Hf isomer is likely due to the insufficient correctness of the procedure used for separating γ peaks from the backgrounds in the measured γ spectra. The new approach to this problem reveals the absence of this effect for $T_{1/2}$ within an experimental accuracy of 1.2%. However, a difference of $2.25 \pm 0.77\%$ between the ^{103m}Rh decay periods $T_{1/2}$ was found for the solid and liquid γ sources. A control experiment with the ^{80m}Br isomer showed that, as expected, the decay periods $T_{1/2}$ for two temperatures coincide with each other within an accuracy of 1%. © 2003 MAIK "Nauka/Interperiodica".

PACS numbers: 21.10.Tg

Vysotskiĭ *et al.* [1–3] discussed the mechanism of controlling the decay periods of the excited nuclear states by perturbing the spectrum of zero-energy electromagnetic modes, which, in the opinion of Vysotskiĭ *et al.* [1–3], are responsible for the spontaneous electromagnetic transitions in nuclei. This perturbation is implemented by placing, near the γ sources, massive screens containing the same atoms as in the sources but with the nuclei in the ground states. In [4, 5], experiments revealed effects that could be treated as the corroboration of the predictions made in [1–3].

Recently, we carried out experiments [6] in order to find the resonance environmental effects on the decay periods $T_{1/2}$ of the ^{180m}Hf and ^{87m}Sr long-lived isomers. In our opinion, if a massive sample distorts the spectrum of zero-energy electromagnetic modes near its location, this effect can be caused only by the virtual photon exchange between the sample nuclei and the field of zero-energy modes. In this case, some nuclei in the sample would be in the virtual excited state, while the intensity of zero-energy modes in the corresponding energy range would decrease and, therefore, more weakly affect the γ decay of the source nuclei, thereby increasing $T_{1/2}$.

However, we note that some authoritative physicists consider spontaneous nuclear transitions independent of zero-energy electromagnetic modes (see, e.g., [7]).

The idea of our experiments was to enhance the assumed influence of the resonance sample on the zero-mode spectrum by narrowing the emission and absorption γ lines of the nuclei under study. This can be achieved, in particular, by cooling the sample and the nearby γ source. If the isomeric transition energy is low, cooling will create Mössbauer conditions for the corre-

sponding γ rays, and very narrow lines with noticeable (sometimes high) intensities will appear in the emission and absorption spectra. For high-energy γ transitions, narrow Mössbauer lines can hardly arise, but cooling of the samples diminishes the Doppler widths of γ lines. If the γ source and the resonance sample are cooled from room temperature to 77 K, the Doppler widths are approximately halved. Thus, the experiment reduces to measuring $T_{1/2}$ for two temperatures 293 and 77 K. The experiments reported in [6] showed that $T_{1/2}$ of the ^{180m}Hf and ^{87m}Sr isomers changes by $2.99 \pm 0.87\%$ and $0.77 \pm 0.53\%$, respectively, upon cooling. Such behavior was expected, because the γ spectrum of the ^{180m}Hf isomer includes low-energy lines, for which the Mössbauer narrowing is possible, whereas the high-energy (388 keV) γ ray, for which the Mössbauer effect is virtually unobservable, is emitted in the isomeric transition of the ^{87m}Sr nucleus.

However, we cast some doubt on the data obtained in that experiment with the ^{180m}Hf isomer. First, the isomeric transition of this nucleus proceeds between the fifth and fourth excited states. Therefore, for the nuclei of resonance environment to affect the zero-mode spectrum in the required way, some of these nuclei must be in the fourth excited state. Thus, one has to adopt an unconvincing hypothesis about the multistep virtual excitation of nuclei of the resonance sample. Second, the experiment in [6] was carried out with a powder sample of hafnium oxide. Therefore, the possibility that the observed decrease in $T_{1/2}$ was caused by gradual compression of the HfO_2 powder under cooling and the ensuing slow approach of the effective center of the γ source to a detector was not excluded. However, experiments with metallic hafnium samples showed that the

sample cooling increases $T_{1/2}$ by 3.6 ± 1.2%, which is comparable with the effect for hafnium oxide. The procedure used to separate peaks of the total γ-ray absorption in the measured spectra from rather high backgrounds is most doubtful. We determined the intensities of 215.3-, 332.3-, and 443.2-keV γ lines for the ^{180m}Hf isomer. In [6] (and in the experiments with metallic hafnium mentioned above), γ peaks were separated through the subtraction of backgrounds determined for a small portion of counts in the analyzer channels immediately above the corresponding peaks (higher in energy). We note that the backgrounds under the 215.3- and 332.3-keV γ lines are much higher than for the 443.2-keV line. All backgrounds grow with an increase in the number of irradiation events for the same sample because of a gradual accumulation of the comparatively long-lived ^{181}Hf nuclide ($T_{1/2}$ = 42.4 d), whose spectrum includes an intense 482-keV γ line in addition to the 345.8-keV γ line. It was found that the decay periods determined from the time dependences of the 215.3- and 332.3-keV γ lines systematically exceed those determined for the 443.2-keV γ line. Moreover, the $T_{1/2}$ values determined for different numbers of successive measurements of the γ radiation intensity were different. It seemed that decay is slightly retarded with an increase in the total measurement duration. This behavior could be associated with an incomplete subtraction of the background when determining the γ-peak areas. A small admixture of background counts, which decreases with time slowly than the γ peak over the background, should strongly distort the actual decay law at the end of the measurement time interval, where the γ-peak intensity is much lower than at its beginning. Under these conditions, the increase in the measured $T_{1/2}$ value with cooling of the hafnium sample could be assigned to a small background contribution of the additional counts from long-lived-activity γ rays that enter the detector as a result of the scattering by liquid nitrogen. These facts all suggested that the procedure of subtracting the background was insufficiently correct. For this reason, experiments with metallic hafnium were repeated and, in addition to the previous background subtraction procedure, the data were processed by the procedure of background determination from the spectral portion below the γ line (in the region close to the γ peak, where counts can be treated as independent of the analyzer channel number). This procedure obviously loses some counts corresponding to the γ peak, but the remaining portion is sure to be free of the counts related to the background.

Measurements were carried out on the same setup as in [6]. Metallic hafnium samples were 2.5 × 2.5-cm plates with a thickness of 1 mm. Two such plates with slightly cut corners were placed in a cylindrical graphite container, one over the other and turned by an angle of 45° with respect to each other. The containers were closed by graphite caps using a BT-200 cryostable glue (boron nitride powder in the epoxy glue). Two such containers were irradiated in turn by neutrons from the ^{236}Pu–Be source for 12 h. Measurements lasted 11 h. Each measurement of the γ spectrum lasted 1700 s with an interval of 30 min between the beginnings of successive measurements. It was found that the previous background subtraction procedure still gave different $T_{1/2}$ values for three γ lines. At the same time, the new procedure gave the same $T_{1/2}$ value for all three γ lines within the experimental accuracy and fully excluded the dependence of the result on the total measurement duration. These experiments show that the new procedure of background subtraction gives well-correlated results for all γ lines and both temperatures. Based on the more correct new procedure of extracting γ peaks, one can state that a decrease in temperature has no effect on the $T_{1/2}$ value of the ^{180m}Hf isomer within the accuracy of our experiments; i.e., our previous result is not confirmed. A change in $T_{1/2}$ value with temperature is

$$T_{1/2}(77 \text{ K}) - T_{1/2}(293 \text{ K}) = (5.366 + 0.049)$$
$$- (5.395 + 0.045) = -0.029 + 0.067 \text{ h},$$

which comprises –0.54 ± 1.20% of $T_{1/2}$(293 K). Clearly, this result must be experimentally verified in the laboratory, where the γ activity of ^{180m}Hf isomer is much higher than in our experiments.

The second experiment was carried out with the ^{103m}Rh isomer using an absolutely different technique. Since the Debye temperature of metallic rhodium is high (480 K [8]), the probability of recoilless emission (absorption) of the 39.75-keV γ ray is equal to ~0.46 even at room temperature. For this reason, we compared the decay periods measured for the ^{103m}Rh isomer in a metallic Rh sample and in an aqueous solution of rhodium nitrate at room temperature. The zero-point vibration spectrum in the range resonant to the γ transitions in the former sample was expected to be distorted more strongly than in the latter sample, because the γ spectrum of a solid sample includes a narrow intense Mössbauer component. Metallic rhodium samples were 0.1-mm-thick foil disks 35 mm in diameter. For liquid samples, 18-mm-high closed cylindrical quartz ampoules 44 mm in diameter with a flat thin bottom were manufactured. Using a syringe, ampoules were filled, through the capillaries at their tops, with a 10% Rh nitrate solution. Then, the capillaries were sealed. Both ampoules each contained 12.5 g of solution. The samples were irradiated by fast neutrons from a ^{236}Pu–Be source, and the ^{103m}Rh isomer was produced due to inelastic neutron scattering. Upon irradiation, a certain amount of radioactive ^{104}Rh nuclei could be produced due to neutron capture. This nuclide has an isomeric excited state with $T_{1/2}$ = 4.41 min, whereas the decay from the ^{104}Rh ground state has $T_{1/2}$ = 44 s. Since $T_{1/2}$ of the ^{103m}Rh isomer was measured by detecting the rhodium x rays, a small admixture of x rays corresponding to the ^{104m}Rh decay could be present, in addition to the

x rays associated with the ^{103m}Rh decay, at the initial measurement stage. Note that the short-lived activity fraction arising upon the irradiation of the samples of rhodium nitrate solution by neutrons was much greater than for the metallic samples. This is, clearly, due to the softening of the neutron spectrum in liquid (the cross section for the formation of the ^{104m}Rh isomer in the capture of thermal neutrons by the ^{103m}Rh nuclei is equal to 10 ± 1 nb [9]). The time interval between the beginnings of successive measurements was equal to 45 min, and the first measurement was ignored when calculating $T_{1/2}$. Thereby, the x-ray contribution from the ^{104}Rh decay was excluded. Each measurement cycle consisted of ten 45-min runs, and the $T_{1/2}$ values were determined from the results of 4, 5, 6, 7, 8, and 9 measurements, beginning with the second measurement. The figure shows that all six variants of $T_{1/2}$ determination for metallic rhodium agree with each other within the adopted accuracy, although a weak tendency to the increase in $T_{1/2}$ with the overall duration of measurements is seen. The most probable cause of this tendency is that the area of background under the x-ray peaks is somewhat larger than for higher energies, from which the subtracted background was derived. The measurements with a liquid rhodium solution show a much stronger increase in $T_{1/2}$ with increasing the overall duration of measurements. In particular, this effect could arise due to a gradual lowering of the effective center of radioactive rhodium distribution in the liquid sample and the ensuing approach of this center and the detector. It is conceivable that the radiolysis of the neutron-irradiated solution gives rise to heavy rhodium-containing conglomerates, which gradually increase the rhodium concentration in the lower solution layers, up to the precipitation. Indeed, a small amount of a dark and very small sediment was found at the bottom of ampoules after measurements with liquid samples. We note that metal ions appearing in solution as a result of the dissociation of salt molecules do not precipitate.

To determine the actual decay periods of the ^{103m}Rh isomer in samples of both types, the dependences of $T_{1/2}$ on the overall duration of measurements should be extrapolated to zero duration. This extrapolation was carried out through the approximation of these dependences by functions $a + bN^2$, where N is the number of successive x-ray intensity measurements for the determination of a given $T_{1/2}$ value, including the first (disregarded) measurement. This procedure gave $T_{1/2} = 55.79 \pm 0.23$ and 54 ± 0.61 min for metallic rhodium and rhodium nitrate solution, respectively. The difference is equal to 1.46 ± 0.65 min or $2.7 \pm 1.2\%$.

The second measurement cycle with the Rh isomer was carried out in a different time regime. The time interval between the beginnings of successive x-ray intensity measurements was equal to 15 min, and 12 measurements were performed in each run. Thus, the total duration of one run was equal to 3 h, which
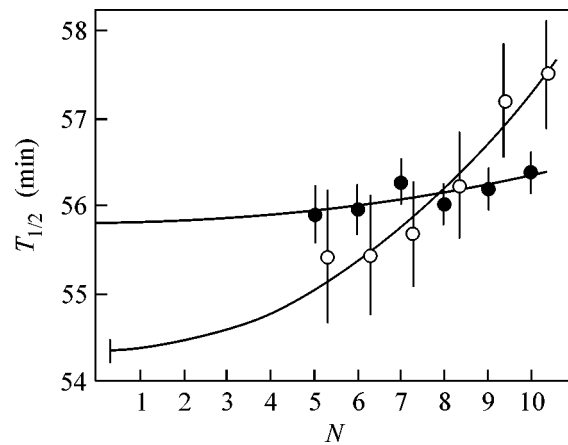
Results of the first measurement cycle for the ^{103m}Rh isomer. The abscissa axis shows the number of successive measurements of x-ray intensity from which the corresponding half-life was determined (including the first (ignored) measurement). Closed and open circles are measurements with metallic rhodium samples and rhodium nitrate solution, respectively. For clarity, open circles are slightly shifted to the right from their real positions. The lines are the least squares approximations of the experimental data by the functions $a + bN^2$.

corresponded to the duration of the first four measurements in the runs of the preceding experimental cycle. Under these conditions, the effective center of a liquid γ source does not descend noticeably to the end of the run, so that the $T_{1/2}$ values obtained for the sources of both types can be compared using the data of nine measurements in each run, beginning with the fourth, i.e., with a 45-min delay to exclude the contribution from the short-lived activity of the ^{104m}Rh isomer.

The second measurement cycle gave the following decay periods:

Metallic samples: $T_{1/2} = 55.84 \pm 0.25$ min

Liquid samples: $T_{1/2} = 54.75 \pm 0.49$ min

It is seen that these values agree well with the results of extrapolation of the data of the first measurement cycle.

Averaging of the data for both measurement cycles gives the following results:

Metallic samples: $T_{1/2} = 55.82 \pm 0.19$ min

Liquid samples: $T_{1/2} = 54.59 \pm 0.38$ min

The difference in these values is equal to $2.25 \pm 0.77\%$ of the ^{103m}Rh isomer half-life in liquid samples.

To verify that the short-lived components have no noticeable effect on the $T_{1/2}$ values derived from nine successive measurements, beginning with the fourth, the $T_{1/2}$ values were determined from eight and seven measurements, i.e., beginning with the fifth and sixth measurements. The corresponding data are presented in the table. No clear-cut tendencies to the increase in $T_{1/2}$ with an increase in the time interval before the first "allowed" measurement are seen within an experimental accuracy.

Table

Samples	$T_{1/2}$ from 9 measurements beginning with the 4th, min	$T_{1/2}$ from 8 measurements beginning with the 5th, min	$T_{1/2}$ from 7 measurements beginning with the 6th, min
Metallic Rh	55.84 ± 0.25	55.93 ± 0.32	55.79 ± 0.38
Rh nitrate solution	54.75 ± 0.49	55.20 ± 0.68	54.72 ± 0.94

Our data can be compared with the results obtained in [10, 11], where, as can be seen from those publications, liquid samples containing a rather pure ^{103m}Rh isomer were used, and in [12], where electrolytically prepared metallic samples of radioactive rhodium were used. The average value obtained in [10, 11] was $T_{1/2} = 56.115 \pm 0.005$ min. The value $T_{1/2} = 56.6 \pm 0.4$ min was reported in [12] for metallic rhodium samples. Although the difference between these values does not contradict our data within the adopted accuracies, but it cannot be considered statistically significant because of a low accuracy of the $T_{1/2}$ value obtained in [12]. We also emphasize that the $T_{1/2}$ values for the sources of both types used in [10–12] exceed our values.

The third experiment was carried out with the ^{80m}Br isomer. This isomer can be obtained in the neutron capture reaction by ^{79}Br nuclei. The 85.9-keV isomer decays through the successive emission of 48.9- and 37-keV γ rays. The first of these γ transitions is strongly converted, whereas 37-keV γ rays are emitted with an intensity of 0.39 per decay event of the ^{80m}Br isomer. The half-life of this isomer was measured by detecting 37-keV γ rays. Since the stable ^{80}Br isotope is absent in nature, it is impossible to create a resonance environment for γ-active ^{80m}Br nuclei. From the very beginning, this experiment was considered as a control experiment. It was performed, similarly to the experiments with ^{180m}Hf isomer, through comparing the measurements at room temperature and at 77 K. Samples were prepared from a potassium bromide powder, which was closely packed into cylindrical graphite containers with caps hermetized by a BT-200 cryostable glue. Each container has an inner diameter of 30 mm and a height of 20 mm. Each $T_{1/2}$ measurement cycle consisted of 20 successive measurements of the 37-keV γ-line intensity using a high-purity germanium detector with a thin entrance window. The time interval between the beginnings of successive measurements was equal to 30 min. The $T_{1/2}$ values determined from different numbers of successive measurements in one run (from all 20 to the first 15) coincide with each other within an experimental accuracy. The half-life determined from 20 measurements in the run is equal to 4.754 ± 0.032 h at room temperature and to 4.791 ± 0.034 h at 77 K. The difference is equal to 0.037 ± 0.047 h or $0.78 \pm 0.99\%$. Thus, as was expected, a difference in the decay periods of the ^{80m}Br isomer was revealed within our experimental accuracy in this case. The ^{103m}Rh isomer is the only isomer for which the difference between the decay periods was detected under the conditions where the spectrum of the zero-point electromagnetic mode should be, at first glance, differently perturbed. However, the accuracy of determination of this difference is low. Therefore, the decay of this isomer should be further investigated by a different method, e.g., by comparing the decay periods at the normal and very high temperatures for metallic rhodium.

REFERENCES

1. V. I. Vysotskiĭ, V. I. Vorontsov, and R. N. Kuz'min, Pis'ma Zh. Tekh. Fiz. **10**, 300 (1984) [Sov. Tech. Phys. Lett. **10**, 126 (1984)].

2. V. I. Vysotskii, in *Technical Digest of 1st International Induced Gamma Emission Workshop* (Bucharest, 1997), p. 81.

3. V. I. Vysotskii, Phys. Rev. C **58**, 337 (1998).

4. V. I. Vysotskii, V. P. Bugrov, A. A. Kornilova, *et al.*, Hyperfine Interact. **107**, 277 (1997).

5. V. I. Vysotskiĭ, A. A. Kornilova, A. A. Sorokin, and S. I. Reĭman, Laser Phys. **11**, 442 (2001).

6. V. G. Alpatov, Yu. D. Bayukov, A. V. Davydov, *et al.*, Pis'ma Zh. Éksp. Teor. Fiz. **73**, 430 (2001) [JETP Lett. **73**, 385 (2001)].

7. V. L. Ginzburg, Usp. Fiz. Nauk **140**, 687 (1983) [Sov. Phys. Usp. **26**, 713 (1983)].

8. P. Boolchand, J. Quant. Spectrosc. Radiat. Transf. **40**, 777 (1988).

9. S. F. Mughabghab, M. Divadeenam, and N. E. Holden, *Neutron Cross Sections* (Academic, New York, 1981), Vol. 1, p. 45-1.

10. E. Günther, K. Knauf, and K. F. Walz, Int. J. Appl. Radiat. Isot. **24**, 87 (1973).

11. F. Lagoutine, J. Legrand, and C. Bac, Int. J. Appl. Radiat. Isot. **29**, 269 (1978).

12. A. Vuorinen, in *Proceedings of a Symposium on the Standardization of Radionuclides, Vienna, 1966* (IAEA, Vienna, 1967).

Translated by R. Tyapaev

Laser Acceleration of Atoms by a Nonlinear Mechanism¶

H. K. Avetissian, A. K. Avetissian, and G. F. Mkrtchian

Department of Quantum Electronics, Plasma Physics Laboratory,
Yerevan State University, Yerevan, 375025 Armenia

Received August 21, 2003; in final form, October 16, 2003

A nonlinear threshold phenomenon at the interaction of atoms with two counter-propagating light beams of different frequencies is presented. The existence of a critical intensity of the interference field is shown, which is the threshold of nonlinear resonance achieved in the field. This phenomenon leads to acceleration or deceleration of the atom, depending on its initial velocity. Such acceleration/deceleration of shock character, because of the impact with the potential barrier, occurs on ultrashort distances on the order of laser wavelengths, and depends neither on the field magnitude nor on interaction length. © 2003 MAIK "Nauka/Interperiodica".

PACS numbers: 32.80.Lg; 32.80.Pj; 42.50.Vk; 81.16.Ta

The problem of the acceleration of atoms has been considered since the period of the appearance of laser sources [1–5]. In recent decades the inverse problem of atoms' deceleration became more important, as it is connected with the intensive experimental research regarding the laser manipulation of atoms [6–9]. The latter is of great interest and involves a large class of atomic and laser spectroscopic issues, especially at very low temperatures (it is worthwhile noting unique experiments that include the trapping of separate atoms or Bose condensation of supercooling atomic gas in optical-dipole or magnetic traps [10–15]). We shall not attempt to review the extensive literature regarding the laser manipulation of atoms by counter-propagating light beams, apart from mentioning the works [16, 17] which consider the acceleration of atoms in moving periodic potentials-traps. The latter relies on the "conveyor belt" provided by a frequency-chirped optical lattice formed by two counterpropagating laser beams.

In this paper we present a nonlinear mechanism of atom acceleration by two counterpropagating light beams of different frequencies, which differs from the mentioned schemes of trapped-atom acceleration. It is a process of the collision of the atom with the moving potential barrier. Thus, it has appeared that in the field of two counterpropagating light beams of different frequencies a critical intensity of the net field exists, above which the atom "reflection" from the slowed interference wave takes place. This type of wave field becomes a potential barrier with respect to the atom, resulting in atom acceleration or deceleration (depending on the initial conditions).

We will study the dynamics of interaction of a two-level atom with the two quasi-monochromatic counter-propagating plane waves of different frequencies in the approximation of a given field (the magnitudes of the wave fields will be assumed to be so strong that the radiation/absorption processes can not change their given values). As will be shown below for the actual cases of strong laser pulses, the approximation of a given field in this process is satisfied with great accuracy.

The Hamiltonian of a two-level atom in the field of two quasi-monochromatic counterpropagating plane waves in the rotating wave approximation is given by the expression

$$H(\mathbf{p}, \mathbf{r}, t) = \frac{\mathbf{p}^2}{2m} + \frac{\hbar\omega_0}{2}\sigma_z + i\hbar\Omega_1 S_1(t)e^{i\omega_1 t - i\mathbf{k}_1\mathbf{r}}\sigma_- \tag{1}$$
$$+ i\hbar\Omega_2 S_2(t)e^{i\omega_2 t - i\mathbf{k}_2\mathbf{r}}\sigma_- + \text{c.c.},$$

where $\mathbf{r}$ and $\mathbf{p}$ are the classical position and momentum of an atom center-of-mass (m), obeying the Hamilton canonical equations of motion

$$\dot{\mathbf{r}} = \partial H/\partial \mathbf{p}, \quad \dot{\mathbf{p}} = -\partial H/\partial \mathbf{r}. \tag{2}$$

Here, ω_0 is the frequency of the atomic transition, being driven by the linearly polarized counterpropagating waves with carrier frequencies ω_1, ω_2 (let $\omega_1 > \omega_2$), wavenumbers $\mathbf{k}_1$, $\mathbf{k}_2$, and amplitudes E_1, E_2. Then $\Omega_{1,2}$ are the Rabi frequencies: $\Omega_{1,2} = E_{1,2}d_{1,2}/\hbar$, where $d_{1,2}$ are the projections of the atomic transition dipole moment along the waves' polarization directions, $\hbar$ is the Plank constant, $S_{1,2}(t)$ are the slowly varying envelopes of quasi-monochromatic waves ($S_{1,2\,\text{max}} = 1$). The variables σ_- and σ_z are the expectation values of the

Pauli pseudo-spin operators describing the atomic internal state. They obey the optical Bloch equations

$$\dot{\sigma}_- = -i\omega_0\sigma_-$$
$$+ [\Omega_1 S_1(t)e^{i\mathbf{k}_1\mathbf{r} - i\omega_1 t} + \Omega_2 S_2(t)e^{i\mathbf{k}_2\mathbf{r} - i\omega_2 t}]\sigma_z,$$
$$\dot{\sigma}_z = -2[\Omega_1 S_1(t)e^{i\omega_1 t - i\mathbf{k}_1\mathbf{r}} \quad (3)$$
$$+ \Omega_2 S_2(t)e^{i\omega_2 t - i\mathbf{k}_2\mathbf{r}}]\sigma_- + c.c.,$$

which include the center-of-mass motion of the atoms.

For the plane waves propagating along the Z axis from Eqs. (6)–(3) one can obtain the velocity of the atom in the field

$$v_z = \frac{c}{n}\left[1 \mp \sqrt{\left(1 - n\frac{v_{0z}}{c}\right)^2 - 2\frac{n^2}{mc^2}V_{sw}(z,t)} \right]; \quad (4)$$

$$v_x = v_{0x}; \quad v_y = v_{0y},$$

where $v_0 = (v_{0x}, v_{0y}, v_{0z})$ is the initial velocity of the atom. The quantity $n > 1$, which is the "effective refractive index" of a slowed interference wave propagating with the phase velocity $v_{ph} = c/n < c$, and the interaction potentials $V_{sw}(z, t)$ of the atom with such a wave field are given by the expressions

$$n = (\omega_1 + \omega_2)/(\omega_1 - \omega_2), \quad (5a)$$

$$V_{sw}(z, t) = V_0 S_1(t)S_2(t)\cos[(\omega_1 - \omega_2)(t - nz/c)], (5b)$$

$$V_0 = 2\hbar\Omega_1\Omega_2(\Delta_1^{-1} + \Delta_2^{-1}). \quad (5c)$$

As may be seen from Eq. (4), if the maximal value of the interaction potential $V_{sw}(z, t)_{max} = |V_0|$ (5) is larger than a certain value

$$V_{cr} = \frac{mc^2}{2n^2}\left(1 - n\frac{v_{0z}}{c}\right)^2, \quad (6)$$

which will be called critical, the expression (4) for the atom velocity may become complex. This complexity is bypassed in the complex plane by continuously passing from one Riemann sheet to another, at which the root changes its sign. Hence, the atom velocity remains real everywhere and the multivalence of the expression (4) vanishes as well. Indeed, if $|V_0| < V_{cr}$, one should take the root in Eq. (4) with the sign (–) if $v_{0z} \leq c/n$, and with the sign (+) if $v_{0z} \geq c/n$, to satisfy the initial condition $v_z = v_{0z}$ at the $V_{sw}(z, t = -\infty) = 0$. Then, after the interaction ($V_{sw}(z, t = +\infty) = 0$) the energy of the atom remains unchanged. However, when $|V_0| > V_{cr}$ the value $V_{sw}(z(t_0), t_0) = V_{cr}$ (where $z(t_0)$ is the atom coordinate at the moment $t = t_0$) steps out as a turn point, and for $t > t_0$ one should change the sign of the root, in respect to the moments $t \leq t_0$. At that, the slowed interference wave

becomes a potential barrier for the atom and the "reflection" of the atom from such a moving barrier occurs. To explain the physics of this phenomenon, it is necessary to clarify the meaning of the critical field. This is an essentially nonlinear phenomenon of a threshold nature, and the critical intensity of the interference wave is the threshold value for this process. Namely, Eq. (4) shows that the critical value V_{cr} is the value of the potential, at which the longitudinal velocity of the atom in the field $v_z(t)$ becomes equal to the phase velocity of the slowed interference wave $v_z(t) = c/n$, irrespective of the atom initial velocity v_{0z}. The latter is the condition of resonance with the Doppler-shifted waves frequencies, at which the coherent scattering, that is, the induced "Compton" scattering of counterpropagating waves on an atom occurs:

$$\omega_1(1 - v_z(t)/c) = \omega_2(1 + v_z(t)/c). \quad (7)$$

Since the resonant velocity of the atom, $v_z(t) = c/n$, is acquired in the field at the value $V_{sw} = V_{cr}$ (due to the wave intensity effect) this is a nonlinear resonance. For this reason, the "reflection" of the atom from the moving barrier occurs. Note that this is actually a reflection in a frame of reference moving with the velocity $V = c/n$, which is the rest frame of the slowed interference wave. In this frame, an atom with the velocity v'_{0z} swoops on the motionless barrier and, as is seen from Eq. (4), an elastic reflection of the atom occurs: $v'_z = -v'_{0z}$.

Thus, if the maximal value of the interaction potential $|V_0| > V_{cr}$, then after the interaction ("reflection") for the atom velocity we have

$$v_{zf} = \frac{c}{n}\left(1 - n\frac{v_{0z}}{c}\right) + \frac{c}{n}. \quad (8)$$

Equation (8) shows that, if $v_{0z} < c/n$, then $v_{zf} > v_{0z}$ and the atom is accelerated. But if $v_{0z} > c/n$, then $v_{zf} < v_{0z}$ and deceleration of the atom takes place. The kinetic energy lost by the atom during deceleration is transferred to the waves according to induced "Compton" scattering, during which conservation of the photon number takes place. In other words, the atom absorbs photons of a small frequency ω_2 and emits the same number of photons with the large frequency ω_1 (and vice versa upon acceleration). For the initially resonant velocity of the atom ($v_{0z} = c/n$), $V_{cr} = 0$ and, consequently, the atom velocity does not change ($v_{zf} = v_{0z}$).

For the kinetic energy change of the atom's center-of-mass we have

$$\Delta\varepsilon = \frac{2mc^2}{n^2}\left(1 - n\frac{v_{0z}}{c}\right). \quad (9)$$

As is seen from this formula, the acceleration of the atom depends neither on the field magnitude (which must only be an above-threshold field) nor the interaction length. This is an impact acceleration/deceleration over ultrashort distances (in the order of laser wavelengths), which may serve as a significant tool for the laser manipulation of atoms. The threshold character of such acceleration may be used for the separation of atoms by the velocities.

To illustrate the entire picture of this nonlinear effect we present the graphics of numerical solutions of Eqs. (3)–(6) for the laser pulses with the Gaussian envelopes. To accentuate this acceleration mechanism due to nonlinear resonance created by the field we especially present the acceleration of an atom at rest—the case when the initial atom velocity is very far from the resonant one (7).

Figure 1a illustrates the temporal evolution of the atom's center-of-mass velocity (solid curve), when $v_0 = 0$ and the intensity is below the critical point: $V_0 < V_{cr}$. Variation of the scaled potential V_{sw}/V_{cr} along the atom trajectory is shown by the dotted curve. As we see, there is no acceleration under the threshold of nonlinear resonance (the net gain is defined by the initial phase). In Fig. 1b the atom dynamics is displayed, when the intensity is above the critical point: $V_0 > V_{cr}$. From these figures it is clearly seen that at the critical point $V_{sw} = V_{cr}$ the longitudinal velocity of the atom becomes equal to the phase velocity of the interference wave ($v_z(t) = v_{ph} = c/n$) and is a turning point for the solid curves. The latter corresponds to Eqs. (4), where the root changes its sign and the further evolution of the velocity proceeds along the second branch of the root with an inverse sign. In the resonance range, the velocity of the atom strictly increases due to the genuine nonlinear character of the resonance in the field (see Eq. (7)). Then, after leaving the resonance range the final velocity of the atom becomes $v_{zf} = 2v_{ph}$ in accordance with the analytical results (see Eqs. (4) and (8)). For the initial condition $v_0 > v_{ph}$, a deceleration of the atom after the "reflection" occurs. Maximal deceleration $v_{zf} = 0$ occures at the initial velocity $v_0 = 2v_{ph}$, for which we have the inverse picture of Figure (b).

The estimates show that an atom at rest can be accelerated up to thermal velocities $\sim 10^5$ cm/s by laser pulses with electric fields strengths $E \sim 10^6$ V/cm, at the "refractive index" $n \sim 10^5$ (corresponding to temporal coherency $(\omega_1 \sim \omega_2)/\omega_1 \sim 10^{-5}$ of lasers) with detunings $\Delta_{1,2}/\omega_0 \sim 10^{-1}$. Note that the fields necessary for this effect are much smaller than the atomic ones and the model of a supposed two-level atom is well enough justified. The energy acquired by the atom at such interaction, i.e., the energy of the wave field transferred to the atom, is about $\sim 10^{-2}$ eV, which is negligibly small in respect to even weak laser pulses. So, the applied approximation of a given field is satisfied with great accuracy. In the inverse regime of deceleration with the
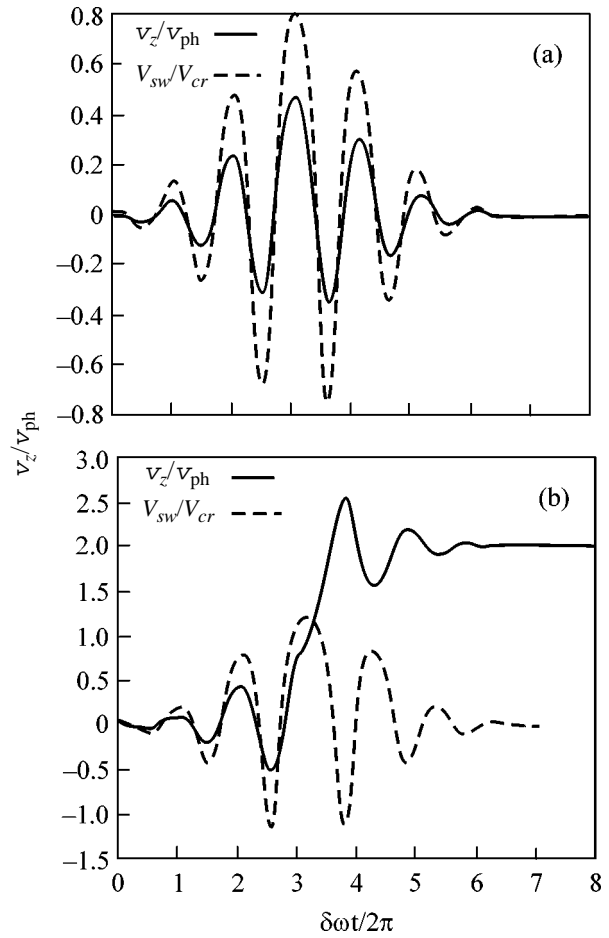

Fig. 1. Solid curves display the temporal evolution of the atom scaled velocity v_z/v_{ph} (time in units of interference wave period $2\pi/(\omega_1 - \omega_2)$). Pulse duration has been chosen to be $(\omega_1 - \omega_2)\tau = 10$. The dotted curve shows the variation of the scaled interaction potential V_{sw}/V_{cr}, sensed by the atom along the trajectory. The initial conditions are: $v_0 = 0$, $z_0 = 0$. (a) The intensity is below the critical point: $V_0 = 0.8V_{cr}$, (b) intensity is above the critical point: $V_0 = 1.3V_{cr}$.

same fields one can stop such a thermal atomic beam at a distance on the order of laser wavelengths.

REFERENCES

1. A. G. Askar'yan, Sov. Phys. JETP **15**, 1088 (1962).

2. A. P. Kazantsev, Sov. Phys. JETP **36**, 861 (1973); Sov. Phys. JETP **39**, 784 (1974).

3. R. J. Cook, Phys. Rev. A **20**, 224 (1979); Phys. Rev. A **22**, 1078 (1980).

4. J. P. Gordon and A. Ashkin, Phys. Rev. A **21**, 1606 (1980).

5. V. S. Letokhov and V. G. Minogin, Phys. Rep. **73**, 1 (1981).

6. S. Chu, Rev. Mod. Phys. **70**, 685 (1998).

7. C. Cohen-Tannoudji, Rev. Mod. Phys. **70**, 707 (1998).

8. W. D. Phillips, Rev. Mod. Phys. **70**, 721 (1998).

9. R. Grimm, M. Weidemüller, and Y. B. Ovchinnikov, Adv. At., Mol., Opt. Phys. **42**, 95 (2000).

10. J. E. Bjorkholm, R. R. Freeman, A. Ashkin, and D. B. Pearson, Phys. Rev. Lett. **41**, 1361 (1978).

11. S. Chu, J. E. Bjorkholm, A. Ashkin, and A. Cable, Phys. Rev. Lett. **57**, 314 (1986).

12. C. S. Adams, M. Sigel, and J. Mlaynek, Phys. Rep. **240**, 143 (1994).

13. T. W. Hänsch and A. L. Schawlow, Opt. Commun. **13**, 68 (1975).

14. D. Wineland and H. Dehmelt, Bull. Am. Phys. Soc. **20**, 637 (1975).

15. S. Chu, L. Hollberg, J. E. Bjorkholm, *et al.*, Phys. Rev. Lett. **55**, 48 (1985).

16. E. Peik, M. B. Dahan, I. Bonchoule, *et al.*, Phys. Rev. A **55**, 2989 (1997).

17. S. Potting, M. Cramer, C. H. Schwalb, *et al.*, Phys. Rev. A **64**, 023604 (2001).

Self-Focusing of Laser Radiation in Cluster Plasma

N. A. Zharova*, A. G. Litvak, and V. A. Mironov

Institute of Applied Physics, Russian Academy of Sciences, ul. Ul'yanova 46, Nizhni Novgorod, 603600 Russia
*e-mail: zhani@appl.sci-nnov.ru
Received July 7, 2003; in final form, October 14, 2003

The self-focusing of laser radiation in plasma with ionized gaseous clusters is studied both analytically and numerically. An electrodynamic model is proposed for cluster plasma in a field of ultrashort laser pulse. The radiation self-action dynamics are studied using the equation for wave-field envelope with allowance for the electronic nonlinearity of the expanded plasma bunches and the group-velocity dispersion in a nanodispersive medium. It is shown that, for a laser power exceeding the self-focusing critical power, the wave-field self-compression occurs in a medium with dispersion of any type (normal, anomalous, or combined). Due to the strong dependence of the characteristic nonlinear field on the size of ionized cluster, the corresponding processes develop faster than in a homogeneous medium and give rise to the ultrashort pulses. © *2003 MAIK "Nauka/Interperiodica".*

PACS numbers: 52.38.Hb; 36.40.-c

Gaseous cluster targets are finding increasing use in experiments on the interaction of laser radiation with substance. Due to the highly dispersed structure of such targets, X-ray generation and generation of charged particle fluxes [1–5] can be much more efficient than in a homogeneous substance. Recent observations of laser radiation self-focusing in cluster plasmas [5, 6] pose the problem of theoretical investigation of this process and its role in the amplification of nonlinear processes accompanying the interaction of field and matter. This paper is devoted to the study of this problem.

When developing the theory of laser interaction with such a strongly inhomogeneous medium, we will assume that the latter consists of a substance in the noncondensed phase and clusters with the distance L_c between them. The laser wavelength λ far exceeds the intercluster spacing and cluster size a ($\lambda \gg L_c \gg a$). Due to this assumptions, one can use the approximation of effective refractive index for the medium. When deriving the relation between the medium polarization and the field, we will take into account (in accordance with the experimental data [1–9]) that the medium is ionized at the pulse leading edge, but electrons, although leave their atoms, remain in the cluster (internal ionization). The resulting plasma bunch is expanded so that the total number of charged particles in the bunch does not change. The evolution of an ultrashort laser pulse in a nonstationary cluster plasma will be studied using the modified nonlinear Schrödinger equation on assumption that the field frequency is much lower than the cluster plasma frequency.

1. We assume for simplicity that the cluster is shaped like a sphere and atoms in the external uniform field $E(t)$ are ionized uniformly over the cluster volume. We, thus, arrive at the model of an ionized cluster consisting of two uniformly charged spheres, namely, a positively charged heavy sphere and a negatively charged light sphere. The displacement x of the centroid of electron subsystem along the field is described by the equation

$$\frac{d}{dt}\left(a^3 n \frac{dx}{dt}\right) + \omega_c^2 \frac{a^6 n x}{(x^2 + a^2)^{3/2}} = \frac{e n a^3}{m} E(t), \qquad (1)$$

where n is the electron density in cluster, $\omega_c = (4\pi e^2 n/3m)^{1/2}$ is the eigenfrequency of the ionized spherical cluster, m is the electron mass, $\dot{x} = dx/dt$ is the velocity of centroid, and a is the cluster radius. The first term on the left-hand side of Eq. (1) is a change in the momentum of electron subsystem, the second term describes the mutual attraction of the spherical electron and ion bunches, and the right-hand side of Eq. (1) is the force acting on electrons from the external field. We also assume that the internal ionization of cluster atoms has tunneling character and is described by the equation

$$\partial n/\partial t = \omega_a (n_a - n) \exp(-E_a/|E|), \qquad (2)$$

where ω_a is the atomic frequency, n_a is the atomic density in cluster, and E_a is the atomic field ($E_a = e/r_a$, where r_a is the atomic size).

The set of Eqs. (1) and (2) can conveniently be written in the dimensionless form

$$\frac{d}{dt}(a^3 n \dot{x}) + \frac{a^3 n^2 x}{(x^2/a^2 + 1)^{3/2}} = \delta \frac{n a^3}{q} E(t), \qquad (3)$$

$$\partial n/\partial t = \beta(1 - n) \exp(-1/|E|), \qquad (4)$$

where the displacement x and the cluster size a are normalized to the initial cluster size a_0 ($x/a_0 \longrightarrow x$ and
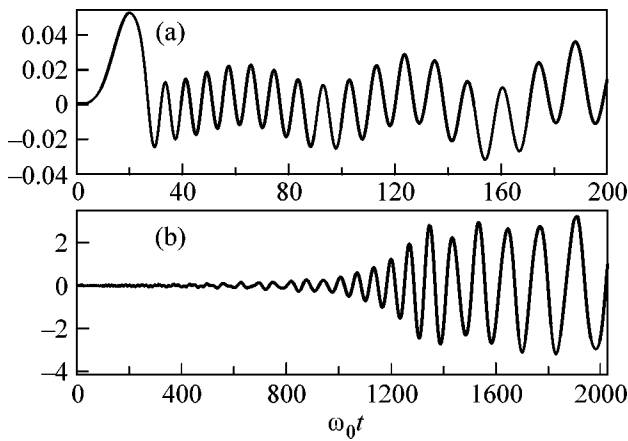
Fig. 1. Time dependence of the centroid of electron sub-system in a cluster oscillating under the action of field $E(t) = 0.3\cos(0.1t)(1 - \exp(-0.1t))$ and expanding according to the law $a = 1 + 0.003t$. (a) Initial stage with small oscillation amplitude and insignificant cluster expansion, and (b) long-time behavior of the system.

$a/a_0 \longrightarrow a$); the concentration n is normalized to the maximal density of charged particles in cluster ($n/n_a \longrightarrow n$); the field E is normalized to the atomic field e/r_a^2; the variable t is related to the dimensional time as $t \longrightarrow \omega_c t$; and the parameters β, δ, and q are defined by the relationships $\beta = \omega_a/\omega_c$, $\delta = r_a/a_0$, and $q = 4\pi n_0 r_a^3/3$ (q is the total number of ionized particles in the atomic volume).

Below, Eqs. (3) and (4) are used to analyze the behavior of a cluster in the field of laser pulse

$$E(t) = E_0(t)\cos(\omega t).$$

As long as the amplitude E_0 is small, the cluster remains nonionized ($n \approx 0$) and shows no reaction to the external field. As the field amplitude increases, the ionization is abruptly "switched on" at a certain moment t_0. At large values of parameter β ($\omega_a \gg \omega_c$), the cluster is almost completely ionized ($n \simeq 1$) in a time much shorter than the natural period of plasma bunch. Such an "instantaneous" ionization results in the excitation of eigenmodes and a broad spectrum of induced modes. In the linear approximation ($x \ll a = 1$) and on assumption that the clusters are ionized instantaneously, one can easily estimate, after substituting $a = 1$, $x(t_0) = 0$, and $n(t) = \theta(t - t_0)$ ($\theta(t)$ is the Heaviside unit step function) in Eq. (3), the amplitudes of excited bunch eigenmodes with frequency $\omega_c = 1$,

$$x_{\text{eigen}} \simeq \delta\frac{E(t_0)}{q}, \tag{5}$$

and low-frequency induced modes with the frequency $\omega \ll \omega_c$ of external field,

$$x_{\text{ind}} \approx \delta\frac{E_0}{nq}. \tag{6}$$

One can see from the comparison of Eqs. (5) and (6) that the dipole moments of cluster eigenmodes excited upon ionization are of the same order as the dipole moments at the field frequency. However, the situation changes with cluster expansion. For a fixed total number of electrons in the cluster ($na^3 = $ const), the eigenfrequency decreases proportionally to $a^{-3/2}$ with increasing radius a. In accordance with the adiabatic invariant, the eigenmode amplitude increases slowly (proportionally to $a^{3/4}$), while the amplitude of induced oscillations, as seen in Eq. (6), increases with cluster size much faster ($x \sim a^3$). For this reason, we will restrict ourselves to the consideration of plasma polarization at the frequency of external field.

The linear approximation $x \ll a$ can break upon cluster expansion. In a sufficiently intense external field ($E \sim qn_0a_0^3/\delta a^2$), the oscillation amplitude can become comparable to the cluster size a even far from the linear resonance. In this case, the cluster interacts with field nonadiabatically, so that the electronic component acquires a constant velocity component and separates from the ionic component, rendering the motion aperiodic. In fact, this corresponds to the cluster destruction.[1] In weak fields, a change to the nonlinear regime $x \sim a$ occurs upon achievement of the resonance condition $\omega \simeq \omega_c$. In this case, an increase in the cluster oscillation amplitude can also result in the cluster destruction.

The results of the above qualitative consideration of the cluster polarization dynamics are confirmed by the numerical analysis of the set of Eqs. (3) and (4). The function $x(t)$ for a cluster expanding according to the law $a = 1 + 0.003t$ is shown in Fig. 1. For such a high expansion rate, the electron plasma frequency in an ionized cluster reduces to the frequency of external field during the laser pulse in experiments [6–9]. One can see (Fig. 1a) that the induced oscillations and the eigenmodes with comparable amplitudes are excited at the pulse leading edge and that the subsequent behavior is in compliance with the qualitative considerations (Fig. 1b). The amplitude of induced oscillations ceases to increase ($x \sim a^3$) at $\omega_0t \simeq 1300$, at the instant the linear oscillation regime changes to the nonlinear regime with the oscillation amplitude on the order of cluster size.

Our molecular dynamics study of cluster polarization in an external field (through the direct solution of the equation of motion for each electron arising upon

---

[1] Estimates suggest that, for the nonresonant cluster destruction, the characteristic laser intensity should be at least 20 times higher than the intensity used in the experiment [6].

cluster internal ionization in a self-consistent electric field) yields the same results. The kinetic model of cluster is augmented by the external ionization effect (electron leakage from plasma bunch). This process is enhanced with an increase in field amplitude and eventually results in the Coulomb explosion. In our further study of the self-action dynamics, we restrict ourselves to the initial stage of cluster expansion under weak nonlinearity conditions.

2. To describe the self-action dynamics of a radiation with frequency ω much lower than the eigenfrequency ω_c of an ionized cluster but higher than the frequency ω_{bq} of the background plasma, we use the wave equation

$$\frac{\partial^2 E}{\partial t^2} - c^2\frac{\partial^2 E}{\partial z^2} - c^2\Delta_\perp E + 4\pi\frac{\partial^2 P_c}{\partial t^2} + \omega_{bq}^2 E = 0, \quad (7)$$

which takes into account the influence of both the condensed phase (clusters) and the background plasma.

In the approximation of slow (on the field period scale) cluster expansion, Eq. (1) gives for the polarization of the cluster subsystem

$$P_c = \frac{3}{4\pi}n_c a^3 E\left(1 + \frac{a^4}{a_0^4}\frac{E^2}{E_{cr}^2}\right) - \frac{3}{4\pi}n_c\frac{a^3}{\omega_c^2 a_0^3}\frac{\partial^2}{\partial t^2}Ea^3. \quad (8)$$

In deriving this expression, the nonlinearity and dispersion of the cluster subsystem were calculated perturbatively under the condition that the number of particles is conserved, $n(t)a^3(t) = n_0 a_0^3$. The characteristic electronic nonlinear field

$$E_{cr} = m\omega_c^2 a_0/e \quad (9)$$

is determined by the initial cluster size a_0. It follows from Eq. (8) that the nonlinearity in the cluster subsystem increases with cluster size in proportion to a^7.

The medium under consideration can be described in terms of effective dielectric constant. In the linear approximation, this brings about the dispersion relation

$$k_z = (\omega^2(1 + \alpha b) - \omega_{bq}^2 + \alpha b^2\omega^4/\omega_c^2)^{1/2}/c, \quad (10)$$

where the parameter

$$k_2 = \frac{\partial^2 k_z}{\partial\omega^2} = \frac{\partial}{\partial\omega}\frac{1}{v_{gr}} \simeq \frac{-\omega_{bg}^2 + 3\alpha b^2\omega_0^2/\omega_c^2}{\omega_0^3 c} \quad (11)$$

determines the dispersion of group velocity v_{gr}. Here, the notation $\alpha = 3n_c a_0^3$ and $b = a^3/a_0^3$ is introduced, where a_0 is the initial size of ionized cluster. One can see from Eq. (11) that, for a low density of the background plasma,

$$\omega_{bg}^2 < 3\alpha b^2\omega_0^4/\omega_c^2 \quad (12)$$

the group-velocity dispersion in cluster plasma is normal, $(v_{gr})'_\omega > 0$. As the cluster expands, inequality (12) is progressively better fulfilled; i.e., the dispersion remains normal. If the background plasma density is high enough, so that the inverse of inequality (12) is fulfilled, then the plasma (anomalous) dispersion will predominate at the wavepacket leading edge. However, as the cluster expands, the anomalous dispersion can change to the normal dispersion during the pulse. This case will be referred to as a regime with a combined dispersion.

When deriving the equation of nonlinear optics, we assume that the cluster size increases smoothly (on the radiation wavelength scale) during the pulse. As a result, we obtain the following equation for the complex amplitude of wave-field envelope in the adiabatic approximation:

$$E(z, t, \mathbf{r}_\perp) = A(z, \xi = z - z_c(t), \mathbf{r}_\perp)\exp(ik_z z - i\phi(z, t)).$$

In the dimensionless variables

$$\Psi = A/A_{cr}, \quad A_{cr} = \sqrt{5}\omega E_{cr}/\omega_c a_{max}^{1/2},$$

$$z_{new} = 10\alpha a_{max}^6\omega^3 z/\omega_c^2 c, \quad \tau = 2\omega\xi/c,$$

$$\mathbf{r}_{new} = \omega^2 a_{max}^6(20\alpha)^{1/2}\mathbf{r}(c\omega_c), \quad d = a^3/a_{max}^3,$$

$$\chi = d^2 - \omega_{bg}^2\omega_c^2/(3\alpha\omega^4 a_{max}^6),$$

it has the form

$$i\frac{\partial\Psi}{\partial z} + id^{7/4}|\Psi|^2\frac{\partial}{\partial\tau}d^{7/12}\Psi - \frac{\partial}{\partial\tau}\chi\frac{\partial\Psi}{\partial\tau}$$
$$+ \Delta_\perp\Psi + d^{7/3}|\Psi|^2\Psi = 0. \quad (13)$$

Without taking into account the dependence of group velocity on the pulse amplitude (second term), Eq. (13) reduces to the usual nonlinear Schrödinger equation (NSE) in a nonstationary medium. For this case, the dynamics of the system described by Eq. (13) are well known (see [10–13] and references cited therein) and depends on the sign of the dispersion of wavepacket group velocity. A pulse propagating in a medium with the normal dispersion ($\chi > 0$) undergoes self-focusing if the pulse power exceeds a certain critical value [10, 11]. In the stationary case with parameters (13), the (local) self-focusing critical power is

$$P_{cr}(\tau) = \left(\frac{a_0}{a(\tau)}\right)^7\frac{c^2}{4\alpha\omega^2}E_{cr}^2 cP_0. \quad (14)$$

The value $P_0 = 11.7$ (dimensionless critical power of an axisymmetric uniform wave beam) is well known in the theory of self-focusing. The conditions for the development of strongly nonlinear phenomena in a medium with anomalous group-velocity dispersion ($\chi > 0$,
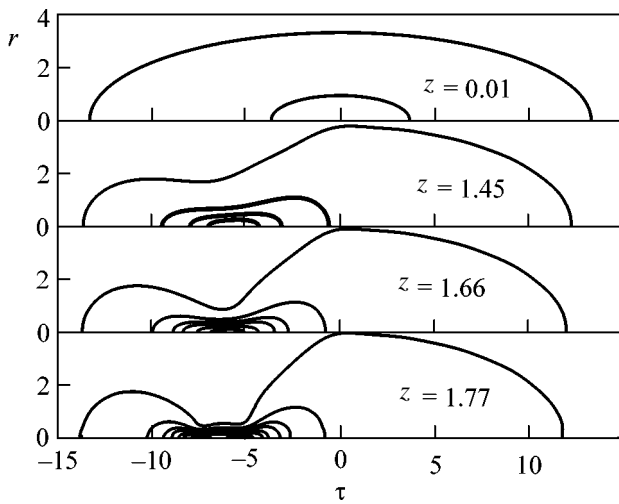
Fig. 2. Ψ isofield curves for the initial distribution $\Psi(z = 0) = 2\exp(-0.5(r/2)^2 - 0.5(\tau/8)^2)$ at different distances from the entrance into cluster plasma.
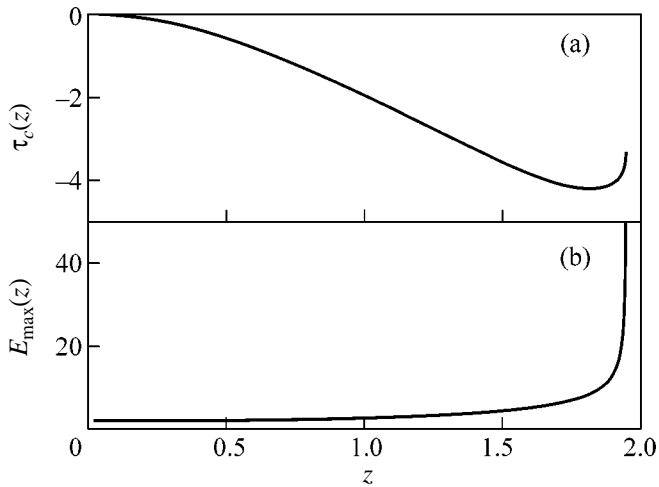

Fig. 3. Dynamics of (a) distribution centroid and (b) maximal field for the same initial distribution as in Fig. 2.

$\omega_{bg}^2/\omega^2 > \alpha a_{max}^3/a_0^3$), where the so-called distributed collapse occurs, are less stringent (for details, see [12, 13]).

The specific features of the solutions to the modified NSE (13) describing the propagation of a short high-power pulse in cluster plasma are primarily caused by the strong dependence of the nonlinear coefficients on the cluster size a (the coefficient of cubic nonlinearity is proportional to a^7, and the nonlinear correction to the group velocity increases toward the pulse end just as rapidly). When normalized to the maximal value, the nonlinear coefficients become negligible at the leading edge. Accordingly, they are operative in the region shifted to the pulse trailing edge.

3. Numerical studies of the evolution of three-dimensional axisymmetric Gaussian wavepackets

$$\Psi(z = 0, r, \tau) = \Psi_0\exp\left(-\frac{r^2}{2a_r^2} - \frac{\tau^2}{2\tau_0^2}\right) \quad (15)$$

have shown that the dynamics are similar for all types of group-velocity dispersion (normal, $\chi > 0$; anomalous, $\chi < 0$; and combined). The nonlinear correction to the group velocity (the second term in Eq. (13)) has a noticeable effect in this case. As the pulse propagates in the medium, its centroid shifts to the trailing edge, where the cluster size increases and the medium is characterized by strong nonlinearity and normal dispersion.[2] In addition, a pulse of a sufficiently high intensity undergoes strong transverse compression (self-focusing).

The meaning of critical power (14) in our problem is as follows. If the power exceeds this value at a certain point of the pulse, the wave field undergoes self-compression in this region, followed by wavepacket modification. Evidently, the centroid shift to the pulse trailing edge (ignored in Eq. (14)) reduces the self-focusing threshold, so that the above value is overestimated.

The results of numerical solution of Eq. (13) are illustrated in Fig. 2 for the case of normal dispersion ($\chi > 0$). A noticeable field strengthening in the pulse trailing portion is caused by the increase in cluster size and the attendant decrease in critical power (14). The isoline structure in the peripheral wavepacket region demonstrates the onset of a fragmentation process similar to that observed for the usual self-action in a medium with normal dispersion. The evolution of distribution is accompanied by field strengthening and a decrease in the characteristic longitudinal scale, so that the energy integral ceases to be conserved from a certain moment. At the end of calculation of this variant, the maximum of field amplitude increased by 50 times relative to its initial level at a distance $z \sim 0.875$ (Fig. 3b). In fields as strong as these, the effect of cluster external ionization may become significant, resulting in nonlinearity saturation. The dynamics of wavepacket centroid are shown in Fig. 3a: toward the pulse end, the initially accelerated motion comes to rest and even reverses after achieving large field amplitudes.

This self-action regime is noticeably different from the corresponding process described by Eq. (13) with constant coefficients and without inclusion of nonlinear dispersion: the pulse halving is stabilized, the pulse becomes noticeably shorter, and the maximum field strength increases. In this case, the wavepacket evolution is, rather, similar to that in a medium with anomalous group-velocity dispersion. The only difference is that the pattern of isolevel curves is distinctly more symmetric in the anomalous dispersion regime.

---

[2] Such an accelerated motion of the pulse centroid can readily be proved by the moments method.

Therefore, the propagation of a high-intensity laser radiation in cluster plasma should be accompanied by a dramatic increase in the field maximum and a decrease in the pulse duration. A shift of the field-distribution centroid toward the trailing edge can manifest itself as a pulse deceleration. These features of the radiation self-action dynamics in a highly dispersed medium of expanding plasma bunches deserve special experimental study. Certain suggestions regarding the optimization of field and medium parameters (cluster density and size, density of background plasma, etc.) with the aim of better observation of self-focusing can be made on the basis of expression (14) for the self-focusing critical power. The latter can be represented as

$$P_{cr} \simeq \left(\frac{a_0}{a}\right)^7 \left(\frac{\omega_c^2}{\omega^2}\frac{\omega}{c}a_0\right)^2 \times 10^{12} \ [\text{W}]. \qquad (16)$$

One can see that the use of smaller clusters and higher-frequency radiation is more preferential in the experiment. This fact, probably, explains the observation of self-focusing in experiments with short-wavelength radiation [5]. In this respect, the parameters used in more detailed experiments on self-focusing [6], where the clusters were rather large ($a_0 \simeq 300$ Å) and the radiation wavelength was four times greater than in [5], seem to be not quite appropriate.

The dependence of P_{cr} on the phenomenological parameter—cluster expansion rate—is more significant. For the parameters used in [6] ($\lambda = 800$ nm, $a_0 \simeq 300$ Å, $n_a \simeq 10^{24}$ cm^{-3}), one can easily estimate the self-focusing critical power

$$P_{cr} \simeq 10^{15}(a_0/a)^7 \ [\text{W}]. \qquad (17)$$

In the experiments [6], the optimal self-focusing was observed for pulses of a duration of 350 fs, while the cluster size increased fivefold in 300 fs. At the same time, for $a/a_0 = 4$, the maximal pulse power ($P \sim 10^{11}$ W) suffices to exceed critical value (17). We, therefore, conclude that the experiments on self-focusing [6] can be interpreted in terms of the mechanism suggested in this work.

REFERENCES

1. A. McPherson, T. S. Luk, D. D. Thompson, *et al.*, Phys. Rev. Lett. **72**, 1810 (1994).
2. Y. L. Shao, T. Ditmire, T. W. G. Tisch, *et al.*, Phys. Rev. Lett. **77**, 3343 (1996).
3. T. Ditmire, T. W. G. Tisch, E. Springate, *et al.*, Phys. Rev. Lett. **78**, 2732 (1997); M. Lezius, S. Dobosz, D. Normand, *et al.*, Phys. Rev. Lett. **80**, 261 (1998).
4. Y. Kumarappan, M. Krishnamurthy, and J. Mathuv, Phys. Rev. Lett. **87**, 085005 (2001).
5. A. B. Borisov, A. McPherson, J. W. Longworth, *et al.*, J. Phys. B **29**, 247 (1996); A. B. Borisov, A. McPherson, *et al.*, J. Phys. B **29**, 113 (1996).
6. I. Alexeev, T. M. Antonsen, K. Y. Kim, and H. M. Milchberg, Phys. Rev. Lett. **90**, 103402 (2003); K. Y. Kim, I. Alexeev, E. Parra, and H. M. Milchberg, Phys. Rev. Lett. **90**, 023401 (2003).
7. T. Donnelly, T. Ditmire, N. Neuman, *et al.*, Phys. Rev. Lett. **76**, 2472 (1996).
8. I. Yu. Skobelev, A. Ya. Faenov, A. I. Magunov, *et al.*, Zh. Éksp. Teor. Fiz. **121**, 88 (2002) [JETP **94**, 73 (2002)].
9. J. Zwelback, T. E. Cowan, R. A. Smith, *et al.*, Phys. Rev. Lett. **85**, 3640 (2000).
10. N. A. Zharova, A. G. Litvak, and V. A. Mironov, Pis'ma Zh. Éksp. Teor. Fiz. **75**, 655 (2002) [JETP Lett. **75**, 539 (2002)]; Zh. Éksp. Teor. Fiz. **123** (4) (2003) [JETP **96**, 643 (2003)].
11. L. Berge, K. Germaschewski, R. Grauer, and J. J. Rasmussen, Phys. Rev. Lett. **89**, 153902 (2002).
12. S. N. Vlasov, L. V. Piskunova, and V. I. Talanov, Zh. Éksp. Teor. Fiz. **95**, 1945 (1989) [Sov. Phys. JETP **68**, 1125 (1989)]; S. N. Vlasov, Izv. Vyssh. Uchebn. Zaved., Radiofiz. **42**, 468 (1999).
13. V. E. Zakharov, N. E. Kosmatov, and V. F. Shvets, Pis'ma Zh. Éksp. Teor. Fiz. **49**, 431 (1989) [JETP Lett. **49**, 492 (1989)]; V. M. Malkin, Pis'ma Zh. Éksp. Teor. Fiz. **48**, 603 (1988) [JETP Lett. **48**, 653 (1988)].

Translated by V. Sakun

The Use of Perfect Crystals in High-Resolution X-ray Spectroscopy

A. V. Vinogradov[1], R. M. Feshchenko[1], *, and V. A. Chernov[2]

[1]Lebedev Physical Institute, Russian Academy of Sciences, Leninskiĭ pr. 53, Moscow, 119991 Russia
*e-mail: rusl@sci.lebedev.ru
[2]Budker Institute of Nuclear Physics, Siberian Division, Russian Academy of Sciences,
pr. Akademika Lavrent'eva 11, Novosibirsk, 630090 Russia
Received October 8, 2003

The possibility of improving the resolution and angular dispersion in the X-ray wavelength region through the use of asymmetric crystals in parallel beams is demonstrated. © 2003 MAIK "Nauka/Interperiodica".

PACS numbers: 07.85.Fv; 41.50.+h; 61.10.-i

High spectral resolution in the X-ray region is of interest for study of magnetic materials (Co, Fe, Mn, Ge, …) near their absorption edges [1, 2], phonon spectra of solids by inelastic X-ray scattering [3], photonuclear processes [4], etc. High resolution is achieved by the use of spectrometers and monochromators based on flat or bent crystals, which serve as selective reflectors in accordance with the Bragg condition

$$2d\sin(\varphi_0 + \alpha) = l\lambda_0, \quad l = 0, 1, 2, \ldots, \tag{1}$$

where λ_0 is the radiation wavelength, $\varphi_0 + \alpha$ is the beam glancing angle with respect to the crystal planes (figure), and d is the interplanar spacing; the index 0 will be omitted for brevity, where this will not cause confusion. The crystal may be symmetric (SC) if $\alpha = 0$ or asymmetric (AC) if $\alpha \neq 0$. In the first case, the crystal surface is parallel to the atomic planes, and in the second case, it makes the angle α (cut angle) with them. In both cases, the spectral resolution is determined by the reflection curve width and is ordinarily equal to 10^{-3}–10^{-6} rad [5]. However, there is a spectroscopically important distinction between SCs and ACs as regards the reflection of a parallel polychromatic beam. Namely, a polychromatic beam is reflected from the SC surface in a specular manner, i.e., without spectral decomposition. At the same time, when reflected from an AC, the beam undergoes spectral decomposition, because AC, in contrast to SC, represents a diffraction grating with period $D = d/\sin\alpha$. The resolution of such a grating is, clearly, determined by the total number of periods $N = L/D$ and is limited only by the crystal size L or by the technological potentialities (in this case, N is the number of phase-matched atomic planes). The reflection curve width (which determines the spectral resolution for SC) for an AC used as a diffraction grating determines the dispersion region, i.e., the spectral region where the diffraction efficiency is high.

Therefore, an AC represents a diffraction grating with (a) large dispersion (due to the small period D); (b) high diffraction efficiency (due to the Bragg effect) in a narrow spectral range determined by condition (1); and (c) high spectral resolution corresponding to the number N of atomic planes cropped out at the surface. These properties can be described quantitatively through solving the problem of diffraction from an AC. Consider a crystal for which condition (1) is fulfilled for a certain l. We first make sure that the Bragg condition for the AC coincides with the grating equation. To this end, we introduce in Eq. (1) the grating parameters $D = d/\sin\alpha$ and $\varphi_n = \varphi + 2\alpha$ instead of the parameters d and α of a multilayer structure. Then, indeed, we obtain the grating equation

$$D(\cos\varphi_n - \cos\varphi) = n\lambda_0, \tag{2}$$

where $n = -l$. Hence, a beam specularly reflected from the atomic planes corresponds to the lth-order diffrac-
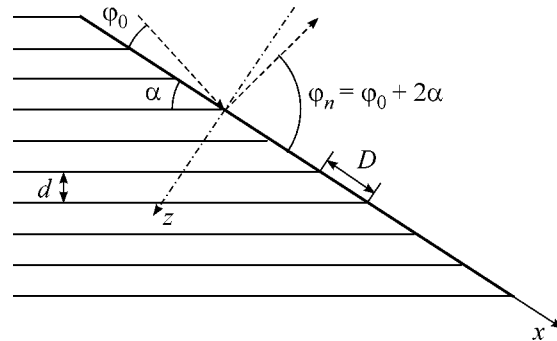
Schematic of reflection from an asymmetric crystal. Solid line is the crystal surface; dashed line is the beam trajectory; horizontal lines are atomic planes; and φ_0, φ_n, and α are the glancing, diffraction, and cut angles, respectively.

Widths of diffraction peaks for some asymmetric crystals (cut angle $\alpha = 10°$)

Crystal	Si			Ge			CaF$_2$	
Miller indices	(422)	(220)	(111)	(422)	(220)	(111)	(220)	(111)
$2d$, nm	0.222	0.384	0.627	0.231	0.400	0.653	0.386	0.631
λ, nm	0.194	0.166	0.275	0.179	0.131	0.607	0.166	0.275
Φ, nm	60.9	25.6	26.0	50.8	19.1	68.4	25.6	26.0
Ω, mrad	0.028	0.030	0.069	0.046	0.052	0.765	0.040	0.040
$\Delta\lambda/\lambda \times 10^5$	1.64	8.62	19.46	4.10	24.64	30.68	11.65	11.52
$\delta\varphi$, mrad	0.005	0.022	0.050	0.013	0.058	0.101	0.030	0.030

tion from the grating formed by the AC. Because of this, a high diffraction efficiency should be expected just for this order. Thus, let us consider a polychromatic beam with glancing angle φ satisfying condition (1) for all beam wavelengths approximately and for $\lambda = \lambda_0$ exactly. By using the slow amplitude approximation, one can obtain the following expression for the field outside and inside the AC in the case of strong coupling between the zeroth and nth diffraction orders:

$$z < 0, \quad E(x, z) = \exp\{ikx\cos\varphi + ikz\sin\varphi\}$$
$$+ R_n \exp\{ikx\cos\varphi_n - ikz\sin\varphi_n\}, \tag{3}$$

$$z > 0, \quad E(x, z) = \exp(i(\omega_0 - \omega_n)(z/2) - \nu z)$$
$$\times (\exp\{ikx\cos\varphi + iz\zeta_0\} \tag{4}$$
$$+ R_n \exp\{ikx\cos\varphi_n - iz\zeta_n\}),$$

where

$$\omega_m = \frac{k^2[\varepsilon_0 - \cos^2\varphi_m] - \zeta_m^2}{2\zeta_m}, \quad m = 0, n;$$

$$\zeta_0 = \frac{2\pi n\cos\alpha\sin\varphi_0}{d(\sin\varphi_0 + \sin\varphi_n)}, \quad \zeta_n = \zeta_0\frac{\sin\varphi_n}{\sin\varphi_0}, \tag{5}$$

$$\nu = \sqrt{\frac{k^4 B_n^2}{\zeta_0\zeta_n} - \frac{(\omega_0 + \omega_n)^2}{4}},$$

$$R_n = \frac{-k^2 B_n}{\zeta_0[(\omega_0 + \omega_n)/2 + i\nu]};$$

$k = 2\pi/\lambda$, φ_n is defined by Eq. (2), and ε_0 is the mean dielectric constant of the crystal. According to Eqs. (3)–(5), the amplitude R_n of the diffracted wave in the absence of absorption depends at $\varepsilon_0 \approx 1$ on only a single (not counting d) material constant B_n, which represents the Fourier-expansion harmonic of the dielectric constant. It can be expressed through the Bragg angle $\Phi = \varphi + \alpha$ and the halfwidth of the SC reflection curve (for some crystals, the relevant data are tabulated in [5]):

$$B_n = \frac{\Omega}{3\sqrt{2}}\sin 2\Phi. \tag{6}$$

One can readily verify that, in the wavelength region where the radicand in Eq. (5) is positive, the diffraction efficiency defined as $\eta_n = |R_n|^2\sin\varphi_n/\sin\varphi_0$ equals 1. The width of this region is given by

$$\frac{\Delta\lambda}{\lambda} = \frac{2\sqrt{2}}{3}\frac{\Omega}{\tan\Phi}\sqrt{\frac{\sin(\Phi + \alpha)}{\sin(\Phi - \alpha)}}. \tag{7}$$

This is just the AC dispersion (operating) region. The angular dispersion, according to grating equation (2), is equal to

$$\frac{d\varphi_n}{d\lambda} = -\frac{n\sin\alpha}{d\sin\varphi_n} \quad \text{or} \quad \lambda\frac{d\varphi_n}{d\lambda} = \frac{2\sin\Phi\sin\alpha}{\sin(\Phi + \alpha)}. \tag{8}$$

Contrary to Eq. (8), the angular dispersion of a ruled or holographic X-ray grating involves a small multiplier $\sim(\lambda/a)$, where a is the grating period.

Using the table, one can determine the spectral intervals $(\lambda - \Delta\lambda/2, \lambda + \Delta\lambda/2)$ where various crystals can be used as dispersive elements with an efficiency close to 100%. The parameters d and Ω, the Bragg angle Φ, the cut angle α, and the spectral $\Delta\lambda/\lambda$ and angular $\delta\varphi_n$ widths of the operating region determined according to Eqs. (7) and (8) are also given in the table for some crystals.

A pyrographite crystal is characterized by the value $\Omega \approx 10$ mrad, which is much greater than the data given in the table. One can, hence, expect the broader operating region $\Delta\lambda/\lambda \sim \Omega \approx 10^{-2}$ for this crystal, despite the fact that theory (2)–(8), strictly speaking, does not apply in this case because of the well-known structural features of pyrographite [6]. For the same reason, the spectral resolution for this crystal is limited by the domain size rather than by the sample size L.

Note in conclusion that, to obtain the spectral resolution $\lambda/\delta\lambda \sim 10^7$ for perfect crystals, it suffices, in principle, to use samples with size $L \sim (\lambda/\delta\lambda)D \approx 1$ cm. Thus, the spectral resolution and angular dispersion in X-ray spectroscopy can be substantially enhanced if an AC is used as a diffraction grating with a period corresponding to the interplanar spacing and cut angle. This approach can serve as an alternative to many-crystal monochromators and spectrometers with diffraction

gratings in which SCs or ACs are used as selective reflectors [1, 7, 8].

REFERENCES

1. K. Gerard, SRN **10**, 26 (1997).
2. Bu Hu, P. Geissbuhler, L. Soreensen, *et al.*, SRN **14**, 11 (2001).
3. K. Hamalainen and S. Manninen, J. Phys.: Condens. Matter **13**, 7539 (2001).
4. C. B. Collins, F. Davanloo, M. C. Iosif, *et al.*, Phys. Rev. Lett. **82**, 695 (1999).
5. B. L. Henke, E. M. Gullikson, and J. C. Davis, At. Data Nucl. Data Tables **54**, 181 (1993).
6. R. Beckhoff, B. Kanngiesser, and W. Malzer, Proc. SPIE **2859**, 190 (1996).
7. Z. G. Pinsker, *X-ray Crystal Optics* (Nauka, Moscow, 1982).
8. A. I. Chumakov, R. Rüffer, J. Metge, and A. Barla, Poverkhnost, No. 1, 42 (2000).

Translated by V. Sakun

Noncollinear Interlayer Exchange in Fe/Cr/Fe Magnetic Structures with Different Interface Roughnesses

N. M. Kreines[1], *, D. I. Kholin[1], S. O. Demokritov[2], and M. Rikart[3]

[1]*Kapitza Institute of Physical Problems, Russian Academy of Sciences, Moscow, 117334 Russia*
*e-mail: kreines@kapitza.ras.ru
[2]*Department of Physics, Kaiserslautern University of Technology, Gottlieb-Daimler-Str., 67663 Kaiserslautern, Germany*
[3]*INESC Microsistemas e Nanotecnologia, Rua Alves Redol 9, 1000-029 Lisboa, Portugal*
Received October 9, 2003

The interaction of iron layers through a chromium spacer in Fe/Cr/Fe trilayers with different roughnesses of interfaces was studied by the Kerr magnetometry and Mandel'shtam–Brillouin light scattering techniques so as to trace the interlayer exchange coupling of the Fe layers depending on the Cr spacer thickness and the sample temperature. It is established that, in a broad range of these parameters, the interlayer exchange in Fe/Cr/Fe structures with sufficiently smooth interfaces is adequately described using the proximity magnetism and half-angle coupling models taking into account the antiferromagnetic properties of chromium. As the interface roughness increases, the well-known biquadratic exchange model becomes valid. This is evidence for the decisive role of the magnetic stiffness of a Cr spacer and the structure of interfaces on the noncollinear exchange coupling in Fe/Cr/Fe trilayers. © *2003 MAIK "Nauka/Interperiodica".*

PACS numbers: 75.70.Cn

1. INTRODUCTION

Multilayer structures comprising ultrathin ferromagnetic layers separated by nonferromagnetic metal spacers have been extensively studied for more than a decade. The phenomena of interlayer exchange coupling and giant magnetoresistance observed in these systems, together with the possibility of obtaining films with preset saturation fields, led to the development of new magnetic memory devices (MRAMs) and miniature magnetic field sensors. At the same time, many basic problems pertaining to the interlayer exchange coupling mechanisms and spin-dependent electron transport in these multilayer structures remain unresolved.

This paper is devoted to interlayer exchange coupling in Fe/Cr/Fe trilayers. Owing to the nontrivial magnetic properties of the chromium spacer, various effects inherent in the interlayer exchange are especially clearly manifested in such structures. On the other hand, it is the complexity of the magnetic structure of chromium that makes the mechanism of the interlayer interaction in this system still unclear.

It has been known for a long time that the interlayer interaction in multilayer magnetic structures exhibits oscillations with the spacer thickness, leading to ferromagnetic or antiferromagnetic ordering of magnetic moments in the neighboring ferromagnetic layers. More recently, these structures were found to feature noncollinear magnetic ordering, whereby the angle θ between magnetic moments of the neighboring ferromagnetic layers is different from both 0 and 180°. Orig-

inally, this noncollinear ordering was observed in this very system, Fe/Cr/Fe, by Rührig *et al.* [1] and explained using the so-called biquadratic exchange model. According to this phenomenological model, the interlayer exchange coupling energy depends on the angle θ between magnetizations of the neighboring Fe layers as

$$E = J_1 \cos\theta + J_2 \cos^2\theta, \qquad (1)$$

where J_1 and J_2 are the bilinear and biquadratic exchange parameters, respectively. Several variants of the microscopic justification of this model have been proposed [2–5]. However, all these mechanisms, including those taking into account the antiferromagnetism of the chromium spacer [6], have proved to be valid only when J_2 is small as compared to J_1. Actually, the J_2 values experimentally determined for Fe/Cr/Fe trilayers are frequently comparable with J_1 or even exceed this value.

In connection with this, several models have been developed using an alternative expression for the interlayer exchange coupling energy. For the case when the spacer between the ferromagnetic layers possesses an intrinsic antiferromagnetic order, Slonczewski [7] proposed the so-called proximity magnetism model, predicting the following dependence of the exchange energy on the angle θ:

$$E = C_+ \frac{\theta^2}{\pi^2} + C_- \frac{(\pi - |\theta|)^2}{\pi^2}. \qquad (2)$$

This model proceeds from the assumption that the spacer represents a laminar antiferromagnet. In this case, oscillations of the spacer thickness lead to "frustrated" interlayer exchange coupling and distorted magnetic order in the spacer. This model was successfully used [8, 9] to describe the properties of metal trilayers with antiferromagnetic manganese spacers. The possibility of applying the same model to the structures with chromium spacers is not obvious. Since the Néel temperature of bulk chromium is 311 K, the room-temperature order parameter in this metal is very small. However, the available neutron diffraction data show that chromium in thin layers adjacent to iron retains antiferromagnetic properties up to significantly higher temperatures [10]. This fact suggested that the proximity magnetism model may be valid for the Fe/Cr/Fe system as well. Schreyer *et al.* [11] studied the possibility to use model (2) for interpretation of the magnetization curves and the neutron diffraction data obtained for [Fe(52 Å)/Cr(17 Å)]$_9$ superlattice. However, the volume of experimental data was insufficient for a reliable quantitative comparison to the theory.

Later, the interlayer exchange through a spacer representing a localized antiferromagnet was theoretically investigated in more detail by Morozov and Sigov [12]. In the case of sufficiently smooth interfaces and strong coupling at the boundary between ferromagnet and antiferromagnet, this theory also led to expression (2). In the other limiting case, when the exchange at the boundaries is small as compared to that inside the chromium spacer, the expression for the exchange energy was different from those proposed previously:

$$E = J_+\cos\frac{\theta}{2} + J_-\sin\frac{\theta}{2}. \tag{3}$$

A substantially different, self-consistent approach to description of the properties of a chromium spacer as an itinerant antiferromagnet was used in the theory developed by Men'shov and Tugushev [13]. Despite the different approach, expression (3) was also obtained for certain relations between layer thicknesses, the scale of interface roughness, and the exchange interactions within the layers and at the boundaries. This expression is referred to as the half-angle coupling model. To the best of our knowledge, no attempts to use this model for the description of experimental data have been reported so far.

To summarize, the state of the art in this field can be briefly characterized as follows. In most papers devoted to Fe/Cr/Fe trilayers, the experimental data have been interpreted within the framework of the biquadratic exchange model, although the values of exchange constants in many cases fall outside the region of applicability of this model. At the same time, other theories aimed at explaining the strong noncollinear exchange coupling in the Fe/Cr/Fe system did not receive sufficient experimental support. In order to elucidate this situation, we have studied in detail the interlayer exchange in Fe/Cr/Fe trilayers with wedge-shaped chromium spacers using Kerr magnetometry and Mandel'shtam–Brillouin light scattering.

2. EXPERIMENTAL

Samples of Fe/Cr/Fe trilayers were grown by molecular beam epitaxy (MBE) on single-crystal MgO(100) substrates at a residual gas pressure of about 10^{-10} mbar and a substrate temperature of 473 K. The substrate was preliminarily covered with a buffer layer of silver approximately 1000 Å thick. The crystallographic axes [001] in both the iron and the chromium layers coincided with the normal to the sample plane. By changing the MBE conditions, it was possible to control the degree of roughness of the interfaces. The interface roughness was monitored by low-energy electron diffraction (LEED) and by measurements of the short-wave oscillations of the interlayer exchange interaction. Below we will demonstrate a qualitative difference in the interlayer exchange coupling observed in the Fe/Cr/Fe trilayer with a wedge-shaped chromium spacer (with the thickness $t_{Cr} = 0$–20 Å) and a relatively high roughness of interfaces studied in [6, 14] (sample 1) and in the trilayer with $t_{Cr} = 0$–40 Å and relatively smooth interfaces studied in this work (sample 2). The wedge slope in both cases corresponded to approximately 2.5 Å/mm, and the iron layer thicknesses were about 100 Å.

The magnitude and character of the interlayer exchange coupling in both samples were studied by two experimental methods: first, by measuring the magnetization curves using the magneto-optic Kerr effect in the temperature range from 77 to 473 K and, second, by measuring room-temperature Mandel'shtam–Brillouin light scattering. In both cases, an external magnetic field H was oriented in the sample plane. The laser beam was focused on the film surface, with a spot diameter not exceeding 0.2 mm. The measurements were performed for various values of the chromium spacer thickness, by gradually shifting the laser beam along the wedge (for more details, see [6, 14]).

3. RESULTS AND DISCUSSION

Figure 1 presents the typical room-temperature magnetization curve of sample 1 (with rougher interfaces) plotted in the so-called Arrott coordinates of HM_S/M vs. $(M/M_S)^2$, where M is the average magnetization and M_S is the saturation magnetization of the sample. The inset in Fig. 1 shows a field dependence of the frequency of the Damon–Eshbach spin wave mode with a wavevector of $q = 1.57 \times 10^5$ cm^{-1}. As can be seen, both the magnetization curve and the field dependence of the spin wave frequency are described well within the framework of the biquadratic exchange model (solid curves). This is clearly manifested by a linear portion of the magnetization curve constructed in
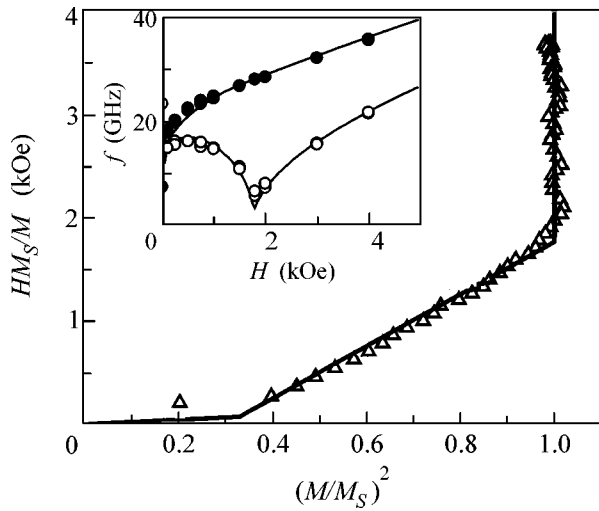
Fig. 1. The typical room-temperature magnetization curve in the Arrott coordinates and the spin wave frequency versus magnetic field (inset) plotted for Fe/Cr/Fe sample 1 with a Cr spacer thickness of 11 Å. Solid curves show the results of numerical modeling based on the biquadratic exchange model.
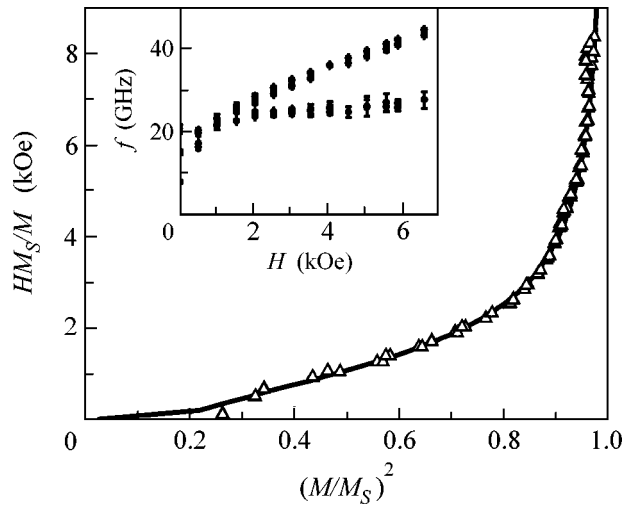

Fig. 2. The typical room-temperature magnetization curve in the Arrott coordinates and the spin wave frequency versus magnetic field (inset) plotted for Fe/Cr/Fe sample 2 with a Cr spacer thickness of 8 Å. Solid curves show the results of numerical modeling based on the proximity magnetism model.

the Arrott coordinates, with a kinklike transition to saturation, and by a characteristic sharp minimum in the frequency of the optical branch of spin waves in the saturation field. A detailed analysis of the interlayer exchange coupling as a function of the spacer thickness and temperature was performed in [6, 14]. The value of J_1 determined from these data oscillates with the chromium spacer thickness t_{Cr}. The value of J_2 monotonically decays as $J_2(t_{Cr}) = J_2^0/t_{Cr}$, where the coefficient J_2^0 decreases with increasing temperature. A linear extrapolation of this dependence to the region of high temperatures gives a conditional point of disappearance of the biquadratic exchange in the region of 700 K.

Figure 2 shows the typical room-temperature magnetization curve and a field dependence of the spin wave frequency for sample 2, with smoother interfaces. There are important qualitative differences of these results from the data presented above for sample 1. Indeed, the magnetization curve reaches saturation asymptotically and exhibits no kinks. The field dependence of the frequency of the optical branch of spin waves is virtually deprived of a minimum. These results cannot be satisfactorily interpreted within the framework of the biquadratic exchange model. On the contrary, the proximity magnetism model (represented by the solid curve in Fig. 2) perfectly describes the magnetization data for sample 2 at all thicknesses of the chromium spacer and all temperatures in the range studied.

Figure 3 shows the plots of the exchange parameters C_+ and C_- versus chromium spacer thickness constructed for sample 2 at room temperature. As can be seen, C_- exhibits pronounced oscillations with a period of 2.8 Å. The curve also reveals a second, long period

of exchange coupling oscillations amounting to ~18 Å. This behavior agrees well with the published data and predictions of the Slonczewski model [7]. In contrast, the curve of $C_+(t_{Cr})$ exhibits no oscillations and rapidly decays with increasing spacer thickness. This result contradicts the commonly accepted notion about counteroscillating constants C_+ and C_- (see, e.g., [9]). However, the possibility to observe different behavior of C_+
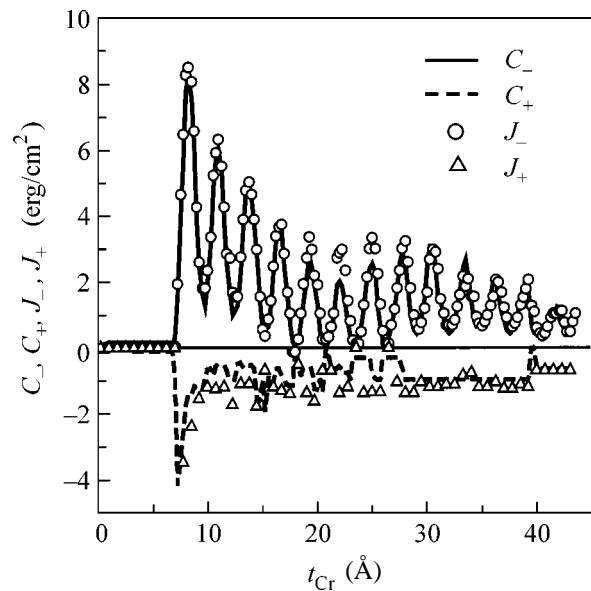

Fig. 3. The plots of the exchange coupling parameters C_+, C_- (for model (2)) and J_+, J_- (for model (3)) versus the Cr spacer thickness constructed for Fe/Cr/Fe sample 2 at room temperature.
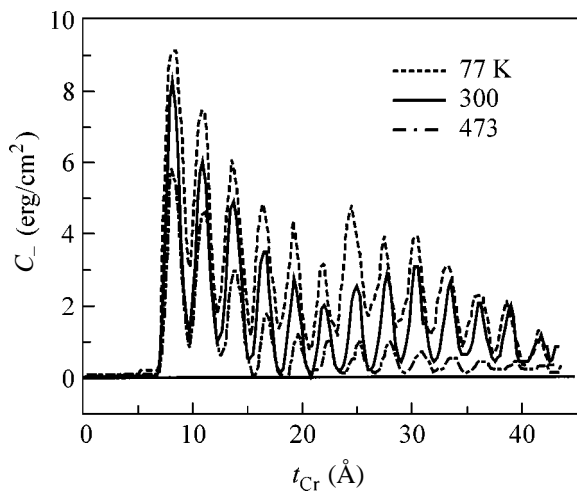
Fig. 4. The plots of the exchange coupling parameter C_- (for model (2)) versus the Cr spacer thickness constructed for Fe/Cr/Fe sample 2 at three temperatures.

and C_- values was also considered by Slonczewski [7]. This possibility was explained by averaging of the shortwave fluctuations in the interlayer exchange coupling as a result of spacer thickness fluctuations, with the average exchange coupling shifted toward the antiferromagnetic region.

Figure 4 shows the plots of the oscillating exchange parameter C_- versus Cr spacer thickness constructed for three temperatures (77, 300, and 473 K). As can be seen, both the absolute exchange magnitude and the amplitude of oscillations significantly decrease with increasing temperature. It is also evident that the exchange coupling more strongly depends on the temperature at a greater spacer thickness t_{Cr}. A more detailed description of the temperature dependence of the exchange coupling will be presented in following papers.

We have analyzed the data obtained for sample 2 in terms of the half-angle coupling model (3). It was found that this model also describes well the magnetization curve in the entire range of variation of the spacer thickness and the sample temperature. The magnetization curves obtained by approximating the experimental data in terms of models (2) and (3) virtually coincided. Moreover, parameters of the latter approximation, J_+ and J_-, numerically coincide with the coefficients C_+ and C_- (Fig. 3). This coincidence is by no means accidental and is explained by the fact that, despite significant differences in the initial assumptions and in the expressions for exchange coupling energies (2) and (3), the curves of $E(\theta)$ determined by these equations are numerically very close.

In conclusion, we briefly summarize the most important results of this investigation. It was found that the interlayer exchange coupling in the Fe/Cr/Fe trilayer is adequately described in the entire range of Cr spacer thicknesses and sample temperatures in terms of the proximity magnetism (2) and half-angle coupling (3) models based on the assumption that the Cr spacer possesses intrinsic magnetic stiffness. This is evidence for the strong noncollinear exchange coupling in the Fe/Cr/Fe system being directly related to the antiferromagnetism of the Cr spacer rather than restricted to mechanisms of the Ruderman–Kittel–Kasuya–Yoside (RKKY) type. It was also demonstrated that trilayer samples differing only in the degree of roughness of the interfaces may exhibit different mechanisms of exchange coupling, obeying either model (1) or models (2) and (3). Therefore, the structure of interfaces plays a decisive role in the interlayer exchange coupling and determines its mechanism.

REFERENCES

1. M. Rührig, R. Schafer, A. Hubert, *et al.*, Phys. Status Solidi A **125**, 635 (1991).
2. P. Bruno, Phys. Rev. B **52**, 411 (1995).
3. J. C. Slonczewski, Phys. Rev. Lett. **67**, 3172 (1991).
4. S. O. Demokritov, E. Tsymbal, P. Grunberg, *et al.*, Phys. Rev. B **49**, 720 (1994).
5. J. C. Slonczewski, J. Appl. Phys. **73**, 5957 (1993).
6. S. O. Demokritov, A. B. Drovosekov, N. M. Kreĭnes, *et al.*, Zh. Éksp. Teor. Fiz. **122**, 1233 (2002) [JETP **95**, 1062 (2002)].
7. J. C. Slonczewski, J. Magn. Magn. Mater. **150**, 13 (1995).
8. M. Chirita, G. Robins, R. L. Stamps, *et al.*, Phys. Rev. B **58**, 869 (1998).
9. D. T. Pierce, A. D. Davies, J. A. Stroscio, *et al.*, J. Magn. Magn. Mater. **222**, 13 (2000).
10. H. Zabel, J. Phys.: Condens. Matter **11**, 9303 (1999).
11. A. Schreyer, J. F. Anker, Th. Zeidler, *et al.*, Phys. Rev. B **52**, 16066 (1995).
12. A. I. Morozov and A. S. Sigov, Fiz. Tverd. Tela (St. Petersburg) **41**, 1240 (1999) [Phys. Solid State **41**, 1130 (1999)].
13. V. N. Men'shov and V. V. Tugushev, Zh. Éksp. Teor. Fiz. **122**, 1044 (2002) [JETP **95**, 901 (2002)].
14. S. O. Demokritov, A. B. Drovosekov, D. I. Kholin, and N. M. Kreines, J. Magn. Magn. Mater. **258–259**, 391 (2003).

Translated by P. Pozdeev

Resonant Tunneling in Superconducting Structures with *s* and *d* Symmetry of Order Parameter

D. V. Goncharov, I. A. Devyatov*, and M. Yu. Kupriyanov

Skobeltsyn Institute of Nuclear Physics, Moscow State University, Vorob'evy gory, Moscow, 119899 Russia
* e-mail: idev@pn.sinp.msu.ru
Received October 14, 2003

Resonant tunneling processes are studied in superconducting junctions of low transparency with the order parameter of the electrodes of different symmetry. A general equation of the resonant current is derived within the Green's function formalism for the junctions of arbitrary dimensionality. The phase dependence of the supercurrent averaged over the set of localized states is analyzed for superconducting junctions with an isotropic order parameter. A numerical analysis of the resonant current transport in junctions with high-T_c superconducting electrodes with the *d* symmetry of the order parameter was carried out. © 2003 MAIK "Nauka/Interperiodica".

PACS numbers: 74.50.+r; 74.78.Fk

Experimental studies of Josephson junctions with an interlayer of semiconducting oxides showed the occurrence of the anomalous proximity effect [1–4]. It lies in the existence of a noticeable critical current in junctions with anomalously large interlayer widths $d > 100$ nm, which are considerably larger than the coherence length of the interlayer materials. This effect in Josephson structures with isotropic *s* pairing in the electrodes was explained within a model that took into account the possibility of resonant tunneling through localized states (LS) [5]. The LS effect on the current transport was also observed in Nb/AlO$_x$/Nb junctions with a high density of critical current [6].

Theoretical studies of the problem of resonant tunneling in normal metal–insulator–normal metal (NIN) structures were previously carried out within the tunneling model [7] and within the three-dimensional model of junctions [8, 9]. Resonant transport was also considered for junctions in which one or both electrodes had the *s* symmetry of the order parameter [10–15]. Resonant current transport with *d* pairing in the electrodes was previously investigated only within a one-dimensional model of the resonant coupling between the edges in [16]. At the same time a consistent theory of resonant supercurrent transport in *d*-type superconductor–insulator–*d*-type superconductor (DID) structures has not been developed to date.

An analysis of the experimental data [17] has shown that the normal current component in a number of high-T_c superconductors is transferred in a resonant way, whereas supercurrent transport is determined by direct tunneling without the participation of LSs. Up to now, this effect has not been explained consistently. At the same time, it has been shown in [18] that the processes of resonant tunneling in normal metal–insulator–*d*-type

superconductor (NID) structures lead to suppressing of the features in the conductivity at low voltages across the junction that arises from the occurrence of bound zero-energy states (ZESs) in the superconducting electrodes [19]. The like can also be expected for the resonant supercurrent transport when one or both of the electrodes have the *d* symmetry of the order parameter. The goal of this work is to develop a theory of resonant transport of the Josephson current in such high-T_c superconducting junctions.

We will consider that the tunnel barrier $V(r)$ in the junction under study is a sum of potentials

$$V(r) = V_{\text{rect}} + V_{\text{imp}}, \tag{1}$$

in which the first term models a rectangular barrier of height V and thickness d $V_{\text{rect}}(x) = V\theta(x(d - x))$ and the second one describes the LS in the interlayer material

$$V_{\text{imp}}(\mathbf{r} - \mathbf{r}_0) = -\begin{cases} \alpha, & \text{if } |\mathbf{r} - \mathbf{r}_0| \leq \rho \\ 0, & \text{if } |\mathbf{r} - \mathbf{r}_0| > \rho, \end{cases} \tag{2}$$

which is localized at a certain point $\mathbf{r}_0$ and has a radius $\rho \ll |\mathbf{k}|^{-1}$, where $\mathbf{k}$ is the Fermi momentum of quasiparticles in the electrodes. We will restrict ourselves with the weak binding limit and consider that vector $\mathbf{k}$ is fixed at the Fermi surface ($|\mathbf{k}| = k \cong k_F$). The potential (2) disturbs the spatial uniformity of the junction and leads to the nonconservation of the quasiparticle momentum component parallel to the barrier in the process of their tunneling. Let the density of LSs in the interlayer be low, so that their mutual influence is insignificant. The barrier thickness will be considered sufficiently large $\lambda_0 d \gg 1$, where $\lambda_0 = \sqrt{2mV_0}$ is the quasiparticle momentum in the interlayer ($V_0 = V - \mu$), *m* is

the electron mass, and μ is the Fermi energy. In addition, we will assume that the conditions $\lambda_0(d - x_0)$, $\lambda_0 x_0$ $\gg 1$ are fulfilled. The fulfillment of the last condition is necessary for the effective localization of the quasiparticle wave function on the defect.

The transport properties of the junction will be calculated using the general equation for the current

$$I(\varphi) = \frac{eT}{2im} \lim_{x' \to x} \left(\frac{\partial}{\partial x'} - \frac{\partial}{\partial x} \right) \sum_{\omega_n} \text{Tr}\{ \mathbf{G}_\omega(\mathbf{r}, \mathbf{r}') \} \Big|_{x=0}, \quad (3)$$

where $\varphi = \varphi_L - \varphi_R$ is the difference between the macroscopic phases of the order parameters of the left-hand and right-hand superconductors, respectively; e is the electron charge; and T is the temperature. The following matrix equation is true for Green's function $\mathbf{G}_\omega(\mathbf{r}, \mathbf{r}')$ [20]:

$$\left[i\omega \hat{I} - \sigma_z \hat{h} - \frac{1}{2}(\Delta(x, \theta)\sigma_+ + \Delta^*(x, \theta)\sigma_-) \right] \\ \times \mathbf{G}_\omega(\mathbf{r}, \mathbf{r}') = \delta(\mathbf{r} - \mathbf{r}')\hat{I}, \quad (4)$$

where operator $\hat{h} = -\nabla^2/2m - \mu + V(\mathbf{r})$; $\omega = (2n+1)\pi T$ are the Matsubara frequencies; and $\Delta(x, \theta)$ is the anisotropic order parameter, which depends on the angle θ of the propagation of quasiparticles with respect to the axis x. In this equation, $\hat{I}$ designates a second-order unit matrix and σ_x, σ_y, and σ_z ($\sigma_\pm = \sigma_x \pm i\sigma_y$) are the Pauli matrices.

Differential equation (4) in our case is conveniently rewritten in the integral form

$$\mathbf{G}_\omega(\mathbf{r}, \mathbf{r}') = \mathbf{G}_\omega^0(\mathbf{r}, \mathbf{r}') \\ + \int \mathbf{r}_1 \mathbf{G}_\omega^0(\mathbf{r}, \mathbf{r}_1) \sigma_z V_{\text{imp}}(\mathbf{r}_1 - \mathbf{r}_0) \mathbf{G}_\omega(\mathbf{r}_1, \mathbf{r}'). \quad (5)$$

Green's function $\mathbf{G}_\omega^0$ of the "unperturbed" problem is determined from Eq. (4) in which operator $\hat{h}$ is replaced by the operator $\hat{h}_0 = -\nabla^2/2m - \mu + V_{\text{rect}}$, which does not contain the LS potential. In this case, Green's function $\mathbf{G}_\omega^0$ is represented by a sum of plane waves with coefficients determined by the continuity condition for the functions themselves and their derivatives at the junction boundaries. Substituting the obtained function $\mathbf{G}_\omega^0$ into Eq. (5) and taking into account the locality of the potential (2) leads to a dimensionally universal equation for the resonant supercurrent (see Eq. (3)) with the trace of the matrix $\mathbf{G}_\omega(\mathbf{r}, \mathbf{r}')$

$$\text{Tr}\{ \mathbf{G}_\omega(\mathbf{r}, \mathbf{r}') \} \\ = \Lambda(\mathbf{r}_0) \sum_{j,l=1}^{2} (-1)^{l+1} G_{jl}^0(\mathbf{r}, \mathbf{r}_0) g_{jl}(\mathbf{r}_0, \mathbf{r}'),$$

$$g_{11} = G_{11}^0(\mathbf{r}_0, \mathbf{r}')(1 + V_{22}(\mathbf{r}_0)) - G_{21}^0(\mathbf{r}_0, \mathbf{r}')V_{12}(\mathbf{r}_0), \\ g_{12} = G_{21}^0(\mathbf{r}_0, \mathbf{r}')(1 - V_{11}(\mathbf{r}_0)) + G_{11}^0(\mathbf{r}_0, \mathbf{r}')V_{21}(\mathbf{r}_0), \quad (6)$$

$$g_{21} = G_{12}^0(\mathbf{r}_0, \mathbf{r}')(1 + V_{22}(\mathbf{r}_0)) - G_{22}^0(\mathbf{r}_0, \mathbf{r}')V_{12}(\mathbf{r}_0),$$

$$g_{22} = G_{22}^0(\mathbf{r}_0, \mathbf{r}')(1 - V_{11}(\mathbf{r}_0)) + G_{12}^0(\mathbf{r}_0, \mathbf{r}')V_{21}(\mathbf{r}_0),$$

$$\Lambda(\mathbf{r}_0) = \frac{1}{\Phi} \int d\mathbf{r}_1 V_{\text{imp}}(\mathbf{r}_1 - \mathbf{r}_0).$$

Here, $\Lambda(\mathbf{r}_0)$ is the absolute value of the resonant scattering amplitude, and

$$\Phi = (1 + V_{22}(\mathbf{r}_0))(1 - V_{11}(\mathbf{r}_0)) + V_{12}(\mathbf{r}_0)V_{21}(\mathbf{r}_0),$$

$$\begin{pmatrix} V_{11}(\mathbf{r}_0) & V_{12}(\mathbf{r}_0) \\ V_{21}(\mathbf{r}_0) & V_{22}(\mathbf{r}_0) \end{pmatrix} = \int d\mathbf{r}_1 \mathbf{G}_\omega^0(\mathbf{r}_0, \mathbf{r}_1) V_{\text{imp}}(\mathbf{r}_1 - \mathbf{r}_0).$$

Of most interest in high-T_c superconducting structures is 2D transport in the *ab* plane. In this case, Eq. (6) results in the equation

$$I_{\text{res}}^{2D} = -2ieT\gamma_0^2 \sum_\omega \frac{1}{\Phi_{2D}} [J_-^R J_-^L + J_+^L J_+^R], \quad (7)$$

where

$$\Phi_{2D} = -\omega^2 - E_R^2 - \frac{\Gamma^2}{4} - \omega V_0(2(J_1 + J_2)\gamma_0 - \Gamma) \\ + \gamma_0^2(\Gamma\gamma_0^{-1}(J_1 + J_2) - (J_1 + J_2)^2 - (J_-^L + J_+^R)(J_-^R + J_+^L)),$$

$$\Gamma_{01} = V_0|t|e^{\lambda_0(d - 2x_0)} \sqrt{\frac{\pi}{\lambda_0 x_0}},$$

$$\Gamma_{02} = V_0|t|e^{-\lambda_0(d - 2x_0)} \sqrt{\frac{\pi}{\lambda_0(d - x_0)}},$$

$$\Gamma_0^2 = \Gamma_{01}\Gamma_{02}, \quad \Gamma = \Gamma_{01} + \Gamma_{02}, \quad \gamma_0 = 2V_0|t|,$$

$$E_R \cong E_0 - \frac{\lambda_0^2 + \kappa^2}{4\lambda k_F} \Gamma.$$

Here, Γ_0 is the width of the level of an electron state on an LS, E_R is the effective energy of the resonance level in which the shift due to the finite width of the barrier is taken into account, and $|t|$ is the absolute value of the transmission coefficient of the potential barrier. In the 2D junction model, the parameters of the problem are selected in such a way that the potential well (2) contains at least one energy level E_0. In this case, the energy parameters of the LS are expressed through the model constants ρ and α similarly to [18].

The other parameters in Eq. (7) are determined in the following way:

$$
\begin{aligned}
\begin{array}{c} J_1 \\ J_-^L \\ J_+^L \end{array} &= \left\langle \begin{array}{c} 1 \\ \dfrac{e^{\lambda_0 d - 2\lambda(k_y)x_0}}{\lambda(k_y)\Gamma_1}\beta_-^L \\ \beta_+^{L*} \end{array} \right\rangle_{k_y} , \\[2ex]
\begin{array}{c} J_2 \\ J_-^R \\ J_+^R \end{array} &= \left\langle \begin{array}{c} 1 \\ \dfrac{e^{\lambda_0 d - 2\lambda(k_y)(d-x_0)}}{\lambda(k_y)\Gamma_2}\beta_-^{R*} \\ \beta_+^R \end{array} \right\rangle_{k_y} ,
\end{aligned}
\tag{8}
$$

where angle brackets $\langle \dots \rangle$ designate averaging over the transverse momentum k_y

$$
\langle f(k_y) \rangle_{k_y} = \frac{k_F}{2} \int_{-\pi/2}^{\pi/2} d\theta \cos(\theta) f(k_F \sin(\theta)),
$$

$$
\Gamma_1 = 1 + \beta_-^L \beta_+^{L*}, \quad \Gamma_2 = 1 + \beta_+^R \beta_-^{R*},
$$

$$
\Gamma_3 = 1 + \beta_-^L \beta_-^{R*}, \quad \Gamma_4 = 1 + \beta_+^R \beta_-^{L*},
$$

$$
\beta_\pm^{L,R} = \frac{-i\,\mathrm{sgn}(\omega)(\Delta_\pm^{L,R})^*}{\omega + \mathrm{sgn}(\omega)\Omega_\pm^{L,R}},
$$

$$
\Omega_\pm^{L,R} = \sqrt{\omega^2 + |\Delta_\pm^{L,R}|^2},
$$

$$
\lambda(k_y) = \sqrt{\lambda_0^2 + k_y^2 - 2mi\omega}.
$$

The order parameters of the left-hand and right-hand superconductors are designated by superscripts L and R and, in the case of the d symmetry of the order parameter in both edges, are determined by the equation

$$
\Delta_\pm(x) = \begin{cases} \Delta^L \cos(2\theta \mp 2\alpha_L)e^{i\varphi_L}, & \text{if } x < 0 \\ 0, & \text{if } 0 < x < d \\ \Delta_R \cos(2\theta \mp 2\alpha_R)e^{i\varphi_R}, & \text{if } x > d. \end{cases}
\tag{9}
$$

Equation (7) describes the general case of resonant current transport in 2D structures with an arbitrary symmetry of the order parameter in the electrodes and represents the main result of this paper. In the limiting case of isotropic order parameters in the electrodes, Eq. (7) describes the supercurrent in an SIS junction

$$
I_{\mathrm{res}} = eT\Delta^2 \sin(\varphi)\Gamma_0^2 \sum_\omega \left[\Gamma_0^2 \Delta^2 \sin^2\!\left(\frac{\varphi}{2}\right) \right.
$$
$$
\left. - (\Delta^2 + \omega^2)\left(\omega^2 + E_R^2 + \frac{\Gamma^2}{4}\right) - \omega^2 \Gamma\sqrt{\Delta^2 + \omega^2} \right]^{-1}.
\tag{10}
$$

The dispersion equation derived from Eq. (7) upon analytic continuation $\omega \longrightarrow -iE$

$$
\Gamma_0^2 \Delta^2 \sin^2\!\left(\frac{\varphi}{2}\right) + (\Delta^2 - E^2)\left(E^2 - E_R^2 - \frac{\Gamma^2}{4}\right)
$$
$$
+ E^2 \Gamma \sqrt{\Delta^2 - E^2} = 0
\tag{11}
$$

was obtained previously in one-dimensional models for a short junction $d \ll \xi_0$ (ξ_0 is the coherence length) [11] and was generalized to arbitrary ratios between the barrier width and the coherence length [12].

The form of relationships (10) and (11) is insensitive to the dimensionality of the problem. Thus, the Beenakker–van Houten dispersion equation (11), which has been obtained in its time within a one-dimensional model, has a more general sense and remains true for junctions with a wide barrier and in problems of high dimensionalities.

Equation (10) allows an analytic summation of the spectrum of Matsubara frequencies in the cases of "broad" ($\Delta/\Gamma_0 \ll 1$) and "narrow" ($\Delta/\Gamma_0 \gg 1$) resonances. An investigation of the supercurrent in these two limits allows the conclusions of [12] to be repeated but now for junctions with 2D and 3D geometries. In this case, we obtained that the resonant transparency is close to unity and the phase dependence of the supercurrent is not sinusoidal $I_{\mathrm{res}}(\varphi) \propto \sin(\varphi/2)$ only when the energy of the resonance level is close to zero ($E_R \sim 0$) and the LS is located near the center of the barrier ($x_0 \sim d/2$). A displacement of the resonance energy of the LS from the zero level or a displacement of the localized state from the center of the barrier decreases the resonant transparency and leads both to a drop in the supercurrent and to the restoration of the sinusoidal character of the dependence $I_{\mathrm{res}}(\varphi)$. Upon averaging over the energies and coordinates of the localized states, the supercurrent in 2D and 3D SIS junctions becomes proportional to $\sin(\varphi)$ in both limiting cases.

In the case of an extended ($\lambda_0 d \gg 1$) junction with low transparency, the limit of a "broad" resonance is difficult to realize in practice. From the experimental point of view, the opposite case when the junction has two boundaries of low transparency is of greater interest. Then, the parameters of the interfaces can be selected in such a way that only the LSs are located at the center of the barrier with $x_0 \approx d/2$. In this case, the supercurrent can be averaged by means of the approach used in [6]. Considering that the distribution of LSs is uniform in energies $\rho(E_R) = \text{const}$ and, when Eq. (10) is averaged, passing from integration over the energy to integration over the resonant transparency $D(E_R) = \Gamma_0^2 / (E_R^2 + \Gamma^2/4)$, one can readily prove that, as in [6], averaging over the energy is equivalent to averaging over the transparency of the conducting channels with the Schep–Bauer distribution function [21] $\rho(D) \propto D^{-3/2}(1-D)^{-1/2}$. Such a distribution $\rho(D)$ is universal for
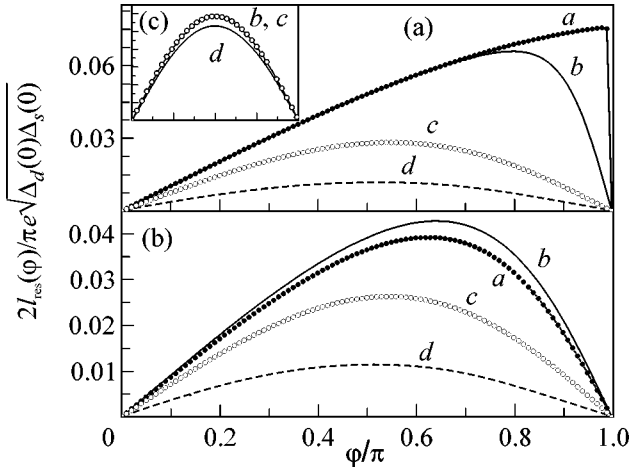
Fig. 1. Phase dependences of the supercurrent $I_{res}(\varphi)$ in a SID junction in the case of $\gamma_0/\Delta_d(0) = 0.1$ at $\lambda d = 6$, $k/\lambda = 2$, $E_R = 0$, and $x_0 = d/2$; (a) $\alpha_R = 0$; (b) $\alpha_R = \pi/12$; and a, $T/T_s = 0$; b, $T/T_s = 0.05$; c, $T/T_s = 0.3$; and d, $T/T_s = 0.6$; and (c) the phase dependences of the nonresonant supercurrent were constructed in arbitrary units for the same parameters and $\alpha_R = 0$.
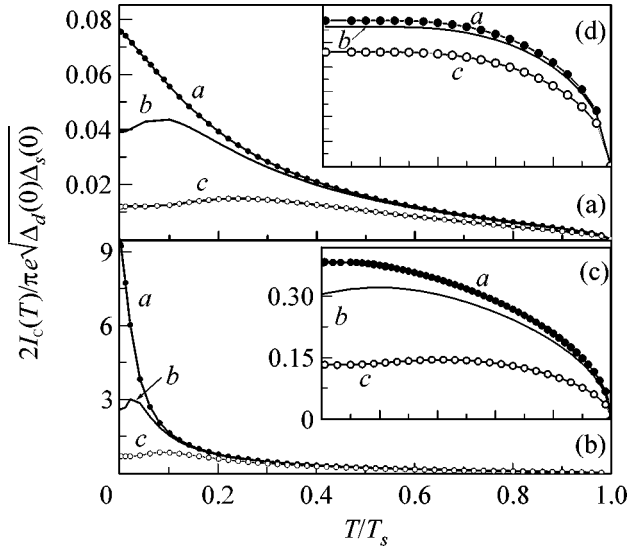

Fig. 2. Temperature dependences of the supercurrent $I_C(T)$ in a SID junction in the cases of (a) $\gamma_0/\Delta_d(0) = 0.1$; (b) $\gamma_0/\Delta_d(0) = 0.01$; and (c) $\gamma_0/\Delta_d(0) = 10$; at $\lambda d = 6$, $k/\lambda = 2$, $E_R = 0$, and $x_0 = d/2$; a, $\alpha_R = 0$; b, $\alpha_R = \pi/12$; c, $\alpha_R = \pi/12$; and (d) the temperature dependences of the nonresonant supercurrent were constructed in arbitrary units for the same parameters.

junctions with disordered boundaries. The same distribution can also be realized in double-barrier structures [22]. Averaging the supercurrent over the transparency $\rho(D) \propto D^{-3/2}(1 - D)^{-1/2}$ in the limit of a "narrow" reso-

nance leads to the following dependence of the resonant current on φ:

$$\langle I_{res}\rangle\big|_{x_0 = d/2} = eT\sin(\varphi)$$

$$\times \sum_\omega \frac{\pi\Delta^2\Gamma_0^2\rho(E_R)}{\sqrt{\omega^2 + \Delta^2}\sqrt{\omega^2(\Delta + \Gamma_0)^2 + \Delta^2\Gamma_0^2\cos^2(\varphi/2)}}. \quad (12)$$

It is of interest that Eq. (12) in its structure is similar to the equation for the supercurrent in double-barrier SINIS junctions in the coherent conduction mode [23, 26] in the limit of a "broad" resonance. Also note that even after averaging, the supercurrent as a function of the phase difference φ differs from a conventional sinusoidal dependence and, at $T = 0$, Eq. (12) is reduced to the form

$$\langle I_{res}\rangle\big|_{x_0 = d/2} = \frac{e\Delta}{(\Delta + \Gamma_0)}\Gamma_0^2\rho(E_R)\sin(\varphi)$$

$$\times K\left(\sqrt{1 - \frac{\Gamma_0^2\cos^2(\varphi/2)}{(\Delta + \Gamma_0)^2}}\right).$$

This equation clearly demonstrates that the dependence $\langle I_{res}(\varphi)\rangle$ deviates from a sinusoidal behavior.

In the general case of anisotropic order parameters, not all the integrals in Eq. (8) are taken in an analytical form. For symmetric junctions with high-T_c superconducting edges, analytical expressions can be obtained from Eq. (7) only in the case of a "narrow" resonance at $\alpha_L = \alpha_R = 0$ and $k/\lambda \gg 1$. The equations obtained in this limit for the supercurrent and the energy spectrum of resonance states are similar to Eqs. (10) and (11).

In studying resonant current transport in high-T_c superconducting junctions, we will assume that the *ab* plane of the high-T_c superconducting crystal is perpendicular to the junction surface and the order parameter is determined by Eq. (9). The electron and hole excitations at the boundary of an anisotropic superconductor at $\alpha \neq 0$ will experience different order parameters. In the case when the sign of the order parameter before the reflection of a quasiparticle from the high-T_c superconductor surface and after it is not conserved, bound Andreev states arise with a zero energy with respect to the Fermi level (zero energy states (ZESs) or midgap states) [19]. The region of the appearance of ZESs depends on the orientation angle of the high-T_c superconductor crystal lattice. For example, in the case of a SID junction, Andreev states will appear in the directions of left-hand incident quasiparticles obeying the condition $\theta \in (\pm\pi/4 - \alpha_R; \pm\pi/4 + \alpha_R)$. The question is of interest as to how the occurrence of ZESs at the high-T_c superconductor surface affects the resonant current.

Plots of the phase and temperature dependences of the supercurrent for a SID junction are presented in Figs. 1 and 2. The plots were obtained at the ratio of critical temperatures $T_s/T_d = 1/9$ under the assumption
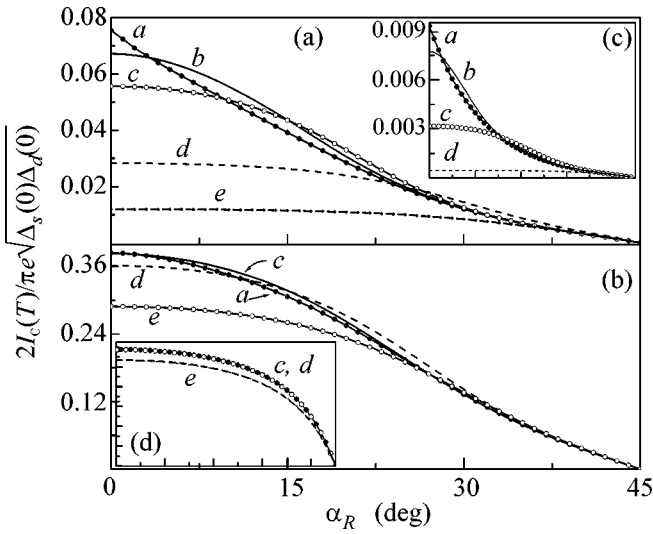
Fig. 3. Dependences of the supercurrent $I_C(\alpha_R)$ in a SID junction in the cases of (a) $\gamma_0/\Delta_d(0) = 0.1$; (b) $\gamma_0/\Delta_d(0) = 10$; (c) $\gamma_0/\Delta_d(0) = 0.01$; at $\lambda d = 6$, $k/\lambda = 2$, $E_R = 0$, and $x_0 = d/2$; a, $T/T_s = 0$; b, $T/T_s = 0.01$; c, $T/T_s = 0.05$; d, $T/T_s = 0.3$; and e, $T/T_s = 0.6$; and (d) the temperature dependences of the nonresonant supercurrent were constructed in arbitrary units for the same parameters.
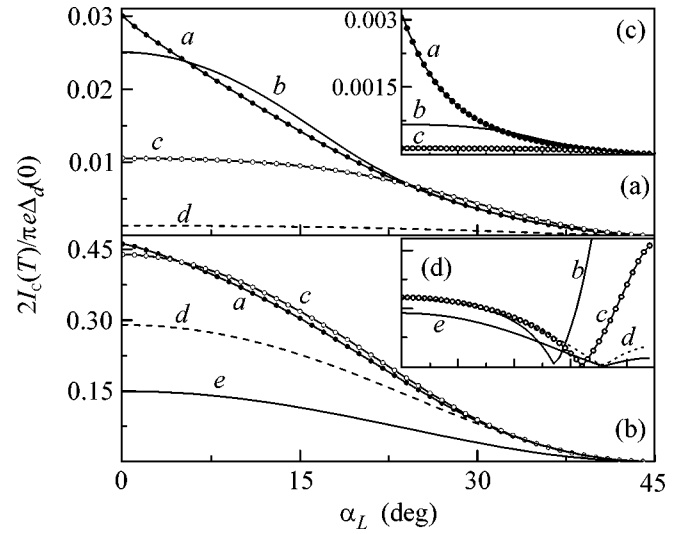
Fig. 4. Dependences of the critical current $I_C(\alpha_L)$ in a DID junction in the cases of (a) $\gamma_0/\Delta_d(0) = 0.1$; (b) $\gamma_0/\Delta_d(0) = 10$; (c) $\gamma_0/\Delta_d(0) = 0.01$; at $\alpha_L = -\alpha_R$, $k/\lambda = 2$, $\lambda d = 6$, $E_R = 0$, and $x_0 = d/2$; a, $T/T_s = 0$; b, $T/T_s = 0.01$; c, $T/T_s = 0.05$; d, $T/T_s = 0.3$; and e, $T/T_s = 0.6$; and (d) the temperature dependences of the nonresonant supercurrent were constructed in arbitrary units for the same parameters.

that the order parameters obey the relationships of the BCS theory. Figures 1a and 1b demonstrate the deviations of $I(\varphi)$ from $\sin(\varphi)$ at low temperatures. An increase in temperature or in orientation angle α_R brings the curves closer to a sinusoidal dependence. For comparison, Fig. 1c gives the phase dependences of the tunnel supercurrent at the same junction parameters and the angle $\alpha_R = 0$ that follow from the theory [25].

The temperature dependences of the critical current for a SID junction are shown in Fig. 2 for different values of the orientation angles of the high-T_c superconductor crystal. The plots in Figs. 2a–2c demonstrate that I_c decreases with increasing temperature more drastically as the resonance becomes narrower. At the same time, the results of the theory [25] presented for comparison in Fig. 2d give a smooth decay of the critical tunneling current with increasing temperature.

It is evident in Figs. 1 and 2 that an increase in the orientation angle of the high-T_c superconductor crystal leads to a drop in the supercurrent. This process is visualized in Fig. 3, which demonstrates the dependences of the critical current on the angle α_R. The plots in Figs. 3a–3c indicate that the "narrower" the resonance, the sharper the decrease in the critical current with increasing of the orientation angle of the high-T_c superconductor. At the same time, the $I_c(\alpha_R)$ curve calculated for the case of direct tunneling (see Fig. 3d) decays with increasing α_R more monotonically.

A similar situation is also observed in the case when the order parameters of both the electrodes have the d symmetry. The plots of the resonant critical current as

functions of the orientation angles of the crystals in a DID junction are shown in Fig. 4. Here, a practically interesting case of the antisymmetric orientation of the crystals $\alpha_L = -\alpha_R$ is considered. It follows from [25] that the direct supercurrent exhibits a pronounced nonmonotonic dependence on the orientation angle of the left-hand superconductor (see Fig. 4d). On the other hand, the plots of the resonant supercurrent of a DID junction in Figs. 4a–4c exhibit quite a monotonic behavior and corroborate the conclusions made when we described the angular dependences of the critical current of a SID junction. We have also shown that the situation remains qualitatively unchanged in the case of junctions with the ratio of angles $\alpha_L = \alpha_R$.

From the results of this work, it follows that, in the case of a "narrow" resonance, which usually occurs in experiments, the finiteness of the temperature and the deviation of the misalignment angles from zero lead to a significant decrease in resonance current. Thus, the situation described in the review [17], when the resonant supercurrent turns out to be suppressed as compared to the supercurrent from direct tunneling through the barrier, actually takes place in long high-T_c superconducting junctions with LSs in the interlayer.

The approach developed above disregards the suppression of the order parameter at the boundaries of high-T_c superconducting structures, and, hence, the contribution of the supercurrent to transport due to resonant tunneling onto Andreev levels with a nonzero energy localized at the boundary has not been investigated. An accurate account of this contribution requires

numerical calculations. Nevertheless, based on the analysis performed, it may be argued that the picture will only slightly change qualitatively, that is, the interaction of the two resonances caused by the occurrence of LSs in the interlayer with Andreev levels in the electrodes will not lead to a noticeable increase in supercurrent.

REFERENCES

1. U. Kabasawa, Y. Tanutani, T. Fukazawa, *et al.*, Jpn. J. Appl. Phys. **30**, 1670 (1991).

2. I. I. Vengrus, M. Yu. Kupriyanov, O. V. Snigirev, *et al.*, Pis'ma Zh. Éksp. Teor. Fiz. **60**, 372 (1994) [JETP Lett. **60**, 381 (1994)].

3. T. Satoh, M. Hidaka, M. Yu. Kupriyanov, *et al.*, IEEE Trans. Appl. Supercond. **5**, 2612 (1995).

4. M. Yu. Kupriyanov and J. S. Tsai, IEEE Trans. Appl. Supercond. **5**, 2531 (1995).

5. I. A. Devyatov and M. Yu. Kupriyanov, Pis'ma Zh. Éksp. Teor. Fiz. **59**, 187 (1994) [JETP Lett. **59**, 200 (1994)].

6. Y. Naveh, Vijay Patel, D. V. Averin, *et al.*, Phys. Rev. Lett. **85**, 5404 (2000).

7. A. I. Larkin and K. A. Matveev, Zh. Éksp. Teor. Fiz. **93**, 1030 (1987) [Sov. Phys. JETP **66**, 580 (1987)].

8. H. Knauer, J. Rihter, and P. Siedel, Phys. Status Solidi A **44**, 303 (1977).

9. I. M. Lifshits and V. Ya. Kirpichenkov, Zh. Éksp. Teor. Fiz. **77**, 989 (1979) [Sov. Phys. JETP **50**, 499 (1979)].

10. I. L. Aleiner, H. Clarke, and L. I. Glazman, Phys. Rev. B **53**, R7630 (1996).

11. C. W. J. Beenakker and H. van Houten, Phys. Rev. Lett. **66**, 3056 (1991).

12. I. A. Devyatov and M. Yu. Kupriyanov, Zh. Éksp. Teor. Fiz. **112**, 342 (1997) [JETP **85**, 189 (1997)].

13. L. G. Aslamazov and M. V. Fistul', Zh. Éksp. Teor. Fiz. **83**, 1170 (1982) [Sov. Phys. JETP **56**, 666 (1982)].

14. M. V. Fistul' and A. V. Tartakovskiĭ, Zh. Éksp. Teor. Fiz. **94** (9), 353 (1988) [Sov. Phys. JETP **67**, 1935 (1988)].

15. L. I. Glazman and K. A. Matveev, Pis'ma Zh. Éksp. Teor. Fiz. **49**, 570 (1989) [JETP Lett. **49**, 659 (1989)].

16. G. Johansson, E. N. Bratus, V. S. Shumeiko, *et al.*, Phys. Rev. B **60**, 1382 (1999).

17. J. Yoshida, IEICE Trans. Electron. **83-C**, 49 (2000).

18. I. A. Devyatov, D. V. Goncharov, and M. Yu. Kupriyanov, Zh. Éksp. Teor. Fiz. **119**, 749 (2001) [JETP **92**, 652 (2001)].

19. C.-R. Hu, Phys. Rev. Lett. **72**, 1526 (1994).

20. Chr. Bruder, Phys. Rev. B **41**, 4017 (1990).

21. K. M. Schep and G. E. W. Bauer, Phys. Rev. Lett. **78**, 3015 (1997).

22. C. W. J. Beenakker, Rev. Mod. Phys. **69**, 731 (1997).

23. M. Yu. Kupriyanov and V. F. Lukichev, Zh. Éksp. Teor. Fiz. **94**, 139 (1988) [Sov. Phys. JETP **67**, 1163 (1988)].

24. A. A. Golubov, M. Yu. Kupriyanov, and E. Il'ichev, Rev. Mod. Phys. (in press).

25. Y. Tanaka and S. Kashiwaya, Phys. Rev. B **56**, 892 (1997).

Translated by A. Bagatur'yants

Phase Diagram of a Surface Superconductor
in Parallel Magnetic Field[¶]

O. V. Dimitrova and M. V. Feigel'man

Landau Institute for Theoretical Physics, Russian Academy of Sciences, Moscow, 119334 Russia

Received October 14, 2003

The universal phase diagram of a 2D surface superconductor with generic Rashba interaction in a parallel magnetic field is found. In addition to the uniform BCS state, we find two inhomogeneous superconductive states, the stripe phase with $\Delta(\mathbf{r}) \propto \cos(\mathbf{Q}\mathbf{r})$ at high magnetic fields, and a new "helical" phase with $\Delta(\mathbf{r}) \propto \exp(i\mathbf{Q}\mathbf{r})$ which intervenes between the BCS state and stripe phase at an intermediate magnetic field and temperature. We prove that the ground state for helical phase carries no current. © *2003 MAIK "Nauka/Interperiodica".*

PACS numbers: 74.25.Dw; 74.25.Ha

Many efforts, both theoretical and experimental, have been made in search of exotic nonhomogeneous superconducting states, beginning with the pioneering papers by Larkin–Ovchinnikov and Fulde–Ferrel (LOFF) [1, 2] which predicted the stripe state in superconductors with competing ferromagnet interaction. Nevertheless, no convincing experimental evidence for the existence of such a state was found until now, partially due to the rather narrow existence range of the LOFF state. Recently, Barzykin and Gor'kov [3] did find a system where such an inhomogeneous superconducting phase could be prominent. It is a two-dimensional surface superconductor with spin-orbital Rashba interaction. One possible realization of such a system probably was reported in very interesting experiments [4], where various signatures of surface superconductivity with $T_c \approx 90$ K were detected in the insulating WO_3 doped by a small amount of Na. Surface spin-orbit superconductivity is unusual due to the absence of inversion symmetry, which results in the presence of the spin-orbital Rashba term [5] and the chiral subband splitting of the free electron spectrum at the surface. In such a superconductor condensate, wave function is a mixture of both singlet and triplet states [6, 7], therefore Pauli susceptibility is not vanishing [7] at $T \longrightarrow 0$; paramagnetic breakdown of superconductivity in a parallel magnetic field is shifted towards much higher field values due to the formation of an LOFF state [3]. The line of transition from normal to (any) superconductive state $T_c(h)$ was determined in [3]; however, the nature of the phase intervening between the uniform BCS and stripe LOFF states was not studied. This question is important because phenomenological theory [8] predicts the possibility for a new helical state distinct from both BCS and stripe LOFF states.

In this letter we provide a detailed phase diagram of a surface superconductor in a parallel magnetic field h. The phase diagram turns out to be universal after normalization of the temperature and the Zeeman energy by the critical temperature in the zero magnetic field T_{c0} for two models of high (I) and low (II) electron density. The model I assumes a normal 2D metal with Fermi energy being much greater than chiral splitting. The model II is suited for an electron gas in field-effect heterostructures where electrons fill only the bottom of one of the chiral bands. We demonstrate the existence of a helical state with order parameter $\Delta \propto \exp(i\mathbf{Q}\mathbf{r})$ (where $\mathbf{Q} \perp \mathbf{h}$) and $Q \sim \mu_B h/v_F$ in a considerable part of the phase diagram, which is summarized in figure. The line $\mathcal{LT}$ is the second-order transition line separating helical state from the homogeneous superconductor. Below the $\mathcal{T}$ point, first-order transition between BCS and inhomogeneous state takes place. The line $\mathcal{ST'}$ is the line of soft instability of the helical state (see below). The point $\mathcal{S}$ in the $T_c(h)$ line is special in that here the order parameter symmetry is $U(2)$ instead of the usual $U(1)$. Full details of our theory will be presented in a separate publication [9].

Near the surface of a crystal, the translational symmetry is reduced and the inversion symmetry is broken even if it is present in the bulk. As a result, a transverse electric field appears at interface and gives rise to the relativistic spin-orbit interaction known as the Rashba term: $H_{so} = \alpha[\boldsymbol{\sigma} \times \hat{\mathbf{p}}] \cdot \mathbf{n}$, where $\alpha > 0$ is the spin-orbit coupling constant, $\mathbf{n}$ is a unit vector perpendicular to the surface, and $\boldsymbol{\sigma} = (\sigma^x, \sigma^y, \sigma^z)$ are spin Pauli matrices. The spin operator does not commute with the Rashba term, thus spin projection is not a good quantum number. On the other hand, the chirality operator $\sigma^x \sin\varphi_\mathbf{p} - \sigma^y \cos\varphi_\mathbf{p}$ does commute with the Hamiltonian, where $\varphi_\mathbf{p}$ is the angle between the momentum of the electron and

---

[¶]This article was submitted by the authors in English.
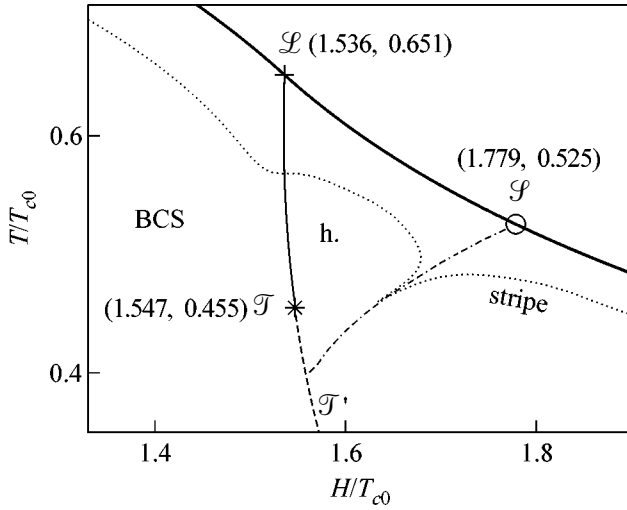
Phase diagram that shows superconducting phase transition line $T_c(H)$ (bold solid) and two second order phase transition lines in the clean case: $\mathscr{L}\mathscr{T}$ line between the homogeneous (BCS) and helical (h.) states and $\mathscr{G}\mathscr{T}'$ line of stability of the helical state. The short-dashed line going downwards from the point $\mathscr{T}$ marks the absolute limit of stability of the BCS state. The dotted line shows the physical $T_{BKT}(H)$ line for values $T_{c0}/\epsilon_F = 0.02$ and $\alpha/v_F = 0.34$.

the x-axis. Its eigenvalue $\lambda = \pm1$ is the quantum number of an electron state $(\mathbf{p}, \lambda)$. The Rashba term preserves the Kramers degeneracy with states $(\mathbf{p}, \lambda)$ and $(-\mathbf{p}, \lambda)$ belonging to the same energy.

In this letter we consider the simplest model of surface superconductor: the Gor'kov model for a two-dimensional metal with the Rashba term included [7], in the limit $\alpha p_F \gg T_c$. The Hamiltonian written in the coordinate representation reads

$$\hat{H} = \int \psi_\alpha^+(\mathbf{r})\left(\frac{\hat{P}^2}{2m}\delta_{\alpha\beta} + \alpha[\boldsymbol{\sigma}_{\alpha\beta} \times \hat{P}] \cdot \mathbf{n}\right.$$
$$\left. - g\mu_B\mathbf{h} \cdot \boldsymbol{\sigma}_{\alpha\beta}/2\right)\psi_\beta(\mathbf{r})d^2r - \frac{U}{2}\int\psi_\alpha^+\psi_\beta^+\psi_\beta\psi_\alpha d^2r, \quad (1)$$

where m is the electron mass and α, β are spin indices, $\hat{P} = -i\nabla + \frac{e}{c}\mathbf{A}(\mathbf{r})$ is the momentum operator in the presence of infinitesimal in-plane vector-potential $\mathbf{A} = \mathbf{A}(\mathbf{r})$. Zeeman interaction with a uniform external magnetic field $\mathbf{h}$ parallel to the interface and in the x-direction is included. The vector potential of such a field can be chosen to have only a z-component, therefore it decouples from the 2D kinetic energy term. μ_B is the Bohr magneton and g is the Lande factor. Hereafter we use the notation $H = g\mu_B h/2$.

The electron operator can be expanded in the basis of plane waves $\hat{\psi}_\alpha(\mathbf{r}) = \sum_{\lambda\mathbf{p}} e^{i\mathbf{p}\mathbf{r}}\hat{c}_{\alpha\mathbf{p}}$. The one-particle part of the Hamiltonian (1) in the momentum representation:

$$\hat{H}_0 = \sum_{\mathbf{p}}\hat{c}_{\alpha\mathbf{p}}^+\left(\frac{p^2}{2m} + \alpha[\boldsymbol{\sigma}_{\alpha\beta} \times \mathbf{p}] \cdot \mathbf{n} - \mathbf{H} \cdot \boldsymbol{\sigma}_{\alpha\beta}\right)\hat{c}_{\beta\mathbf{p}} \quad (2)$$

can be diagonalized by the transformation $\hat{c}_{\alpha\mathbf{p}} = \eta_{\lambda\alpha}(\mathbf{p})\hat{a}_{\lambda\mathbf{p}}$ with the two-component spinor $\eta_\lambda(\mathbf{p}) = (1, i\lambda\exp(i\varphi_{\mathbf{p}}))/\sqrt{2}$. Eigenvalues of the Hamiltonian (2) corresponding to the chiralities $\lambda = \pm1$ are

$$\epsilon_\lambda(\mathbf{p}) = p^2/2m - \lambda\sqrt{\alpha^2 p^2 - 2\alpha p_y H + H^2}. \quad (3)$$

In the case of high electron density and respectively chemical potential $\mu \gg m\alpha^2$ (model I), both chirality branches are filled and the equal momentum electron states are split by $2\alpha p_F$. Fermi circles with different chiralities are split with the radii $p_F = \sqrt{2m\mu + m^2\alpha^2} \pm m\alpha$. Densities of states on the two Fermi circles are almost the same, $\nu_\pm = \frac{m}{2\pi}\left(1 \pm \frac{\alpha}{v_F}\right)$, and in this paper we neglect the difference $\nu_+ - \nu_-$. In the case of the low electron density (model II) $-m\alpha^2/2 < \mu < 0$, the electrons fill the bottom of only one chiral branch $\lambda = 1$, i.e., a ring. The two Fermi circles of the ring in the zero magnetic field have radii $p_F = m\alpha + l\sqrt{2m\mu + m^2\alpha^2}$, where $l = \pm1$ is the number specifying the inner and the outer part of the ring and is analogous to chirality. Density of states on the outer and inner part of the Fermi ring ($l = \pm1$) is almost the same $\nu_\pm = m\alpha/2\pi v_F$ in the case of a narrow ring where $v_F \ll \alpha$. If magnetic field is applied, the two Fermi circles are displaced in opposite y-directions by a momentum $Q = \pm H/v_F$, where $v_F = \sqrt{2\mu/m + \alpha^2}$ is the Fermi velocity in the I model, or one half the width of the ring divided by m in the II model. The pairing interaction (the last term in Eq.(1)) can be factorized in the chiral basis: $\hat{H}_{int} = -\frac{U}{4}\sum_{\mathbf{q}}\hat{A}^+(\mathbf{q})\hat{A}(\mathbf{q})$, where the pair annihilation operator $\hat{A}(\mathbf{q}) = \sum_{\mathbf{p}\lambda}\lambda e^{i\varphi_{\mathbf{p}}}\hat{a}_{\lambda-\mathbf{p}_-}\hat{a}_{\lambda\mathbf{p}_+}$ with $\mathbf{p}_\pm = \mathbf{p} \pm \mathbf{q}/2$.

To calculate thermodynamic potential $\Omega = -T\ln Z$, we employ an imaginary-time functional integration technique with Grassmanian electron fields $a_{\lambda,\mathbf{p}}$, $\bar{a}_{\lambda,\mathbf{p}}$ and introduce an auxiliary complex field $\Delta(\mathbf{r}, \tau)$ to

decouple pairing term H_{int}, cf. [10]. The resulting effective Lagrangian is of the form:

$$L[a, \bar{a}, \Delta, \Delta^*] = \sum_{\mathbf{p}} \bar{a}_{\lambda\mathbf{p}}(-\partial_\tau - \epsilon_\lambda(\mathbf{p}))a_{\lambda\mathbf{p}}$$

$$+ \sum_{\mathbf{q}}\left[-\frac{|\Delta_{\mathbf{q}}|^2}{U} + \frac{1}{2}\sum_{\mathbf{p}\lambda}(\Delta_{\mathbf{q}}\lambda e^{-i\varphi_{\mathbf{p}}}\bar{a}_{\lambda,\,\mathbf{p}_+}\bar{a}_{\lambda,\,-\mathbf{p}_-}\right. \qquad (4)$$

$$\left. + \Delta_{\mathbf{q}}^*\lambda e^{i\varphi_{\mathbf{p}}}a_{\lambda,\,-\mathbf{p}_-}a_{\lambda,\,\mathbf{p}_+}\right].$$

Below, we will work within the mean-field approximation which is controlled by the small Ginzburg number $Gi \sim T_c/E_F$. It is equivalent to the saddle-point approximation for the functional integral over Δ and Δ^*, thus we will be studying minima of the functional $\Omega[\Delta, \Delta^*]$ appearing after Gaussian integration over Grassmanian fields.

Near the normal-superconducting phase transition, the order parameter $\Delta(\mathbf{r})$ is small and Ω may be expanded in powers of $\Delta(\mathbf{r})$ and its gradients. We consider the order parameter as a superposition of the finite number of harmonics, $\Delta(\mathbf{r}) = \sum_i \Delta_{\mathbf{Q}_i}(\mathbf{r})\exp(i\mathbf{Q}_i\mathbf{r})$, where $\Delta_{\mathbf{Q}_i}(\mathbf{r})$ are slowly varying in 2D space functions, and derive the corresponding Ginzburg–Landau functional:

$$\Omega = \int\left[\sum_i \alpha_i|\Delta_{\mathbf{Q}_i}|^2 + c_i\left|\left(-i\frac{\partial}{\partial\mathbf{r}} + \frac{2e}{c}\mathbf{A}\right)\Delta_{\mathbf{Q}_i}\right|^2\right.$$

$$\left. + \sum_{ijk}\beta_{ijk}\Delta_{\mathbf{Q}_i}\Delta_{\mathbf{Q}_j}^*\Delta_{\mathbf{Q}_k}\Delta_{\mathbf{Q}_i-\mathbf{Q}_j+\mathbf{Q}_k}^*\right]d^2\mathbf{r}. \qquad (5)$$

The coefficient $\alpha(\mathbf{Q})$ includes a Cooper loop diagram with transferred momentum Q:

$$\alpha(\mathbf{Q}) = \frac{1}{U} - \frac{T}{2}\sum_{\omega,\lambda,\mathbf{p}}G_\lambda^n(\omega, \mathbf{p}_+)G_\lambda^n(-\omega, -\mathbf{p}_-), \qquad (6)$$

where in the I model the normal-state Green function in the in-plane magnetic field $H \ll \alpha p_F$ is $G_\lambda^n(\omega, \mathbf{p}) = (i\omega - \xi - \lambda H\sin\varphi_{\mathbf{p}})^{-1}$, and $\xi = p^2/2m - \lambda\alpha p_F - \mu$ is assumed to be small compared to αp_F, whereas in the II model $H \ll m\alpha^2$ and $\xi_l = v_F(l\pi - mv_F)$ is assumed to be small compared to $m\alpha^2$ (π is related to the center of the ring). Hereafter, we present the results for high density (model I), but results for low density are identical. The condition $\min_Q\alpha(\mathbf{Q}) = 0$ determines the second-order transition line (if $\beta > 0$) between the normal metal and the superconductor:

$$\frac{1}{U} = \max_Q\sum_{\lambda,\,\omega > 0}\frac{\pi\nu T}{\sqrt{\omega^2 + H_\lambda^2}}, \qquad (7)$$

hereafter $H_\lambda = \lambda H + v_F Q/2$. Depending on H, the maximum in Eq. (7) is attained either at $Q = 0$ or at nonzero $\pm|Q|$. $T_c(H)$ line is shown on figure, where both T_c and H are normalized by the critical temperature at the zero magnetic field $T_{c0} = 2\omega_D\exp(-1/\nu U + C)/\pi$, where $C = 0.577$ is the Euler constant. Near $\mathcal{L}$ point $v_FQ(H) \sim \sqrt{H^2 - H_L^2}$. In the limit $H/T_{c0} \longrightarrow \infty$ we recover the asymptotics of the $T_c(H)$ line [7], and find $v_FQ(H) = 2H - \pi^4 T_{c0}^4/7\zeta(3)e^{2C}H^3$. Note that $Q = 2H/v_F$ is the momentum splitting of two $\lambda = \pm 1$ Fermi surfaces in a parallel magnetic field. The Lifshitz point $\mathcal{L}$ separates $Q = 0$ and $Q \neq 0$ solutions on the $T_c(H)$ line; it is the end point of the second order phase transition between the two superconducting phases. At $H > H_L$, an inhomogeneous superconductive phase is formed below the $T_c(H)$ line. No more than two harmonics contribute to $\Delta(\mathbf{r})$ just below the $T_c(H)$ line: $\Delta(y) = \Delta_+ e^{iQy} + \Delta_- e^{-iQy}$. Below $T_c(H)$, the density of the thermodynamic potential Ω is lower in the superconductive state than in the normal one by the amount:

$$\Omega_{sn} = \alpha|\Delta|^2 + \beta_s|\Delta|^4 + \beta_\alpha(|\Delta_+|^2 - |\Delta_-|^2)^2, \qquad (8)$$

where $|\Delta|^2 = |\Delta_+|^2 + |\Delta_-|^2$. We find coefficients $\beta_{s,a}$ using standard diagram expansion around the normal state. At the symmetric point $\mathcal{S}$ where $\beta_a(T_c(H), H) = 0$, the free energy (8) is invariant under $U(2)$ rotations of the order parameter spinor (Δ_+, Δ_-). At $H < H_S$, we find $\beta_a < 0$ and the free energy at $T < T_c(H)$ is minimized by the choice of either $\Delta_+ = 0$ or $\Delta_- = 0$, both corresponding to a helical state. At $H > H_S$, we find $\beta_a > 0$ and, in the free energy minimum, $|\Delta_+| = |\Delta_-|$, which corresponds to the LOFF-like stripe phase with $\Delta(y) \propto \cos(Qy)$. At lower temperatures in this phase $\Delta(y)$ contains higher harmonics and is time-reversal symmetric.

In the helical state with only one harmonics $\Delta(y) = \Delta e^{iQy}$, the thermodynamic potential reads:

$$\Omega_{\text{hel}} = -\nu T\sum_{\omega,\lambda}\int\sqrt{(\omega + iH_\lambda\sin\varphi)^2 + \Delta^2}\frac{d\varphi}{2} + \frac{\Delta^2}{U}. \qquad (9)$$

In equilibrium, the stationary conditions $\partial\Omega_{\text{hel}}/\partial\Delta = 0$ and $\partial\Omega_{\text{hel}}/\partial Q = 0$ are satisfied and can be found explicitly:

$$\frac{1}{2\nu U} = T\sum_{\omega > 0,\lambda}\frac{\mathbf{K}(k)}{r(H_\lambda, \omega)}; \quad \sum_{\omega > 0,\lambda}f(H_\lambda, \omega) = 0, \quad (10)$$

where $r(H_\lambda, \omega) = \sqrt{\omega^2 + (|H_\lambda| + \Delta)^2}$, the Jacoby modulus $k = 2\sqrt{\Delta|H_\lambda|}/r(H_\lambda, \omega)$ and the function $f(H_\lambda, \omega)$ is

defined through the Jacoby complete elliptic integrals of the first and the second kind:

$$f(H_\lambda)$$
$$= \frac{1}{H_\lambda}\left((\omega^2 + H_\lambda^2 + \Delta^2)\frac{\mathbf{K}(k)}{r(H_\lambda, \omega)} - r(H_\lambda, \omega)\mathbf{E}(k)\right). \quad (11)$$

We prove by direct microscopic calculation that $\mathbf{j}_s = \frac{2e}{\hbar}\partial\Omega/\partial\mathbf{Q}$, therefore the equilibrium state carries no supercurrent.

The minimum of the thermodynamic potential (9) over Δ can be expanded in a series of small Q:

$$\Omega_{\text{hel}}(Q) = \Omega_{\text{hel}}(0) + \frac{\hbar}{8m}n_s^{yy}Q^2 + bQ^4 + cQ^6, \quad c > 0.$$

The condition $n_s^{yy} = 0$, $b > 0$ determines the second order Lifshitz transition line $\mathscr{LT}$, which ends at the point $\mathscr{T}$, where coefficient $b = 0$ changes sign. We compute the coordinates of point $\mathscr{T}$ using Eqs. (9), (10). At lower temperatures, $b < 0$ and first-order transition out of the BCS state occurs.

The domain of helical-state local stability was determined via consideration of the thermodynamic potential variations due to weak static modulation of the form $\delta\Delta(\mathbf{r}) = v_{-q}\exp(-iqy) + v_{q+2Q}\exp(i(q + 2Q)y)$ (the presence of two Fourier harmonics in the perturbation is due to inhomogeneity of the background helical state):
$\delta\Omega_{\delta v} = \mathbf{v}^+\hat{\mathscr{A}}(q)\mathbf{v}$, where $\mathbf{v} = (\delta v_{-q}, \delta v_{q+2Q}^*)$ and

$$\hat{\mathscr{A}}(q) = \frac{\hat{1}}{U}$$
$$- \sum_{\omega > 0, \lambda, \mathbf{p}}\begin{pmatrix} G_{\lambda p_-}G_{\lambda - p_+} & F_{\lambda p_-}F_{\lambda - p_+} \\ F_{\lambda p_-}^*F_{\lambda - p_+}^* & G_{\lambda p_+ + Q}G_{\lambda - p_- + Q} \end{pmatrix}. \quad (12)$$

The matrix $\mathscr{A}$ has two eigenvalues $\epsilon_1(q) < \epsilon_2(q)$. We define the helical state metastability line $\mathscr{ST}'$ as a collection of points where one mode δv becomes energetically favorable: $\min_q\epsilon_1(q) = 0$. We numerically solve four equations simultaneously: two gap equations (10) that determine equilibrium Δ and Q, together with the two equations $\partial_q\epsilon_1(q) = 0$ and $\epsilon_1(q) = 0$. By means of expansion of the Ginzburg–Landau functional up to the terms on the order of $|\Delta_\pm|^8$, we checked that the next-order "anisotropic" term in the expansion (8) is of the form $\epsilon(|\Delta_+|^2 - |\Delta_-|^2)^4$, with $\epsilon > 0$. This fact ensures that the phase transition out of the helical state is of the second order (at least, near the $T_c(H)$ line).

We calculated electromagnetic the response function $\delta j_\alpha/\delta A_\beta = -\frac{e^2}{mc}n_s^{\alpha\beta}$ for the helical state using standard diagram methods and found that $n_s^{yy} = 4\frac{m}{\hbar}\frac{\partial^2\Omega}{\partial Q^2}$.

Thus, on the Lifshitz line $\mathscr{LT}$ there is no linear supercurrent in the direction perpendicular to the magnetic field. The component n_s^{xx} does not vanish anywhere in the helical state region and is on the order of n_s of the BCS state. This is in contrast with the classical LOFF problem, where n_s was shown to vanish in the whole helical state; the difference is probably due to the fact that in our problem the direction of $\mathbf{Q}$ is fixed by an applied field $\mathbf{h}$, while for the case of the ferromagnetic superconductor it is arbitrary. The obtained behaviour of the $n_s^{\alpha\beta}$ tensor indicates the strongly anisotropic electromagnetic response of surface superconductor near the Lifshitz line $\mathscr{LT}$.

So far, we have discussed the clean case; below we demonstrate that a sufficiently high concentration of nonmagnetic impurities suppresses both helical and stripe states. Consider impurities with weak short-range potential, characterized by elastic scattering time τ. By means of diagram technique [11], we calculate the coefficient $\alpha(\mathbf{Q})$ in the Ginzburg–Landau expansion (5), which is the electron–electron vertex in the Cooper channel in the presence of nonmagnetic impurities. It is given by a sum of ladder diagrams which are an alternating sequence of blocks of two normal metal Green functions $G_\lambda = \left(i\omega - \xi - \lambda H\sin\varphi_\mathbf{p} + \frac{i}{2\tau}\text{sgn}\,\omega\right)^{-1}$ and an impurity line. In every block, momenta on the upper and lower lines are opposite, whereas the chiralities are the same. The $T_c(H)$ line is found from $\min_Q\alpha(\mathbf{Q}) = 0$, where $\alpha(\mathbf{Q}) = 1/U - \pi\nu T\max_Q\sum_{\omega > 0}K(\omega, H, \tau, Q)$, with the Cooper kernel K given by

$$K(\omega, H, \tau, Q) = 4\tau\frac{I_s^0[1 - I_s^2] + (I_a^1)^2}{(1 - I_s^0)[1 - I_s^2] - (I_a^1)^2}, \quad (13)$$

where $I_{s,a}^\gamma = I_+^\gamma \pm I_-^\gamma$ ($\gamma = 0, 1, 2$) are functions of (T, H, τ, Q):

$$I_\lambda^0 = (\tilde{\omega}^2 + H_\lambda^2)^{-1/2}/4\tau, \quad I_\lambda^1 = i\left(\tilde{\omega}I_\lambda^0 - \frac{1}{4\tau}\right)/H_\lambda,$$

$$I_\lambda^2 = i\tilde{\omega}I_\lambda^1/H_\lambda, \quad \tilde{\omega} = \omega + \frac{1}{2\tau}.$$

At $H = 0$, time-reversal symmetry is recovered and Eq. (13) simplifies to $K = 2/\omega$ independently of disorder, in agreement with the Anderson theorem. We numerically evaluate $\alpha'' = \partial^2\alpha(\mathbf{Q})/\partial\mathbf{Q}^2$ along the transition line $\alpha(T, H, \mathbf{Q}) = 0$. At $\tau T_{c0}/\hbar \le 0.11$, we found $\alpha'' > 0$ at any H, i.e., both stripe and helical state disappear from the phase diagram at $\tau \le \hbar/9T_{c0}$. A similar condition for usual LOFF state is more stringent, cf.

[12]. In the dirty limit $\tau T_{c0} \ll 1$, the kernel K simplifies to $K = 2/(\omega + 2H^2\tau + v_F^2 Q^2\tau/4)$. From this form of K, one easily concludes that the paramagnetic critical field *grows* with an increase of disorder as $H_p = \sqrt{\pi T_{c0}/4\tau e^C}$, cf. similar result in [13].

The phase diagram figure was obtained neglecting the small parity-breaking term of the order $\alpha/v_F \ll 1$ in the thermodynamic potential (9): $\delta\Omega = \eta Q$ with $\eta = -\alpha\nu T\sum_\omega f(H,\omega)$, where function f is defined for the clean case in Eq. (11). Taking this term into account while minimizing Ω, one finds that the uniform BCS state transforms into a weakly helical state (predicted phenomenologically in [8]) with the small wave vector $\tilde{Q} \approx 2\alpha H/v_F^2$ and without supercurrent (a homogeneous state would carry supercurrent, as was found in [14], but it is not the ground-state). The line of 2nd order transition $\mathcal{LT}$ then broadens into a sharp crossover region between two helical states with small and large values of Q. Within this crossover region, the superfluid density tensor is strongly anisotropic, with $n_s^{yy}/n_s^{xx} \sim (\alpha/v_F)^{2/3}$. In the dirty limit long wavelength, helical modulation is present everywhere in a superconducting state; near the transition line its wave-vector $\tilde{Q} = 4\alpha H/v_F^2$.

We have calculated the $T_c(H)$ line within mean-field approximation, whose accuracy is usually on the order of T_c/ϵ_F for a clean 2D superconductor. The actual transition is of the Berezinsky–Kosterlitz–Thouless vortex depairing type, and is shifted downwards in temperature by about T_c^2/ϵ_F. In our system, fluctuations are enhanced strongly around points $\mathcal{L}$ and $\mathcal{S}$. Near the $\mathcal{L}$ point, this is due to the smallness of n_s^{yy}, and the enhancement factor is on the order of $\sqrt{n_s^{xx}/n_s^{yy}} \sim (\alpha/v_F)^{-1/3}$. In the vicinity of the point $\mathcal{S}$, fluctuations are enhanced due to extended $U(2)$ symmetry of the order parameter; 2D renormalization group calculation shows that $U(2)$ fluctuation modes shift actual T_c by

$\Delta T_c \sim 4(T_c^2/\epsilon_F)\log\beta_s/\beta_a$ downwards at $\beta_a \ll \beta_s$. As a result, the phase transition line $T_c(H)$ is deformed in the vicinities of points $\mathcal{L}$ and $\mathcal{S}$, as shown on figure.

In conclusion, we have demonstrated the existence of three different superconductive states (two helical states and stripe state) in a clean surface superconductor in a parallel magnetic field, and have located transition lines between them. Strong disorder eliminates short-wavelength helical and stripe states, whereas the long-wavelength helical state survives.

REFERENCES

1. A. I. Larkin and Yu. N. Ovchinnikov, Sov. Phys. JETP **20**, 762 (1965).
2. P. Fulde and R. A. Ferrel, Phys. Rev. **135**, A550 (1964).
3. V. Barzykin and L. P. Gor'kov, Phys. Rev. Lett. **89**, 227002 (2002).
4. S. Reich and Y. Tsabba, Eur. Phys. J. B **9**, 1 (1999); Y. Levi, O. Millo, A. Sharoni, *et al.*, Europhys. Lett. **51**, 564 (2000); S. Recih, G. Leitus, Y. Tsabba, *et al.*, J. Supercond. **13**, 855 (2000).
5. E. I. Rashba, Sov. Phys. Solid State **2**, 1109 (1960).
6. V. M. Edelstein, Zh. Éksp. Teor. Fiz. **95**, 2151 (1989) [Sov. Phys. JETP **68**, 1244 (1989)].
7. L. P. Gor'kov and E. I. Rashba, Phys. Rev. Lett. **87**, 037004 (2001).
8. D. F. Agterberg, cond-mat/0204592.
9. O. V. Dimitrova and M. V. Feigel'man (in preparation).
10. V. N. Popov, *Functional Integrals and Collective Excitations* (Cambridge Univ. Press, Cambridge, 1987).
11. A. A. Abrikosov, L. P. Gor'kov, and I. E. Dzyaloshinski, *Methods of Quantum Field Theory in Statistical Physics* (Dover, New York, 1975).
12. L. G. Aslamazov, Sov. Phys. JETP **28**, 773 (1969).
13. R. A. Klemm, A. Luther, and M. R. Beasley, Phys. Rev. B **12**, 877 (1975).
14. S. K. Yip, Phys. Rev. B **65**, 144508 (2002).

Coulomb Oscillations of Conductance in an Open Ring Interferometer in a Strong Magnetic Field

A. A. Bykov[1, *], D. V. Nomokonov[1], A. K. Bakarov[1], O. Estibals[2], and J. C. Portal[2]

[1] *Institute of Semiconductor Physics, Siberian Division, Russian Academy of Sciences, Novosibirsk, 630090 Russia*
* e-mail: bykov@thermo.isp.nsc.ru
[2] *Grenoble High Magnetic Fields Laboratory, MPI-FKF and CNRS B.P.166, F-38042 Grenoble, France*
Received October 15, 2003

Under the conditions corresponding to tunnel-coupled edge current states in an open ring interferometer, oscillations of conductance as a function of gate voltage with two noticeably different periods are observed. The large-period oscillations are attributed to the electron tunneling between the source and drain regions via a closed edge state of the ring, when an integral number of magnetic flux quanta passes through its contour at the Fermi level. The small-period oscillations are explained by the effect of single-electron variations of the ring potential on the transparency of the barriers between the localized and delocalized edge states of the interferometer. © 2003 MAIK "Nauka/Interperiodica".

PACS numbers: 73.23.-b; 73.63.Hs

This paper presents an experimental study of the transport properties of submicron rings under the conditions corresponding to the formation of tunnel-coupled edge current states. Under these conditions in electron ring interferometers, double-frequency Aharonov–Bohm oscillations [1, 2] are observed. The origin of this frequency doubling remains unclear to this day. A similar effect was observed for magnetoconductivity of antidots [3, 4]. In [4], it is explained by a Coulomb blockade of tunneling through closed compressible edge states, which arise in a strong magnetic field along the edges of 2D electron gas [5]. However, some of the experimental results can be explained without using the model of compressible edge states [6]. Hence, the presence of the Coulomb blockade and the origin of the frequency doubling of Aharonov–Bohm oscillations in rings in a strong magnetic field remain open to question.

A schematic diagram of a ring interferometer is presented in Fig. 1a. The samples studied in our experiments were fabricated on the basis of high-mobility and high-concentration 2D electron gas in a GaAs quantum well with AlAs/GaAs superlattice barriers [7]. The X-electrons appearing in these barriers were characterized by low concentration and low mobility, and they made almost no contribution to the conductivity of the structure. However, owing to the screening of the scattering potential of the doping impurity, they could considerably increase the concentration of 2D electron gas in the GaAs quantum well without loss in mobility. The effective radius of the rings was determined from the period of h/e oscillations and was equal to $r_{\text{eff}} \simeq 0.13 \ \mu m$. A two-layer Au/Ti metal film served as the gate. Experiments were carried out at temperatures from 50 mK to 1.5 K in magnetic fields up to 28 T. The resistance was measured in the ac regime by the four-terminal method using a phase-sensitive amplifier.

Figure 1b shows the longitudinal (R_L) and transverse (R_H) resistances of an interferometer in the open regime versus magnetic field B varying from 0 to 28 T. Near zero magnetic field, the rings under study exhibit a negative magnetoresistance caused by the suppression of the resonance backscattering in triangular regions at the branch points of electron channels [2, 8, 9]. In this regime of interferometers under study, the Aharonov–Bohm oscillations manifest themselves in magnetic fields up to 17–21 T, above which the edge states in the ring channels are separated and the transport becomes adiabatic. In magnetic fields above 20 T, R_L takes on quantized values ($h/4e^2$ and $h/6e^2$); in the fields above 28 T, R_L tends to zero. Figure 2a shows the dependences $R_L(B)$ in the tunneling regime and in the case of intermediate conduction. In the latter case, the frequency doubling of Aharonov–Bohm oscillations takes place, which can be clearly seen from Fig. 2b.

Figure 3a shows the dependence $R_L(B)$ for an open ring and its periodic component $\Delta R_L(B)$ at a temperature of 50 mK. One can see that the amplitude of Aharonov–Bohm oscillations increases as B grows from 0 to 10 T. We attribute this behavior to the suppression of the geometric backscattering at the ring input (output). Using formula $G = 1/(R_L + R_H)$ given in [10], we calculated the conductance of a ring interferometer in a strong magnetic field, and the results of this calculation are shown in Fig. 3b. From the experimental curves, it follows that, at $T = 50$ mK, the frequency doubling of
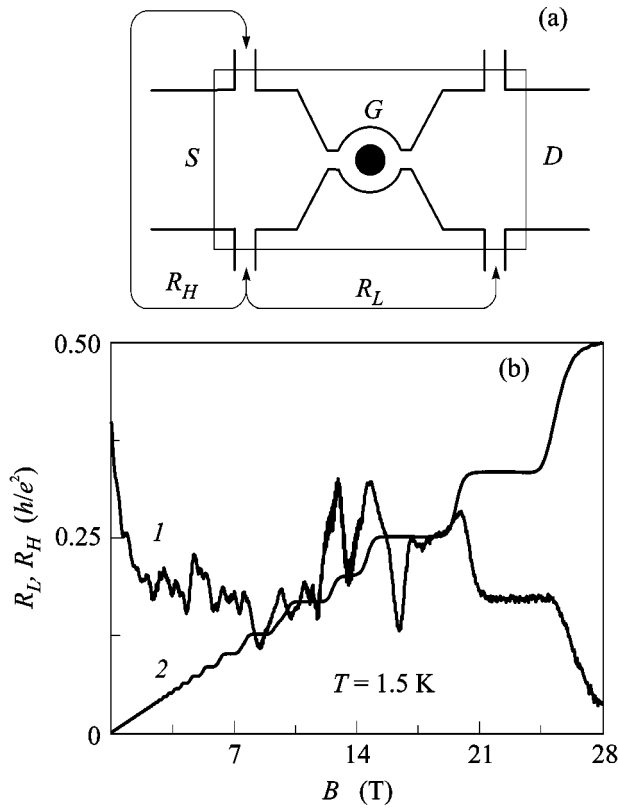
Fig. 1. (a) Schematic diagram of a ring interferometer: S, D, and G are the source, drain, and thin-film metal gate, respectively. (b) Dependences (1) $R_L(B)$ and (2) $R_H(B)$ obtained for a ring interferometer in the open regime at $T = 1.5$ K.

Fig. 2. (a) Experimental dependences $R_L(B)$ at $T = 1.5$ K (1) for a closed ring and (2) for an intermediate situation between an open and closed ring. The circle indicates the region of frequency doubling of Aharonov–Bohm oscillations. (b) Dependence $\Delta R_L(B)$ representing the difference between the experimental and smoothed curves in the encircled region.

Aharonov–Bohm oscillations begins to manifest itself in magnetic fields higher than 14.5 T.

The dependences of the conductance of a ring interferometer on the voltage applied to the planar gate are presented in Fig. 4a. One can see that the dependences $G(V_g)$ exhibit quasi-periodic oscillations of a complex form with an amplitude approximately equal to that of h/e oscillations in the dependences $G(B)$ and with a period of about 25–30 mV. However, unlike the corresponding dependences for antidots [6], the peaks of these oscillations are "incised." Detailed experimental studies showed that, when B changes, the oscillations with a period of 25–30 mV become shifted while the higher-frequency oscillations do not change their positions.

Now, let us discuss the experimental results. For the interferometers under study in the integer quantum Hall regime, the quantities R_L and R_H are determined by the expressions [10] $R_L = (h/e^2)(1/N_{min} - 1/N_{wide})$ and $R_H = (h/e^2)/N_{wide}$, where N_{min} and N_{wide} are the numbers of occupied Landau levels in the ring and in the wide part of the sample, respectively. Proceeding from the values of R_H and R_L and using the aforementioned relations, we can conclude that, in fields $B > 21$ T, the transport in an open interferometer occurs in the adiabatic regime
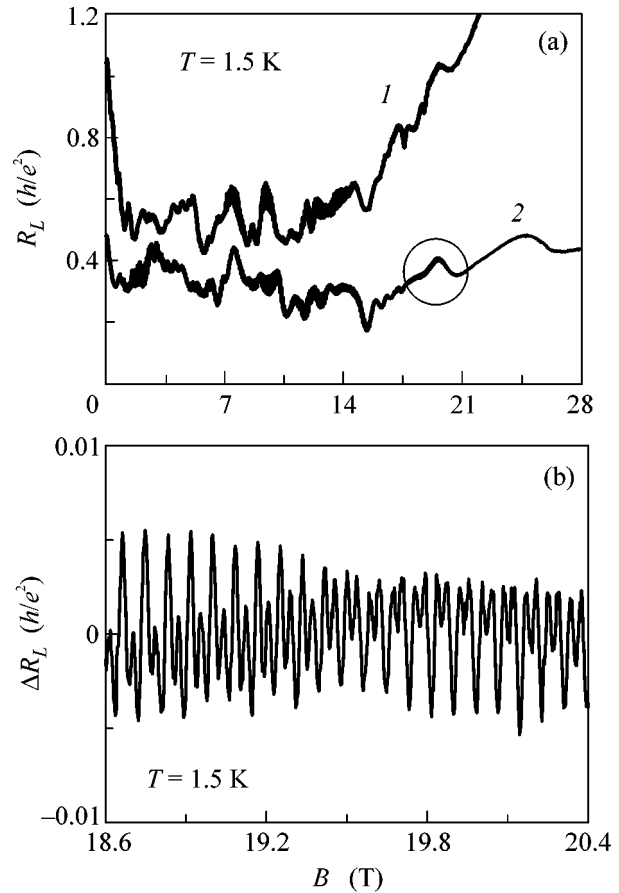
through two edge states (Fig. 1b). In the field $B \sim 28$ T, the number of occupied levels in the region of potential leads and in the ring is equal to two, i.e., $N_{wide} = N_{min} = 2$. As B decreases, the number of occupied Landau levels in the ring remains equal to two up to a field of 17 T. In lower fields, quantization of R_L is absent and the open interferometer operates in the situation with tunnel-coupled edge current states. As seen from Fig. 3b, when B is within 14.4 to 15 T, the Aharonov–Bohm oscillations manifest themselves in the form of split peaks on the background of a doubled conductance quantum. This means that they are caused by tunneling of charge carriers from the source (S) to drain (D) regions via a closed state of the ring while the number of delocalized edge states passing through the ring is equal to two. In this field range, R_H takes on a quantized value and the number of levels in the source and drain regions is equal to $N_{wide} = (h/e^2)/R_H = 5$. A schematic diagram that represents the edge current states in the
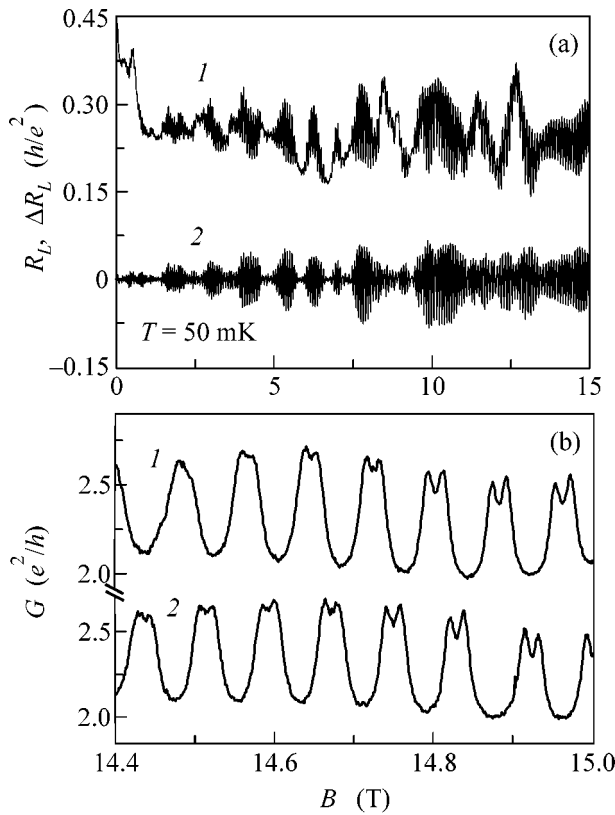
Fig. 3. (a) Experimental dependence (*1*) $R_L(B)$ at $T = 50$ mK and (*2*) the difference $\Delta R_L(B)$ between the experimental and smoothed curves. (b) Dependences $G(B)$ at $T = 50$ mK for two different gate voltages: $V_g = $ (*1*) 0 and (*2*) 15 mV.

Fig. 4. (a) Dependences $G(V_g)$ for two values of B separated by $\Delta B \sim \Phi_0/2\pi r_{\text{eff}}^2$: $B = $ (*1*) 15 and (*2*) 14.95 T. (b) Schematic diagram of edge states in a ring interferometer at $B \sim$ 15 T in the interval of V_g from –0.05 to 0.1 V. The black color shows the etch regions, the arrows indicate the directions of electron motion through the edge states, and the gray color shows the regions of tunneling between them.

interferometer in the aforementioned situation is shown in Fig. 4b.

Figure 4a shows the dependences $G(V_g)$ for two values of B that differ by approximately $\Delta B = \Phi_0/2\pi r_{\text{eff}}^2$, where Φ_0 is the magnetic flux quantum and πr_{eff}^2 is the effective area of the ring. In this case, according to the experiment, the curves are shifted by half the large period in V_g. The curves $G(V_g)$ obtained for two magnetic fields separated by $\Delta B = \Phi_0/r_{\text{eff}}^2$ were practically coincident. The curves $G(B)$ obtained for two gate voltages differing by 25–30 mV were also practically coincident. However, similar curves obtained for two V_g that differed by ~15 mV were shifted in magnetic field by half the period of h/e oscillations, $\Delta B = \Phi_0/2\pi r_{\text{eff}}^2$, as shown in Fig. 3b. This behavior allows us to conclude that the oscillations of the dependences $G(V_g)$ with a period of 25–30 mV are caused by tunneling from S to D via a closed edge state of the ring, when an integral number of magnetic flux quanta passes through its contour at the Fermi level. The splitting of h/e states observed in the dependences $G(B)$ (Fig. 3b) can be
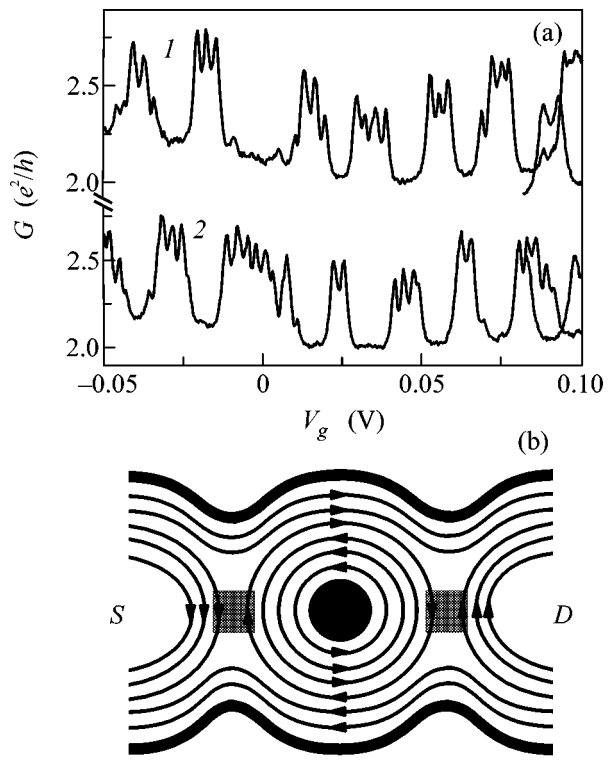
qualitatively explained in terms of the schematic diagram shown in Fig. 4b with the use of the single-particle model of edge current states [11]. However, this simplified model does not allow us to explain the presence of the component with a period of about 3 mV in the dependences $G(V_g)$. The appearance of the component with a period of ~3 mV also cannot be explained by the transformation of the single-particle energy spectrum of the ring due to the charging of closed compressible states by analogy with the interpretation proposed for the frequency doubling of Aharonov–Bohm oscillations at antidots [3, 4].

We believe that the most consistent explanation of the complex structure of transmission peaks in the dependences $G(V_g)$ lies in the single-electron variations of the self-consistent potential of the ring, which lead to periodic variations of the ballistic current through the closed edge state that is tunnel-coupled with the S and D regions. Qualitatively, a similar model was recently proposed for explaining the Coulomb oscillations of the ballistic conductance of an open quantum dot in zero magnetic field [12]. The variation of the interferometer transparency that is synchronous with single-electron variations is most likely to occur in the regions indi-

cated by gray color in Fig. 4b, i.e., in the regions where the outer closed edge state "contacts" the delocalized states in the two-dimensional source and drain regions. Presumably, single-electron variations of the ring potential lead to periodic variations of the distance between the edge states in these regions thus controlling the conductivity of the interferometer, as in the case of a point contact located in the immediate vicinity of a quantum dot [13]. However, this qualitative consideration does not reveal the microscopic mechanism responsible for the single-electron variations in the ring. A Coulomb blockade of tunneling through closed compressible edge states in an open system was observed in [14]. If we assume that a similar mechanism is realized in the rings under study, the dependences $G(B)$ and $G(V_g)$ should be similar, which disagrees with our experiment.

In our structure, we have two X-electron layers that lie in the AlAs/GaAs superlattice barriers on both sides of the GaAs quantum well with 2D Γ-electron gas. Therefore, we assume that the origin of the single-electron variations in the interferometer is not the Coulomb blockade of tunneling through closed compressible edge states of the ballistic Γ-ring but it should be the charging of diffusion X-rings (or one of them) lying in the AlAs/GaAs barriers. The Γ-ring lies between two X-rings, one of which, in its turn, lies between the gate and the Γ-ring. Hence, this X-ring should switch to the tunneling regime at lower gate voltages V_g, as compared to the underlying Γ-ring. The mobility and concentration of X-electrons are much lower than those of Γ-electrons, and, therefore, the contribution of X-rings to the conductivity of the interferometer is negligibly small even in the open regime and is even less significant in the tunneling regime. However, the Coulomb charging of these rings (or one of them) will lead to single-electron variations of the self-consistent potential of the Γ-ring and, hence, manifest itself in its conductivity. The aforementioned origin of short-period oscillations in the dependences $G(V_g)$ is confirmed by the fact that their period coincides with the period of single-electron oscillations in the conductivity of a ring of the same dimensions when its triangular quantum dots, into which the ring is separated in the tunneling regime, are charged as a single whole [15]. Hence, the results obtained from our experiments can be explained in the framework of a single-particle model of tunnel-coupled edge states without using the model of compressible edge states, in accordance with [6, 11]. We believe that the results reported in [3, 4, 14] can also be qualitatively explained in terms of the single-particle model with allowance for the effects of charging in the doped layers of microstructures.

Thus, for the first time, in an open ring interferometer with tunnel-coupled edge current states, we observed oscillations of the conductance as a function of the gate voltage with two periods that differed by an order of magnitude. We have found that the large period (~30 mV) is associated with the tunneling of charge carriers between the source and drain regions via the outer closed edge state of the ring. The small-period oscillations (~3 mV) are qualitatively explained by the effect of single-electron variations of the self-consistent potential of the ring on the ballistic current through it.

REFERENCES

1. A. A. Bykov, Z. D. Kvon, E. B. Ol'shanetskiĭ, *et al.*, Pis'ma Zh. Éksp. Teor. Fiz. **58**, 897 (1993) [JETP Lett. **58**, 839 (1993)].

2. A. A. Bykov, D. G. Baksheev, L. V. Litvin, *et al.*, Pis'ma Zh. Éksp. Teor. Fiz. **71**, 631 (2000) [JETP Lett. **71**, 434 (2000)].

3. C. J. B. Ford, P. J. Simpson, I. Zailer, *et al.*, Phys. Rev. B **49**, 17456 (1994).

4. M. Kataoka, C. J. B. Ford, G. Faini, *et al.*, Phys. Rev. B **62**, R4817 (2000).

5. D. B. Chklovskii, B. I. Shklovskii, and L. I. Glazman, Phys. Rev. B **46**, 4026 (1992).

6. I. Karakurt, V. J. Goldman, J. Liu, and A. Zaslavsky, Phys. Rev. Lett. **87**, 146801 (2001).

7. A. A. Bykov, A. K. Bakarov, L. V. Litvin, and A. I. Toropov, Pis'ma Zh. Éksp. Teor. Fiz. **72**, 300 (2000) [JETP Lett. **72**, 209 (2000)].

8. O. A. Tkachenko, V. A. Tkachenko, D. G. Baksheev, *et al.*, Pis'ma Zh. Éksp. Teor. Fiz. **71**, 366 (2000) [JETP Lett. **71**, 255 (2000)].

9. A. A. Bykov, D. V. Nomokonov, A. K. Bakarov, *et al.*, Pis'ma Zh. Éksp. Teor. Fiz. **78**, 36 (2003) [JETP Lett. **78**, 30 (2003)].

10. H. van Houten, C. W. J. Beenakker, P. H. M. Loosdrecht, *et al.*, Phys. Rev. B **37**, 8534 (1988).

11. D. R. Mace, C. H. W. Barnes, G. Faini, *et al.*, Phys. Rev. B **52**, R8672 (1995).

12. V. A. Tkachenko, D. G. Baksheev, O. A. Tkachenko, and C.-T. Liang, Pis'ma Zh. Éksp. Teor. Fiz. **74**, 229 (2001) [JETP Lett. **74**, 209 (2001)].

13. M. Field, C. G. Smith, M. Papper, *et al.*, Phys. Rev. Lett. **70**, 1311 (1993).

14. M. Kataoka, C. J. B. Ford, G. Faini, *et al.*, Phys. Rev. Lett. **83**, 160 (1999).

15. V. A. Tkachenko, A. A. Bykov, D. G. Baksheev, *et al.*, Zh. Éksp. Teor. Fiz. **124**, 351 (2003) [JETP **97**, 317 (2003)].

Translated by E. Golyamina

Study of Magnetic Correlations in Nanostructured Ferromagnets by Correlation Magnetometry

R. S. Iskhakov*, V. A. Ignatchenko, S. V. Komogortsev, and A. D. Balaev

Kirensky Institute of Physics, Siberian Division, Russian Academy of Sciences,
Krasnoyarsk, 660036 Russia
* e-mail: rauf@iph.krasn.ru
Received October 16, 2003

We propose a theoretically justified experimental magnetometric technique for determining the size of stochastic domains spontaneously formed in the spin system of nanostructured ferromagnets and for evaluating the effective anisotropy in these magnetically correlated regions. The method is based on monitoring the $\Delta M \sim H^{-2}$ relationship in the low-field part of the integral magnetization curve. © 2003 MAIK "Nauka/Interperiodica".

PACS numbers: 75.75.+a; 75.30.Gw; 75.60.Ej

1. INTRODUCTION

Nanocrystalline and amorphous ferromagnets belong to the class of nanostructured materials extensively studied both in basic aspects and in view of possible applications. A currently important problem is the establishing of relationships between macroscopic and microscopic parameters of these materials. For nanostructured ferromagnets, such a relationship has been described within the framework of the so-called random anisotropy model [1–4]. According to this approach, the spin system of a ferromagnet is described in terms of the following microscopic parameters: exchange interaction A, magnetization M_s, local anisotropy K, and the length $2R_c$ of its homogeneous orientation. It is assumed that the easy axes of local anisotropy in the grains (clusters) of a ferromagnet are randomly oriented. Some cases of spatially inhomogeneous anisotropy, exchange, and magnetization have been also considered (see, e.g., [2]).

A characteristic feature of the random anisotropy model in systems of dimension $d < 4$ is instability of the ferromagnetic state with respect to the appearance of an arbitrarily small random anisotropy even at a zero temperature, which is completely analogous to breakage of the ferromagnetic order in the random field model [5]. In both cases, the ferromagnetic order is established over a characteristic distance—the magnetic orientation coherence length $2R_L$ ($R_L \gg R_c$). Both models predict an increase in the length of magnetic correlations with decreasing correlation length of the random perturbations.

Thus, a magnetic structure of nanostructured ferromagnets can be represented by an ensemble of stochastic domains (with a size of $2R_L$) obeying an approximation analogous to the model of exchange-independent grains in polycrystalline solids. This well-known approximation has been widely used for calculating macroscopic parameters such as coercive force, susceptibility, and residual magnetization in the region of irreversibility of the magnetization curve (beginning with the original paper of Stoner and Wohlfarth [6]). The same approximation was used to describe the law of the magnetization approach to saturation employed (beginning with the works of Akulov [7, 8]) for determining the microscopic anisotropy K from the reversible magnetization curve. Herzer [9] showed that this method provides an adequate description of nanostructured ferromagnets: determination of the coercive force as a function of the grain size, $H_c \sim R_c^6$, was equivalent to estimating the macroscopic anisotropy in a stochastic domain as $K \sim (R_c/R_L)^{3/2}$ and the domain size as $R_L \sim A^2/K^2 R_c^3$.

It should be emphasized that R_L is a very important parameter. Unfortunately, the possibilities of experimental determination of the magnetic correlation length are rather restricted. It is commonly accepted that the main experimental method is offered by small-angle neutron scattering (SANS). Using this method, Löffler *et al.* [10] recently measured the value of $L_m = 2R_L$ and studied the dependence of L_m on the grain size $D = 2R_c$ for nanostructured Fe. Ryne [11] used SANS to measure L_m and studied the dependence of L_m on the applied magnetic field H in a TbFe$_2$ amorphous alloy.

This paper demonstrates the possibility to measure the magnetic correlation length R_L in nanostructured ferromagnets and to evaluate the macroscopic anisotropy in these magnetically correlated regions using a magnetometer—a commonly available instrument.

2. THEORETICAL JUSTIFICATION OF THE PROPOSED METHOD

For an inhomogeneous ferromagnet characterized by a local magnetic anisotropy of arbitrary origin and symmetry, the law of the magnetization approach to saturation can be written as

$$\langle M_z \rangle / M_s \approx 1 - d_m(H), \tag{1}$$

where d_m is the normalized mathematical dispersion (variance) of the transverse magnetization components [2]:

$$d_m = \frac{\langle M_\perp^2 \rangle}{M_s^2} = (aH_a)^2 \int \frac{S(k)d^3k}{((2A/M_s)k^2 + H)^2}. \tag{2}$$

Here, $H_a = 2K/M_s$ is the local anisotropy field, a is the symmetry factor (for uniaxial anisotropy, $a = 1/15^{1/2}$) and $S(k)$ is the normalized spectral density of the correlation function $K(r)$ of orientation of the local anisotropy axes.

For an exponential model correlation function of the type e^{-r/R_c}, we obtain

$$d_m = \frac{(aH_a)^2}{H^{1/2}(H_R^{1/2} + H^{1/2})^3}, \tag{3}$$

where $H_R = 2A/M_s R_c^2$ is a correlation field (for the reasons presented below, this parameter will be referred to as the "upper" correlation field) and R_c is the correlation radius of the anisotropy inhomogeneities. As can be seen, the character of the behavior of magnetization as a function of the field changes in the vicinity of H_R, so that

$$d_m = (aH_a)^2 \begin{cases} H^{-2}, & H \gg H_R \\ H^{-1/2}H_R^{-3/2}, & H \ll H_R. \end{cases} \tag{4}$$

In the coordinates of $\log d_m$ versus $\log H$, this change is manifested by a characteristic bending of the experimental $M(H)$ curve in the region of $H \sim H_R$. Note that, if any other monotonically decreasing function (rather than exponent) is selected as the model correlation function, the analytical expression for $d_m(H)$ will change, but the asymptotic behavior (4) and the correlation field H_R remain the same.

Let us consider the physical reasons for the appearance of a characteristic point H_R in the $d_m(H)$ function. Deviations of the magnetization vector $\mathbf{M}(\mathbf{x})$ from the magnetic field direction in nanostructured ferromagnets are correlated within a region of size $R_H = (2A/M_sH)^{1/2}$, this value depends on the magnetic field and exchange. For $R_H \ll R_c$ (i.e., for $H \gg H_R$), the fluctuations of magnetization orientation are uncorrelated. On the contrary, for $R_H \gg R_c$, the magnetization vector orientation is strongly correlated. Therefore, $H \sim H_R$

corresponds to a change in the character of the magnetization curve. For this reason, the value of H_R and, hence R_c, can be experimentally measured. A method for processing the magnetization curve so as to extract data on the correlation radius and the effective magnetic anisotropy is called the correlation magnetometry [12].

The low-field effects related to the formation of stochastic domains are not manifested in formulas (3) and (4). This is explained by the fact that these expressions were obtained in the linear approximation of the perturbation theory that fails to be valid in the range of small fields. However, the correlation properties of the inhomogeneous orientation of $\mathbf{M}(\mathbf{x})$ in this range can be determined by numerical methods. In particular, the correlation function $K_m(r)$ and the corresponding correlation radius $R_m(H)$ were calculated [13] for a chain of exchange-coupled grains with random anisotropy. The main result of such numerical calculations consists in the appearance of another characteristic field $H_L = 2A/M_s R_L^2$, called the "lower" correlation field, where $2R_L$ is the size of a stochastic domain. In the range of $H > H_L$, the behavior of $R_m(H)$ is described by the linear theory, while for $H < H_L$, the $R_m(H)$ function tends to the constant value R_L (instead of infinitely increasing as predicted by the linear theory).

In order to take into account the formation of stochastic domains, we suggest modifying expression (3) as follows:

$$d_m = \left(\frac{aH_a}{H}\right)^2 \left(\frac{H_L^{1/2} + H^{1/2}}{H_R^{1/2} + H^{1/2}}\right)^d, \tag{5}$$

where d is the dimension of the system of exchange-coupled ferromagnetic nanoparticles. This expression, in contrast to the exact formula (3), represents an interpolation and has to be verified in experiment. Indeed, in the range of $H > H_L$, expression (5) describes the experimental $M(H)$ curves for $d = 3$ [14], $d = 2$ [15], and $d = 1$ [16]. Below we will demonstrate that this expression also adequately describes the experimental data for $H < H_L$. To this end, we will need expressions for the asymptotic behavior of $d_m(H)$:

$$d_m = \begin{cases} \dfrac{(aH_a)^2}{H^2}\dfrac{H_L^{d/2}}{H_R^{d/2}} = \dfrac{(a\langle H_a \rangle_L)^2}{H^2}, \\ a\langle H_a \rangle_L < H < H_L \\ \dfrac{(aH_a)^2}{H_R^{d/2}}\dfrac{1}{H^{(4-d)/2}} = \dfrac{(a\langle H_a \rangle_L)^2}{H_L^{d/2}}\dfrac{1}{H^{(4-d)/2}}, \\ H_L < H < H_R \\ \dfrac{(aH_a)^2}{H^2}, \quad H_R < H \end{cases} \tag{6}$$
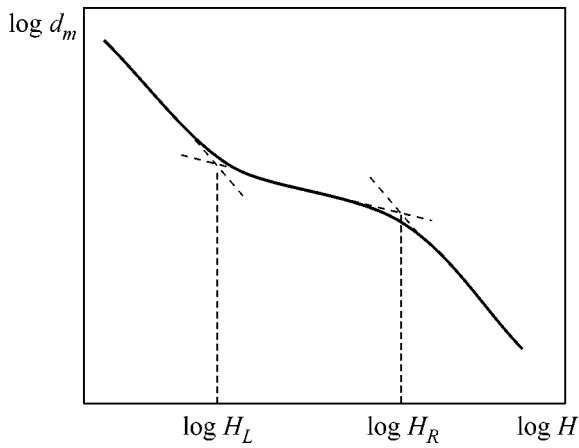
Fig. 1. A schematic curve of the magnetization dispersion $d_m(H)$ of a nanostructured ferromagnet.

Fig. 2. A plot of the magnetization dispersion $\Delta M/M_s$ versus magnetic field strength for a 2000-Å-thick $Co_{90}P_{10}$ amorphous alloy film at $T = 4$ K ($H_L = 80$ Oe, $H_R = 3$ kOe).

Here, the macroscopic anisotropy field in a stochastic domain is given by the formula

$$\langle H_a \rangle_L = H_a (H_L/H_R)^{d/4} = H_a (R_c/R_L)^{d/2} = H_a/\sqrt{N}, \quad (7)$$

where N is the number of nanoparticles in this domain. Figure 1 schematically presents the function (5) and shows the asymptotes (6) on the double logarithmic scale. As can be seen, the experimental task reduces to monitoring the low-field crossover (bending) in d_m, the presence of which proves the formation of stochastic domains in the system.

3. RESULTS AND DISCUSSION

Figure 2 presents a double logarithmic plot of a reversible part of the magnetization curve $M(H)$ for a 2000-Å-thick $Co_{90}P_{10}$ amorphous alloy film. The films of amorphous and nanocrystalline alloys were obtained by chemical deposition onto cover glasses. The magnetization curves were obtained (with the substrate background subtraction) using a vibrating-sample magnetometer with a superconducting coil operating in a range of fields up to 30 kOe.

As can be seen from Fig. 2, the experimental field dependence $M(H)$ is well described by expressions (5) and (6) with $d = 3$. As the field H decreases, the magnetization sequentially obeys the high-field Akulov law ($\Delta M \sim H^{-2}$), the cooperative dependence ($\Delta M \sim H^{-1/2}$), and the low-field dependence ($\Delta M \sim H^{-2}$). The theoretical asymtotes described by expressions (6) are represented by straight lines. The points of intersection of these lines determine the characteristic fields $H_L \approx 80$ Oe and $H_R \approx 3$ kOe corresponding to the low- and high-field crossovers (bending points) in the magnetization curve $M(H)$. Upon substituting the values of exchange A and magnetization M_s into the expressions for H_L and H_R, we obtain the values of $R_L \approx 500$ Å and $R_c \approx 80$ Å. Using the portions described by the dependence $\Delta M \sim$
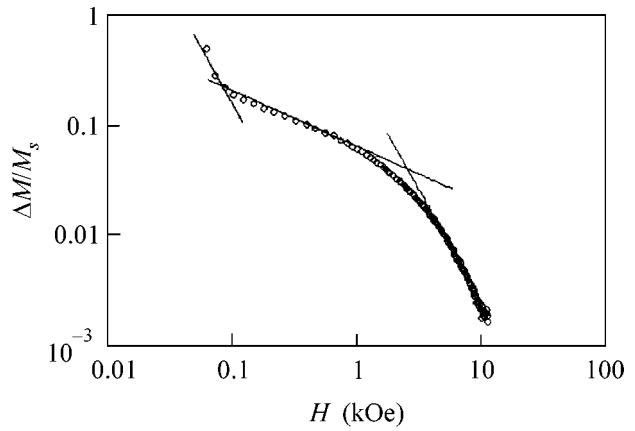
H^{-2}, we determine the macroscopic and microscopic anisotropy fields: $\langle H_a \rangle_L \approx 150$ Oe and $H_a \approx 2$ kOe. Substitution of the measured and calculated values into expression (7) proves the validity of this relation.

Figure 3 shows a reversible part of the magnetization curve for a 100-Å-thick $Co_{93}P_7$ nanocrystalline alloy film. This curve reveals the low-field dependence $\Delta M \sim H^{-2}$, followed by a clearly identified dependence of the type $\Delta M \sim H^{-3/4}$ (for H from 0.2 to 2 kOe), a statistically reliable dependence of the type $\Delta M \sim H^{-1}$ (for H from 2 to 6 kOe), and a noisy signal in the fields above 10 kOe (reflecting the fact that the dispersion of magnetization becomes comparable with the accuracy of magnetization measurements).

The grain size in the $Co_{93}P_7$ nanocrystalline alloy is on the order of the film thickness. Therefore, this film features a two-dimensional system of ferromagnetically coupled grains ($d = 2$). According to expressions (5) and (6), this system has to exhibit a low-field crossover in $M(H)$ (reflecting the transition from $\Delta M \sim H^{-2}$ to $\Delta M \sim H^{-1}$). However, our experimental curve initially exhibits an intermediate transition from $\Delta M \sim H^{-2}$ to $\Delta M \sim H^{-3/4}$ and only then changes to $\Delta M \sim H^{-1}$. This behavior is not an artifact. Indeed, the rms deviation $d_m^{1/2}$ of magnetization has to be determined from the condition of minimum for the total energy including a magnetic dipole interaction (which is significant in the case of thin films). The most exhaustive theoretical analysis of this situation has been performed in [17–19]. In our notations, the final expression for d_m is as follows [19]:

$$d_m = \frac{1}{2} \frac{(aH_a)^2}{M_s^{1/2} H_R^{3/4}} \frac{1}{H^{3/4}} \equiv \frac{1}{2} \frac{(a\langle H_a \rangle_L)^2}{M_s^{1/2} H_L H_R^{1/4}} \frac{1}{H^{3/4}}. \quad (8)$$

To our great surprise, an analysis of the available literature showed that the region of $\Delta M \sim H^{-3/4}$ in the
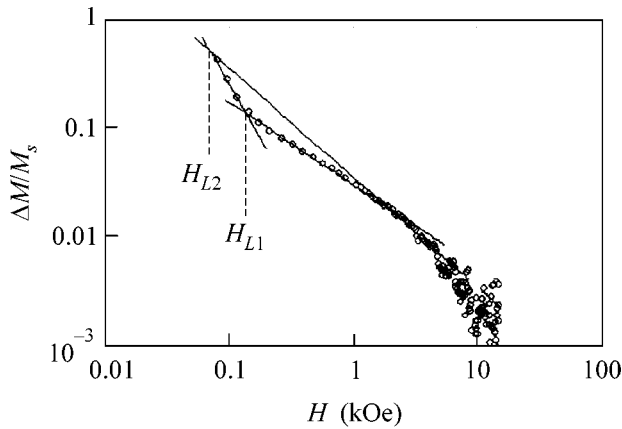
Fig. 3. A plot of the magnetization dispersion $\Delta M/M_s$ versus magnetic field strength for a 100-Å-thick $Co_{93}P_7$ film ($T = 90$ K).

Fig. 4. A plot of the magnetization dispersion $\Delta M/M_s$ versus magnetic field strength for two multilayer $[Co_{93}P_7(x)/Pd(14$ Å$)]_{20}$ structures with individual nanocrystalline Co layer thicknesses $x = 80$ and 55 Å ($T = 4$ K).

experimental curve of Fig. 3 is the first observation of the well-known theoretical dependence (8). The intersections of asymptotes $H^{-3/4}$ and H^{-1} with the line H^{-2} give two values of the characteristic field: $H_{L1} \approx 140$ Oe and $H_{L2} \approx 70$ Oe. This is indirect evidence of a modification of the shape of a stochastic domain in the thin film under consideration related to the magnetostatic effects, whereby a disk with a circular base existing at $H < H_{L2}$ transforms into a disk with an ellipsoidal base in higher fields.

Figure 4 presents the reversible parts of the magnetization curves $M(H)$ for two multilayer $[Co_{93}P_7(x)/Pd(14$ Å$)]_{20}$ structures with individual nanocrystalline Co layer thicknesses $x = 80$ and 55 Å. Note that the total ferromagnetic layer thickness was 1600 or 1100 Å, respectively; hence, the useful signal magnitude was more than ten times greater as compared to that from a single ultrathin film. In the range of magnetic fields from 1–1.5 to 20 kOe, these samples obeyed the law $\Delta M \sim H^{-1}$ that confirmed the two-dimensional character of the system of ferromagnetically coupled grains. In the region of low fields, the magnetization follows the dependence $\Delta M \sim H^{-2}$, but the portion of the $M(H)$ curve in greater fields cannot be described by a power function. In our opinion, this is explained by more complicated magnetostatic phenomena (related to the magnetic dipole interactions between the magnetizations of individual ferromagnetic layers) as compared to those in a thin single-layer film.

Assuming that the characteristic fields H_L correspond to the H values at which the experimental data deviate from the low-field dependence $\Delta M \sim H^{-2}$, we conclude that a decrease in the ferromagnetic layer thickness (and, hence, in the R_c value) leads to a decrease in H_L (and to a corresponding increase in R_L), in agreement with the main stipulations of models [1–5]. Another physically reasonable observation is a
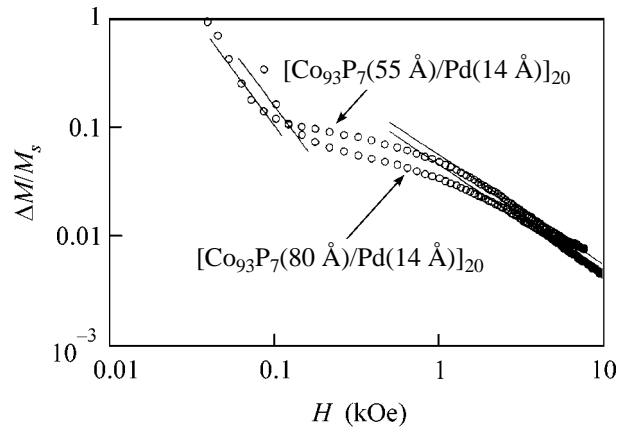
decrease in the macroscopic anisotropy field $\langle H_a \rangle_L$ with increasing size of stochastic domains. Therefore, stochastic domains are also formed in individual ferromagnetic layers of multilayer structures, but the shape of these domains (like that in an ultrathin nanocrystalline ferromagnetic film) is significantly modified by magnetostatic interactions.

Thus, the proposed interpolation formula (5) and asymptotic expressions (6) qualitatively explain the effects observed on the magnetization curves measured in the entire range of magnetic fields. In the high-field range, $H \gg H_L$, formula (5) coincides with the exact theoretical expression (3), and in the low-field region, this formula describes the behavior of $M(H)$ related to the formation of stochastic domains in nanostructured ferromagnets. This approach allows effective quantitative characteristics (H_L, $\langle H_a \rangle_L$, R_L) to be introduced for description of the low-field magnetic correlations.

REFERENCES

1. R. Harris, M. Plischke, and M. J. Zukermann, Phys. Rev. Lett. **31**, 160 (1973).
2. V. A. Ignatchenko and R. S. Iskhakov, Zh. Éksp. Teor. Fiz. **72**, 1005 (1977) [Sov. Phys. JETP **45**, 526 (1977)]; Izv. Akad. Nauk SSSR, Ser. Fiz. **44**, 1434 (1980).
3. R. Alben, J. J. Becker, and M. C. Chi, J. Appl. Phys. **49**, 1653 (1978).
4. E. M. Chudnovsky, W. M. Saslow, and R. A. Serota, Phys. Rev. B **33**, 251 (1986).
5. Y. Imry and S.-K. Ma, Phys. Rev. Lett. **35**, 1399 (1975).
6. E. C. Stoner and E. P. Wohlfarth, Philos. Trans. R. Soc. London, Ser. A **240**, 599 (1948).
7. N. S. Akulov, Z. Phys. **69**, 278 (1931).
8. N. S. Akulov and L. V. Kirenskiĭ, Zh. Tekh. Fiz. **9**, 1145 (1939).

9. G. Herzer, IEEE Trans. Magn. **26**, 1397 (1990).

10. J. F. Löffler, H. B. Braun, and W. Wagner, Phys. Rev. Lett. **85**, 1990 (2000).

11. J. J. Ryne, IEEE Trans. Magn. **21**, 1990 (1985).

12. V. A. Ignatchenko and R. S. Iskhakov, *Magnetic Properties of Crystalline and Amorphous Media* (Nauka, Novosibirsk, 1989), p. 128.

13. A. V. Luk'yanenko and S. V. Komogortsev, in *Proceedings of II Baykal International Conference on Magnetic Materials* (Irkutsk, 2003), p. 72.

14. V. A. Ignatchenko, R. S. Iskhakov, and G. V. Popov, Zh. Éksp. Teor. Fiz. **82**, 1518 (1982) [Sov. Phys. JETP **55**, 878 (1982)].

15. R. S. Iskhakov, S. V. Komogortsev, A. D. Balaev, *et al.*, Pis'ma Zh. Éksp. Teor. Fiz. **72**, 440 (2000) [JETP Lett. **72**, 304 (2000)].

16. R. S. Iskhakov, S. V. Komogortsev, A. D. Balaev, *et al.*, Pis'ma Zh. Éksp. Teor. Fiz. **78**, 271 (2003) [JETP Lett. **78**, 236 (2003)].

17. H. Hoffman, IEEE Trans. Magn. **4**, 32 (1968).

18. K. J. Harte, J. Appl. Phys. **38**, 1503 (1968).

19. V. A. Ignatchenko, Zh. Éksp. Teor. Fiz. **54**, 303 (1968) [Sov. Phys. JETP **27**, 162 (1968)].

Translated by P. Pozdeev

Amplification of Plasma Oscillations in an Asymmetric Double Quantum Well

R. Z. Vitlina and A. V. Chaplik

Institute of Semiconductor Physics, Siberian Division, Russian Academy of Sciences,
pr. Akademika Lavrent'eva 13, Novosibirsk, 630090 Russia
Received October 6, 2003; in final form, October 20, 2003

It is shown that the subband population inversion in an asymmetric double quantum well can result in the amplification of optical plasma oscillations. © *2003 MAIK "Nauka/Interperiodica".*

PACS numbers: 73.21.Fg; 71.45.Gm

The structures with double quantum wells have been drawing attention of researchers over several last years. Most of the work has been devoted to the quantum Hall effect and the resonance tunneling phenomena in such systems. In both cases, one deals with the zero-frequency effects, i.e., effects caused by the passage of a dc (longitudinal or transverse) current. In this letter, we call attention to some intriguing high-frequency properties of a double quantum well, namely, to the specific damping mechanism of two-dimensional plasmons and to the possibility of plasma-wave amplification through the creation of an inverse level population in the system.

The key idea can conveniently be demonstrated by the following simple example: let only the lowest energy level be occupied in each well, so that, in the presence of tunneling, one deals with a two-level system (as regards the single-particle spectrum) and with a two-component plasma (as regards the collective degrees of freedom). The plasma-wave spectrum in such a system was studied in our work [1]. In that work, in line with the terminology of the day, we spoke about a quantum film with two occupied transverse-quantization subbands. There are three plasma oscillation branches: two gapless branches corresponding to optical and acoustic plasmons with the root and linear small-momentum dispersion laws, respectively, and an intersubband plasmon with the finite zero-momentum frequency ω_{int}:

$$\omega_{int}^2 = \Omega^2 + \mathrm{const}\frac{e^2 L}{\varepsilon}\Omega(N_1 - N_2). \qquad (1)$$

Here, Ω is the separation between the first and second transverse-quantization levels ($\hbar = 1$), e is the electron charge, L is the characteristic wave-function size (on the order of film thickness) in the normal direction to the structure, ε is the dielectric constant, $N_{1,2}$ are the electron surface concentrations in the first and second subbands, and const is on the order of unity and

depends on the wave function of transverse motion (e.g., $\mathrm{const} = 2\sqrt{2\pi}$ in the oscillator model). The second term on the right-hand side of Eq. (1) accounts for the depolarization shift and is equal to the difference between the resonance IR frequency and the separation Ω between the single-particle levels (i.e., difference between the actual and incident IR fields) because of the dynamic screening effect.

Simultaneously, a system of two spatially separated plasma layers was considered in [2] without allowance for the tunneling between them (squared wave functions for the transverse motion were approximated by δ functions). Clearly, the authors of [2] obtained one less branch, because intersubband plasmons were absent in this model. Later on, the problem of plasma oscillations in two-dimensional multicomponent systems became the subject of many publications (cf., e.g., Chaplik's review [3] and recent works [4–7]). Despite certain distinctions in the computational schemes, the common conclusion of these publications is that the gapless plasma-spectrum branches correspond to the intrasubband excitations, while the branch with a zero-momentum gap appears in the presence of intersubband transitions, e.g., tunneling splitting in a double well; plasmons undergo Landau damping in the wave-vector and frequency regions corresponding to the single-particle continuum (each subband's own).

A film symmetric about its middle plane, i.e., with a certain parity of the function $\varphi_n(z)$ describing the transverse motion, was considered in [1] and many subsequent publications. For such a film, the characteristic determinant of the dielectric function χ_{ijkl}, whose zeros determine the plasma-wave spectrum, is factored into two multipliers. One of them includes only the intrasubband elements χ_{ijkl} and determines the dispersion of the optical $\omega_{opt}(\mathbf{k})$ and acoustic $\omega_{ac}(\mathbf{k})$ branches, while the second involves only the intersubband elements and corresponds to the intersubband plasmon $\omega_{int}(\mathbf{k})$, where $\mathbf{k}$ is the wave vector. Therefore, the branches do not
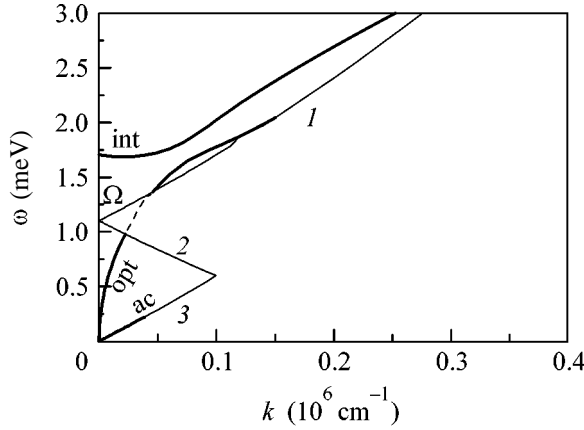
Plasma spectrum for $m = 0.07m_0$, $d = 2.5 \times 10^{-6}$ cm, and $N_1 + N_2 = 6.4 \times 10^{10}$ cm^{-2}. The parameters V_1 and V_2 are chosen so that $E_1 = -1.8$ meV and $E_2 = -0.7$ meV. The dashed line indicates the damping region of the optical branch. Curves 1, 2, and 3 are the boundaries of the electron–hole continuum.

interact, and, if $\omega_{\text{opt}}(k_c) = \omega_{\text{int}}(k_c)$ at a certain $k = k_c$, the branches intersect without distorting their dispersion laws in the vicinity of the intersection point. These frequencies may well be equal to each other, because Ω, N_1, and N_2 are the free parameters of the problem. The graphs of plasmon dispersion curves with intersecting branches are presented in [7].

If the structure has no symmetry plane, $\varphi_n(z)$ cannot be assigned a certain parity, and the intersection of the optical and acoustic branches transforms to anticrossing. This fact was pointed out in [8, 9]. We demonstrate below that the asymmetric structure has another interesting feature, namely, the specific damping mechanism of optical plasmons in a certain wave-vector and frequency "window" $k_1 < k < k_2$, $\omega_1 < \omega < \omega_2$ and the ensuing possibility of instability development (amplification of plasma oscillations).

The mechanism under discussion is quite analogous to Landau damping (inverse Cherenkov effect) and differs from the well-known effect in that only one of the electron momentum components is quantized. Therefore, the wave energy expends on the excitation of "skewed" intersubband transitions:

$$\omega(\mathbf{k}) = E_2(\mathbf{p} + \mathbf{k}) - E_1(\mathbf{p}) = \Omega + \frac{\mathbf{p}\mathbf{k}}{m} + \frac{k^2}{2m}, \quad (2)$$

where $E_n(\mathbf{k})$ is the electron energy for the momentum $\mathbf{p}$ in the subband n. It is this process that is responsible for the collisionless plasma-wave damping. One can see from the figure that Eq. (2), when applied to the optical branch, is valid for small k in a finite interval of wave vectors and frequencies (damping window).

The damping is calculated as follows. Let us consider a system with one-electron spectrum of the quan-

tum-well type; its nth transverse-motion subband is described by the wave functions $\varphi_n(z)$. We will seek for the linear response to the perturbation $U(z, \mathbf{k})\exp\{i(\mathbf{k}\boldsymbol{\rho} - \omega t)\}$ with allowance for the self-consistent field effects; z and $\boldsymbol{\rho}$ are the coordinates in the transverse and longitudinal directions, respectively. By performing the standard perturbative calculations, one can find the corrections to the wave functions of the system and, next, the perturbation-induced charge-density increment. If the retardation effects are neglected (they are irrelevant to the problem of interest, except for the narrow region of anomalously small k), the equation of the self-consistent field becomes merely a Poisson equation for the Fourier component of the induced potential U_{ind}:

$$\frac{d^2 U_{\text{ind}}}{dz^2} - k^2 U_{\text{ind}} = -\frac{4\pi e^2}{\varepsilon(z)}\sum_{n, m} U_{mn}(\mathbf{k})\varphi_n(z)\varphi_m(z)$$

$$\times \sum_q \frac{f_n(\mathbf{q}) - f_m(\mathbf{k} + \mathbf{q})}{E_n(\mathbf{q}) - E_m(\mathbf{k} + \mathbf{q}) + \omega + i\delta}. \quad (3)$$

Here, U_{nm} are the matrix elements of $U(z)$ between the transverse-motion (real) wave functions; f_n are the Fermi occupation numbers; and $\varepsilon(z)$ is the dielectric constant, which may be different for different z. By writing the solution to Eq. (3) in terms of the Green's function and taking the matrix elements of this solution in the $\varphi_n(z)$ basis, one arrives at the closed set of equations for the quantities $U_{nm}(\mathbf{k})$. Its particular form depends on the function $\varepsilon(z)$. Here, we present the results for the simplest case $\varepsilon = $ const, which corresponds to a quantum well embedded in a homogeneous dielectric medium. A multilayer GaAs–Ga$_x$Al$_{1-x}$As structure is the structure of this type. For $\varepsilon = $ const, the Green's function of Eq. (3) is

$$G(z, z_0) = \frac{1}{2k}\exp(-k|z - z_0|),$$

and we obtain the system of equations for the matrix elements of the renormalized potential $\tilde{U} = U + U_{\text{ind}}$:

$$\tilde{U}_{ij} + \frac{2\pi e^2}{\varepsilon k}\sum_{nm} I_{ij, nm}(k)\Pi_{nm}(k, \omega)\tilde{U}_{nm} = U_{ij}, \quad (4)$$

where

$$I_{ij, nm}(k)$$

$$= \int_{-\infty}^{+\infty} \varphi_i(z)\varphi_j(z)\exp(-k|z - z_0|)\varphi_n(z_0)\varphi_m(z_0)dzdz_0,$$

$$(5)$$

$$\Pi_{nm}(k, \omega) = -\sum_q \frac{f_n(\mathbf{q}) - f_m(\mathbf{k} + \mathbf{q})}{E_n(\mathbf{q}) - E_m(\mathbf{k} + \mathbf{q}) + \omega + i\delta},$$

$$\delta \longrightarrow +0.$$

Next one should calculate the work Q executed by the *external* field $U(z, k)$ upon the system; it is determined

by a current induced by the *renormalized* (acting) field $\tilde{U}(z, k)$. This quantity is given by the Kubo formula, which should be modified with allowance for the quantization of one of the momentum components. Leaving aside the details of calculation, we present the result

$$Q = \frac{1}{2mS} \text{Im} \sum_{nk\mathbf{p}} \frac{\tilde{U}_{nk}U_{kn}\mathbf{q}(\mathbf{q} + 2\mathbf{p})(f_{n\mathbf{p}} - f_{k,\mathbf{p}+\mathbf{q}})}{E_{k,\mathbf{p}+\mathbf{q}} - E_{n\mathbf{p}} - \omega - i\delta}, \quad (6)$$

where S is the area of the system.

To pass from the general relationships to a two-level (and two-component) system, we use the following exactly soluble model. The electron potential energy in an asymmetric double quantum well can be written as

$$V(z) = -V_1\delta(z + d) - V_2\delta(z - d), \quad (7)$$

where $V_{1,2} > 0$ and $2d$ is the separation between the well centers. The wave functions corresponding to two coupled states in potential (7) can easily be found:

$$\begin{aligned} \varphi_1(z) &= A_1(e^{-\kappa_1|z+d|} + a_1 e^{-\kappa_1|z-d|}), \\ \varphi_2(z) &= A_2(e^{-\kappa_2|z+d|} - a_2 e^{-\kappa_2|z-d|}). \end{aligned} \quad (8)$$

Two negative energy levels are given by the roots $\kappa_{1,2}$ of the equation

$$\begin{aligned} (\kappa - mV_1)(\kappa - mV_2) &= m^2 V_1 V_2 e^{-4\kappa d}, \\ E_{1,2} &= -\kappa_{1,2}^2/2m, \end{aligned} \quad (9)$$

where $a_{1,2} = \sqrt{\dfrac{V_2}{V_1}\left|\dfrac{\kappa_{1,2} - V_1}{\kappa_{1,2} - V_2}\right|}$ and $A_{1,2}$ are the normalization coefficients. The second bound level exists only if the inequality $4V_1V_2dm > (V_1 + V_2)$ is fulfilled.

Now, all indices in Eqs. (4)–(6) take the values 1 and 2. We now calculate the quantities I_{ijnm} with functions (8) and the polarization operators Π_{nm}. We also take into account that the electromagnetic wavelength at plasma frequency is much larger than the thickness d, so that the bare perturbation U can be considered uniform; i.e., one can put $U_{ij} = U_0(k)\delta_{ij}$ on the right-hand side of Eq. (5). Thereafter we solve the system of Eqs. (4), which, in our case, consists of three equations because $\tilde{U}_{12} = \tilde{U}_{21}$, to find $Q(\mathbf{k}, \omega)$.

It is clear from physical considerations that, in the absence of electron scattering, $Q(\mathbf{k}, \omega)$ is nonzero only in the interval marked by the dashed line in the figure. Below, we consider in more detail the case where this interval ($k_1 < k < k_2$) falls within the region of root dispersion $\omega_{opt} = \sqrt{k(v_1^2 + v_2^2)/a^*}$ of optical plasmon, where $v_{1,2}$ are the Fermi velocities in the subbands 1 and 2 and a^* is the Bohr effective radius. The inequality $k_2 a^* \ll 1$ is the corresponding sufficient condition which is fulfilled if $\Omega \ll \sqrt{v_1^2 + v_2^2} a^*$. Rather cumber-

some calculations yield the formula (for $|\omega - \Omega| \ll \omega$ and $k = k_c = \Omega^2 a^*/(v_1^2 + v_2^2)$)

$$Q = \frac{E_0^2 m e^2}{16\pi\Omega z^2 a^{*2}}\left(\frac{p_1 - p_2}{k_c}\right)\frac{(v_1^2 I_{11,12} + v_2^2 I_{12,22})^2}{(\omega - \Omega + \Delta)^2 + \Gamma^2}. \quad (10)$$

Here, Δ is the resonance frequency shift that is much smaller than Ω if $k_c a^* \ll 1$ (as it was assumed above). We do not present the corresponding formula because of its unwieldy form. The linewidth Γ is given by the formula

$$\begin{aligned} \Gamma &= \frac{1}{2a^{*2}\Omega z^2}\left|\frac{p_1 - p_2}{k_c}\right|\frac{(v_1^2 I_{11,12} + v_2^2 I_{12,22})^2}{v_1^2 + v_2^2}, \\ z^2 &= \left(1 + \frac{\alpha}{a^*}\right)^2 + \frac{\alpha^2}{a^{*2}}\left(\frac{p_1 - p_2}{k_c}\right)^2. \end{aligned} \quad (11)$$

In formulas (10) and (11), the subband boundary momenta $p_{1,2} = \sqrt{2\pi N_{1,2}}$ are introduced together with the coefficient α specifying the law according to which the form factor $I_{12,22}$ turns to zero (see Eq. (5)) at $k \longrightarrow 0$: $I_{12,12} \sim \alpha k$. One can see from Eq. (10) that Q becomes negative upon the subband population inversion ($N_1 < N_2$), and, then, the plasma oscillations can, in principle, be amplified (clearly, if $|Q|$ exceeds the losses). It is significant that this effect disappears if the skew form factors $I_{11,12}$ and $I_{12,22}$ are zero, i.e., in the symmetric structures. The subband population inversion can, probably, be created upon the vertical (tunneling) transport through the asymmetric structure.

REFERENCES

1. R. Z. Vitlina and A. V. Chaplik, Zh. Éksp. Teor. Fiz. **81**, 1011 (1981) [Sov. Phys. JETP **54**, 536 (1981)].
2. S. Das Sarma and A. Madukhar, Phys. Rev. B **23**, 805 (1981).
3. A. V. Chaplik, Surf. Sci. Rep. **5**, 289 (1985).
4. G. Gumbs and G. B. Aizin, Phys. Rev. B **51**, 7074 (1995).
5. L. Wender and T. Kraft, Phys. Rev. B **54**, 11436 (1996).
6. S. Das Sarma and E. H. Hwang, Phys. Rev. Lett. **81**, 4216 (1998).
7. X.-H. Liu, X.-H. Wang, and B.-X. Gu, Phys. Rev. B **64**, 195322 (2001).
8. C.-M. Hu, C. Schuller, and D. Heitmann, Phys. Rev. B **64**, 073303 (2001).
9. S. Holland, C.-M. Hu, C. H. Heyn, and D. Heitmann, Phys. Rev. B **66**, 073305 (2002).

Translated by V. Sakun

Elementary Excitations in Tunnel-Coupled Electron Bilayers

S. V. Tovstonog[1, 2, *], L. V. Kulik[1, 2], V. E. Kirpichev[1], I. V. Kukushkin[1, 2],
W. Dietsche[2], and K. von Klitzing[2]

[1] *Institute of Solid-State Physics, Russian Academy of Sciences, Chernogolovka, Moscow region, 142432 Russia*
[2] *Max-Planck-Institut für Festkörperforschung, 70569 Stuttgart, Germany*
* e-mail: tovstons@issp.ac.ru
Received October 22, 2003

A new class of single-particle excitations in tunnel-coupled electron bilayers is investigated by inelastic light scattering. The dispersion law and the dependence of the energies of these excitations on the degree of unbalance between the layers have been measured. A new spectroscopic method is proposed for determining the degree of unbalance between bilayers. © 2003 MAIK "Nauka/Interperiodica".

PACS numbers: 73.20.Mf; 73.21.Fg

The development of the growth technology of semiconductor nanostructures offers scope for studying physical phenomena associated with electron–electron interaction in systems with reduced dimensionality. It is known that electron–electron interaction in two-dimensional (2D) systems leads to such fundamental physical phenomena as the fractional quantum Hall effect and Wigner crystallization [1]. The creation of 2D electron systems with spatial charge separation allows an additional degree of freedom (pseudospin) associated with electron motion in the direction perpendicular to the 2D layers to be introduced in a controlled way. Such systems can be obtained in GaAs/AlGaAs heterostructures with double quantum wells (DQWs), in which high carrier mobility is combined with the possibility of controlling the electron density in each well independently. Recent experimental and theoretical studies of the ground state in DQWs have demonstrated that the coexistence of the spin and pseudospin degrees of freedom in a strongly correlated electron system can lead to the formation of radically new ferro- and antiferromagnetic phases [2], high-T_c superconductivity [3], and a two-component Wigner crystal [4]. New branches of charge and spin density excitations associated with the pseudospin degree of freedom can be observed in the excitation spectrum in the DQW electron system. It was shown that the degree of system asymmetry or unbalance is an essential parameter determining the ground and excited states of an electron system with a pseudospin. By increasing the unbalance of the system, one can smoothly vary the magnitude of the tunnel coupling between electron layers, which is accompanied by a qualitative modification of the electron spectrum in the DQW. Ideas have been advanced of using tunnel-coupled DQWs for creating the basic elements of a quantum computer, so-called cubites, and the dependence of the tunnel coupling on the DQW unbalance for creating quantum switches [5, 6].

The electron excitation spectrum in a DQW has been studied theoretically [7, 8] and experimentally [9, 10] in symmetric and asymmetric bilayers with weak tunnel coupling, in which the pseudospin degree of freedom can be disregarded. Two collective plasma modes—the acoustic and optical plasmons corresponding to the out-of-phase and in-phase oscillations of the charge density in the electron layers—were observed in inelastic light scattering spectra. The acoustic plasmon exhibits a linear dispersion at small quasi-momenta ($ka_B \ll 1$, where k is the quasi-momentum and a_B is the electron Bohr radius), and the optical plasmon exhibits a root behavior. It has been shown that a change of the symmetry of the bilayers only slightly affects the energy of the acoustic and optical phonons, which are principally determined by the magnitude of the quasi-momentum and the total electron density. In this work, excitations in tunnel-coupled electron bilayers are considered. Excitation branches associated with interlayer tunneling have been identified, and the dependence of their energies on the degree of DQW skewness has been investigated. The dispersion of these excitations has been measured. Based on the experimental results, a new spectroscopic method has been proposed for determining the Fermi energy of electrons and the degree of DQW skewness.

The investigations were carried out with a high-quality DQW structure grown by molecular-beam epitaxy. Two symmetrically doped GaAs quantum wells 200 Å thick were separated with a narrow $Al_{0.3}Ga_{0.7}As$ barrier 25 Å thick (Fig. 1). The electron mobility and density in each well were 10^6 cm^2 V^{-1} s^{-1} and 3.6×10^{11} cm^{-2},

respectively. The tunnel gap in the DQW (Δ_{SAS}) found from a self-consistent solution of the one-dimensional Schrödinger and Poisson equations was found to be 0.28 meV. The photodepletion effect was used for changing the electron density and balancing the DQW: under continuous photoexcitation with the photon energy exceeding the band-gap energy of the barrier, the ionized donors in the barrier were neutralized and the electron density in the DQW decreased [11, 12]. The mechanism of this phenomenon was considered in detail in [13]. Because the barrier absorption coefficient in the region of photodepleting radiation is high and quantum-well dopants are located in the barrier on different sides of the DQW, the well located closer to the heterostructure surface was depleted significantly stronger than the well located farther from the surface. Thus, it was possible to smoothly vary the degree of DQW skewness by selecting the power density of photodepleting radiation.

The energy difference between the two lowest subbands of dimensional quantization in the DQW (E_{10}, E_{20}) was determined from luminescence spectra in an external transverse magnetic field. For this purpose, the dependences of the energies of optical transitions from Landau levels of electrons in the conduction band to the valence band of the DQW on the magnitude of the magnetic field were measured. Then, these dependences were extrapolated to a zero magnetic field. The difference in the approximations for the optical transitions from E_{10} and E_{20} gives an approximate skewness parameter (Δ), which characterizes the unbalance of the DQW [12]. Though such a procedure is an effective method for extracting approximate DQW parameters, it, nevertheless, involves uncontrolled errors because of the complex structure of the valence band in the DQW and unknown Coulomb corrections in the energy of optical transitions. The Fermi energy of electrons in the DQW (E_F) was also determined from magnetoluminescence spectra by jumps in the chemical potential at integer occupation numbers [13].

The measurement of inelastic light scattering (ILS) spectra was performed using a tunable Ti/Sp laser with a photon energy of 1.545–1.570 eV and a characteristic value of the power density $W = 0.1–1$ W/cm^2. The measurements were carried out in an optical cryostat at a temperature of 4.2 K in the back-scattering geometry. A triple monochromator served as the spectral instrument, which, combined with a semiconductor detector with charge coupling, provided a spectral resolution of 0.02 meV. In order to determine the nature of spectral lines, the ILS spectra were recorded in two different polarization configurations of the pumping and scattered radiation. The polarization planes were parallel in one configuration and perpendicular in the other. The ILS signals from electron excitations of the charge and spin densities were detected in the parallel and perpendicular configurations, respectively [14]. The quasi-momentum of excitations was determined by the differ-
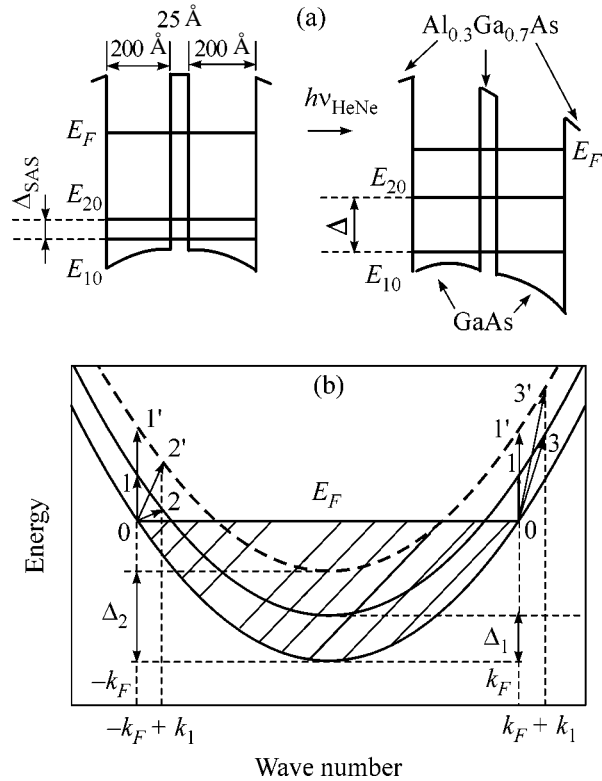

Fig. 1. Schematic diagram of (a) the DQW under study and (b) the electron spectrum in the two lowest size-quantized DQW subbands. Arrows show single-particle tunnel excitations for two values of the parameter of DQW skewness, Δ_1 and Δ_2.

ence in the momenta of the pumping and scattered photons, which were specified by the mutual configuration of the directions of the exciting radiation and the scattered ILS signal with respect to the normal to the sample surface. By varying the experimental configuration, the quasi-momentum of excitations can be varied in the range from 0.2 to 1.5×10^5 cm^{-1}. In order to separate the inelastic light scattering and hot luminescence lines, the experimental spectra were recorded at various energies of Ti/Sp laser radiation. The hot luminescence lines did not change their spectral positions under variation of the pumping photon energy, whereas the spectral positions of the inelastic light scattering lines followed the laser position. Thus, the Raman shift of the ILS lines remained constant.

Examples of ILS spectra in various polarization configurations and at various degrees of DQW skewness are shown in Fig. 2. The spectra exhibit one line, observed in the parallel configuration (AP). The AP energy is characterized by a linear dispersion. Based on the dispersion dependence and polarization measurements, the conclusion can be made that the AP line is associated with the acoustic plasmon. The dependence of the acoustic-plasmon energy on the carrier concen-
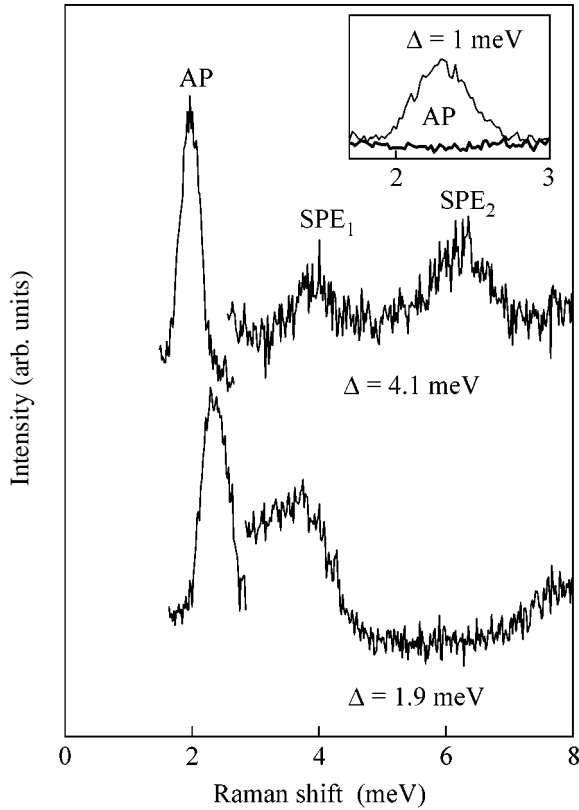
Fig. 2. Nonpolarized inelastic light scattering spectra at a fixed value of the transferred momentum $k = 8.6 \times 10^4$ cm^{-1} and two values of the parameter of skewness, $\Delta = 1.9$ meV and $\Delta = 4.1$ meV. The inset displays the ILS spectrum at $k = 8.6 \times 10^4$ cm^{-1} and $\Delta = 1$ meV in two polarization configurations, parallel (thin line) and perpendicular (thick line).

Fig. 3. Dependence of the energies of the *AP* and SPE$_{1, 2}$ lines on the degree of DQW skewness for two values of the transferred momentum, (a) $k = 11.7 \times 10^4$ cm^{-1} and (b) $k = 3.5 \times 10^4$ cm^{-1}. Black points indicate the *AP* line detected only in the parallel polarization configuration, and white points indicate lines detected in both configurations [16].

tration in the DQW and the quasi-momentum is described by the following equation [8]:

$$
\omega_{AP}^2 = \frac{e^2 k}{2\epsilon\epsilon_0 m^*}(n_1 + n_2)
$$
$$
\times \left[\frac{1}{2} - \frac{1}{2}\sqrt{1 - \frac{4n_1 n_2}{(n_1 + n_2)^2}(1 - e^{-2kd})} \right], \tag{1}
$$

where e is the electron charge, k is the quasi-momentum, $m^* = 0.067m_0$ is the effective electron mass in GaAs, ϵ is the dielectric constant of the medium (12.5 for GaAs), n_1 and n_2 are the electron densities in the two wells, and d is the effective distance between the wells. The phenomenological parameter d includes the nonlocality of the electron wave functions in the heterostructure growth direction. For the structures with sufficiently narrow quantum wells, the distance between the well centers (225 Å in our case) is a good approximation for d. The experimental and calculated behavior of the acoustic-plasmon energy as a function of the degree of DQW skewness is shown in Fig. 3 for two quasi-
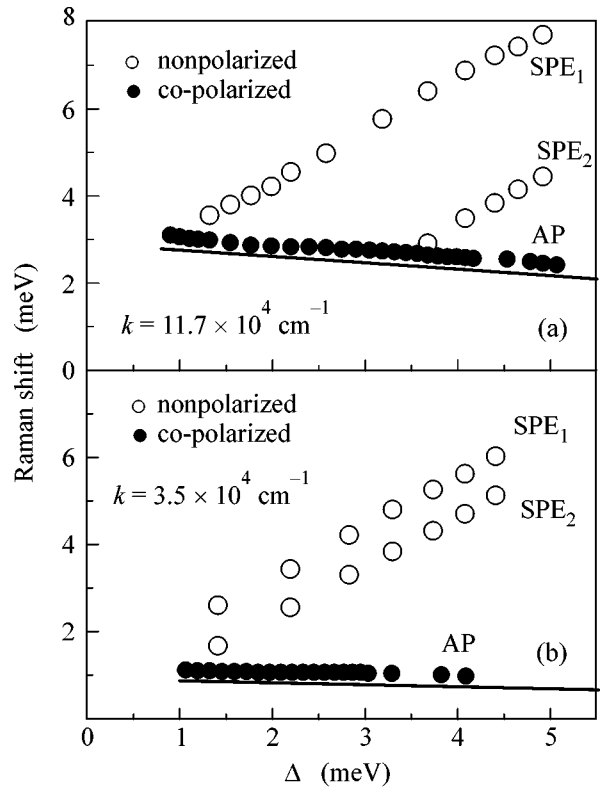
momentum values. The observed decrease in energy is in good agreement with theory.

In addition to the acoustic-plasmon line, two new spectral features are revealed in the ILS spectra. These features (SPE$_1$ and SPE$_2$ lines) have not been observed previously in the spectra of double quantum wells with weak tunnel coupling. Both lines have the same intensity in the crossed and parallel polarization configurations; therefore, these lines can be associated with single-particle excitations (the energies of single-particle excitations with and without spin flip are equal to each other). The dependences of the SPE$_1$ and SPE$_2$ energies on the degree of DQW skewness are qualitatively different from the similar dependence for the acoustic-plasmon line. Whereas the acoustic-plasmon energy decreases with decreasing total electron density, the energies of the SPE$_1$ and SPE$_2$ lines exhibit similar linear growth. The linear slope is almost independent of the electron density in the DQW and the transferred momentum, and the absolute energy splitting between SPE$_1$ and SPE$_2$ grows with increasing momentum (Fig. 3).

It may be concluded that the SPE$_1$ and SPE$_2$ lines are associated with single-particle tunnel excitations from the Fermi surface in the DQW. Such excitations result from the additional electron degree of freedom due to interwell tunneling. Consider the electron energy spectrum in the effective mass approximation in the two lower size-quantized subbands (Fig. 1b). The spectrum represents two parabolas separated by the value of the intersubband splitting, which coincides with the tunnel gap for a symmetric DQW. For each fixed value of the quasi-momentum, there exists a continuum of single-particle excitations from the Fermi surface of electrons of the lower size-quantized subband to the empty states above the Fermi surface of the upper subband. In the case of an asymmetric DQW, these excitations can be considered as interwell transitions. The excitation energies of the continuum coincide at a zero quasi-momentum (0 $\longrightarrow$ 1 transitions) but differ at nonzero quasi-momenta. The boundary energies of the continuum are reached for excitations whose quasi-momentum is either parallel or antiparallel to the momentum of the Fermi electrons in the lower size-quantized subband (0 $\longrightarrow$ 2 and 0 $\longrightarrow$ 3 transitions). As the quasi-momentum increases, the boundary energies vary in opposite directions. In turn, an increase in the degree of DQW skewness leads to an equal increase in the boundary energies of the continuum, which is observed experimentally for the SPE$_1$ and SPE$_2$ lines (Fig. 3). It is necessary to emphasize that, even though the excitations form a continuum, the density of initial and final states for the ILS resonances with boundary energies is higher than that for the other part of the continuum. Therefore, the ILS spectrum of the continuum consists of two lines with boundary energies and a spectral footing between them. This shape of the spectrum of tunnel single-particle excitations is in agreement with theoretical calculations [15].

The experimental dependence of the energies of the SPE$_1$ and SPE$_2$ lines on the quasi-momentum is shown in Fig. 4a for a fixed degree of skewness $\Delta = 4.1$ meV. The line energies vary linearly in opposite directions. The approximation at $k = 0$ gives the intersubband splitting $\Delta E_{12} = 5.4$ meV, and the slope of the linear dependences gives the Fermi velocity of electrons in the first size-quantized subband (~2.2×10^7 cm/s in this case). The accuracy of the determination of the Fermi velocity is improved if one takes the slope of the difference in the energies of the SPE$_1$ and SPE$_2$ lines rather than the slope of their energies (Fig. 4a). Correspondingly, the electron densities in the two lowest size-quantized subbands n_1 and n_2 are equal to

$$n_1 = (m^* v_F)^2 / 2\pi\hbar^2, \qquad (2)$$

$$n_2 = n_1 - m^* \Delta E_{12} / \pi\hbar^2. \qquad (3)$$

The differences in the electron densities measured by two experimental techniques (ILS and magnetoluminescence) are within the limits of experimental error.
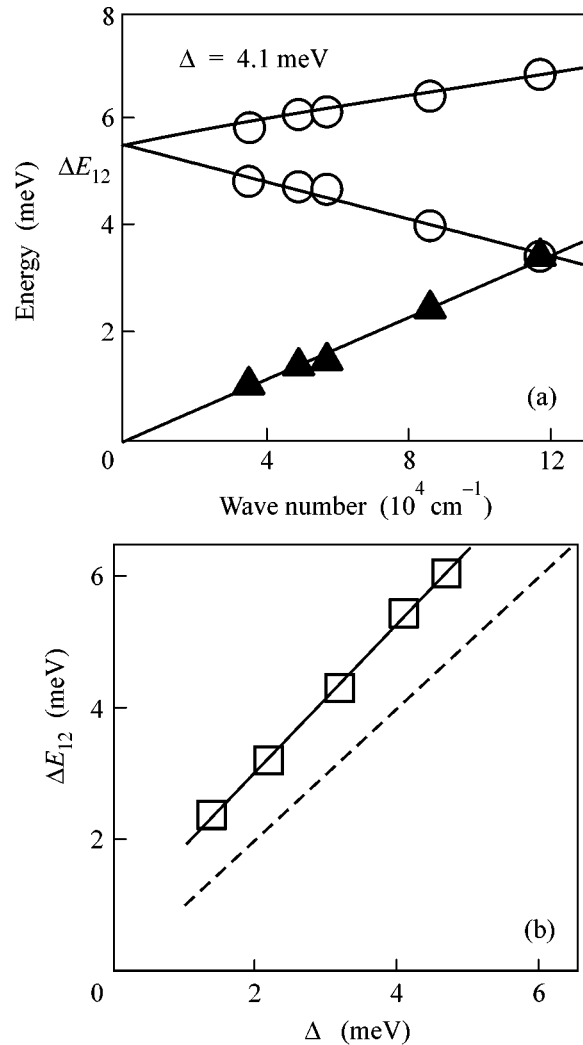
Fig. 4. (a) Dependence of the energy of the SPE$_{1,2}$ lines on the transferred momentum at $\Delta = 4.1$ meV (light points). Black triangles indicate the dependence of the difference in the SPE$_1$ and SPE$_2$ energies. Solid lines correspond to the extrapolation of the dependences to the region of small momenta. (b) Dependence of the parameter of skewness measured with the use of the ILS technique on the value of Δ obtained from magnetoluminescence spectra (points). Lines are drawn for convenience.

However, the error in the main characteristic of tunnel-coupled DQWs—the parameter of DQW skewness or unbalance—obtained from magnetoluminescence spectra can be large. At the same time, the absolute error weakly depends on the degree of DQW skewness; that is, the error of determining Δ at small degrees of skewness becomes of the order of Δ itself (Fig. 4b). The error in the parameter of skewness obtained from ILS spectra (ΔE_{12}) is determined in essence by only the magnitude of the smallest quasi-momentum reachable in the experiment. Thus, ΔE_{12} can be measured significantly more accurately than Δ. The ILS technique can be effectively used both for complete characterization

of the DQW unbalance (for the determination of the electron Fermi energy and the degree of skewness) and in combination with the experimentally simpler magnetoluminescence technique. In strongly asymmetric DQWs, when Δ becomes much higher than the Coulomb corrections in the optical transition energies, it is sufficient to use the magnetoluminescence technique alone.

REFERENCES

1. For a review, see *Perspectives in Quantum Hall Effect*, Ed. by S. Das Sarma and A. Pinczuk (Wiley, New York, 1997).

2. K. Moon, H. Mori, K. Yang, *et al.*, Phys. Rev. B **51**, 5138 (1995).

3. P. M. Plazman and T. Lenosky, Phys. Rev. B **52**, 10327 (1995).

4. H. C. A. Oji, A. H. MacDonald, and S. M. Girvin, Phys. Rev. Lett. **58**, 824 (1987).

5. C.-M. Hu and D. Heitmann, Appl. Phys. Lett. **77**, 1475 (2000).

6. A. Bertoni, P. Bordone, R. Brunetti, *et al.*, Phys. Rev. Lett. **84**, 5912 (2000).

7. S. Das Sarma and A. Madhukar, Phys. Rev. B **23**, 805 (1981).

8. R. Z. Vitlina and A. V. Chaplik, Sov. Phys. JETP **54**, 536 (1981).

9. D. S. Kainth, D. Richards, A. S. Bhatti, *et al.*, Phys. Rev. B **59**, 2095 (1999).

10. S. V. Tovstonog, L. V. Kulik, I. V. Kukushkin, *et al.*, Phys. Rev. B **66**, 241308 (2002).

11. I. V. Kukushkin, K. von Klitzing, K. Ploog, *et al.*, Phys. Rev. B **40**, 4179 (1989).

12. S. V. Tovstonog, I. V. Kukushkin, L. V. Kulik, *et al.*, JETP Lett. **76**, 511 (2002).

13. I. V. Kukushkin and V. B. Timofeev, Adv. Phys. **45**, 147 (1996).

14. A. Pinczuk, S. Schmitt-Rink, G. Danan, *et al.*, Phys. Rev. Lett. **63**, 1633 (1989); G. Abstreiter, R. Merlin, and A. Pinczuk, IEEE J. Quantum Electron. **22**, 1771 (1986).

15. J. K. Jain and S. Das Sarma, Phys. Rev. B **36**, 5949 (1987).

16. Collective excitations dominate in the region $\Delta < 1$ MeV in the spectrum. Experimental data and theoretical consideration of these excitations will be presented in the further publications.

Translated by A. Bagatur'yants

Experimental Scheme of Quantum Cryptography on the Nonorthogonal States with Time Shift and a Minimum Number of Optical Components

S. N. Molotkov

Institute of Solid State Physics, Russian Academy of Sciences, Chernogolovka, Moscow region, 142432 Russia
Faculty of Computational Mathematics and Cybernetics, Moscow State University,
Vorob'evy gory, Moscow, 119899 Russia
e-mail: molotkov@issp.ac.ru

A new scheme of experimental quantum cryptography on the nonorthogonal states is described. Nonorthogonality is achieved by the time shift of states in different messages. For this scheme to be efficient, it is sufficient to balance the arms of an interferometer at the receiver and transmitter ends to an accuracy of 1–2 cm. This is a fundamental advantage of this scheme over, e.g., the most developed cryptosystem based on phase coding, where the maximum transmission distance has been achieved. In the latter system, the arms of the interferometer need to be balanced with an accuracy of fractions of a micron for a distance of several tens of kilometers. © 2003 MAIK "Nauka/Interperiodica".

PACS numbers: 03.67.Dd; 03.67.Hk

Quantum cryptography, or, more precisely, quantum key distribution, allows the implementation of the absolute stable coding system with disposable keys [1, 2]. Secure key distribution between remote legitimate users is unconditionally ensured by the fundamental laws of nature rather than by the limited computational or technical capabilities of an eavesdropper. The unconditional security of quantum cryptography in the non-relativistic domain[1] is essentially based on the Heisenberg uncertainty principle or, more formally, on the impossibility of simultaneous measurements of the observables described by noncommuting operators. In terms of a pair of state vectors of a quantum system in which classical information about the key is encoded, this means that it is impossible to gain any information about the transmitted quantum states without their distortion if they are nonorthogonal [3]. Another fundamental quantum-mechanical exclusion closely connected with the exclusion mentioned above is the impossibility of copying an *a priori* unknown quantum state [4].

Several different prototypes of quantum cryptosystems based on optical fiber communication lines have been already created [5]. The maximum distances of secure key distribution over a quantum cryptosystem with so-called self-compensation by means of the Fara-

day optical fiber reflectors were achieved by Japanese (100 km) [6] and Swiss (67 km) [7] groups. The available prototypes of quantum cryptosystems are generally based on the following principles: (i) information about the key is encoded in the polarization degrees of freedom [8]; (ii) phase coding, where a Mach–Zehnder interferometer is used and information is encoded in the phase shift accumulated at the receiver and transmitter arms of the interferometer [9, 10]; (iii) quantum cryptosystems with frequency modulation of the carrier frequency [11]; and (iv) quantum cryptography on the coherent states with homodyne detection at the receiver end [12]. The most progress has been achieved in cryptosystems with phase coding and self-compensation by the Faraday reflectors [6, 7, 13]. It is rather difficult to implement the above cryptosystems. In this work, a new quantum cryptosystem is suggested which is, in my opinion, much simpler than the available systems and includes a minimum number of fiber optic components. The other parameters of this cryptosystem are no worse than the respective parameters of the most developed systems based on phase coding. The proposed variant can be conventionally called time shift quantum cryptography.

The idea of a cryptosystem is exceedingly simple. A pair of nonorthogonal single-photon states are used as information carriers. Each message with a duration of about $3T$ consists of one of the states 0 or 1 randomly sent through a communication channel (see Fig. 1). The states are certainly indistinguishable because they overlap (are nonorthogonal; Fig. 1). Therefore, an eavesdropper cannot distinguish between the states propagat-

---

[1] Hereinafter, nonrelativistic quantum cryptography is treated as cryptography that is based only on the geometric properties of vectors in the Hilbert state space and does not involve additional Special-Relativity properties, such as the existence of maximum velocity and massless information carriers (photons). For relativistic quantum cryptography, see, e.g., [17].
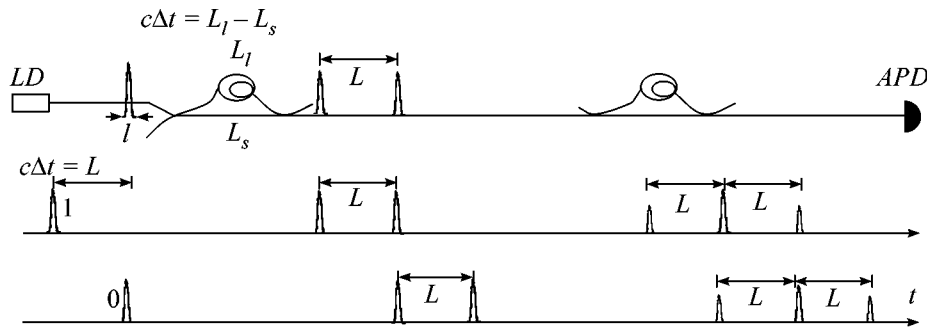
Fig. 1.

ing through the channel. Owing to the indistinguishability, any intrusion into the communication channel increases the flow of errors at the receiver end of the legitimate user [3]. The legitimate user makes measurements at the receiver end. The states are also certainly indistinguishable (with unit probability) for him. If a measurement outcome is obtained from the "back" part of state 1, the state is uniquely identified. However, the probability of this overcome is less than unity. The case of state 0 sent to the channel is similar. If a photodetector changes state in a time window where the states overlap certain distinction is impossible (a so-called inconclusive outcome). After a sufficiently long measurement run, the receiver retains only the outcomes in time windows where states do not overlap. Then, the users randomly open half of the outcomes through a public channel and check the correspondence at the receiver and transmitter ends. As can be shown, the probability of errors in unopened messages coincides with that in opened messages for a sufficiently long measurement run. Intrusion into the communication channel changes the statistics of measurement outcomes. If the probability of errors in the open part does not exceed a certain critical value, the use of correcting classical codes can correct errors in the unopen part with the guarantee that the resulting bit sequence (key) is the same for the legitimate users and is unknown for the eavesdropper [14–16].

Figure 1 shows the prototype of the quantum cryptosystem.

Input states are a pair of single-photon states shifted in time in each message (the insignificant polarization index is omitted):

$$|\varphi_0\rangle = \int d\hat{k}\tilde{\varphi}(\hat{k})\delta(\hat{k}^2)\theta(k_0)a^+(\hat{k})|0\rangle$$
$$= \int \frac{dk}{\sqrt{k}}\frac{\tilde{\varphi}(k, k_0 = |k|)}{\sqrt{k}}|k\rangle, \tag{1}$$

$$|\varphi_1\rangle = \int d\hat{k}e^{-i\hat{k}\hat{T}}\tilde{\varphi}(\hat{k})\delta(\hat{k}^2)\theta(k_0)a^+(\hat{k})|0\rangle$$
$$= \int \frac{dk}{\sqrt{k}}e^{-ikT}\frac{\tilde{\varphi}(k, k_0 = |k|)}{\sqrt{k}}|k\rangle, \tag{2}$$

where $\hat{k} = (k, k_0)$. The phase factor e^{-ikT} describes the relative shift in the state preparation time for different messages corresponding to 0 and 1 (see Fig. 1). We consider states propagating in the same direction. These states carry information between remote users. Denote $\varphi(k) \equiv \tilde{\varphi}(k, k_0 = |k|)/\sqrt{k}$. It is convenient to represent the states in the following coordinate–time representation, where the time shift reduces to the shift of the argument in the state amplitude:

$$|\varphi_0\rangle = \int_{-\infty}^{\infty} d\tau\varphi(\tau)|\tau\rangle, \quad |\varphi_1\rangle = \int_{-\infty}^{\infty} d\tau\varphi(\tau - T)|\tau\rangle, \tag{3}$$

$$\varphi(\tau) = \frac{1}{2\pi}\int_0^{\infty} dke^{-ik\tau}\varphi(k), \quad |\tau\rangle = \int_0^{\infty} \frac{dk}{\sqrt{k}}e^{ik\tau}|k\rangle, \tag{4}$$

where $\tau = x - t$. The amplitude of these states depends only on τ; i.e., if a measurement outcome is obtained at time t in the vicinity of the point $(x, x + dx)$, the same outcome can be obtained at time t' in the vicinity of the point $(x' - x + t, x' - x + t + dx)$.

The states have form (3) at the source exit before the interferometer arm at the transmitter end (see Fig. 1). The states are taken so that they have a characteristic time localization scale cl (below, the speed of light is taken to be $c = 1$); i.e., the normalization integral is almost completely saturated (i.e., is arbitrarily close to unity) in the region of size l:

$$\int_l d\tau|\varphi(\tau)|^2 \approx 1. \tag{5}$$

The spacetime localization scale must be much smaller than the time shift between states; i.e., $cl \ll T$.

Immediately after the source and before the entrance into the transmitting interferometer, short states do not overlap and are orthogonal. The interferometer arm at the transmitter end is represented by two optical fiber beam splitters, each heaving the working entry and "dummy" (vacuum) entry and exit, as well as the delay lines in one of the arms (Fig. 1). The long arm of the interferometer at the transmitter end is necessary for the extension of short input states with a length of about l to longer states consisting of two "halves" spaced by $L \gg l$. A time shift between two halves in each state should be equal to the time shift of states in different messages (see Fig. 1) in order to ensure the overlap of the front half of state 1 with the back half of state 0. At the exit of the interferometer arm and, correspondingly, the entry of the communication line, the states become nonorthogonal and certainly indistinguishable. At the working exit of the communication channel, state 0 has the form (except for the normalization factor and the common translation by the arm length)

$$|\varphi_0\rangle + |\varphi_0(T)\rangle$$

$$= \int_{-\infty}^{\infty} d\tau \varphi(\tau)|\tau\rangle + \int_{-\infty}^{\infty} d\tau \varphi(\tau - T)|\tau\rangle, \qquad (6)$$

where a half of the state is delayed by L. Correspondingly, state 1 has the form

$$|\varphi_1(T)\rangle + |\varphi_1(2T)\rangle$$

$$= \int_{-\infty}^{\infty} d\tau \varphi(\tau - T)|\tau\rangle + \int_{-\infty}^{\infty} d\tau \varphi(\tau - 2T)|\tau\rangle. \qquad (7)$$

Recall that the time shift (T) of states in different messages for 0 and 1 is equal to the path difference between the long and short arms of the interferometer at the transmitter end ($T = L = L_l - L_s$), so that the halves overlap. The overlap integral is equal to $\langle\varphi_0|\varphi_1\rangle = 1/2$ for $L \gg l$.

At the receiver end, two halves for each extended state are joined together by a unitary transformation, similarly to the input transformation. Except for the normalization factor and translation by the communication channel length, state 0 at the operating exit of the interferometer at the receiver end has the form

$$|\varphi_0\rangle + 2|\varphi_0(T)\rangle + |\varphi_0(2L)\rangle = \int_{-\infty}^{\infty} d\tau \varphi(\tau)|\tau\rangle$$

$$+ 2\int_{-\infty}^{\infty} d\tau \varphi(\tau - T)|\tau\rangle + \int_{-\infty}^{\infty} d\tau \varphi(\tau - 2T)|\tau\rangle. \qquad (8)$$

Correspondingly, state 1 has the form

$$|\varphi_1(T)\rangle + 2|\varphi_1(2T)\rangle + |\varphi_1(3T)\rangle$$

$$= \int_{-\infty}^{\infty} d\tau \varphi(\tau - T)|\tau\rangle + 2\int_{-\infty}^{\infty} d\tau \varphi(\tau - 2T)|\tau\rangle \qquad (9)$$

$$+ \int_{-\infty}^{\infty} d\tau \varphi(\tau - 3T)|\tau\rangle.$$

Roughly speaking, the three terms in Eqs. (8) and (9) have the following origin. The first term, e.g., in Eq. (8) corresponds to the case where both halves cover a long path L_l at both transmitter and receiver ends. The second term arises because the first half covers the long path L_l at the transmitter end and the short path L_s at the receiver end, while the second half covers the short path at the transmitter end and the long path at the receiver end. The third term corresponds to the case where both halves cover the short path at the receiver and transmitter ends.

We now discuss measurements at the receiver end. Any measurement of a single-photon quantum state is described by a certain unity decomposition in the single-particle state subspace:

$$I = \int_0^{\infty} \frac{dk}{k}|k\rangle\langle k| = \int_{-\infty}^{\infty} \mathcal{M}(d\tau). \qquad (10)$$

Here, the operator-valued measure

$$\mathcal{M}(d\tau) = \frac{d\tau}{2\pi}\left(\int_0^{\infty} \frac{dk}{\sqrt{k}} e^{-ik\tau}|k\rangle\right)\left(\int_0^{\infty} \frac{dk'}{\sqrt{k'}} e^{ik'\tau}\langle k'|\right) \qquad (11)$$

describes the probability of observation of a photon in the interval $(\tau, \tau + d\tau)$. Therefore, the probability of observation of a photon in the finite spacetime domain Ω (recall that the amplitude depends only on the difference $\tau = x - t$) is

$$\Pr(\tau \in \Omega) = \text{Tr}\{\mathcal{M}(\Omega)|\varphi\rangle\langle\varphi|\} = \int_{\Omega} d\tau |\varphi(\tau)|^2, \qquad (12)$$

$$\mathcal{M}(\Omega) = \int_{\Omega} \mathcal{M}(d\tau).$$

The space of outcomes at the receiver end consists of three time domains. The first domain covering the back front of state 1 (Fig. 1) is denoted by $\Omega_1 \sim l$. The time window covering only the head front of state 0 is denoted by $\Omega_0 \sim l$. The time window covering the time domain where states 0 and 1 overlap corresponds to the domain of inconclusive outcomes and is denoted as $\Omega_? \sim 2T$. The complement to the entire time axis is
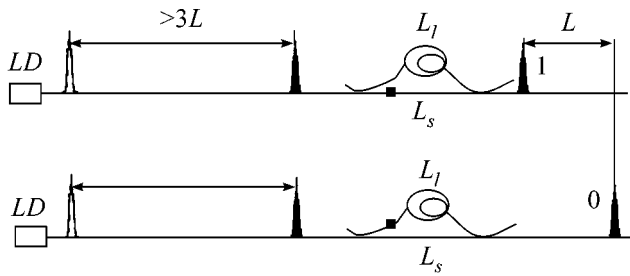
Fig. 2.

denoted by $\overline{\Omega} = (-\infty, \infty)/(\Omega_0 \cup \Omega_1 \cup \Omega_?)$. The unit decomposition has the form

$$I = \mathcal{M}(-\infty, \infty)$$
$$= \mathcal{M}(\Omega_0) + \mathcal{M}(\Omega_1) + \mathcal{M}(\Omega_?) + \mathcal{M}(\overline{\Omega}). \tag{13}$$

For the key distribution protocol, only the outcomes in the time windows $\Omega_{0,1}$ and $\Omega_?$ are important. The key generation protocol is a variant of the so-called BB92 protocol [3]. The legitimate user Bob at the receiver end retains only the conclusive outcomes in the time windows Ω_0 and Ω_1. The probabilities of such outcomes are determined by the operator-valued measures $\mathcal{M}(\Omega_0)$ and $\mathcal{M}(\Omega_1)$. These measures are similar to projectors $(\mathcal{P}_{0,1})$ in the BB92 protocol, which are orthogonal to states $|\varphi_{0,1}\rangle$ at the receiver end. However, measures (11) and (13) are not projectors, because the basis vectors $|\tau\rangle$ are nonorthogonal.

The protocol with the use of measurements described by decomposition (13) is similar to the original B92 protocol [3], where a measurement is described by the projectors $\mathcal{P}_0 = 1 - |\varphi_1\rangle\langle\varphi_1|$ and $\mathcal{P}_1 = 1 - |\varphi_0\rangle\langle\varphi_0|$. If the state $|\varphi_0\rangle$ is sent, the nonzero outcome occurs in the channel $\mathcal{P}_0$ with the probability $1 - |\langle\varphi_1|\varphi_0\rangle|^2$, and the outcome is always zero on the state $|\varphi_1\rangle$ (the probability of such outcome is zero). Similarly, if the state $|\varphi_1\rangle$ is sent, the nonzero outcome occurs in the channel $\mathcal{P}_1$ with the probability $1 - |\langle\varphi_1|\varphi_0\rangle|^2$, and the outcome is always zero on the state $|\varphi_0\rangle$. Only such nonzero outcomes are retained in the original B92 protocol. In our protocol, the operator-valued measures $\mathcal{M}(\Omega_0) \sim \mathcal{P}_1$ and $\mathcal{M}(\Omega_1) \sim \mathcal{P}_0$ are analogues of projectors (this indexing order seems to be more natural). Similarly to the B92 protocol, outcomes in the window $\mathcal{M}(\Omega_0)$ are nonzero only on the state $|\varphi_0\rangle$ and always zero on the state $|\varphi_1\rangle$. Conversely, if the state $|\varphi_1\rangle$ is sent, the nonzero outcome occurs only in the channel $\mathcal{M}(\Omega_1)$ and never occurs in the channel $\mathcal{M}(\Omega_0)$. Similarly to the B92 protocol, only outcomes in the channels $\mathcal{M}(\Omega_{0,1})$ are retained.

In addition to the above outcomes, the B92 protocol also includes zero outcomes in the channels $\mathcal{P}_0$ and $\mathcal{P}_1$ if the states $|\varphi_0\rangle$ and $|\varphi_1\rangle$ are sent, respectively. In our

protocol, such inconclusive outcomes correspond to the outcomes described by the projector-valued measure $\mathcal{M}(\Omega_?)$. We emphasize that the interferometer arm at the receiver end is fundamentally important for security.

Further, the protocol has the standard form. After a long measurement run, legitimate users retain only the conclusive outcomes. Then, part of the outcomes is randomly opened and the probability of errors is estimated. If this probability does not exceed a certain critical value (in nonrelativistic schemes, the limit is likely equal to $\approx 11\%$ [14–16]),[2] errors in the unopened part can be corrected by means of classical codes and the key can be further compressed (privacy amplification) to obtain the resulting secure key.

We present some numerical estimates for the parameters of the system and a brief comparison of this scheme with the most developed scheme based on phase coding. The main advantages of this scheme over other schemes are the simplicity of implementation and stability. This scheme does not require very accurate balance of the interferometer arms at the receiver and transmitter ends. Since $l \ll L$ from the very beginning, ideally accurate balance of arms between the receiver and transmitter ends of the interferometer is not required. In other words, the halves of a state at the receiver end need not be exactly joined into a state localized in the time window l. It is only necessary that the shift due to the difference in the arm lengths at the receiver and transmitter ends not exceed L in order to distinguish between 0 and 1 in the corresponding time windows. In particular, such is the case if the duration of an input pulse is $l \approx 1 \times 10^{-9}$ s = 1 ns and the shift of the halves is $T \approx 10$ ns. This shift arises due to the difference between the long and short paths in the interferometer arm at the transmitter end. This shift, when recalculated to the difference between the paths in optical fiber, is $L = T(c/n) \approx 200$ cm (n is the index of refraction of optical fiber). The junction of two halves at the receiver end requires the same difference in the arm lengths, with an accuracy of about the duration of an individual half. This difference, when recalculated to the length, is $l \approx 20$ cm. This is the principal advantage of this scheme over the phase-coding scheme, where the information is encoded in the phase difference, i.e., in the difference between the arm lengths of the interferometers at the transmitter and receiver ends. The accuracy of this difference must be equal to fractions of the wavelength; i.e., the difference between the arm lengths of the interferometer at a distance of several tens of kilometers must be equal to fractions of a micron. Otherwise, the scheme does not operate. Centimeter accuracy is sufficient for this scheme.

At the entry to this system, the overlap of two halves of states 0 and 1 in different messages must be ensured (see Fig. 1) for the states to be nonorthogonal. The necessary overlap of the halves of states 0 and 1 in different

---

[2] Note that the limiting error threshold in relativistic quantum cryptosystems is equal to 43.75% [17].

messages can be achieved if the original single-peak states are shifted by time T at the interferometer entry with an accuracy of ≈ 1–2 cm. Such a shift can be realized with an additional interferometer at the input (Fig. 2). In this case, a laser is turned on by a clock pulse generator with a constant relative pulse duration $>3T$ ($\approx 3T$ is the overall duration of one message). Then, a laser pulse is sent through a randomly chosen, long or short path of an additional beam splitter. The choice of the path is controlled by means of a computer cutoff, which blocks one of the arms of the additional interferometer. The path difference for different paths is equal to T. In this case, the required T-shifted single-peak states are obtained at the exit in different messages. Then, they are extended as was described above. The accuracy of the path lengths that ensures the overlap between the halves of states 0 and 1 is also sufficient and is on the order of 1 cm. When the additional interferometer is used, it is not necessary to adjust the distance between the laser pulses in different messages. It suffices to use an ordinary pulsed laser with a fixed pulse repetition rate.

REFERENCES

1. S. Wiesner, SIGACT News **15**, 78 (1983).
2. C. H. Bennett and G. Brassard, in *Proceedings of IEEE International Conference on Computer Systems and Signal Processes, Bangalore, India* (1984), p. 175.
3. C. H. Bennett, Phys. Rev. Lett. **68**, 3121 (1992).
4. W. K. Wootters and W. H. Zurek, Nature **299**, 802 (1982).
5. N. Gisin, G. Ribordy, W. Tittel, and H. Zbinden, quant-ph/0101098; Rev. Mod. Phys. **74**, 145 (2002).
6. H. Kosaka, A. Tomita, Y. Nambu, *et al.*, quant-ph/0306066.
7. D. Stucki, N. Gisin, O. Guinnard, *et al.*, quant-ph/0203118.
8. A. Muller, J. Breguet, and N. Gisin, Europhys. Lett. **23**, 383 (1993); A. Muller, H. Zbinden, and N. Gisin, Nature **378**, 449 (1995); Europhys. Lett. **33**, 335 (1996).
9. Ch. Marand and P. D. Tounsend, Opt. Lett. **20**, 1695 (1995); P. D. Tounsend, Nature **385**, 47 (1997); IEEE Photonics Technol. Lett. **10**, 1048 (1998).
10. R. Hughes, G. G. Luther, G. L. Morgan, and C. Simmons, Lect. Notes Comput. Sci. **1109**, 329 (1996); R. Hughes, G. Morgan, and C. Peterson, J. Mod. Opt. **47**, 533 (2000).
11. P. C. Sun, Y. Mazurenko, and Y. Fainman, Opt. Lett. **20**, 1062 (1995); Y. Mazurenko, R. Giust, and J. P. Goedgebuer, Opt. Commun. **133**, 87 (1997).
12. F. Grosshans, G. Van Assche, J. Wenger, *et al.*, Nature **421**, 238 (2003).
13. M. Martinelli, Opt. Commun. **72**, 341 (1989); J. Mod. Opt. **39**, 451 (1992).
14. D. Mayers and A. Yao, quant-ph/9802025.
15. E. Biham, M. Boyer, P. O. Boykin, *et al.*, quant-ph/9912053.
16. P. W. Shor and J. Preskill, quant-ph/0003004.
17. S. N. Molotkov, Zh. Éksp. Teor. Fiz. **124** (10) (2003) (in press); Pis'ma Zh. Éksp. Teor. Fiz. **78**, 194 (2003) [JETP Lett. **78**, 162 (2003)].

Translated by R. Tyapaev

Active Suppression of Dephasing in Josephson-Junction Qubits[¶]

D. V. Averin[1] and R. Fazio[2]

[1] Department of Physics and Astronomy, SUNY Stony Brook, Stony Brook, NY 11794-3800, USA
[2] NEST-INFM & Scuola Normale Superiors, 56126 Pisa, Italy
Received September 22, 2003

Simple majority code correcting k dephasing errors by encoding a qubit of information into $2k + 1$ physical qubits is studied quantitatively. We derive an equation for quasicontinuous evolution of the density matrix of encoded quantum information under the error correction procedure in the presence of correlated dephasing noise. A specific design of a Josephson-junction nanocircuit implementing this scheme is suggested. © 2003 MAIK "Nauka/Interperiodica".

PACS numbers: 03.67.Lx; 03.67.Pp; 85.25.Cp

Josephson qubits are among the most promising devices to implement solid-state quantum computation [1, 2]. Quantum manipulations of individual [3–9] and coupled [10] qubits has been demonstrated experimentally. At present, an important task is to develop strategies to minimize the effects of decoherence on the dynamics of the qubit systems. Error-avoiding schemes suggested for reduction of decoherence either employ symmetries of the qubit–environment interaction to create areas of the Hilbert space not affected by decoherence [11, 12] or use rapid random dynamic perturbations of the system to average out the effects of external noise [13, 14]. Both approaches appear to be problematic for the solid-state qubits where noise typically does not have any particular symmetry and its correlation time is short. This leaves error-correction as the main strategy for suppression of decoherence in solid-state qubits. In this work, we suggest an implementation of one of the basic error-correction algorithms for the suppression of dephasing errors (which can be expected to be the dominant type of errors in solid-state circuits—see, e.g., [9]), and develop its quantitative description. Our implementation employs Josephson-junction qubits that combine charge and flux dynamics [6, 15, 16], and requires only a small number of qubit transformations to operate.

An interesting feature of the scheme considered in this work is the possibility of developing its detailed quantitative description within the realistic model of the qubit-environment interaction. Most importantly, we have analyzed the effect of the correlations in the noise acting on different qubits. While discussions of the error-correction rely typically in an essential way on independent noise models, environments of the solid-state qubits can be to a large degree correlated because of the finite distance between qubits in a circuit. A clear illustration of this is provided by the background charge fluctuations that are the main source of dephasing in charge qubits [3, 6, 10, 17]. Long-range nature of the Coulomb interaction creates noise correlations by coupling the qubits to the same charge fluctuators.

We specifically consider the problem of a "quantum memory." The task here is to preserve the stationary state of the qubit in the presence of dephasing noise. The Hamiltonian of the qubit register then contains only the coupling to the environment. Within the standard oscillator model of the reservoir [18–21] this coupling is:

$$H = \sum_j \sigma_z^{(j)} \xi_j,$$

$$\xi_j = \sum_{m, \omega} [\lambda_{m, j}(\omega) a_{m, \omega} + \lambda_{m, j}^*(\omega) a_{m, \omega}^\dagger].$$

$$(1)$$

Here we assumed several independent ensembles of environmental oscillators (numbered by m) as required to model different profiles of spatial correlations of random forces ξ_j. The index $j = 1,\ldots, N$ in (6) labels the qubits, and coefficients $\lambda_{m, j}(\omega)$ are coupling constants of the qubit j to the oscillators of reservoir m in the mode ω and creation/annihilation operators $a_{m, \omega}, a_{m, \omega}^\dagger$. Time evolution of the "qubits + environment" system is described conveniently in the interaction representation, and the evolution operator $U(t)$ is:

$$U(t) = \exp\left\{-i \sum_j \varphi_j(t) \sigma_z^{(j)}\right\} U_r(t),$$

$$U_r(t) = \exp\left\{i \sum_{m, \omega} \frac{\omega t - \sin \omega t}{\omega^2} \left| \sum_j \lambda_{m, j} \sigma_z^{(j)} \right|^2\right\}.$$

$$(2)$$

[¶] This article was submitted by the authors in English.

The first term in $U(t)$ represents fluctuating phases $\varphi_j(t)$ of the qubit basis states induced by the environmental forces $\xi_j(t)$: $\varphi_j(t) = \int_0^t \xi_j(t')dt'$. The second term, $U_r(t)$, results from the renormalization of the qubit parameters by the qubit–environment interaction. To see this more explicitly, we note that the sum over frequencies ω in this exponent has a natural cut-off at large frequencies $\omega \simeq \tau_c^{-1}$, where τ_c is the time scale at which environment forces acting on different qubits are correlated. For weak decoherence, we are interested in time scales much larger that τ_c. In this regime, the phase represented by $U_r(t)$ is dominated by the term that grows linearly with t, and can be viewed as arising from the renormalization of the qubit energy. Equation (7) shows that such a renormalization includes a shift of the total energy of the register and a term which induces an effective qubit–qubit interaction. The total energy shift is irrelevant as long as we consider an individual register. Neglecting it, we see that $U_r(t)$ results from the Hamiltonian evolution with the Hamiltonian

$$H_r = -\sum_{j,\,j'} V_{jj'}\sigma_z^{(j)}\sigma_z^{(j')},$$

$$V_{jj'} = 2\mathrm{Re}\sum_{m,\,\omega}(\lambda_{m,\,j}^{(\omega)}\lambda_{m,\,j}^{(\omega)*}/\omega). \tag{3}$$

In dropping the oscillatory term, one should be careful for the convergence of the sum over frequencies. In the case of an Ohmic bath, for example, this can be done and leads to an effective interaction which scales with the dissipation strength and with the cut-off of the environmental modes. The qubit–qubit interaction strength $V_{jj'}$ is non-vanishing only if the same reservoir m couples to more than one qubit, so that the reservoir forces ξ_j at different qubits are correlated. The time evolution with the Hamiltonian H_r, and, more generally, the evolution operator U_r in Eq. (7), represent the deterministic part of the qubit evolution induced by the qubit–reservoir interaction. Nevertheless, it is more appropriate to still treat it as dephasing, because $V_{jj'}$ are unknown and, in general, incommesurate quantities.

The time evolution of the density matrix $\rho(t)$ of the qubit register is obtained from Eq. (7) through the relation $\rho(t) = \mathrm{Tr}_{env}\{U^\dagger(t)\sigma(0)U(t)\}$, where σ is the total density matrix of the "qubits + environment" system. The environment will dephase the qubits if they are prepared initially in a state $\rho(0)$ that is uncorrelated with the state of the environment, $\sigma(0) = \rho_{env}\rho(0)$. Assuming that the environment is in thermal equilibrium at temperature Θ, and no error correction procedure is

applied, using the standard property of the Gaussian noise we get:

$$\rho(t) = \exp\left\{-\frac{1}{2}\sum_{j,\,j'}\langle\varphi_j(t)\varphi_{j'}(t)\rangle(\sigma_z^{(j)} - \bar{\sigma}_z^{(j)})\right.$$
$$\left.\times(\sigma_z^{(j')} - \bar{\sigma}_z^{(j')})\right\}U_r^\dagger(t)\rho(0)U_r(t). \tag{4}$$

Here, we introduced the convention that the bar over σ_z operators means that they act on ρ from the right. Qualitatively, Eq. (4) shows that the matrix elements of ρ that are farther away from the diagonal in the σ_z basis decay faster. The diagonal elements (on which $\sigma_z - \bar{\sigma}_z = 0$) remain constant. In the case of one physical qubit, Eq. (4) gives $\rho(t) = e^{-\langle\varphi^2(t)\rangle(1 - \sigma_z\bar{\sigma}_z)}\rho(0)$, i.e., the off-diagonal elements of ρ are suppressed with time as $e^{-2\langle\varphi^2(t)\rangle} \equiv e^{-P(t)}$. If the environment density of states is ohmic, i.e., $\sum_{m,\,\omega}|\lambda_m(\omega)|^2\ldots = g\int_0^\infty d\omega\,\omega e^{-\omega\tau_0}\ldots$, direct evaluation for $\Theta \ll 1/\tau_0$ gives: $P(t) = 2g\ln[\sinh(\pi t\Theta)/\pi\tau_0\Theta]$. At large t, when the random force ξ appears δ-correlated, $P(t)$ reduces to $P(t) = \Gamma t$, where $\Gamma = 2\pi g\Theta$ is the dephasing rate.

One can reduce the effective dephasing rate by the encoding that corrects the phase errors [22, 23]. Generalized to k errors, this encoding is:

$$\alpha|0\rangle + \beta|1\rangle \longrightarrow \alpha\underbrace{|++\ldots+\rangle}_{2k+1} + \beta\underbrace{|--\ldots-\rangle}_{2k+1}. \tag{5}$$

In Eq. (5), a bit of quantum information is encoded in the state of the $2k + 1$ physical qubits, and the $|\pm\rangle$ states of each of these qubits are obtained through the Hadamard transform $\hat{H}$ (the $\pi/2$-rotation around the y axis) from the $|0, 1\rangle$ states. All of the σ_z operators in the time evolution, Eq. (7), are changed by $\hat{H}$: $\hat{H}\sigma_z\hat{H} = \sigma_x$, so that for the states on the right-hand-side of Eq. (5), the dephasing looks like transitions between the $|\pm\rangle$ states of each qubit, and can be directly detected by measurements in this basis and corrected by applying simple pulses returning the qubit to the initial state. The error-detecting measurements, however, should not destroy the quantum information encoded in the state (5), i.e., it should not distinguish the α and β parts of this state. This condition is not satisfied by measurements on individual qubits but can be satisfied by measurements on pairs of the nearest-neighbor qubits comparing their states. Despite the apparent complexity of this scheme, it has quite natural implementation in the Josephson-junction qubits—see figure.

To describe this process quantitatively, we assume that its measurement/correction part can be done on a time scale that is much shorter than the one set by char-

2k + 1
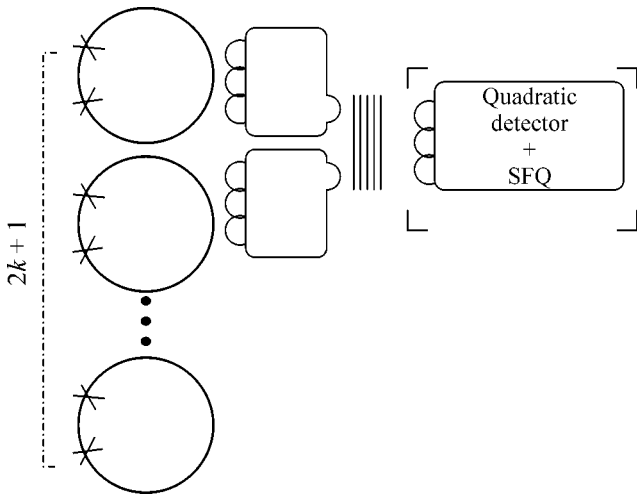
Schematics of the Josephson-junction circuits implementing suppression of dephasing. Crosses denote tunnel junctions, the electrodes between them act as charge qubits. Monitored currents in the nearest-neighbor loops enclosing qubits allow one to detect dephasing errors.

acteristic dephasing rate Γ. Different terms in the environment-induced evolution of the encoded state, Eq. (5), during the time interval T between the successive application of the "measurement + correction" operations can be conveniently classified by the number of qubits flipped during this time interval. In the relevant regime of sufficiently short T: $P(T) \ll 1$, the probability amplitude of these terms decreases rapidly when this number increases. If we keep only the terms that flip up to k qubits, we see directly from Eq. (7) that the time evolution at this level of accuracy (denoted by $U_k(T)$) preserves the superposition of the α and β parts of the encoded state:

$$ U_k(T)[\alpha|\oplus\rangle + \beta|\ominus\rangle] = \sum_q [\alpha|\psi_q\rangle + \beta\hat{R}|\psi_q\rangle]u_q. \quad (6) $$

Here, index q runs over 2^{2k} different register states obtained from the state $|\oplus\rangle \equiv |+\ldots+\rangle$ by flipping up to k qubits, u_q are the probability amplitudes of these states, $\hat{R}|\psi_q\rangle$ denotes the state $|\psi_q\rangle$ with all $2k + 1$ qubits inverted, and $|\ominus\rangle \equiv |-\ldots-\rangle$.

The measurements that compare the qubit states in all pairs of the nearest-neighbor qubits do not distinguish states $|\psi_q\rangle$ and $\hat{R}|\psi_q\rangle$, and therefore also preserve the superposition of the α and β terms in Eq. (6). The 2^{2k} different outcomes ("equal" or "different") of the $2k$-type measurements distinguish all terms with different q in Eq. (6) and enable one to decide what qubits were flipped during the time interval T. Application of the correcting pulses should then bring the state of the qubit register back to its initial form, Eq. (5), so that the encoded quantum state does not change in this approx-

imation. The residual evolution of the encoded state is associated with the possibility that the environment flips more that k different qubits; for $P(T) \ll 1$—precisely $k + 1$ qubits. Following the same steps as above, we see that when $k + 1$ qubits are flipped, the measurement/correction cycle interchanges the α and β weights in the encoded state (5), with probability p. Since p is small, $p \ll 1$, the encoded state changes substantially only on a time scale larger than the period T of one error-correction cycle, and its evolution on this scale can be conveniently described by the continuous equation for the density matrix $\rho^{(c)}$ in the basis of $|\oplus\rangle$ and $|\ominus\rangle$ states:

$$ \dot{\rho}_{++}^{(c)} = \frac{\gamma_k}{2}(\rho_{--}^{(c)} - \rho_{++}^{(c)}), \quad \dot{\rho}_{+-}^{(c)} = \frac{\gamma_k}{2}(\rho_{-+}^{(c)} - \rho_{+-}^{(c)}). \quad (7) $$

Here $\gamma_k \equiv 2p/T$ is the effective dephasing rate of the encoded quantum information, the superscript (c) indicates that $\rho^{(c)}$ is the reduced density matrix in the presence of error correction. Thus, our error-correcting procedure replaces the dephasing in the individual physical qubit with the dephasing of encoded quantum information at a smaller rate. Indeed, if one writes Eqs. (7) in the rotated basis $|\oplus\rangle \pm |\ominus\rangle$, they explicitly acquire the form characteristic for pure dephasing: constant diagonal elements of the density matrix and decay of the off-diagonal elements with the rate γ_k. The dephasing rate γ_k can be calculated from the evolution operator (7).

For $k = 1$, when the relevant errors flip 2 out of 3 qubits, we get:

$$ \gamma_1 = \frac{2}{T}\sum_{j > j'} (T^2 V_{jj'}^2 + 2\langle \varphi_j(T)\varphi_{j'}(T)\rangle^2 $$
$$ + \langle \varphi_j^2(T)\rangle\langle \varphi_{j'}^2(T)\rangle). $$

The first two terms in this expression represent the contribution to dephasing from noise correlations at different qubits, while the last term exists also for uncorrelated noise. If the noise is δ-correlated in tune, γ_1 reduces to $\gamma_1 = T\sum_{j > j'} (2V_{jj'}^2 + \Gamma_{jj'}^2 + \Gamma_j\Gamma_{j'}/2)$, where Γ_j is the dephasing rate in the jth qubit, and $\Gamma_{jj'}$ is introduced through $2\langle \varphi_j(t)\varphi_{j'}(t)\rangle = \Gamma_{jj'} t$.

If the dephasing forces at different qubits are uncorrelated, the encoded dephasing rate can be easily calculated for arbitrary k:

$$ \gamma_k = \frac{1}{2^k T}\sum_{j_1 > j_2 > \ldots E > j_{k+1}} P_{j_1}(T)P_{j_2}(T)\ldots P_{j_{k+1}}(T), \quad (8) $$

and one sees that γ_k decreases exponentially with the "degree of encoding" k. When the probabilities $P(T)$ of dephasing errors in individual qubits can be expressed through the dephasing rate Γ, Eq. (8) reduces to $\gamma_k =$

$\Gamma(\Gamma T)^k(2k+1)!/(2^k k!(k+1)!)$, if Γ is the same for all qubits.

Exponential suppression of γ_k with k is limited in the scheme considered above by possible imperfections of the measurement/correction operations. The most important is direct dephasing of the encoded states by measurements, which, in contrast to correction steps, need to be performed each period T. For example, one of the specific nonidealities of measurement detectors that leads to direct dephasing of the state is the residual linear response coefficient of the quadratic detectors needed to perform pair-wise comparison of the qubit states—see Eq. (10) below. Linear terms couple the detector directly to the $|\pm\rangle$ states of individual qubits and introduce finite phase shifts between them. Since the number of required measurements is proportional to k, the rate of introduced dephasing should also be proportional to k, and can be denoted as $\bar{\gamma}k$. The effect of this dephasing on the evolution of encoded quantum information is then described by adding the usual dephasing term to the equation for the off-diagonal element of the density matrix $\rho^{(c)}$(7):

$$\dot{\rho}_{+-}^{(c)} = \frac{\gamma_k}{2}(\rho_{-+}^{(c)} - \rho_{+-}^{(c)}) - \bar{\gamma}k\rho_{+-}^{(c)}. \qquad (9)$$

Qualitatively, the two types of dephasing processes in Eq. (9) have a similar effect of suppressing the fidelity of the encoded state, but depend differently on k. The optimum degree of encoding is estimated crudely by minimizing the total dephasing rate: $k_{\mathrm{opt}} \sim \ln(\bar{\gamma}/\Gamma)/\ln(T\Gamma)$. One obvious result of this optimization is that for the considered scheme of the dephasing suppression to make sense, the dephasing introduced by imperfections of the correcting procedure should be much weaker than the original qubit dephasing Γ.

This condition can be satisfied in Josephson-junction qubits, where the dynamics of magnetic flux characterized by longer coherence times (at least tens of nanoseconds—see, e.g., [9]) can be used to suppress dephasing in charge-based qubits. Charge qubits have quite short decoherence times, ~1 ns [3, 10], limited by the background charge fluctuations, but offer some advantages, e.g., demonstrated simplicity of qubit–qubit coupling [10]. Therefore, it would be of interest to use the approach discussed in this work to suppress the dephasing of charge degrees of freedom with the help of controlled flux dynamics. A sketch of the possible setup achieving this is shown in figure. Its main elements are the charge qubits, formed by two small tunnel junctions in series, enclosed in small superconducting loops threaded by magnetic flux Φ equal to half of the magnetic flux quantum Φ_0. It can be shown [16] that the current in each loop represents the σ_x component of the qubit dynamics, and its monitoring therefore measures the qubit in the σ_x basis as needed for detection of the dephasing errors. Comparison of the states of the nearest-neighbor qubits can be achieved not by directly

measuring the currents in the loops, but the square of the difference (or of the sum) between the currents. Such a quadratic detection measures the product operator $\sigma_x^{(j)}\sigma_x^{(j+1)}$:

$$(\sigma_x^{(j)} \pm \sigma_x^{(j+1)})^2 = 2(1 \pm \sigma_x^{(j)}\sigma_x^{(j+1)}), \qquad (10)$$

and provides information on whether the states of the two qubits are the same or not without measuring them. Quadratic measurements can be realized by the usual magnetometers but operated at a point where the linear response coefficient vanishes. These measurements, subsequent classical calculations, and the application of correction pulses, can be done with sufficient frequency by existing "SFQ" superconductor electronics compatible with the qubits [24].

In summary, we suggested a simple scheme of performing basic error-correction in Josephson-junction qubits. The scheme suppresses dephasing errors and can be analyzed quantitatively within the realistic model of the environment, including the possibility of noise correlations at different qubits. If the errors introduced by the correction procedure are negligible, the residual dephasing rate for the encoded quantum information decreases exponentially with the degree of encoding.

REFERENCES

1. D. V. Averin, Fortschr. Phys. **48**, 1055 (2000).

2. Yu. Makhlin, G. Schön, and A. Shnirman, Rev. Mod. Phys. **73**, 357 (2001).

3. Y. Nakamura, Yu. A. Pashkin, and J. S. Tsai, Nature **398**, 786 (1999).

4. J. R. Friedman, V. Patel, W. Chen, *et al.*, Nature **406**, 43 (2000).

5. C. H. van der Wal, A. C. J. ter Haar, and F. K. Wilhelm, Science **290**, 773 (2000).

6. D. Vion, A. Aassime, A. Cottet, *et al.*, Science **296**, 886 (2002).

7. Y. Yu, S. Y. Han, X. Chu, *et al.*, Science **296**, 889 (2002).

8. J. M. Martinis, S. Nam, J. Aumentado, and C. Urbina, Phys. Rev. Lett. **89**, 117901 (2002).

9. I. Chiorescu, Y. Nakamura, C. J. P. M. Harmans, and J. E. Mooij, Science **299**, 1869 (2003).

10. Yu. A. Pashkin, T. Yamamoto, O. Astafiev, *et al.*, Nature **421**, 823 (2003).

11. P. Zanardi and M. Rasetti, Phys. Rev. Lett. **79**, 3306 (1997).

12. L. Viola, E. M. Fortunato, M. A. Ptavia, *et al.*, Science **293**, 2059 (2001).

13. L. Viola, E. Knill, and S. Lloyd, Phys. Rev. Lett. **82**, 2417 (1999).

14. L.-A. Wu and D. A. Lidar, Phys. Rev. Lett. **88**, 207902 (2002).

15. J. R. Friedman and D. V. Averin, Phys. Rev. Lett. **88**, 050403 (2002).

16. D. V. Averin, Phys. Rev. Lett. **88**, 207901 (2002).

17. E. Paladino, L. Faoro, G. Falci, and R. Fazio, Phys. Rev. Lett. **88**, 228304 (2002).

18. U. Weiss, *Quantum Dissipative Systems*, 2nd ed. (World Sci., Singapore, 1999).

19. W. G. Unruh, Phys. Rev. A **51**, 992 (1995).

20. G. M. Palma, K.-A. Suominen, and A. K. Ekert, Proc. R. Soc. London, Ser. A **452**, 567 (1996).

21. J. H. Reina, L. Quiroga, and N. F. Johnson, Phys. Rev. A **65**, 032326 (2002).

22. S. L. Braunstein, quant-ph/9603024.

23. M. A. Nielsen and I. L. Chuang, *Quantum Computation and Quantum Information* (Cambridge Univ. Press, Cambridge, 2000), Chap. 10.

24. V. K. Semenov and D. V. Averin, IEEE Trans. Appl. Supercond. **13**, 960 (2003).

Nonlinear-Laser Effects in χ(3)- and χ(2)-Active Organic Single Crystals¶

A. A. Kaminskiĭ

Institute of Crystallography, Russian Academy of Sciences, Moscow, 119333 Russia
e-mail: kaminalex@mail.ru
Received October 9, 2003

The process of stimulated Raman scattering (SRS) allows one to convert laser emission wavelength of crystals, providing suitable molecular or lattice modes which contribute to third-order nonlinear optical susceptibility. Renewed interest in this field emerged because of the discovery of SRS in crystals that contain molecular units exhibiting Raman active modes. Particularly, organic nonlinear optical crystals used so far for frequency doubling and third harmonic generation seem to have a great potential for SRS application. This review paper reported same results on efficient SRS lasing effects that were discovered recently in organic crystals. © *2003 MAIK "Nauka/Interperiodica".*

PACS numbers: 42.70.Hj; 42.65.Dr; 42.70.Mp; 42.70.Jk

1. INTRODUCTION

Stimulated Raman scattering (SRS) in optical crystalline materials is of topical interest in modern solid-state laser physics. The SRS process allows one to shift laser emission wavelength and compress laser pulses, and can improve the spatial quality of laser beams as well as the contrast between peak and background intensities of ultrashort laser pulses, etc. In the last two decades, solid-state SRS science and technology have become more widespread (see, e.g. [1–3]). Growth in the activity has been made possible by the discovery of several new SRS-active inorganic crystals, including a successful application given by nano- and picosecond Raman lasers generating specific and otherwise hard-to-reach wavelengths in a wide spectral range [3–5]. Among other current applications of new Raman lasers, remote sensing of the atmosphere is of great interest [6]. Furthermore, crystalline lasers using SRS conversion process are very attractive for medical treatments and for laser guide stars in precise astronomical experiments (see, e.g. [7]).

New generation of Raman lasers requires crystalline materials providing large frequency shifts up to 3000 cm^{-1} or more. Unfortunately, with inorganic crystals such shifts are difficult if not impossible to realize due to their ionic structure. As can be seen from Table 1, among known SRS-active inorganic crystals, the largest Raman frequency shift has been measured for calcite ($CaCO_3$) [8] and lithium formate monohydrate ($LiHCOO \cdot H_2O$) [9]. During the last three years we have been discovered efficient SRS effects in several organic crystals, many of them (as indicated in Table 2) possessing frequency shifts as large as 3000 cm^{-1} and

relatively high steady-state Raman gain coefficients for the first Stokes generation. A number of them also offer both nonlinear $\chi^{(3)} + \chi^{(2)}$ susceptibilities, which may give rise to diverse parametric generation acts. It is of interest that in the field of nonlinear optical organic crystals attention has mainly been directed towards second and third harmonic generation (see, e.g., [25, 26]), but not towards SRS. This is rather astonishing, because the bright optical $\chi^{(3)}$ effect, such as the SRS, was discovered in organic liquid (nitrobenzene) in the 60s—at just the beginning of the laser era [27].

The present short review represents some main results on SRS spectroscopy of organic crystals—the newer family of nonlinear laser solid-state materials, and on new self-frequency conversion parametric effects observed in them under ultrashort laser excitation.

2. THE STEADY-STATE SRS

The nonlinear frequency conversion effects (SHG, SRS, etc.) are possible in any optically transparent crystals in which the electron cloud of atoms tend to be polarized, i.e., the refractive index *n* is a function of the electric-field strength **E** of the propagating laser emission through these crystals (see, e.g. [28–30])

$$n(\mathbf{E}) = n_0 + n_1\mathbf{E} + n_2\mathbf{E}^2 + \dots. \qquad (1)$$

Here, n_0 is the "linear" refractive index, and n_1, n_2 and so on are the higher-order coefficients of $n(\mathbf{E})$. A dielectric polarization vector **P**, defined as the electric dipole moment of the optical crystal, can be described phenomenologically in terms of the nonlinear susceptibil-

---
¶ This article was submitted by the author in English.

Table 1. Selected easily accessible inorganic SRS-active crystals with laser frequency shift (ω_{SRS}) more than 900 cm^{-1} [2, 3, 5, 8–11]*

Crystal	Space group		Nonlinearity (class)	SRS-active vibration mode with the largest frequency shift (cm^{-1})
	notation	number		
LiHCOO · H$_2$O	C_{2v}^9–$Pna2_1$	(No. 33)	$\chi^{(2)} + \chi^{(3)}$ (polar)	≈1372
NaClO$_3$	T^4–$P2_13$	(No. 198)	$\chi^{(2)} + \chi^{(3)}$	≈936
NaY(WO$_4$)$_2$	C_{4h}^6–$I4_2/a$	(No. 88)	$\chi^{(3)}$	≈914
KH$_2$PO$_4$(KDP)	D_{2d}^{12}–$I\bar{4}_22d$	(No. 122)	$\chi^{(2)} + \chi^{(3)}$	≈915
KAl(SO$_4$)$_2$ · 12H$_2$O	T_h^6–$Pa3$	(No. 205)	$\chi^{(3)}$	≈989
α-KY(WO$_4$)$_2$	C_{2h}^6–$C2/c$	(No. 15)	$\chi^{(3)}$	905
α-KGd(WO$_4$)$_2$	C_{2h}^6–$C2/c$	(No. 15)	$\chi^{(3)}$	901
α-KYb(WO$_4$)$_2$	C_{2h}^6–$C2/c$	(No. 15)	$\chi^{(3)}$	≈907
α-KLu(WO$_4$)$_2$	C_{2h}^6–$C2/c$	(No. 15)	$\chi^{(3)}$	907
CaCO$_3$	D_{3d}^6–$R3c$	(No. 167)	$\chi^{(3)}$	≈1085
Ca$_4$Gd(BO$_3$)$_3$O	C_s^3–Cm	(No. 8)	$\chi^{(2)} + \chi^{(3)}$ (polar)	933
CaWO$_4$	C_{4h}^6–$I4_2/a$	(No. 88)	$\chi^{(3)}$	≈908
ZnWO$_4$	C_{2h}^4–$P2/c$	(No. 13)	$\chi^{(3)}$	907
Sr$_5$(PO$_4$)$_3$F	C_{6h}^2–$P6_3/m$	(No. 176)	$\chi^{(3)}$	950
SrWO$_4$	C_{4h}^6–$I4_2/a$	(No. 88)	$\chi^{(3)}$	922
Ba(NO$_3$)$_2$	T_h^6–$Pa3$	(No. 205)	$\chi^{(3)}$	≈1047
BaWO$_4$	C_{4h}^6–$I4_2/a$	(No. 88)	$\chi^{(3)}$	924
β'-Gd$_2$(MoO$_4$)$_3$	C_{2v}^8–$Pba2$	(No. 32)	$\chi^{(2)} + \chi^{(3)}$ (polar)	960
PbWO$_4$	C_{4h}^6–$I4_2/a$	(No. 88)	$\chi^{(3)}$	901

*Most of these crystals are already commercial materials as laser host crystals (indicated by bold letters) and crystals for second harmonic generation (SHG), and some of them are well-known birefringent and scintillator crystals (see, e.g., [12–15]). Diamond is also an $\chi^{(3)}$-active crystal with $\omega_{SRS} \approx 1333$ cm^{-1} [16], but it is not easily accessible.

ity tensor of a crystal by expressing its polarization as a power series in electric-field strength **E** as

$$\mathbf{P(E)} = \chi^{(0)}\mathbf{E} + \chi^{(2)}\mathbf{E}^2 + \chi^{(3)}\mathbf{E}^3 + \ldots \qquad (2)$$

where $\chi^{(0)}$ is the linear susceptibility tensor responsible for linear optical phenomena such as refraction and reflection of light; and $\chi^{(2)}$, $\chi^{(3)}$, etc., are the nonlinear optical susceptibilities of a crystal. These tensors are related to the linear and nonlinear refractive index as follows:

$$\chi^{(0)} \cong \frac{1}{4\pi}(n_0^2 - 1), \quad \chi^{(2)} \cong \frac{1}{2\pi}n_0 n_1,$$

$$\chi^{(3)} \cong \frac{1}{2\pi}n_0 n_2, \qquad (3)$$

and are responsible for a large variety of nonlinear optical phenomena. The most important nonlinear frequency conversion effects arise from the second and third terms in Eq. (2), which are connected to electrical polarization, as they are quadratic and cubic functions of the electrical field strength. The second term in

Table 2. SRS-active organic and organometallic crystals [17–21]

Crystal	Space group		Nonlinearity (class)	SRS-active vibration mode (cm^{-1})	Observed nonlinear laser effect[1]
	notation	number			
Organic					
$C_{12}H_{22}O_{11}$[2] (sucrose, sugar)	$C_2^2 - P2_1$	(No. 4)	$\chi^{(2)} + \chi^{(3)}$ (polar)	≈ 2960	SHG, SRS, self-FD, self-SFM
$C_{13}H_{10}O$ (benzophenone)	$D_2^4 - P2_12_12_1$	(No. 19)	$\chi^{(2)} + \chi^{(3)}$	3070, 1650, 998, ≈ 103	SHG, SRS
$C_{13}H_{10}O_3$ (salol)	$D_{2h}^5 - Pbca$	(No. 61)	$\chi^{(3)}$	≈ 3150	SRS
α-$C_{14}H_{12}O$[3] (4-methylbenzophenone)	$C_{2h}^5 - P2_1/c$	(No. 14)	$\chi^{(3)}$	3065	SRS
$C_{14}H_{10}O_2$[4] (benzil, dibenzoyl)	$D_3^4 - P3_121$	(No. 152)	$\chi^{(2)} + \chi^{(3)}$	≈ 1000	SHG, SRS
$C_{15}H_{19}N_3O_2$ (AANP)[5]	$C_{2v}^9 - Pna2_1$	(No. 33)	$\chi^{(2)} + \chi^{(3)}$ (polar)	≈ 1280	SHG, SRS, self-SFM
$C_{16}H_{15}N_3O_4$ (MNBA)[6]	$C_s^4 - Cc$	(No. 9)	$\chi^{(2)} + \chi^{(3)}$ (polar)	≈ 1587	SHG, SRS, self-FD, self-SFM
Organometallic					
$C_{14}H_{26}N_8O_{13}Zr$ (CuZN-III)[7]	$D_2^5 - C222_1$	(No. 20)	$\chi^{(2)} + \chi^{(3)}$	$\approx 1008, \approx 2940$	SHG, SRS
$C_{13}H_{22}N_5TlZr$ (TlGuZN)[8]	$C_2^2 - P2_1$	(No. 4)	$\chi^{(2)} + \chi^{(3)}$ (polar)	$\approx 1005, \approx 2950$	SHG, SRS

[1] Used abbreviations self-FD and self-SFM are the self-frequency doubling and the self-sum-frequency mixing, correspondingly.

[2] Strongly shifted Stokes and anti-Stokes picosecond generation ($\omega_{SRS} \approx 2915$ cm^{-1}) was also observed in glassy sugar caramel. Both sugar materials (single crystals and glassy caramel) are easily accessible and very cheap. They were bought in pastry shops.

[3] It is also known as the metastable β-$C_{14}H_{12}O$ phase which has trigonal space group $C_3^2 - P3_1$ (No. 144) or $C_3^3 - P3_2$ (No. 145) [22].

[4] In accordance with [23] space group, this could also be $D_3^6 - P3_221$ (No. 154).

[5] Full chemical name is the 2-adamantylamino-5-nitropyridine.

[6] Full chemical name is the 4'-nitrobenzylidene-3-acetamino-4-methoxyaniline.

[7] Full chemical name is the bis(guanidinium) zirconium bis(nitrilotriacetate) hydrate.

[8] Full chemical name is the thallium quanidinium zirconium bis(nitrilotriacetate) dihydrate [24]. Refined data on SRS and SHG will be published soon with Dr. E. Haussühl, who grew and characterized of this crystal.

Eq. (2) gives rise to frequency mixing, particularly SHG in acentric crystals, whereas the tensor $\chi^{(3)}$ of the third term is not subsided to symmetry restrictions. Therefore, in $\chi^{(3)}$-active crystals, several nonlinear processes, such as SRS, third harmonic generation and so on are available in optically isotropic and anisotropic crystals (Table 3).

The Raman lasers based on $\chi^{(3)}$-crystals (as mentioned above) are extensively an area of growth in modern laser material science and solid-state laser physics. It is not feasible to present an examination of the main theoretical aspects of SRS laser frequency conversion in solids used so far. A few such comprehensive reviews are already present in the literature (see [1, 3, 28, 29, 31–34]). Depending on the pump pulse duration τ_p, two temporal SRS regimes, steady-

state and transient, can be considered. The main condition for the steady-state pumping condition, which is of more interested for many practical cases and which was realized in most known nano- and picosecond crystalline Raman lasers, is

$$\tau_p \gg T_2 = (\pi \Delta \nu_R)^{-1}. \tag{4}$$

Here T_2 is the dephasing (phonon relaxation) time of the SRS-active vibration mode and $\Delta \nu_R$ is the linewidth (FWHM) of the corresponding Raman-shifted line with a frequency ω_{SRS} in the spontaneous Raman scattering spectrum. The condition for the first Stokes steady-state generation regime in Raman lasers based on $\chi^{(3)}$-active crystals [35]

$$R_m \exp[2(g_{ssR}^{St_1} I_p l_{SRS} - \alpha l_{cr})]\lambda_{St_1} = 1 \tag{5}$$

Table 3. Some possible $\chi^{(2)}$- and $\chi^{(3)}$-effects in undoped nonlinear-laser crystals (see, e.g., [31])

Nonlinear effect[1]	Frequency		Nonlinear Susceptibility	Note
	incident	created		
Second harmonic generation[2]	ω, ω	2ω	$\chi^{(2)}$	UV and visible generation
Sum frequency mixing[2]	ω_1, ω_1	$\omega_3 = \omega_1 + \omega_2$	$\chi^{(2)}$	Up-conversion
Difference frequency mixing[2]	ω_1, ω_2	$\omega_3 = \omega_1 - \omega_2$	$\chi^{(2)}$	IR generation
Third harmonic generation[2]	ω, ω, ω	3ω	$\chi^{(2)}$	VUV generation
Sum frequency mixing[2]	$\omega_1, \omega_2, \omega_3$	$\omega_4 = \omega_1 + \omega_2 + \omega_3$		VUV and UV generation
Stimulated Raman scattering[3]	ω_1	ω_2	$\chi^{(3)}$	$\omega_2 = \omega_1 \pm \omega_{SRS}$
Two-photon absorption[3]	ω, ω	–	$\chi^{(3)}$	$\omega_c = 2\omega$

[1] It is also available as a self-frequency conversion effect, namely self-FD, self-SRS, etc.
[2] Phase matching required.
[3] ω_{SRS} and ω_c are the crystal frequencies.

is very nearly the same as the condition for stimulated-emission (SE) generation in the usual lasers on the base of activated crystals [36]

$$R_m \exp[2(\Delta N \sigma_{SE} l_{SE} - \rho l_{cr})]_{\lambda_{SE}} = 1. \qquad (6)$$

In Eqs. (5) and (6): $g_{ssR}^{St_1} I_p l_{SRS}$ is the Raman gain factor (here: $g_{ssR}^{St_1}$ is the steady-state Raman gain coefficient, I_p is the laser pumping intensity, and l_{SRS} is the SRS-active crystal length), α is the loss coefficient at the first Stokes wavelength λ_{St_1}, l_{cr} is the total crystal length, $R_m = R_{m1} R_{m2}$ is the reflectivity of resonator mirrors, $\Delta N \sigma_{SE}$ is the gain coefficient (here ΔN is the inversion population of the Stark laser levels and σ_{SE} is the cross section of inter-Stark laser transition of an activator ions), and ρ is the loss coefficient at the SE wavelength λ_{SE}.

If the intensity of plane-wave fundamental pump-laser radiation is much higher than the intensity of the first Stokes generation ($I_p \gg I_{St_1}$), i.e., when the level of pump depletion is very small, the SRS amplification at the first Stokes emission can be written [37] as

$$\frac{dI_{St_1}}{d_{SRS}} = g_{ssR}^{St_1} I_p(l_{SRS}) I_{St_1}(l_{SRS})$$

$$+ I_p(l_{SRS}) \frac{d\sigma}{d\Omega} N_{SRS} \Delta\Omega \qquad (7)$$

$$= g_{ssR}^{St_1} I_p(l_{SRS})[I_{St_1}(l_{SRS}) + I_{St_1}(l_{SRS} = 0)],$$

where $I_{St_1}(l_{SRS} = 0)$ is the intensity of the spontaneous Raman scattering at the wavelength λ_{St_1} of the first Stokes generation (in the beginning $l_{SRS} = 0$ of the

amplified crystal, i.e., from zero-point fluctuation of spontaneous scattering)

$$g_{ssR}^{St_1} = \frac{2\lambda_{St_1}^2 N_{SRS}}{\pi n_{St_1}^2 h\nu_p} \frac{d\sigma}{d\Omega} \frac{1}{\Delta\nu_R}. \qquad (8)$$

Clearly, in the first Stokes lasing process, very weak spontaneous Stokes Raman scattering provides the major contribution, because its frequency-shifted emission at ω_{SRS} of the intensive line (s) acts as a "seed" for SRS amplification. This situation is analogous to the luminescence (spontaneous emission) in the laser action in activated crystals. In Eqs. (7) and (8): $d\sigma/d\Omega$ is the Raman scattering cross section of the vibration transition of the crystal, N_{SRS} is the number (concentration) of SRS-active scattering centers, n_{St_1} is the refractive index of the crystal at wavelength λ_{St_1}, and $\Delta\Omega$ is the small solid angle of SRS lasing. As seen from Eq. (8), the $g_{ssR}^{St_1}$ coefficient is linearly proportional to the Raman scattering cross section and inversely proportional to the linewidth of the spontaneous Raman scattering transition. The product $\frac{d\sigma}{d\Omega}\frac{1}{\Delta\nu_R}$ may be considered as the spectroscopic parameter providing a measure for peak intensity of a spontaneous Raman transition. This figure of merit, as shown in [38, 39], can be used in a comparative selection for suitable SRS-active crystals. Therefore, high-gain Raman crystals for steady-state SRS laser converters should have a small $\Delta\nu_R$ value and strong spontaneous Raman scattering transition. Solving Eq. (7) yields (see, e.g., [29])

$$I_{St_1}(l_{SRS}) = I_{St_1}(l_{SRS} = 0)\exp(g_{ssR}^{St_1} I_p l_{SRS}). \qquad (9)$$

In many known experimental cases (see, e.g., [3, 30, 32, 33, 40]), SRS lasing at the first Stokes wavelength

$(\omega_{St_1} = \omega_p - \omega_{SRS})$ becomes with any assurance measurable when the increment in Eq. (9) reaches a value of $g_{ssR}^{St_1} I_p l_{SRS} = 25\text{--}30$, which corresponds to an energy conversion efficiency of approximately 1%. The laser pumping intensity $(I_p = I_{thr})$ providing such an efficiency value is conditionally considered to be the first Stokes steady-state threshold pumping intensity $(I_{St_1}/I_{thr} \approx 0.01)$. Thus approach makes possible a tentative estimate of the $g_{ssR}^{St_1}$ value for $\chi^{(3)}$-active crystals in rather simple pumping geometries, as in the single-pass SRS experiments (see [11, 41]).

Due to very strong $\chi^{(3)}$- and $\chi^{(2)}$-nonlinearities of the most used organic crystals (see Table 2), the pumping condition in conducted SRS experiments were slightly different from the model mentioned above. To avoid a manifestation of other possible nonlinear effects (SHG, two-photon absorption and so on) in them, we can only make a comparative estimate of their $g_{ssR}^{St_1}$ coefficients applying several reference $\chi^{(3)}$-active crystals (PbWO$_4$, α-KY(WO$_4$)$_2$, α-KGd(WO$_4$)$_2$, and NaClO$_3$ [14, 42, 43]) and a relatively "soft" excitation condition.

As a threshold intensity in these comparative experiments, we assumed the pumping energy at which the steady-state first Stokes lasing becomes confidently perceptible (usually with signal/noise ratio ≈ 2). Conducted measurements with our organic crystals showed that in most cases their first-Stokes pumping "soft" threshold is significantly less than the "1%-threshold."

Fig. 1. The orientational SRS and SHG spectrum of an orthorhombic C$_{14}$H$_{26}$N$_8$O$_{13}$Zr (GuZN-III) crystal obtained in pumping geometry $c(aa)c$ under picosecond excitation $\lambda_{f1} = 1.06415$ μm wavelength (fundamental pump line is asterisked), as well as a scheme of the experimental single-pass set-up (above) [20]. Wavelengths of all lines are given in μm and their intensity are shown without correction of spectral sensitivity of used analyzing CSMA system (see Fig. 2). Anti-Stokes line related to SRS-active vibration mode of the crystal $\omega_{SRS2} \approx 2940$ cm^{-1} is indicated by the horizontal arrow.

3. SRS SPECTROSCOPY OF ORGANIC SINGLE CRYSTALS

The spectroscopic single-pass SRS experiments in [17–21] were done using oriented samples of organic single crystals with different active length (from $l_{SRS} \approx 0.5$ mm for AANP to $l_{SRS} \approx 25$ mm for benzophenone and GuZN-III). The reference and measured crystals were equal in length and their optical faces were polished plane-parallel but not antireflection coated. For the excitation steady-state Stokes and anti-Stokes generation in organic crystals, we used a homemade picosecond Nd^{3+} : Y$_3$Al$_5$O$_{12}$ laser with $\approx 30\%$ efficient frequency doubler that generates ≈ 110 ps pulses (FWHM) at $\lambda_{f1} = 1.06415$ μm and an energy of 3 mJ, and ≈ 80 ps SHG at $\lambda_{f2} = 0.53207$ μm wavelength [44]. Pump radiation with Gaussian beam profile, as needed, was focused onto the investigated crystal by a lens with a focal distance adjusted ($F = 25$ cm) such that the SRS lasing was maximum without a surface and volume optical damage sample, resulting in a beam waist diameter of about 160 μm (see used setup in the frame of Fig. 1). The spectral composition of the Stokes and anti-Stokes, as well as the self-FD and self-SFM generation emission, was measured with a CCD-spectro-
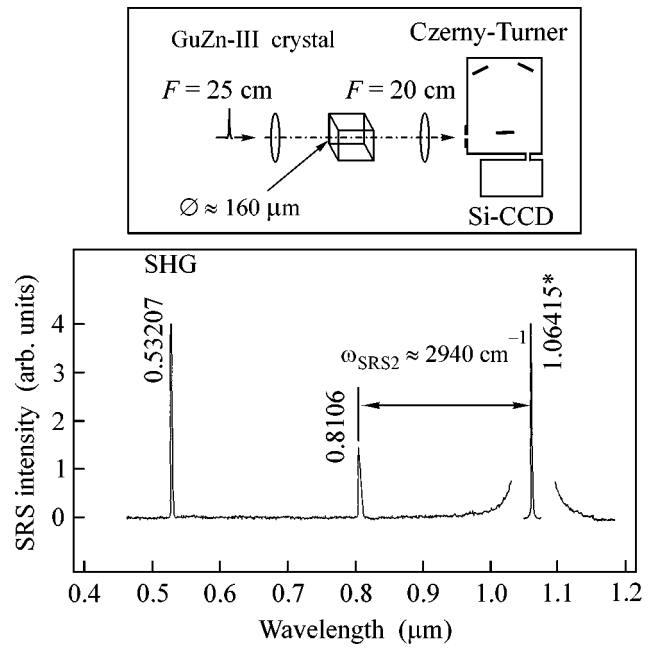
scopic multichannel analyzer (CSMA) consisting of a scanning grating monochromator (with a Czerny-Turner arrangement), an analyzer, and a Si-CCD array-sensor (Hamamatsu S3923–1024Q) as a detector. The sensitivity dispersion of this CSMA system is given in the inset of Fig. 2. Below are shown several selected SRS spectra of investigated organic crystals.

3.1. C$_{14}$H$_{22}$N$_8$O$_{13}$Zr (GuZN-III) crystal [20]. Two SRS-spectra (see Fig. 1 and 2) are shown an identification of observed Stokes and anti-Stokes lines related to two SRS-active optical vibration modes of the crystal $\omega_{SRS1} \approx 1008$ cm^{-1} and $\omega_{SRS2} \approx 2940$ cm^{-1}. The analysis is shown that for the 62-atom molecule C$_{14}$H$_{26}$N$_8$O$_{13}$Zr of a GuZN-III structure with orthorhombic space group D_2^5 and $Z = 4$ (2 for a primitive unit cell), overall degrees of freedom $(3N \times 2) = 372$ are distributed into (at **k** = 0, center of Brillouin zone)

$$\Gamma_N = 92A + 94B_1 + 93B_2 + 93B_3$$

irreducible representations. In accordance with [45], the A modes of a GuZN-III crystal are Raman active only, and those of B_1, B_2, and B_3 are both Raman and IR active. Among them the $(B_1 + B_2 + B_3)$ species are acous-
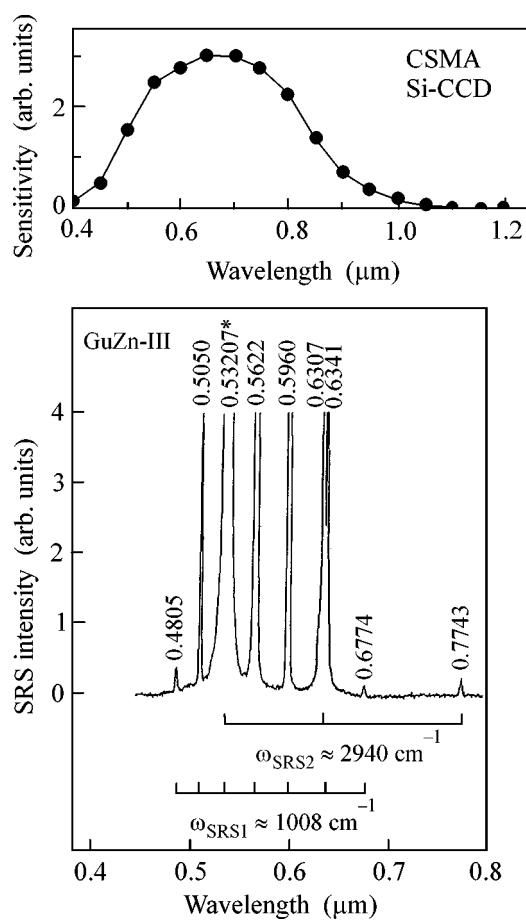
Fig. 2. The orientational SRS and RFWM spectrum of an orthorhombic $C_{14}H_{26}N_8O_{13}Zr$ (GuZN-III) crystal obtained in pumping geometry $a(cc)a$ under picosecond excitation at $\lambda_{f2} = 0.53207$ μm wavelength, as well as wavelength dependence the spectral sensitivity of used analyzing CSMA system (above) [20]. Stokes and anti-Stokes lines related to SRS-active vibration modes of the crystal $\omega_{SRS1} \approx 1008$ cm^{-1} and $\omega_{SRS2} \approx 2940$ cm^{-1} are indicated by horizontal brackets. Other notations are as in Fig. 1.

Fig. 3. The room-temperature polarized spontaneous Raman scattering spectrum of an orthorhombic $C_{14}H_{26}N_8O_{13}Zr$ (GuZN-III) crystal registered under experimental geometry $\approx a(cc) \approx a$ [20]. Raman shift of several intensive lines are given in cm^{-1}. The arrow at zero corresponds to excitation by CW Nd^{3+}:$Y_3Al_5O_{12}$ laser at 1.06415 μm wavelength.

tic modes. As an illustration, Fig. 3 shows the Raman spectrum of the fully symmetric A species, which was practically recorded under excitation geometry $\approx a(cc) \approx a$ as in the case of the SRS spectrum exhibited in Fig. 2. The assignment of its strongest Raman shifted lines to the respective vibration modes of a GuZN-III crystal yields that the A-symmetry lines at ≈ 1008 and ≈ 2940 cm^{-1} are promoting modes of observed SRS lasing components. They correspond to the stretching vibrations of the CH_2 and N–C–O bond systems, respectively.

3.2. $C_{13}H_{10}O$ (benzophenone), α-$C_{14}H_{12}O$ (4-methyl-benzophenone), and $C_{14}H_{10}O_2$ (benzil) crystals [18]. Their Stokes and anti-Stokes spectra are given in Figs. 4 and 5. The analysis conducted in [18] shows that most of their SRS-active modes (with the frequencies
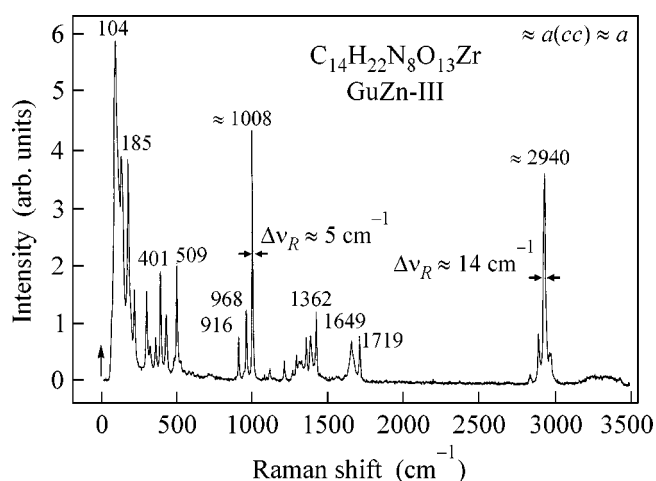
of ≈ 3070, 1650, and ≈ 1000 cm^{-1}) correspond to the $\nu(CH)$ vibrations of the benzene ring, $\nu(C = O)$ vibrations of the carbonyl unit, and symmetric $\nu(CC)$ vibrations of the benzene ring, respectively. The ≈ 103 cm^{-1} SRS mode is lattice vibration.

4. NONLINEAR LASER $\chi^{(3)}$- AND $\chi^{(2)}$-EFFECTS

In addition to very large Raman shift and efficient first Stokes generation in discovered SRS-active organic crystals in some an acentric of them, more polar crystals were observed combining nonlinear lasing effects, namely self-FD and self-SFM [19–21]. This potential allows to classify these materials as a promising $(\chi^{(3)} + \chi^{(2)})$-medium for a new type of laser-frequency converters.

4.1. $C_{12}H_{22}O_{11}$ (sucrose or sugar) crystal [21]. Due to its low symmetry and, hence, the large number of vibrational modes ($3NZ = 270$; $\Gamma_N = 133A + 137B$, here $(A + 2B)$ are acoustic modes), it is quite difficult at this initial stage of the research to establish the relation of observed SRS-mode $\omega_{SRS} = 2960$ cm^{-1} (Fig. 6a) to the specific C–H vibrational bond ($\nu[CH]$ or $\nu[CH_2]$). It is interesting to note here that food-sugar glassy caramel also offers very efficient SRS lasing (Fig. 6b). Besides intensive Stokes and anti-Stokes lasing components, under picosecond pumping in a sugar which is sufficiently good UV crystal, rather efficient $(\chi^{(3)} + \chi^{(2)})$-nonlinear self-frequency conversion effects were also observed, namely self-FD ($\lambda_{self-FD} = 0.3158$ μm, i.e.,
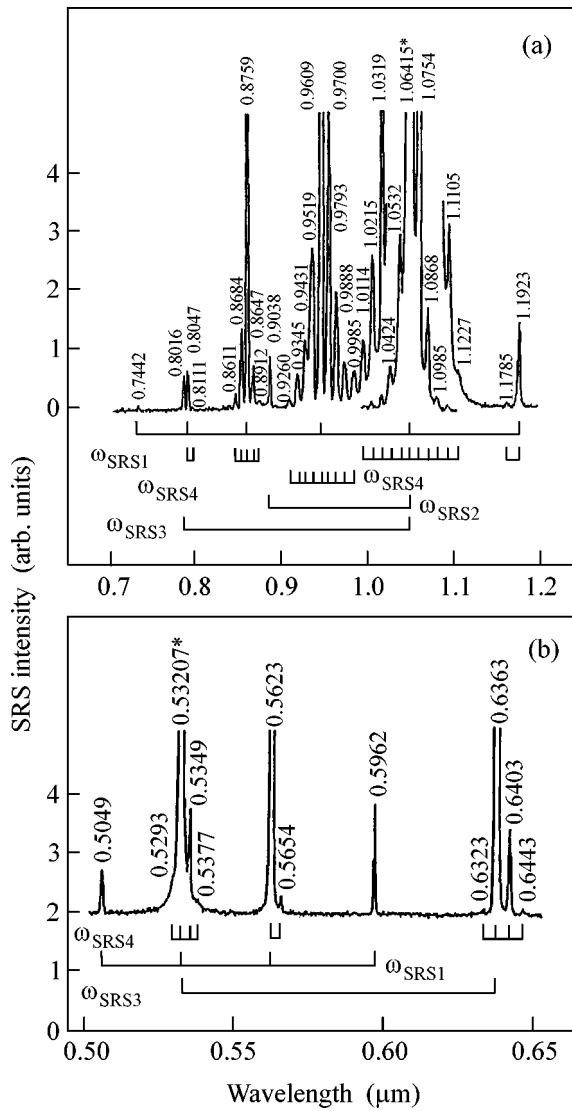
Fig. 4. The orientational SRS and RFWM spectra of an orthorhombic $C_{13}H_{10}O$ (benzophenone) crystal obtained in pumping geometry $\approx b(\approx c \approx c) \approx b$ under picosecond excitation at (a) $\lambda_{f1} = 1.06415$ μm and (b) $\lambda_{f2} = 0.53207$ μm wavelengths [18]. Stokes and anti-Stokes lasing lines related to SRS-active vibration modes of the crystals $\omega_{SRS1} = 998$ cm^{-1}, $\omega_{SRS2} = 1650$ cm^{-1}, $\omega_{SRS3} = 3070$ cm^{-1}, and $\omega_{SRS4} \approx 103$ cm^{-1} are indicated by horizontal brackets. Other notations are as in Fig. 1.
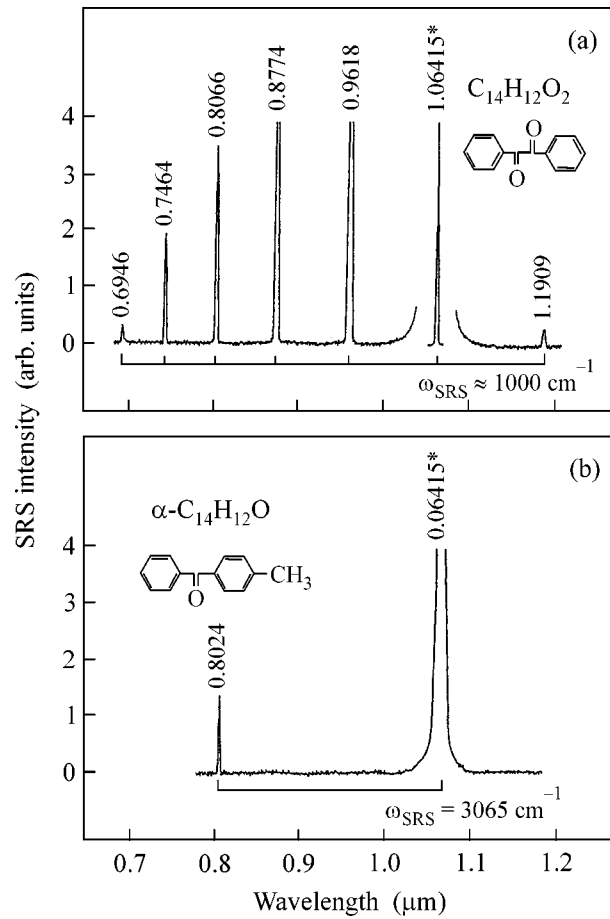

Fig. 5. Stokes and anti-Stokes lasing spectra of (a) a trigonal $C_{14}H_{10}O_2$ (benzil) and (b) a α-$C_{14}H_{12}O$ (4-methylbenzophenone) crystals obtained under picosecond excitation at $\lambda_{f1} = 1.06415$ μm wavelength [18]. Pumping geometry for $C_{14}H_{10}O_2$ crystal was $\perp b(\approx b \approx b) \perp b$ and the α-$C_{14}H_{12}O$ crystal was oriented randomly. The SRS-active vibration modes of these crystals are indicated by horizontal brackets. Other notations are as in Fig. 1.

$1/2\lambda_{St_1}$, or $\omega_{SHG} = 2\omega_{St_1}$) and self-SFM ($\lambda_{self\text{-}SFM} = 0.2887$ μm, i.e., $\Sigma\lambda_{f2}$, λ_{St_1} or $\omega_{SFM} = \omega_{f2} + \omega_{St_1}$). The SHG- and SRS-potential, availability, very low cost, and various structural modifications of a $C_{12}H_{22}O_{11}$ make this crystal quite attractive for application in modern laser physics and nonlinear optics.

4.2. $C_{15}H_{19}N_3O_3$ (AANP) [19] and **$C_{16}H_{15}N_3O_4$** (MNBA) [20] crystals. In these papers, a great potential

for very efficient SRS acting of these two polar organic crystals has been discovered. To the best of our knowledge, among all known $\chi^{(3)}$-active crystals they offer the greatest value of the steady-state Raman gain coefficient in near IR. These crystals are a promising candidate for a new generation of Raman laser converters, where their relatively short SRS-interaction lengths (less then 1 mm) allow for miniaturization. In AANP and MNBA several new parametric lasing effects were also observed, which are illustrated in Table 4 and Fig. 7. According to [19], for the 39-atom $C_{15}H_{19}N_3O_3$ molecule of a AANP structure, overall degrees of freedom $3NZ = 468$ are distributed into

$$\Gamma_N = 117A_1 + 117A_2 + 117B_1 + 117B_2$$

irreducible representations. The vibration modes can be divided into acoustic $\Gamma_T = A_1 + B_1 + B_2$, internal $\Gamma_i =$
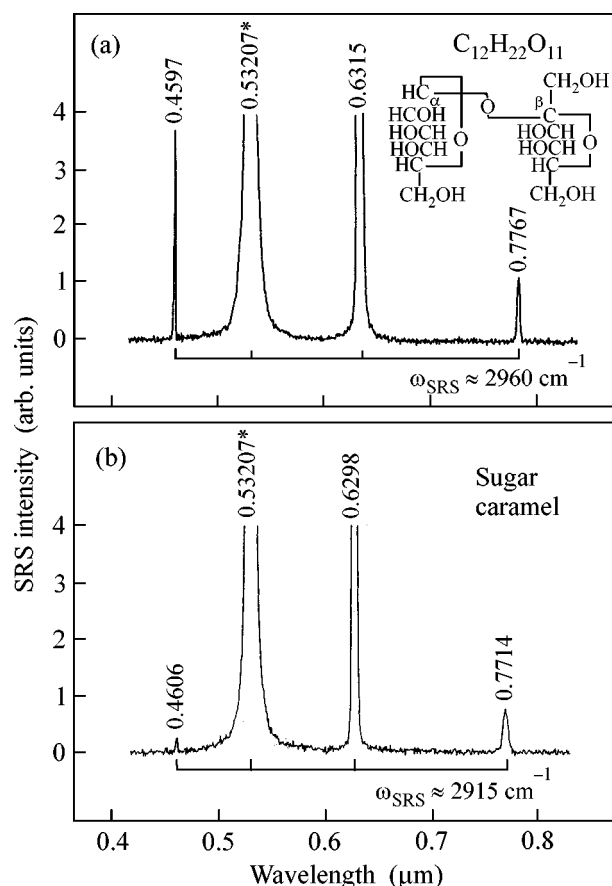
Fig. 6. Random-oriented Stokes and anti-Stokes lasing spectra of (a) a monoclinic $C_{12}H_{22}O_{11}$ (sugar) crystal and (b) glassy sugar caramel obtained under picosecond excitation at $\lambda_{f2} = 0.53207$ μm wavelength [21]. The SRS-active vibration modes of these organic materials are indicated by horizontal brackets. Other notations are as in Fig. 1.
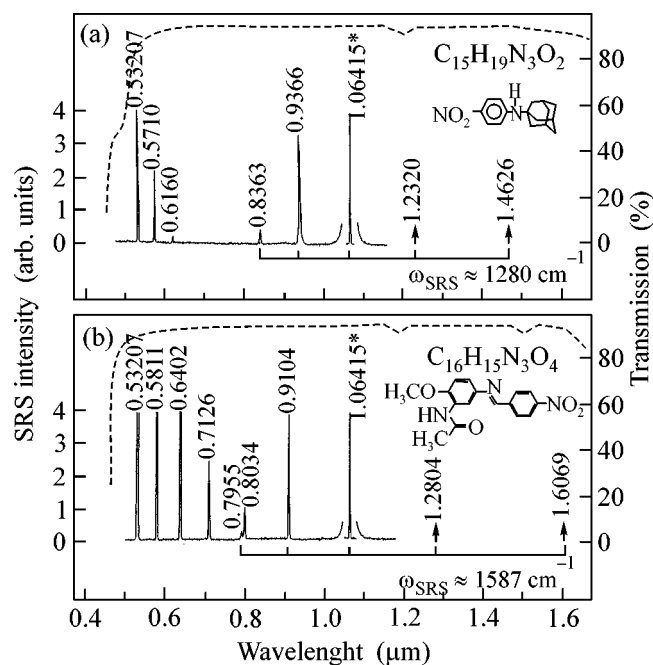

Fig. 7. Parametric Raman lasing spectra of (a) orthorhombic $C_{15}H_{19}N_3O_2$ (AANP) and (b) monoclinic $C_{16}H_{15}N_3O_4$ (MNBA) crystals obtained in pumping geometry $b(aa)b$ for AANP and $b(\approx a \approx a)b$ for MNBA under picosecond excitation at $\lambda_{f1} = 1.06415$ μm wavelength [17, 19]. The arrows indicate the spectral positions of the first and second Stokes lines which are nondetectable by the Si-CGD sensor used (see Fig. 2). The fragments of nonpolarized transmission spectra of 0.4- and ≈1-mm thick samples for AANP and MNBA, respectively, are shown by dashed lines. The SRS-active vibration modes of these strongly nonlinear crystal are indicated by horizontal brackets. Other notations are as in Fig. 1.

$111A_1 + 111A_2 + 111B_1 + 111B_2$, and translatory and rotatory $\Gamma_{T'} = 2A_1 + 3A_2 + 2B_1 + 2B_2$ and $\Gamma_R = 3A_1 + 3A_2 + 3B_1 + 3B_2$, respectively. All optical modes are Raman active. The observed SRS spectrum shows (Fig. 7a) Stokes and anti-Stokes lines which relate to the $\omega_{SRS} \approx 1280$ cm^{-1} vibration mode. It is connected with the strongest vibration of the bond C–N–C, which links the pyridine ring and adamantylamino system of the AANP crystal. Unfortunately, vibration mode analysis for a MNBA crystal is embarrassing at present due to an absence of precise x-ray data. It should be done in the future. The large nonlinearities and hence a very efficient Stokes and anti-Stokes generation related to the $\omega_{SRS} \approx 1587$ cm^{-1} vibration mode and other manifestations of frequency conversion lasing of MNBA with aromalic rings, donor –OCH$_3$ and acceptor group—NHCOCH$_3$, are due to extended π-electron conjugation [25, 46].

5. CONCLUSION

We have demonstrated a great potential for efficient SRS laser action in several organic and organometallic crystals. These first observation of their large frequency shifts, high steady-state first Stokes Raman gain coefficients, as well as self-FD and self-SFM parametric effects let us hope that these novel materials may be used for a new generation of Raman laser converters, where their relatively short nonlinear $\chi^{(3)}$-interaction lengths allow for very attractive miniaturization. Our paper to illustrate the results of our experimental estimations of corresponding value of the gain $g_{ssR}^{St_1}$ coefficients for several investigated crystals is near completion. These data are given in Table 5.

First of all, the author is obliged to note that the idea to start the SRS experiments with organic crystals was actively discussed during the 3rd International Symposium on "Modern Problems of Laser Physics" in Novosibirsk and was encouraged by Academician

Table 4. Parametric lasing effects of $(\chi^{(3)} + \chi^{(2)})$-interaction in organic polar crystals $C_{15}H_{19}N_3O_2$ and $C_{16}H_{15}N_3O_4$ under picosecond $Nd^{3+} : Y_3Al_5O_{12}$-laser excitation at $\lambda_{fl} = 1.06415$ μm wavelength [17, 19]

$\chi^{(3)}$ and $\chi^{(2)}$ generation component			SRS-active crystal vibration mode (cm^{-1})
wavelength (μm)[1]	line	attribution	
C$_{15}$H$_{19}$N$_3$O$_2$ crystal, $l_{SRS} \approx 0.4$ mm^2 (Fig. 7a)			
0.53207	SHG ($1/2\lambda_{fl}$)	$2\omega_{fl}$	–
0.5710	$\Sigma_{fl}, \lambda_{St1}$ ($\lambda_{self\text{-}SFM}$)[3]	$\omega_{fl} + (\omega_{fl} - \omega_{SRS})$	≈ 1280
0.6160	$\Sigma\lambda_{fl}, \lambda_{St2}$ ($\lambda_{self\text{-}SFM}$)[3]	$\omega_{fl} + (\omega_{fl} - 2\omega_{SRS})$	≈ 1280
0.8363	$ASt_2(\lambda_{ASt_2})$	$\omega_{fl} + 2\omega_{SRS}$	≈ 1280
0.9366	$ASt_1(\lambda_{ASt_1})$	$\omega_{fl} + \omega_{SRS}$	≈ 1280
1.06415	λ_{fl}	ω_{fl}	–
1.2320[4]	$St_1(\lambda_{St_1})$	$\omega_{fl} - \omega_{SRS}$	≈ 1280
1.4626[4]	$St_2(\lambda_{St_2})$	$\omega_{fl} - 2\omega_{SRS}$	≈ 1280
C$_{16}$H$_{15}$N$_3$O$_2$ crystal, $l_{SRS} \approx 1$ mm^2 (Fig. 7b)			
0.53207	SHG ($1/2\lambda_{fl}$)	$2\omega_{fl}$	–
0.5811	$\Sigma\lambda_{fl}, \lambda_{St_1}$ ($\lambda_{self\text{-}SFM}$)[3]	$\omega_{fl} + (\omega_{fl} - \omega_{SRS})$	≈ 1587
0.6402	SHG ($1/2\lambda_{St_1}$)	$2\omega_{St1} = 2(\omega_{fl} - \omega_{SRS})$	≈ 1587
0.7126	$\Sigma\lambda_{St_1}, \lambda_{St_2}$ ($\lambda_{self\text{-}SFM}$)[5]	$(\omega_{fl} - \omega_{SRS}) + (\omega_{fl} - 2\omega_{SRS})$	≈ 1587
	$\Sigma\lambda_{fl}, \lambda_{St_3}$ ($\lambda_{self\text{-}SFM}$)[6]	$\omega_{fl} + (\omega_{fl} - 3\omega_{SRS})$	≈ 1587
0.7955	$ASt_2(\pi\lambda_{ASt_2})$	$\omega_{fl} + 2\omega_{SRS}$	≈ 1587
0.8334	SHG ($1/2\lambda_{St_2}$)	$2\omega_{St_2} = 2(\omega_{fl} - 2\omega_{SRS})$	≈ 1587
0.9104	$ASt_1 (\lambda A_{St_1})$	$\omega_{fl} + \omega_{SRS}$	≈ 1587
1.06415	λ_{fl}	ω_{fl}	–
1.2804[4]	$St_1 \lambda_{St_1}$	$\omega_{fl} - \omega_{SRS}$	≈ 1587
1.6069[4]	$St_2 \lambda_{St_2}$	$\omega_{fl} - 2\omega_{SRS}$	≈ 1587

[1] Measurement accuracy is ±0.0003 μm.

[2] ω_{SRS} is the SRS-lasing length of crystalline element.

[3] $\lambda_{self\text{-}SFM}$ is the wavelength of the self-sum-frequency mixing generation with which pumping with the fundamental ω_{fl} frequency and arising in the crystal first or second Stokes lasing with $\omega_{St_1} = \omega_{fl} - \omega_{SRS}$ or $\omega_{St_2} = \omega_{fl} - 2\omega_{SRS}$ frequency were associated.

[4] Due to zero sensitivity of the used Si-CCD sensor (see Fig. 2), the Stokes lasing at this wavelength is not detectable.

[5] $\lambda_{self\text{-}SPM}$ is the wavelength of the self-sum-frequency mixing generation with which pumping with the first and second Stokes lasing emissions with $\omega_{St_1} = \omega_{fl} - \omega_{SRS}$ and $\omega_{St_2} = \omega_{fl} - 2\omega_{SRS}$ frequency was associated.

[6] Due to strong absorption (optical transparent of this crystal covers the spectral range of $\approx 0.51 - \approx 2.2$ μm, see also Fig. 7b), weak third Stokes lasing at the wavelength $\omega_{St_3} = 2.1570$ μm are in general possible, but this self-sum-frequency mixing generation process is unreal.

Table 5. The steady-state Raman gain coefficients of Raman spectroscopic properties of organic and organometallic crystals[1]

Crystal	First Stokes lasing characteristics				Raman spectroscopic property		
	$\lambda_{f1} = 1.06415$ μm		$\lambda_{f2} = 0.53207$ μm		ω_{SRS} (cm^{-1})	$\Delta\nu_R$ (cm^{-1})	T_2 (ps)
	λ_{St1} (μm)	g_{ssR}^{St1} (cm/GW)	λ_{St1} (μm)	g_{ssR}^{St1} (cm/GW)			
Organic							
$C_{12}H_{22}O_{11}$	–	–	0.6315	>6.5	≈2960	≈7	≈2
$C_{13}H_{10}O$	1.1906	≈2.8	0.5619	>10	998	≈3.5	≈3
			0.6360	>10	3070	≈6.5	≈1.6
$C_{15}H_{19}N_3O_2$	1.2320	>15[2]	–	–	≈1280	≈24[3]	≈0.44
$C_{16}H_{15}N_3O_4$	1.2804	>14[2]	–	–	≈1587	1.5	≈7
Organometallic							
$C_{14}H_{26}N_8O_{13}Zr$	1.1920	≈3.8	0.5622	>10	≈1008	≈5	≈2
	1.5487	3.2[2]	0.6307	>9	≈2940	≈14[3]	≈0.8

[1] Some listed data are unpublished.

[2] For this case, using nanosecond $Nd^{3+} : Y_3Al_5O_{12}$ laser ($\tau_p \approx 20$ ns) and an avalanche Ge detector we can estimated only the lower limiting value of the g_{ssR}^{St1} coefficient.

[3] Inhomogeneously broadened line.

REFERENCES

1. J. T. Murray, R. C. Powell, and N. Peyghambrarian, J. Lumin. **66–67**, 89 (1996).

2. A. A. Kaminskii, in *Raman Scattering—70 Years of the Research*, Ed. by V. I. Gorelik (Physical Inst., Moscow, 1998), p. 206.

3. T. T. Basiev and R. C. Powell, Opt. Mater. **11** (4), 301 (1999).

4. G. A. Pasmanik, Laser Focus World **35**, 137 (1999).

5. J. Hulliger, A. A. Kaminskii, and H. J. Eichler, Adv. Funct. Mater. **11**, 243 (2001).

6. J. Barnes, in *Proceedings of the 19th International Laser Lidar Conference* (1998), p. 619.

7. W. T. Roberts, J. T. Murray, W. L. Austin, *et al.*, Proc. SPIE **3353**, 347 (1998).

8. B. Chiao and B. P. Stoicheff, Phys. Rev. Lett. **12**, 290 (1964).

9. K. K. Lai, W. Schusslbauer, H. Silberbauer, *et al.*, Phys. Rev. B **42**, 5834 (1990).

10. S. N. Korpukhin and A. I. Stepanov, Sov. J. Quantum Electron. **16**, 1027 (1986).

11. P. Cerny, P. G. Zverev, H. Jelinkova, and T. T. Basiev, Opt. Commun. **177**, 397 (2000).

12. A. A. Kaminskii, *Crystalline Lasers: Physical Processes and Operating Schemes* (CRC Press, Boca Raton, 1996).

13. V. G. Dmitriev, G. G. Gurzadyan, and D. N. Nikogosyan, *Handbook of Nonlinear Optical Crystals* (Springer, Berlin, 1999).

14. A. A. Kaminskii, H. J. Eichler, K. Ueda, *et al.*, Appl. Opt. **38**, 4533 (1999).

15. *CRC Handbook of Laser Science and Technology*, Ed. by M. J. Weber (CRC Press, Boca Raton, 1986), Vol. 4.

16. G. Eckhard, D. P. Bortfeld, and M. Geller, Appl. Phys. Lett. **3**, 137 (1963).

17. A. A. Kaminskii, J. Hulliger, and H. J. Eichler, Phys. Status Solidi A **186**, R19 (2001).

18. A. A. Kaminskii, H. Klapper, J. Hulliger, *et al.*, Laser Phys. **12**, 1041 (2002).

19. A. A. Kaminskii, T. Kaino, T. Taima, *et al.*, Jpn. J. Appl. Phys. **41**, L603 (2002).

20. A. A. Kaminskii, E. Haussühl, J. Hulliger, *et al.*, Phys. Status Solidi A **193**, R167 (2002).

21. A. A. Kaminskii, Crystallogr. Rep. **48**, 295 (2003).

22. H. Kutzke, M. Al-Mansour, and H. Klapper, J. Mol. Struct. **374**, 129 (1996).

23. C. J. Brown and R. Sadanga, Acta Crystallogr. **18**, 158 (1965).

24. E. Haussuhl, G. Giester, and E. Tillmanns, Z. Kristallogr.—New Cryst. Struct. **214**, 375 (1999).

25. Ch. Bosshard, K. Sutter, Ph. Pretre, J. Hulliger, M. Flörsheimer, P. Kaatz, and P. Günter, *Organic Nonlinear Optical Materials* (Gordon and Beach, Bassel, 1995).

26. *Nonlinear Optics of Organic Molecules and Polymers*, Ed. by H. S. Nolwa and S. Miyat (CRC Press, Boca Raton, 1996).

27. E. L. Woodbury and W. K. Ng, Proc. IRE **50**, 2367 (1962).

28. R. W. Boyd, *Nonlinear Optics* (Academic, New York, 1992).

29. Y. R. Shen, *The Principles of Nonlinear Optics* (Wiley, New York, 1984).

30. J. F. Reintjes, in *CRC Handbook of Laser Science and Technology*, Suppl. 2: *Optical Materials*, Ed. by M. J. Weber (CRC Press, Boca Raton, 1995), p. 346.

31. *Nonlinear Optics*, Ed. by P. G. Harper and B. S. Wherrett (Academic, London, 1977).

32. W. Kaiser and M. Maier, in *Laser Handbook*, Ed. by F. T. Arichi and E. O. Schulz-Dubois (North-Holland, Amsterdam, 1972), Vol. 2, p. 10007.

33. A. Laubereau, in *Non-Linear Raman Spectroscopy and Its Chemical Applications*, Ed. by W. Kiefer and D. A. Long (Reidel, Dorderect, 1982), p. 183.

34. N. Bloembergen, *Nonlinear Optics*, 3rd ed. (Benjamin, San Diego, 1992; Mir, Moscow, 1966).

35. A. Z. Grasyuk, Sov. J. Quantum Electron. **4**, 269 (1974).

36. A. A. Kaminskii, *Laser Crystals, Their Physics and Properties* (Springer, Berlin, 1981).

37. A. Z. Grasyuk, S. B. Kurbasov, L. L. Losev, *et al.*, Quantum Electron. **28**, 162 (1998).

38. T. T. Basiev, A. A. Sobol, P. G. Zverev, *et al.*, Appl. Opt. **38**, 594 (1999).

39. M. Maier, Appl. Phys. **11**, 209 (1976).

40. D. C. Hanna, D. J. Poiner, and D. J. Pratt, IEEE J. Quantum Electron. **22**, 332 (1986).

41. P. Cerny, H. Jelinkova, T. T. Basiev, and P. G. Zverev, IEEE J. Quantum Electron. **38**, 1471 (2002).

42. A. A. Kaminskii, S. N. Baghayev, J. Hulliger, *et al.*, Appl. Phys. B **67**, 157 (1998).

43. A. A. Kaminskii, C. L. McCray, H. R. Lee, *et al.*, Opt. Commun. **183**, 277 (2000).

44. H. J. Eichler and B. Liu, Opt. Mater. **1**, 21 (1992).

45. D. L. Rousseau, R. P. Baumann, and S. P. S. Porto, J. Raman Spectrosc. **10**, 253 (1981).

46. *Nonlinear Optics of Organic Molecules and Polymers*, Ed. by H. S. Nalwa and S. Miyat (CRC Press, Boca Raton, 1996).

Bloch Electrons in a Magnetic Field:
Topology of Quantum States and Transport

V. Ya. Demikhovskiĭ

Nizhni Novgorod State University, pr. Gagarina 23, Nizhni Novgorod, 603950 Russia
e-mail: demi@phys.unn.ru
Received October 14, 2003

Quantum states and Hall conductances of electrons in *n*-type heterojunctions and holes in *p*-type heterojunctions in a field of a lateral superlattice and a perpendicular magnetic field were studied. It is shown that the energy spectrum of magnetic subbands in a periodic potential without inversion center is not symmetric about the reversal of the quasi-momentum sign. The properties of wave functions and the related topological invariants determining the Hall conductance were examined. The method of calculating the magnetic Bloch states of holes was developed on the basis of the Luttinger Hamiltonian, allowing the spin and spin–orbit interactions to be taken into account in this problem. The Hall conductance quantization law was determined for 2D holes in a periodic superlattice potential. © 2003 MAIK "Nauka/Interperiodica".

PACS numbers: 73.40.-c; 73.43.Cd; 71.70.Di

1. INTRODUCTION

The problem of quantum states of an electron moving in a periodic potential and simultaneously exposed to a static magnetic field has been topical for several last decades. The nontrivial character of the energy spectrum in this problem is caused by the interaction of the lattice periodic potential, which forms energy bands, with a magnetic field, which tends to form discrete Landau levels. The fundamental results in this field were obtained in the early works of Harper [1], Azbel [2], and Wannier [3] and in the work of Hofstadter [4], who used computer visualization of the spectrum (which came to be known as the Hofstadter butterfly) of a magnetic Bloch electron. The key parameter determining the structure of the spectrum is the magnetic flux Φ passing through the crystal unit cell. If this flux, measured in magnetic flux quanta $\Phi_0 = 2\pi\hbar c/|e|$, is equal to a rational function p/q, with p and q being mutually prime numbers, one can introduce new primitive translation vectors determining the magnetic unit cell and, correspondingly, the new Brillouin magnetic zone [5, 6]. Here, c is the velocity of light and e is the absolute value of electron charge. For instance, if the vector potential corresponding to the magnetic field **H** directed along the z axis is taken in the Landau gauge $\mathbf{A} = (0, Hx, 0)$, then the magnetic translations in a simple square lattice with lattice parameter a will be determined as $x \longrightarrow x + qna$ and $y \longrightarrow y + ma$, where n and m are integer numbers. In the two-dimensional problem, the shape of the magnetic Brillouin zone will be determined by the inequalities

$$-\pi/qa \le k_x \le \pi/qa, \quad -\pi/a \le k_y \le \pi/a. \quad (1)$$

If the quasi-momentum vector sweeps all values in the magnetic Brillouin zone (1), the energy varies within a single magnetic subband. The number of subbands also depends on the magnetic flux through the crystal unit cell. If this flux (measured in flux quanta) is equal to p/q, then an individual Landau level splits into p energy subbands. The wave functions of magnetic Bloch electrons also possess unusual properties. For instance, the transformation law for these functions upon magnetic translations, or the Bloch–Peierls law, has the form [7]

$$\psi_{k_x, k_y}(x, y) = \psi_{k_x, k_y}(x + qa, y + a)$$
$$\times \exp(-ik_x qa)\exp(-ik_y a)\exp(-2\pi i p y/a). \quad (2)$$

This is the cause of the unusual topological properties of magnetic Bloch functions. The topological aspects of the problem considered were discussed by Novikov in [8]. He showed that the formation of p magnetic subbands near a single Landau level can be treated as a vector bundle of magnetic Bloch functions on a T^2 torus, i.e., in the magnetic Brillouin zone. The same problem was discussed by Avron, Seiler, and Simon within the framework of homotopy theory [9]. Simon [10] found the relation between the topological invariants and the Berry geometric phase [11]. Kohmoto showed that the Hall conductance of magnetic subbands is determined by the type of wave-function singularities and that this value is proportional to the first Chern number [12]. Later on, it was established that, similar to the Kubo formula, the Hall conductance can be represented as a two-dimensional integral over the magnetic Brillouin zone. This integral came to be known as "Berry curvature" [13–15]. The universal role of topological invariants in the quantum Hall effect was also demonstrated

for substrate-supported disordered systems [16] and for the problem with multiparticle interactions [17].

The unusual character of the quantum states of Bloch electrons in a strong magnetic field causes a number of intriguing physical effects. In particular, unusual quantization rules were revealed in a series of theoretical and experimental works for the Hall conductance of a 2D electron gas in an additional periodic potential. As was shown by Thouless *et al.* [18], the Hall conductance of a 2D electron gas, in which the Fermi level falls within the *r*th energy gap of the *N*th Landau level, is equal to

$$\sigma_H = \frac{e^2}{h}(t_r + N - 1), \qquad (3)$$

where the integer number t_r is a solution to the Diophantus equation

$$t_r p + s_r q = r, \qquad (4)$$

which has integer-valued solutions at s_r satisfying the inequality $|s_r| \leq p/2$.

Another method of calculating the Hall conductance of a 2D electron gas in the presence of a periodic potential was developed by Streda [19]. He showed that, if the Fermi level falls within the energy gap between two filled subbands, this conductance is given by the expression

$$\sigma_H = ec\frac{\partial N(E)}{\partial B}, \qquad (5)$$

where $N(E)$ is the number of quantum states per area unit with energy lower than the bandgap. Both the Diophantus equation and the Streda formula have been repeatedly used to calculate the electron-gas conductance in the presence of an additional periodic potential (see, e.g., [20, 21]). These approaches have also been used in studying 3D systems [22–24], where the generalized Streda formula is known as the Kohmoto–Halperin–Wu formula [23].

Regarding usual 3D crystals, the effects caused by the specific Bloch quantum states can be observed experimentally in magnetic fields on the order of 10^4 T. Fields as high as those are presently unattainable. However, if the lattice parameter is equal to 5–6 Å, then the flux through the unit cell will be equal to $p/q = 0.2$–0.3 of the magnetic flux quantum in a field of 2800 T that was achieved in the Federal Nuclear Center (Sarov) [25]. In such fields, the broadening of Landau levels can be observed. Nevertheless, the main hopes for the observation of magnetic quantum states, in particular, of the Hofstadter butterfly, are associated with the use of artificial 2D crystals—quantum dot crystals.

In recent years, the structures with a 2D electron gas modulated by a surface potential have drawn attention of many experimenters. The periodic potential in such structures is produced using a metallic gate to form quantum dot chains (antidots). Both classical effects

(commensurability of the lattice parameter with the cyclotron radius [26, 27], transition to the chaotic regime, etc.) and spectra consisting of magnetic subbands were observed in these systems. In the latter case, the superlattice parameters were 100 nm or smaller and the electron mobility in these subbands was high enough. In the cited experiments, the magnetic fields were on the order of 1 T. The splitting of magnetic levels into subbands in an *n*-type heterojunction with a surface superlattice was likely observed for the first time in [28]. A spectrum consisting of magnetic subbands was observed in [21], where the magnetoresistance of a heterojunction with a surface superlattice was also studied. A recent work [29] is also noteworthy. In [29] the structure of magnetic subbands was studied under conditions where the interactions between the neighboring Landau levels were essential.

This work is devoted to studying the quantum states of electrons and holes in heterojunctions with the surface superlattice exposed to an external static magnetic field. For the electron problem, periodic potentials without inversion center are considered and it is shown that, in this situation, the energy spectrum of magnetic subbands is asymmetric about the reversal of the quasi-momentum sign. A method for calculating the hole valence-band magnetic quantum states described by the Luttinger Hamiltonian is developed, allowing the spin and spin–orbit interactions to be taken into account. The topological invariants determining the quantization laws for the Hall conductance of 2D electrons and holes are investigated.

2. MAGNETIC BLOCH STATES AND HALL CONDUCTANCE OF A 2D ELECTRON GAS IN A PERIODIC POTENTIAL WITHOUT AN INVERSION CENTER

In the absence of a magnetic field, the energy spectrum of an electron moving in a periodic potential is invariant about the reversal of the quasi-momentum sign; i.e., $E(\mathbf{k}) = E(-\mathbf{k})$. This symmetry holds even if the periodic potential has no inversion center. The symmetry in the quasi-momentum space is due to the invariance of the stationary Schrödinger equation about the time reversal. In a magnetic field, the $t \longrightarrow -t$ symmetry is violated. As a result, the energy of a Bloch electron in a crystal without an inversion center in the presence of magnetic field will not be an even function of quasi-momentum within the magnetic Brillouin zone. One can expect that the crystal in which the energy spectrum is not symmetric in the $\mathbf{k}$ space would display unusual physical properties [30].

It is worth noting that the breaking of symmetry about the spatial inversion of the periodic potential affects the transport characteristics of electron gas in the classical case as well. This was demonstrated, e.g., in [31], where high- and low-frequency electron transport was studied for a square 2D lattice consisting of triangular dots. The system was exposed to an external
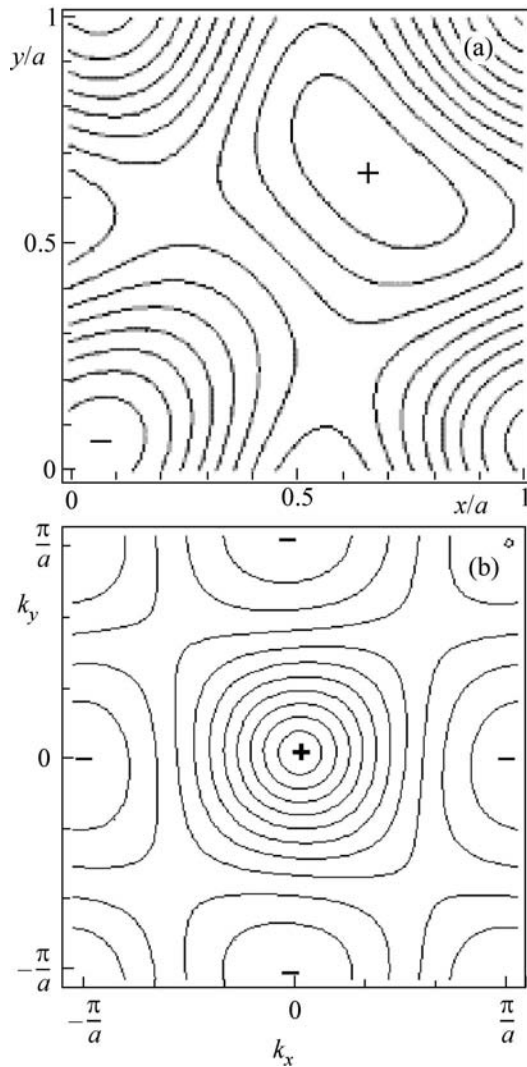
Fig. 1. (a) Equipotential lines for the crystal lattice potential $V(x, y)$ given by Eq. (8) with $V_2/V_1 = 0.1$. The signs "+" and "−" mark the potential maxima and minima. (b) Isoenergetic lines $E_1^1(\mathbf{k}) = $ const for the lower magnetic subband of the first Landau level $N = 1$; $V_2/V_1 = 0.1$ and $p/q = 3/1$. The signs "+" and "−" mark the energy maxima and minima in the subband.

magnetic field. The classical electron dynamics for such a lattice was examined in [32]. The irradiation of the system by an electromagnetic field in the far-IR region induced a dc voltage because of the absence of an inversion center in the potential.

Note that the symmetry of the energy spectrum of 3D crystals without a spatial inversion center can be violated in the **k** space by the spin–orbit interaction as well. This also occurs in a zero magnetic field, for which the $t \longrightarrow -t$ symmetry is not violated. In this case, only the Kramers degeneracy $E(\mathbf{k}, 1/2) = E(-\mathbf{k}, -1/2)$ holds. In semiconductors, such spectra are described, e.g., by the Luttinger Hamiltonian, which

includes Dresselhaus' terms linear and cubic in the wavevector projections. However, the spin–orbit mechanism violates symmetry only in a small region of the **k** space. Below, we will see that the spectrum of magnetic subbands in a periodic potential without an inversion center loses its symmetry over the entire magnetic Brillouin zone.

Choice of the model. Below, we calculate the quantum states of an electron gas and consider the quantization law for its Hall conductance in a periodic potential without an inversion center [30]. The electron Hamiltonian in a uniform magnetic field and in a field of a two-dimensional periodic potential can be written in the form

$$\hat{H} - \hat{H}_0 + V(x, y), \qquad (6)$$

where

$$\hat{H}_0 = \frac{1}{2m^*}\left(\hat{\mathbf{p}} - \frac{e\mathbf{A}}{c}\right)^2 \qquad (7)$$

is the Hamiltonian in a magnetic field. Here, c is the velocity of light, e is the electron charge, and m^* is the electron effective mass. The vector potential is chosen in the Landau gauge $\mathbf{A} = (0, Hx, 0)$, so that the magnetic field **H** is directed along the z axis. The model potential of a square lattice without an inversion center is written as

$$V(x, y) = V_1\cos^2(\pi x/a)\cos^2(\pi y/a)$$
$$+ V_2[\sin(2\pi x/a) + \sin(2\pi y/a)], \qquad (8)$$

where a is the lattice parameter. The equipotential lines are shown in Fig. 1a. The second term on the right-hand side of this expression is proportional to V_2 and determines the degree of breaking the lattice symmetry about the spatial inversion. At $V_2 = 0$, this symmetry is regained. In what follows, the amplitude V_1 will be fixed.

As was mentioned above, the structure of the eigenstates of Hamiltonian (6) and the spectrum of its eigenvalues depend on the magnetic flux through the crystal unit cell. We will assume that the magnetic flux p/q is a rational number. Otherwise the spectrum would consist of an infinite number of magnetic subbands and have the fractal structure [4]. If the inequalities

$$\hbar\omega_c \gg V_1, V_2; \quad l_H \ll a, \qquad (9)$$

are fulfilled, where l_H and ω_c are the magnetic length and the cyclotron frequency, respectively, then the quantum states can be calculated perturbatively, i.e., without taking into account the interaction between different Landau levels. A simple estimate suggests that the condition $p/q = 3$ for a lattice with parameter $a = 80$ nm is fulfilled in the magnetic field $H \simeq 2$ T and inequalities (9) are fulfilled for $V_1, V_2 \approx 1$ meV. The electron wave function satisfying the Bloch–Peierls conditions for the μth magnetic subband is sought as the

expansion in the Landau functions corresponding to the Nth level [18]:

$$\Psi^N_{\mathbf{k},\mu}(x, y)$$

$$= \sum_{n=1}^{p} C^N_{n\mu}(\mathbf{k}) \sum_{l=-\infty}^{+\infty} \varphi_N \left[\frac{x - x_0 - lqa - nqa/p}{l_H} \right] \quad (10)$$

$$\times e^{ik_y y} e^{ik_x(lqa + nqa/p)} e^{2\pi i y(lp+n)/a},$$

where φ_N is the eigenfunctions of the harmonic oscillator and $x_0 = c\hbar k_y/|e|H = k_y l_H^2$. Note that condition (2) is fulfilled if the coefficients of expansion (10) satisfy the relationship

$$C^N_{n+p,\mu}(\mathbf{k}) = C^N_{n\mu}(\mathbf{k}). \quad (11)$$

In the representation of functions (10), the stationary Schrödinger equation $\hat{H}\Psi = E\Psi$ is written as

$$H^N_{nm}(\mathbf{k})C^N_{m\mu}(\mathbf{k})$$

$$= [E^0_N(p/q)\delta_{nm} + V^N_{nm}(p/q, \mathbf{k})]C^N_{m\mu} \quad (12)$$

$$= E^N_\mu(\mathbf{k})C^N_{n\mu}(\mathbf{k}),$$

where $E^0_N = \hbar\omega_c(N + 1/2)$.

Due to the periodicity of Eq. (11) in n and m with period p, the tridiagonal matrix V^N_{nm} in Eq. (12) has the size $(p \times p)$ [30], whence it follows that, for the rational values p/q of flux, each discrete magnetic level splits into p magnetic subbands. We now calculate the wave functions and the spectra.

Quantum states. For the prime rational values of flux, the energy spectrum and wave functions $C^N_{n\mu}(\mathbf{k})$ can easily be found analytically. Large Hamiltonian matrices can be diagonalized numerically. In the work of Demikhovskii and Perov [30], the quantum states of magnetic Bloch electrons in a lattice without an inversion center were calculated analytically for the flux $p/q = 3/1$. Figure 1b shows the isoenergetic lines for the calculated spectrum, which, as seen, does not possess an inversion center in the $\mathbf{k}$ space. This figure demonstrates the energy distribution in the lowest of the three magnetic subbands corresponding to the Landau level with $N = 1$. It can readily be verified that, upon reversal of the magnetic-field direction ($\mathbf{H} \longrightarrow -\mathbf{H}$), the spectrum transforms as

$$E_\mu(\mathbf{k}, \mathbf{H}) = E_\mu(-\mathbf{k}, -\mathbf{H}).$$

Despite the spectrum asymmetry, the energies

$$E_\mu(k_x, \pi/a) = E_\mu(k_x, -\pi/a),$$

$$E_\mu(\pi/qa, k_y) = E_\mu(-\pi/qa, k_y)$$

are equal at the opposite boundaries of the magnetic Brillouin zone, as also are the corresponding partial

derivatives $\partial E/\partial k_\alpha$ ($\alpha = x, y$). However, because of the absence of central symmetry at the center and boundaries of the magnetic zone, the derivatives $\partial E/\partial k_\alpha$ are nonzero. The structure of the energy spectrum depends explicitly on the parameter V_2. It was shown in [30] that, for certain critical values V_2^{cr}, the energy gap between the neighboring subbands disappears and the surfaces $E^N_\mu(\mathbf{k})$ touch at a certain point $\mathbf{k}_0$ lying on the diagonal of the magnetic Brillouin zone. For instance, at $(V_2/V_1)^{cr} = 0.051706$ and $p/q = 3/1$, the energy in the lower subband of the zeroth Landau level becomes equal to the energy of the middle subband. This touch occurs at the point $\mathbf{k}_0$ where the energy of the lower subband is maximal. With a further increase in the parameter V_2, this degeneracy is removed and the neighboring subbands become again separated by the energy gap. We will show below that, as V_2 reaches its critical value, the singularities of the eigenvector $C^N_{n\mu}(\mathbf{k})$ of system (12) undergo jumpwise change in the $\mathbf{k}$ space at the point of gap collapse. The topological invariants (Chern classes determining the Hall conductance) change simultaneously.

The eigenvectors $C^N_{n\mu}(\mathbf{k})$ can be chosen proportional to the cofactors $D_{jn}(\mathbf{k})$ of any (e.g., jth) row of the determinant corresponding to the set of Eqs. (12) at $E = E_\mu(\mathbf{k})$. N.A. Usov [33] showed that, in these terms, the components of the normalized eigenvector are

$$C^{(j)}_n(\mathbf{k}) = R^{(j)}_n(\mathbf{k})\exp(i\phi^{(j)}_n(\mathbf{k})),$$

$$R^{(j)}_n(\mathbf{k}) = \left(D_{nn}(\mathbf{k})/\sum_{s=1}^{p} D_{ss}(\mathbf{k}) \right)^{1/2}, \quad n \neq j. \quad (13)$$

In the last formula, the quantity $D_{nn}(\mathbf{k})$ is a cofactor of the matrix element $[H^N_{nn} - E^N_\mu]$ and the phase $\phi^{(j)}_n(\mathbf{k})$ is defined by the relationship

$$\cos\phi^{(j)}_n = \frac{\mathbf{Re}D_{jn}}{|D_{jn}|}, \quad \sin\phi^{(j)}_n = \frac{\mathbf{Im}D_{jn}}{|D_{jn}|}, \quad n \neq j. \quad (14)$$

One can readily verify that $C^{(j)}_j(\mathbf{k})$ is a purely real component and turns to zero at the points $\mathbf{k}_m$ of the so-called expanded magnetic Brillouin zone defined by the inequalities $-\pi/qa \leq k_x \leq \pi/qa$ and $-\pi p/qa \leq k_y \leq \pi p/qa$ [33]. The other $C^{(j)}_n(\mathbf{k}_m)$ components with $n \neq j$ do not tend to any definite limit at $\mathbf{k} \longrightarrow \mathbf{k}_m$, so one can say that the corresponding point $\mathbf{k}_m$ is the phase branch point. Hereafter, the index in the brackets will stand for the representation, i.e., for the row number, and we will omit the magnetic subband index μ and the Landau level number N.

Quantization of Hall conductance. The Hall conductance of 2D electrons in a periodic potential with

several completely filled magnetic subbands, so that the Fermi level lies within the energy gap, is quantized in e^2/h units. Although one could assume that the Hall conductance of each subband would be equal to e^2/ph, where p is the number of magnetic subbands and e^2/h is the conductance of the unsplit Landau level, this is, nevertheless, not the case. According to the well-known Laughlin arguments, the Hall-current transfer for each magnetic subband should be a multiple of the current corresponding to the entire filled Landau level. The nature of such a Hall conductance quantization in the presence of an additional periodic potential can be clarified by a simple model introduced by Thouless *et al.* in [18]. To this end, we assume that the rectangular lattice is strongly anisotropic, so that the overlap integrals in the x direction are much smaller than the ones in y. Let now the electric field be directed along the y axis. Then the wavevector component k_y will monotonically vary with time and, in compliance with the definition of x_0, the coordinate specifying the center of gravity of the harmonic oscillator eigenfunction $\varphi_N(x - x_0)$ will also change monotonically. The resulting electric current is directed along x. However, the position of $\varphi_N(x)$ depends not only on x_0 but, as seen from Eq. (10), can also change with changing the number n. If, for a given k_y, the eigenvector component C_n dominates some magnetic subband, then, with a further change in k_y, the separation between the neighboring subbands reaches its minimum and the role of the dominant component will go from C_n to the other component C_{n+s}, where s is an integer number. At this point, the corresponding oscillator function in Eq. (10) will move jumpwise at a distance of sqa/p in the x direction. It is shown in [18] that, for the simple case of a parabolic one-dimensional spectrum, the value of s can be found as a solution to the Diophantus equation (4). Then, to calculate the overall Hall conductance, it suffices to sweep k_y within the entire one-dimensional Brillouin zone and make allowance for both monotonic and all jumplike shifts of the wave-function center of gravity along the z axis. Unfortunately, it is unclear how these simple considerations can be extended to more realistic potentials. For this reason, we will consider below different approaches that are based on the use of the Kubo formula.

In the absence of disorder, the zero-temperature contribution from the subband α to the Hall conductance is given by the following formula, which is a direct consequence of the Kubo formula [12, 18, 33]:

$$\sigma_{xy}^{\alpha} = \frac{e^2}{\pi^2 \hbar} \int \text{Im} \left\langle \frac{\partial u_{\mathbf{k}}}{\partial k_y} \middle| \frac{\partial u_{\mathbf{k}}}{\partial k_x} \right\rangle d^2 k, \qquad (15)$$

where $u_{\mathbf{k}} = \Psi_{k_x k_y}(\mathbf{r}) e^{-i\mathbf{k}\mathbf{r}}$ is the periodic part of the total wave function of the subband. This formula can be used to obtain a comparatively simple and explicit expres-

sion for the conductance of a filled magnetic subband corresponding to the Nth Landau level [33]:

$$\sigma_{xy} = -\frac{e^2}{h} \left[\frac{1}{p} + \frac{q}{p} \sum_{\mathbf{k}_m} S(\mathbf{k}_m) \right]. \qquad (16)$$

Here, the integer number $S(\mathbf{k}_m)$ is the phase incursion (in units of 2π) $\phi_n^{(j)}(\mathbf{k})$ for the functions $C_n^{(j)}(\mathbf{k})$ from Eq. (13) upon going clockwise around the singular point $\mathbf{k}_m$.

As an example, we calculated in [30] the Hall conductance of a 2D electron gas in a magnetic subband with $p/q = 3/1$. The periodic potential was chosen in the form of (8). The eigenstates of Hamiltonian (6) were calculated in the representation of the first row of the determinant for the system of Eqs. (12). The sections and singularities of the function $C_1^{(1)}(\mathbf{k})$ in the expanded magnetic Brillouin zone are shown in Figs. 2a and 2b. The ratio V_2/V_1 in these two figures is, respectively, smaller and larger than the critical value. The remaining parameters of the system are given in the subscript to the figure. Two singularities correspond to the phase branch points where the function $C_1^{(1)}(\mathbf{k})$ turns to zero; they are denoted by A and B (Fig. 2a). Direct calculation showed that, upon going around each of these points along the contour shown in the figure, the phases of the $C_2^{(1)}(\mathbf{k})$ and $C_3^{(1)}(\mathbf{k})$ components change by $+2\pi$. Hence it follows that $S(\mathbf{k}_A) = S(\mathbf{k}_B) = 1$ and, according to Eq. (16), the conductance in the lower band is $\sigma_{xy} = -e^2/h$. The contributions to the conductance from other magnetic subbands can be calculated in a similar manner. This proved that the conductance of the filled middle and upper subbands of the zeroth Landau level is zero. The Hall conductances for different positions of the Fermi level in magnetic subbands are shown for this case in Fig. 3 and marked by the number *1*. As the parameter V_2 varies, the singular points A and B move in the expanded Brillouin zone, with small changes in V_2 bringing about small shifts in singularities. In accordance with the topological nature of the invariants, the conductance σ_{xy} changes jumpwise only at the instant the branches of the neighboring subbands touch each other (become degenerate) at the point $\mathbf{k}_0$ (in the case at hand, we deal with the degeneracy of the lower and middle subbands). At the critical value of parameter V_2, the A and B singularities simultaneously disappear, so that the function $C_1^{(1)}(\mathbf{k})$ does not turn to zero. At this moment, new singularity arises, and they are denoted by C in Fig. 2b. The scenario for the singularity rearrangement is as follows. The two initial points do not annihilate and do not leave the expanded Brillouin zone. At this moment, the component $C_1^{(1)}(\mathbf{k})$ merely turns to zero at the point C, while the two other components at points A and B are no
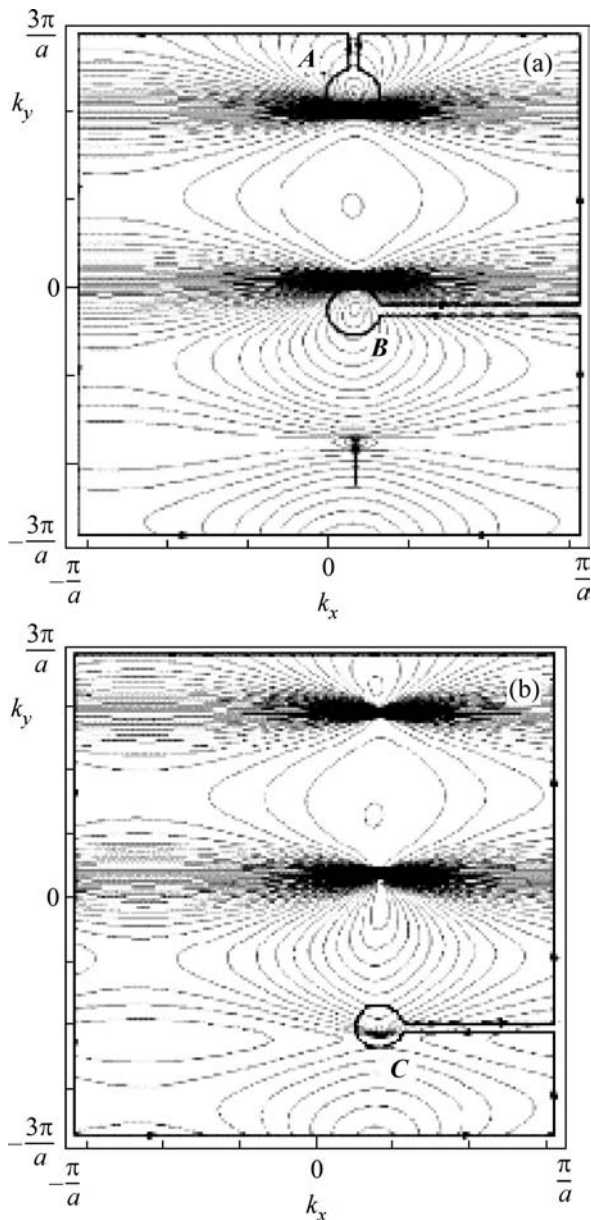
Fig. 2. Equivalue lines of the real function $C_1^1(\mathbf{k})$ and its singularities in the expanded Brillouin zone for the $N = 0$ Landau level and $p/q = 3/1$; $V_2/V_1 = $ (a) 0.02 and (b) 0.06.

Fig. 3. Hall conductances of the filled magnetic subbands for different positions of the Fermi level and (*1*) below-critical and (*2*) above-critical value of V_2/V_1; $N = 0$ and $\mu = 1$, 2, 3.

longer zero. At $V_2 < V_2^{cr}$, the position of the local minimum of the function $C_1^{(1)}(\mathbf{k})$, which is a nucleus of the future singularity C, is indicated by an arrow in Fig. 2a.

After going around the point C along the contour shown in Fig. 2b, the phase of each of the $C_2^{(1)}(\mathbf{k})$ and $C_3^{(1)}(\mathbf{k})$ components changes by -2π, so that, according to Eq. (16), the contribution from the lower magnetic subband of the zeroth Landau level to the conductance becomes zero. The position of Hall plateaus cor-
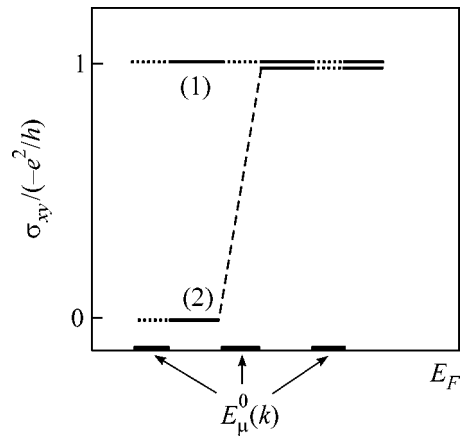
responding to the three magnetic subbands is denoted for this case by the number *2* in Fig. 3. In this case, the contribution to the conductance equals $-e^2/h$ and comes from the middle magnetic subband $E_2(\mathbf{k})$, which touches the lower energy subband upon reaching the critical value V_2^{cr}. At the same time, it is clear that, at $V_2 = 0$, the variation of V_1 cannot affect the Hall conductance quantization law, because only the ratio of these coefficients is significant. Thus, in the crystals without an inversion center, Hall conductance obeys a new quantization law which, together with the topological parameters, can change abruptly upon reaching critical values of the parameter characterizing the degree of breaking the central symmetry.

Photovoltaic effect. In the absence of inversion symmetry in the $\mathbf{k}$ space, the so-called photovoltaic effect should be observed; i.e., an electromagnetic wave propagating along the normal to the heterostructure surface should induce a surface dc electric current. This effect was predicted and experimentally studied in semiconductor crystals without an inversion center, where the symmetry in the $\mathbf{k}$ space is broken due to the spin–orbit interaction. The nature of the quantum photovoltaic effect that should be observed for a 2D electron gas in a periodic potential without an inversion center is illustrated in Fig. 4. In this figure, the energies $E_\mu^{0,1}(\mathbf{k})$ are plotted against the projection of quasi-momentum $\mathbf{k}$ onto the diagonal of the magnetic Brillouin zone. It is assumed that the direct electron transitions proceed between the magnetic subbands of the zeroth and first Landau levels. The upper subband $E_3^0(\mathbf{k})$ of the zeroth level is partially filled. If the photon energy is such that the transitions occur to the lower subband $E_1^1(\mathbf{k})$ of the first Landau level, then the radiation-induced dc current will flow in the direction of the
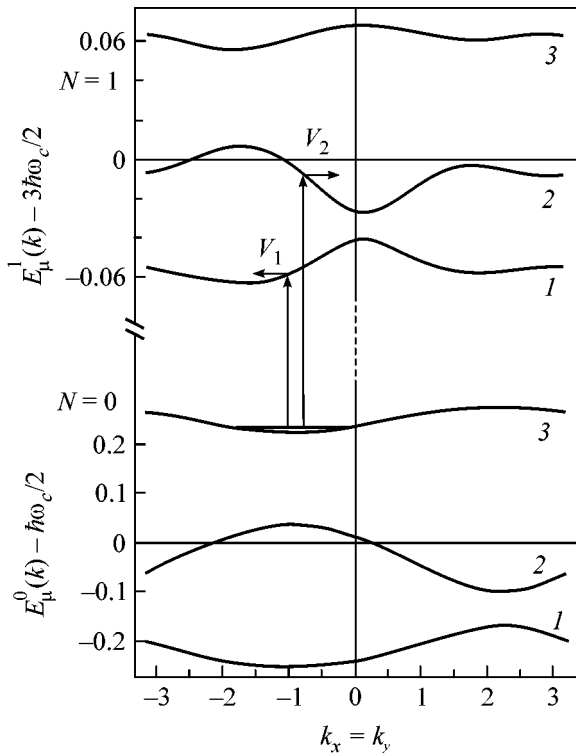
Fig. 4. Quantum transitions between the magnetic subbands in a two-dimensional crystal without an inversion center. Arrows indicate the velocity directions in the final state.

group velocity vector $\mathbf{V}_1 = \partial E_1^1/\partial \mathbf{k}$. For the other resonance photon energies, e.g., for the case where the electron transitions occur to the $E_2^1(\mathbf{k})$ subband, the photocurrent direction will be opposite. It is worth noting that the dipole transitions in the potential $V(\mathbf{r})$ without an inversion center are allowed between the magnetic subbands belonging to any Landau level. This effect should be observed for both linear and circular polarizations of an electromagnetic field. To estimate the magnitude of the photovoltaic current for a given photon flux, one

must calculate the transition probabilities and velocities in the final states of magnetic subbands.

3. QUANTUM STATES AND HALL EFFECT IN *p*-TYPE HETEROJUNCTIONS WITH A SURFACE SUPERLATTICE

In recent years, considerable progress has been achieved in the fabrication of low-dimensional *p*-type structures based on GaAs/AlGaAs heterojunctions [34–36]. As a result, 2D hole channels have come to display practically the same effects as are observed for the *n*-type structures. The first experiments on studying transport in a surface-modulated hole gas were carried out in [37]. In this connection, the hole quantum states in a heterojunction with a surface potential in a perpendicular magnetic field were studied in [38, 39], where the quantum Hall effect and magneto-optics were also examined. The calculation of the hole magnetic Bloch states in the Luttinger model was also of interest in that the spin and spin–orbit interactions of charged particles were taken into account in this problem for the first time.

Spectrum and wave functions: computational schemes. In the presence of an external magnetic field $\mathbf{H} \parallel z$ with the vector potential $\mathbf{A}$, light and heavy holes near the Γ points are described by the Luttinger Hamiltonian. In this Hamiltonian, the wavevector components $k_\pm = k_x \pm i k_y$ are replaced by the operators

$$k_\alpha \longrightarrow \hat{k}_\alpha = -i\frac{\partial}{\partial x_\alpha} + \frac{e}{c}A_\alpha. \tag{17}$$

In addition, the terms describing the interaction of spin κ with the external magnetic field should be added to all elements of the main diagonal. After passing to the creation and annihilation operators defined as

$$\hat{a}^+ + \frac{R_c}{\sqrt{2}}\hat{k}_+, \quad \hat{a} = \frac{R_c}{\sqrt{2}}\hat{k}_-, \tag{18}$$

where $R_c = [c/eH]^{1/2}$, one arrives at the following matrix:

where

$$\hat{H}_L = \begin{bmatrix} \hat{H}_{11} & \bar{\gamma}\sqrt{3}(eH/c)\hat{a}^2 & \gamma_3\sqrt{6eH/c}\,k_z\hat{a} & 0 \\ & \hat{H}_{22} & 0 & -\gamma_3\sqrt{6eH/c}\,k_z\hat{a} \\ & & \hat{H}_{33} & \bar{\gamma}\sqrt{3}(eH/c)\hat{a}^2 \\ & & & \hat{H}_{44} \end{bmatrix}, \tag{19}$$

where

$$H_{11} = -(\gamma_1/2 - \gamma_2)k_z^2 - (eH/c)\left[(\gamma_1 + \gamma_2)\left(\hat{a}^+\hat{a} + \frac{1}{2}\right) + \frac{3}{2}\kappa\right] + V_h(z) + V(x, y),$$

$$H_{22} = -(\gamma_1/2 + \gamma_2)k_z^2 - (eH/c)\left[(\gamma_1 - \gamma_2)\left(\hat{a}^+\hat{a} + \frac{1}{2}\right) - \frac{1}{2}\kappa\right] + V_h(z) + V(x, y),$$

$$H_{33} = -(\gamma_1/2 + \gamma_2)k_z^2 - (eH/c)\left[(\gamma_1 - \gamma_2)\left(\hat{a}^+\hat{a} + \frac{1}{2}\right) + \frac{1}{2}\kappa\right] + V_h(z) + V(x, y),$$

$$H_{44} = -(\gamma_1/2 - \gamma_2)k_z^2 - (eH/c)\left[(\gamma_1 + \gamma_2)\left(\hat{a}^+\hat{a} + \frac{1}{2}\right) - \frac{3}{2}\kappa\right] + V_h(z) + V(x, y).$$

The lower triangular part of matrix (19) is related to its upper triangular part by Hermitian conjugation. Here, e is the absolute value of an elementary charge; the Luttinger parameters are chosen as [34] $\gamma_1 = 6.85$, $\gamma_2 = 2.1$, $\gamma_3 = 2.9$, and $\kappa = 1.2$; $V_h(z)$ is the heterojunction potential; and $V(x, y)$ is the periodic potential. The solutions to the Schrödinger equation with Luttinger Hamiltonian (19) have the form of envelopes of wave functions constructed from the p-type atomic functions that transform as eigenfunctions of the angular momentum operator for $J = 3/2$. We assume that holes in a heterojunction grown in the z direction are confined in a smoothly varying potential $V_h(z)$. We also assume that $V_h(z)$ has a triangular profile, while the heterojunction boundary is impermeable, so that the boundary condition is $\psi(0) = 0$. Since the triangular profile has no inversion center, i.e., $V_h(z) \neq V_h(-z)$, the twofold spin degeneracy will be removed. The eigenvectors of operator (19) have four components and are written in the basis set of functions J; $|J; m_J\rangle$ [34]. The translational properties in the (x, y) plane for each of the components of the envelope function are the same as for the one-component electronic states; i.e., each component satisfies the Bloch–Peierls condition (2). For this reason, the components of envelope $\psi_{k_x k_y}^j$ can be written as a superposition of the Landau quantum states [18]:

$$\psi_{k_x k_y}^j(\mathbf{r}) = \frac{1}{La\sqrt{q}}\sum_\nu C^\nu(z)\sum_{N}\sum_{n=1}^{p} d_{j\nu Nn}$$

$$\times \sum_{l=-L/2}^{L/2} \phi_{Nj}\left(\frac{x - x_0 - lqa - nqa/p}{l_H}\right)$$

$$\times \exp\left(ik_x\left[lqa + \frac{nqa}{p}\right]\right)$$

$$\times \exp\left(2\pi iy\frac{lp + n}{a}\right)\exp(ik_y y). \tag{20}$$

We now discuss the structure of hole functions (20). In the calculations, one usually takes into account the limited number of size-quantization subbands in the sum over ν, e.g., two heavy hole subbands and one light hole subband. In addition, the number N of Landau levels in each subband is taken to be finite. In our calculations, it varied from 7 to 11. As in the expression for the electron wave function, the summation over n goes from 1 to p.

After substituting total hole function (20) into the Schrödinger equation with Hamiltonian (19), one arrives at a eigenvalue problem with a matrix of size $Np \times Np$ for the Np components $d_{j\nu Nn}(k_x, k_y)$ in each of the Np hole magnetic subbands $\varepsilon_{\nu Nn}(k_x, k_y)$:

$$\sum_{j'\nu'N'n'} (H_{j\nu Nn}^{j'\nu'N'n'} + V_{j\nu Nn}^{j'\nu'N'n'}(p/q, k_x, k_y))d_{j'\nu'N'n'}$$

$$= \varepsilon d_{j\nu Nn}. \tag{21}$$

Here, we introduce the notation $H_{j\nu Nn}^{j'\nu'N'n'}$ for the matrix elements of Hamiltonian (19) between the expansion functions in Eq. (20) and $V_{j\nu Nn}^{j'\nu'N'n'}(p/q, k_x, k_y)$ for the corresponding matrix elements of periodic potential (8) with $V_2 = 0$. The system of Eqs. (21) was diagonalized in [38, 39] for various magnetic-field strengths and amplitudes of the periodic potential. The maximum size of matrix (21) corresponded to $p/q = 20$ and was 220×220. The results of these calculations are used below for determining the Hall conductance (see next section).

In closing this section, mention should be made of one more intriguing feature of the eigenfunctions: each magnetic Bloch function satisfying the Bloch–Peierls conditions (2) has at least p zeros within one magnetic cell (if the flux through it is equal to p/q). This rule can be extended to multicomponent wave functions [39]. Namely, let $\theta_\mathbf{k}^j$ denote the phase for the periodic part $u_\mathbf{k}^j(\mathbf{r}) = \exp(-i\mathbf{kr})\psi_\mathbf{k}^j(\mathbf{r})$ of the jth hole-function component $\psi_\mathbf{k}^j(\mathbf{r})$ given by Eq. (20). Then, similar to the electronic problem [12], one can introduce for each phase the circulation Γ_j defined as

$$\Gamma_j = \frac{1}{2\pi}\oint d\mathbf{l}\frac{\partial\theta_\mathbf{k}^j(x, y)}{\partial\mathbf{l}}, \tag{22}$$

where the integration contour goes in the positive direction along the magnetic cell boundary. Since the Peierls conditions (2) are fulfilled simultaneously for each of the hole wave-function components, it seems natural that circulations (22) are identical for all components:

$$\Gamma_j = -p, \quad j = 1, 2, 3, 4. \tag{23}$$

The calculations show that the positions of zeros for different components do not coincide and that the total number of zeros can be both larger and smaller than p, with the overall circulation being always fixed. These

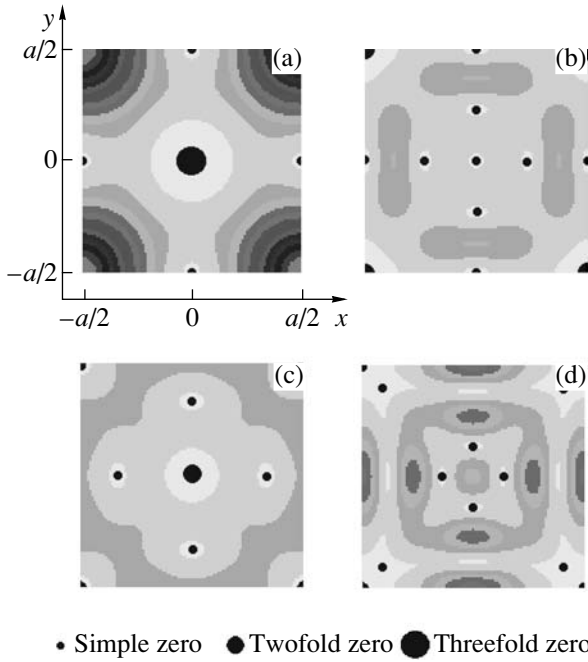• Simple zero   ● Twofold zero   ⬤ Threefold zero

Fig. 5. (a)–(d) Probability density at the point $k_x = k_y = 0$ for the four wave-function components of the state with index $N = 2+$ and $p/q = 5$. Dark regions correspond to the higher probability densities. The positions of the wave-function zeros are marked by black circles of different diameter corresponding to the multiplicity of zero.
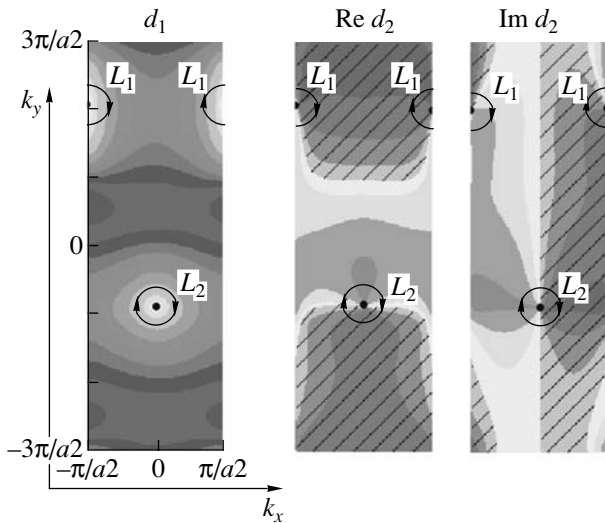

Fig. 6. Typical distribution of the singularities of eigenvector components d_1 and d_2 in the d_1 representation for $p/q = 3/2$. The distribution for the third component is not shown. The dark regions correspond to the larger absolute values of $d_{1,2}$, and the regions of negative values are cross-hatched.

conclusions are illustrated in Fig. 5, where the probability density is plotted in the (x, y) plane for different wave-function components of one of the Landau-level subbands with the number $N = 2+$ and flux $p/q = 5$. The

black circles in Fig. 5 indicate the positions of zeros and their multiplicities. Without going into detail, we note that the above-mentioned wave-function singularities in the coordinate space, as well as the singularities in the momentum space σ_H, have a topological nature, because they are independent of the particular form of the Hamiltonian.

Quantization of Hall conductance. As in the case of electron gas, the Hall conductance for holes is quantized in units e^2/h if the Fermi level lies in the energy gap. The value of σ_H is equal to the sum of contributions from all subbands lying below the Fermi level. For this reason, we first determine the Hall conductance of a single completely filled subband α. For the four-component function (20), Eq. (15) is replaced by the sum of four terms:

$$\sigma_H^\alpha = \frac{e^2}{\pi^2 \hbar} \sum_{j=1}^{4} \int \mathrm{Im} \left\langle \frac{\partial u_{\mathbf{k}}^j}{\partial k_y} \middle| \frac{\partial u_{\mathbf{k}}^j}{\partial k_x} \right\rangle d^2 k, \qquad (24)$$

where $u_{\mathbf{k}}^j = \Psi_{k_x k_y}^{(j)}(\mathbf{r}) e^{-i\mathbf{k}\mathbf{r}}$ is given by Eq. (20). In [39], we restricted ourselves to the magnetic subbands of only the lower size-quantization band, which is the only one that is filled at typical carrier concentrations. The upper size-quantization bands were disregarded. Next, the hole function $u_{\mathbf{k}}^j$ was substituted into Eq. (24). Considering that the basis-set functions in Eq. (20) are mutually orthogonal and normalized, one can express Eq. (24) through the partial derivatives of the eigenvector components $d_{jvNn}(k_x, k_y)$. This part of the calculation is similar to the computational procedure in the problem with a one-component electronic function. For the sake of brevity, the set of indices ($jvNn$) of the vector $d_{jvNn}(k_x, k_y)$ are replaced by a single index $n = 1, ..., Np$, which sweeps sequentially over all required values. As a result, the following expression for σ_H is obtained from Eq. (24):

$$\sigma_H = \frac{e^2}{\pi^2 \hbar} \int \mathrm{Im} \left[\frac{i}{2} l_H^2 + \sum_{n=1}^{N_p} \frac{\partial d_n^*}{\partial k_y} \frac{\partial d_n}{\partial k_x} \right] d^2 k, \qquad (25)$$

which reduces to expression (16) in the same manner as in the electronic problem. A typical picture of the d_1, $\mathrm{Re}\, d_2$, and $\mathrm{Im}\, d_2$ distributions in one of the magnetic subbands is shown in Fig. 6 for the magnetic flux $p/q = 3/2$, lattice parameter $a = 80$ nm, and amplitudes of periodic potential (8) $V_1 = 0.7$ meV and $V_2 = 0$, which corresponds to the nonoverlapping hole magnetic subbands. The contours $L_{1,2}$ of going around the singularities are shown schematically.

The conductance σ_H as a function of the number of filled magnetic subbands (or the position of Fermi level) is shown in Figs. 7 and 8 for the nonoverlapping and overlapping magnetic subbands, respectively. If the amplitude V_1 of the periodic potential does not exceed the gap between the neighboring Landau levels, the
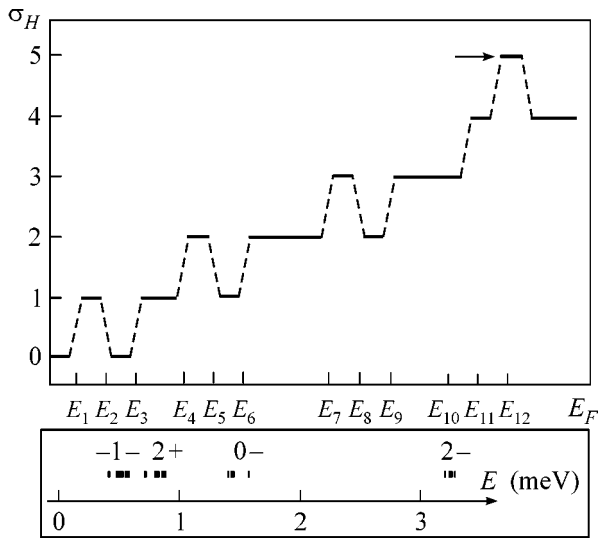
Fig. 7. Hall conductance σ_H (solid lines) for different positions of the Fermi level. The values E_n indicate schematically positions of the subband centers. The dashed lines denote the transition regions, and arrow points to the region where the conductance differs from the corresponding value for electrons. The spectrum of magnetic subbands and the Landau level indices are shown in the inset.
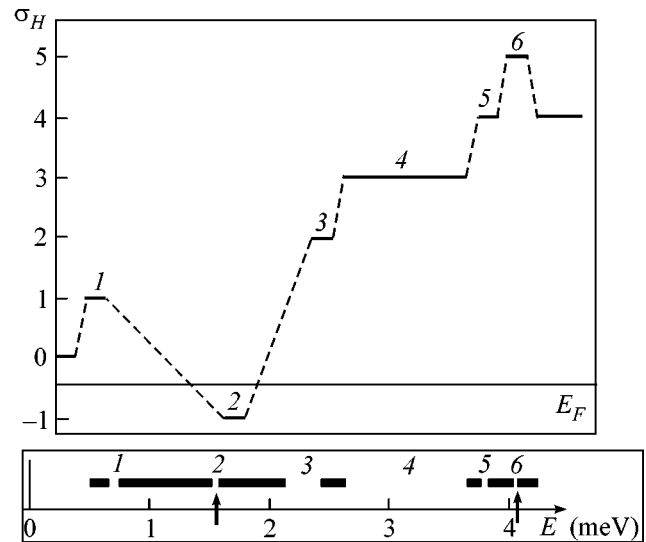

Fig. 8. The quantized σ_H values for different positions of the Fermi level in the regions between the overlapped magnetic subbands. The calculation is for the same Landau levels as in Fig. 7 but for a larger amplitude of the periodic potential: $V_1 = 3$ meV. The numbers indicate energy gaps, and arrows indicate the regions where σ_H takes extreme values.

magnetic subbands do not overlap (Fig. 7) and the possible distinctions from the σ_H quantization in the electronic problem are caused by the interaction between the hole Landau levels through the off-diagonal matrix elements of the Luttinger Hamiltonian [39]. It should be noted that, upon a smooth increase in the hole concentration accompanied by moving the Fermi level through the magnetic subband (or through a group of overlapped subbands), the Hall conductance smoothly varies between the neighboring quantum values indicated in Figs. 7 and 8 by heavy lines. A smooth change in σ_H is shown by the dashed lines. In this region, the exact behavior of conductance is unknown to us.

As the amplitude V_1 of the periodic potential increases, the magnetic subbands corresponding to different Landau levels overlap. Moreover, the subbands may also touch each other at a certain point in the magnetic Brillouin zone. At this point, the spectrum is degenerate and formula (16) cannot be used to calculate the Hall conductance. However, our numerical calculations have shown that, with a further increase in V_1, the subbands push themselves apart and the degeneracy in the spectrum is removed. For this reason, the use of formula (16) at large V_1 becomes again valid even if $|V_1| > |\Delta E_{12}|$, i.e., in the system with overlapped subbands. An example of such a spectrum for $V_1 = 3$ meV is shown at the bottom of Fig. 8. One can see that, as the amplitude of the potential increases, the total number of gaps and their maximal width decrease, as compared to the spectrum shown in Fig. 7. For convenience, the retained gaps and the corresponding Hall plateaus are numbered

in succession in Fig. 8. The transition regions are indicated by dashed lines. A comparison of Figs. 7 and 8 shows that the distinction in the quantization law for the nonoverlapping and overlapping subbands is observed only for subbands 4 and 8. The calculations showed that, at a certain intermediate amplitude of the periodic potential, larger than in Fig. 7 but smaller than in Fig. 8, degeneracy enters these subbands. At the instant the neighboring subbands touch each other, they "exchange" Chern classes, bringing about a change in the quantization law. The abnormally large and abnormally small (negative) values of σ_H are indicated by arrows. For negative σ_H, the Hall current is in opposition to its standard direction. Note that the appearance of the negative σ_H in some gaps was earlier predicted for a 2D electron gas in a periodic potential as well [20, 21].

REFERENCES

1. P. G. Harper, Proc. R. Soc. London, Ser. A **68**, 874 (1955).
2. M. Ya. Azbel, Zh. Éksp. Teor. Fiz. **46**, 929 (1964) [Sov. Phys. JETP **19**, 634 (1964)].
3. F. H. Claro and J. H. Wannier, Phys. Rev. B **19**, 6068 (1979).

4. D. R. Hofstadter, Phys. Rev. B **14**, 2239 (1976).

5. J. Zak, Phys. Rev. **136**, A776 (1964); Phys. Rev. **136**, A1647 (1964).

6. E. M. Lifshitz and L. P. Pitaevsky, *Course of Theoretical Physics*, Vol. 5: *Statistical Physics* (Nauka, Moscow, 1978; Pergamon, New York, 1980), Part 2.

7. R. E. Peierls, Z. Phys. **80**, 763 (1933).

8. B. A. Dubrovin and S. P. Novikov, Zh. Éksp. Teor. Fiz. **79**, 1006 (1980) [Sov. Phys. JETP **52**, 511 (1980)]; S. P. Novikov, Dokl. Akad. Nauk SSSR **257**, 538 (1981).

9. J. Avron, R. Seiler, and B. Simon, Phys. Rev. Lett. **51**, 51 (1983).

10. B. Simon, Phys. Rev. Lett. **51**, 2167 (1983).

11. M. V. Berry, Proc. R. Soc. London, Ser. A **392**, 45 (1984).

12. M. Kohmoto, Ann. Phys. (N.Y.) **160**, 343 (1985).

13. M. Kohmoto, J. Phys. Soc. Jpn. **62**, 659 (1993).

14. M.-C. Chang and Q. Niu, Phys. Rev. B **53**, 7010 (1996).

15. J. Goryo and M. Kohmoto, Phys. Rev. B **66**, 085118 (2002).

16. H. Aoki and T. Ando, Phys. Rev. Lett. **57**, 3093 (1986).

17. Q. Niu, D. J. Thouless, and Y.-S. Wu, Phys. Rev. B **31**, 3372 (1985).

18. D. J. Thouless, M. Kohmoto, M. P. Nightingale, *et al.*, Phys. Rev. Lett. **49**, 405 (1982).

19. P. Streda, J. Phys. C **15**, L717 (1982).

20. B. Huckestein and R. N. Bhatt, Surf. Sci. **305**, 438 (1997).

21. C. Albrecht, J. H. Smet, K. von Klitzing, *et al.*, Phys. Rev. Lett. **86**, 147 (2001).

22. G. Montambaux and M. Kohmoto, Phys. Rev. B **41**, 11417 (1990).

23. M. Kohmoto, B. I. Halperin, and Y. Wu, Phys. Rev. B **45**, 13488 (1992).

24. M. Koshino, H. Aoki, K. Kuroki, *et al.*, Phys. Rev. Lett. **86**, 1062 (2001).

25. B. A. Boyko, A. I. Bykov, M. I. Dolotenko, *et al.*, in *Book of Abstracts of the VIII International Conference on Megagauss Magnetic Field, Tallahassee, USA* (1999), p. 149.

26. D. Weiss, P. Grambow, K. von Klitzing, *et al.*, Appl. Phys. Lett. **58**, 2960 (1991).

27. J. Eroms, M. Zitzlsperger, D. Weiss, *et al.*, Phys. Rev. B **59**, R7829 (1999).

28. T. Schlösser, K. Ensslin, J. P. Kotthaus, *et al.*, Semicond. Sci. Technol. **11**, 1582 (1996).

29. M. G. Geisler, J. H. Smet, V. Umansky, *et al.*, in *Conference Workbook of the 15th International Conference on Electronic Properties of Two-Dimensional Systems, Nara, Japan, 2003* (2003), p. 149.

30. V. Ya. Demikhovskii and A. A. Perov, JETP Lett. **76**, 620 (2002).

31. A. Lorke, S. Wimmer, B. Jager, *et al.*, Physica B (Amsterdam) **249–251**, 312 (1998).

32. E. M. Baskin, G. M. Gusev, Z. D. Kvov, *et al.*, Pis'ma Zh. Éksp. Teor. Fiz. **55**, 649 (1992) [JETP Lett. **55**, 678 (1992)].

33. N. A. Usov, Zh. Éksp. Teor. Fiz. **94**, 305 (1988) [Sov. Phys. JETP **67**, 2565 (1988)].

34. D. A. Broido and L. J. Sham, Phys. Rev. B **31**, 888 (1985).

35. O. V. Volkov, V. E. Zhitomirskii, I. V. Kukushkin, *et al.*, Phys. Rev. B **56**, 7541 (1997).

36. M. Kubisa, L. Bryja, K. Ryczko, *et al.*, Phys. Rev. B **67**, 035305 (2003).

37. D. Weiss, *Book of Abstracts of the 15th International Conference on High Magnetic Fields in Semiconductor Physics, Oxford, UK, 2002* (Inst. of Physics, Portsmouth, 2002), p. 7.

38. V. Ya. Demikhovskii and D. V. Khomitsky, Phys. Rev. B **67**, 035321 (2003).

39. V. Ya. Demikhovskii and D. V. Khomitskiy, Phys. Rev. B **68**, 165301 (2003).

Translated by V. Sakun